Development of a compact test facility for SRF Photoelectron injectors

Dissertation

zur Erlangung des akademischen Grades

doctor rerum naturalium
(Dr. rer. nat.)

im Fach: Physik
Spezialisierung: Experimentalphysik

eingereicht an der
Mathematisch-Naturwissenschaftlichen Fakultät
der Humboldt-Universität zu Berlin

von

M. Sc. Jens Völker

Präsidentin der Humboldt-Universität zu Berlin:
Prof. Dr.-Ing. Dr. Sabine Kunst

Dekan der Mathematisch-Naturwissenschaftlichen Fakultät
Prof. Dr. Elmar Kulke

Gutachter: 1. Prof. Dr. Andreas Jankowiak
2. Prof. Dr. Kurt Aulenbacher
3. Prof. Dr. Wolfgang Hillert

Tag der mündlichen Prüfung: 27. November 2017

Abstract

Superconducting radio-frequency photoelectron injectors (SRF photoinjectors), operated in continuous wave (CW) mode, are promising electron sources for high brightness accelerators with high average current and short pulse duration like free electron laser (FELs) and energy recovery linacs (ERLs). For the ERL project bERLinPro, currently under construction at the Helmholtz-Zentrum Berlin (HZB), the SRF photoinjectors will be commissioned and studied in an independent test facility called GunLab.
GunLab was developed and set up to optimize the operation performance of SRF photoinjectors and to characterize the parameters of the beam core, as well as to study dark current and beam halo. Furthermore, GunLab allows to investigate the operation of different kinds of photocathodes in the environment of an SRF accelerator and to study new beam diagnostic concepts.
Of outmost importance is the characterization of the full six dimensional phase space as a function of drive laser, RF and solenoid parameters. GunLab consists of the compact diagnostic beam line, connected to the SRF photoinjetor module, and a drive laser, extracting the electron bunches from the photocathode.
In the context of this thesis, analytical and numerical investigations of the SRF photoinjector were performed to estimate beam parameter ranges and to determine the diagnostics requirements of GunLab. Furthermore, different analysis techniques for the determination and separation of various emittance contributors of the injector were developed and tested in simulations. One of these methods quantifies the impact of the lens aberration of the superconducting (SC) solenoid on the transverse phase space. It was also used to optimize the geometry of such an SC solenoid. Additionally, the magnetic field of the final designed solenoid was measured in a test cryostat at the GSI (Darmstadt) to determine the amplitudes of higher order multipole terms, which are one major source of emittance growth.
The design of the diagnostic beamline was optimized with extensive beam dynamic simulations of the photoinjector and the measuring processes. One of the central diagnostic components of the beamline is the phase space scanner system, visualizing the horizontal phase space of the electron bunches. For this purpose, a dedicated air-coil magnet design, used for dipole and quadrupole magnets, was developed, built and tested.
Additional components for the visualization of the longitudinal phase space include an optimized spectrometer system and a transverse deflecting cavity (TCav). In combination with the two quadrupole magnets, the sliced emittance can be determined with a developed reconstruction algorithm. A temporal resolution of 200 fs is achievable with this system.
For GunLab different optical measurement systems were developed and optimized, the most challenging setup is a beam halo measurement system. This device is able to observe potential beam halo regions with low charge densities simultaneously to the intense beam core with a dynamic range of up to 6 orders of magnitude.
The performance and the resolution of all measurement systems and routines for GunLab were determined to ensure the visualization of the electron beam phase space and an efficient characterization of the SRF photoinjectors under different operating conditions. The construction of all described elements, their test, setup and installation in the GunLab system, was accompanied. At the time being, GunLab is ready for first operation with beam.

Zusammenfassung

Supraleitende Hochfrequenz (SHF) Photoelektroneninjektoren, die im Dauerstrichbetrieb verwendet werden können, sind eine vielversprechende Elektronquelle für hochbrillante Teichenbeschleuniger mit hohem mittlerem Strom und kurzen Teilchenpulsen, wie Freie-Elektronen-Laser (FEL) und Linearbeschleuniger mit Energierückgewinnung (ERL). Für das ERL Projekt bERLinPro, dass derzeit am Helmholtz-Zentrum Berlin (HZB) gebaut wird, werden alle Phoinjektoren in einer unabhängigen Testanlage GunLab das erste Mal in Betrieb genommen und studiert. GunLab wurde entwickelt um die Leistungsfähigkeit der Injektoren zu überprüfen und um die Parameter des extrahierten Elektronstrahls zu charakterisieren, aber auch um Dunkelstrom und Strahl-Halo zu untersuchen. Darüber hinaus können unterschiedliche Photokathodenmaterialien innerhalb eines SHF Photoinjektors und neue Komponenten zur Strahldiagnose getestet werden. Die Hauptaufgabe von GunLab ist die Beschreibung des vollständigen sechsdimensionalen Phasenraums der Elektronen in Abhängigkeit der Parameter des Kathodenlasers, der HF und des Solenoiden. Die Anlage besteht aus einer kompakten Diagnosestrahlführung, verbunden mit dem SHF Photoelektroneninjektoren, und einem Kathodenlasersystem zur Erzeugung der Elektronenpulse aus der Photokathode.
Im Rahmen dieser Arbeit wurden analytische und numerische Studien zu den SHF Photoelektroneninjektoren durchgeführt, um zu erwartende Strahlparameter zu detektieren und die Anforderungen an die Strahldiagnose festzulegen. Darüber hinaus wurden verschiedene Analysetechniken entwickelt und numerisch getestet um die verschiedenen Emittanzbeiträge der Injektorkomponenten zu rekonstruieren. Eine dieser Methoden quantifiziert den Einfluss von Aberrationen eines supraleitenden Solenoiden auf den transversalen Phasenraum. Damit ließ sich auch die Geometrie eine solchen Solenoiden optimieren. Des Weiteren wurde das Magnetfeld des aktuellen Solenoiden in einem Testkryostaten an der GSI (Darmstadt) kartiert um die Amplituden der magnetischen Multipolterme zu bestimmen. Diese Terme tragen ebenfalls zu einer Emittanzvergrößerung bei.
Der Aufbau der Diagnosestrahlführung wurde mit Hilfe von umfangreichen Simulationen des Photoinjektors und der Messsysteme optimiert. Eine der wesentlichen Komponenten ist das Phasenraummesssystem, das den horizontalen Phasenraum des Elektronenstrahls darstellt. Hierfür wurde eine besondere Magnetausführung entwickelt, getestet und gebaut, die in der Anlage für Dipol- und Quadrupolmagneten verwendet wird.
Weitere Komponenten für die Visualisierung des longitudinalen Phasenraums sind installiert. Das beinhaltet einen optimierten Spektrometerdipol und eine transversal ablenkende Kavität. Zusammen mit den zwei Quadrupolmagneten lässt sich auch die Scheibenemittanz der Elektronenpakete durch einen Rekonstruktionsalgorithmus bestimmen. Mit diesem System ist eine zeitliche Auflösung von 200 fs möglich.
Für GunLab wurden unterschiedliche optische Messsysteme entwickelt und optimiert. Der herausforderndste Aufbau ist dabei das Strahl-Halo Messsystem. Es ermöglicht die gleichzeitige Beobachtung des Hauptelektronenstrahls und möglicher Strahl-Halo-Regionen mit geringeren Ladungsdichten über einen Dynamikbereich von bis zu 6 Größenordnungen.
Die Leistungsfähigkeit und die Auflösung aller Messsysteme und Messroutinen wurden bestimmt, um die Visualisierung des kompletten Phasenraums durch GunLab und eine effiziente Charakterisierung der SHF Photoinjektoren unter verschiedensten Einstellungen sicher zu stellen. Der Aufbau aller beschriebenen Komponenten (Entwicklung, Test und Einbau in GunLab) wurde mit begleitet. Zu diesem Zeitpunkt ist GunLab bereit für ersten Strahlbetrieb.

Contents

Chapter 1

Introduction

Particle accelerators are used in several scientific areas as dedicated particle and radiation sources. In the case of radiation sources, a strong motivation is to improve the particle beam quality to increase the spatial resolution of the generated photon beams.
Therefore the size of the emission source is important. It is included in the brightness of the radiation source.

$$\text{Brightness} = \frac{\text{Photon flux}}{\text{Source point area}}. \tag{1.1}$$

Here, the *Photon flux* (intensity) of the source is a function of the wavelength and depends on the spectra of the radiation. The *Source point area* describes the projected transverse beam area, combined with the beam divergence at the source point. In *rms* values this can be written as

$$\text{source point area} = \sigma_x \sigma_{x'} \sigma_y \sigma_{y'} \tag{1.2}$$

with x and y as the coordinates and x' and y' as the divergences of the beam in horizontal and vertical direction. The product of the *rms beam size* σ_x and the *beam divergence* $\sigma_{x'}$ is in first order the area of the horizontal or vertical phase space, determined by the *emittance* ε of the beam. For a high brightness radiation source, a particle accelerator has to combine small transverse emittances with a high charge particle beam, for high photon flux. The increase of the brightness is one of the central drivers for the development of modern particle accelerators.

Particle accelerators

There are several techniques of electron accelerators to achieve this goal. All of them can be divided into two groups: circular and linear accelerators. In a circular accelerator the electron beam is stored in a circular beam optic structure, passed by the beam many times. In such a multi-turn machine the beam is damped and excited by different mechanisms, such as synchrotron radiation and Touschek scattering. The resulting beam quality is given by the equilibrium state between excitation and damping. It is a natural limit for a circular accelerator. On the other hand, the stored charge in a multi-turn machine results in high virtual beam power, depending on the average beam current and kinetic energy. It allows the generation of high power photon beams. Only energy losses by synchrotron radiation and charge losses have to be replenished.
In a linear accelerator the electron beam is generated in an electron source and accelerated in several stages up to the final energy, without generation of significant synchrotron

radiation. In contrast to a circular accelerator, no equilibrium state of the electron beam exists and the beam quality is mainly defined by the beam quality, provided by the electron source. However, there are other effects that can lead to a beam breakup and have to be considered for linear accelerators. Furthermore, the single pass acceleration of the individual bunches leads to a real power value of the beam that needs to be dumped after the experimental use. Therefore, only comparable small average beam currents are possible in the regime of high kinetic energies at the GeV scale.

ERL

An Energy Recovery Linac (ERL) combines the advantages of both accelerator methods without their limitations.

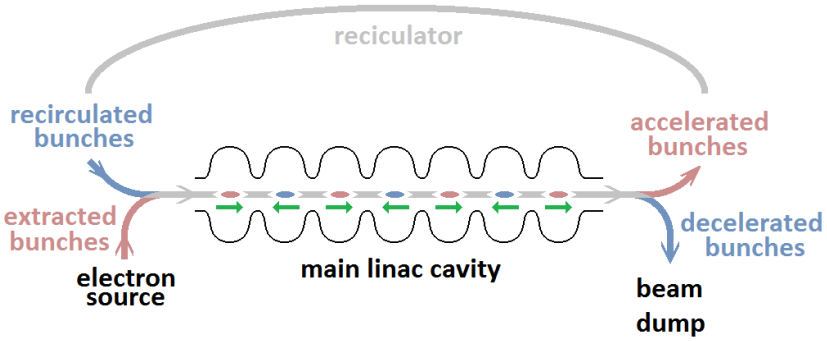

Figure 1.1: Sketch of the ERL principle inside the RF resonator (cavity). The green arrows in the cavity cells indicate the direction of the acceleration at the time of beam passing. This direction oscillates with a frequency of 1.3 GHz.

An ERL consists of a closed circular structure with an RF linear accelerator section (Linac), an electron source and a beam dump. The ERL principle is depicted in Fig. 1.1. The extracted electron bunch is accelerated in the Linac and passes through the recirculator. After one turn, the recirculated beam again enters the Linac, shifted by 180 degree in phase, relative to the RF accelerating field. The kinetic energy of the recirculated beam is recovered via the RF fields to the fresh incident beam. Thus, the net energy for the beam acceleration is zero. The decelerated beam is separated from the accelerated beam and dumped.

Each electron bunch passes the recirculator only ones so that an equilibrium state cannot appear. The resulting beam emittance is determined by the electron source and the proper set up for the beam optics of the accelerator. Furthermore the energy recovery allows higher average beam currents than in a linear accelerator. In a longterm run with ideal recovery efficiency the current is only limited by the maximal beam power at the electron source. The ERL principle was demonstrated in several projects like at the JLAB ERL [1], Budker [2], Darsbury (ALICE) [3], JAERI [4] and 2014 with the compact ERL (cERL) at KEK [5]. All of them operate with either low repetition rates, small beam currents or large transverse emittances. The goal for future ERLs is to improve all three parameters simultaneously. The Berlin Energy Recovery Linac Project (bERLinPro) will demonstrate the feasibility to combine a high average beam current in an ERL mode with small transverse emittances and short bunch lengths.

1.1 bERLinPro

bERLinPro [6] is the compact Energy Recovery Linac (ERL) project of the Helmholtz Zentrum Berlin (HZB) to demonstrate the combination of a high average beam current and low transverse emittances with an ERL mode. All accelerating structures of the bERLinPro accelerator consist of superconducting RF (SRF) cavities to achieve a high beam current in a continuous wave (CW) ERL mode. The bunch repetition rate can be increased up to 1.3 GHz, the resonance frequency of the accelerating mode of the SRF cavities. A graphic of the complete accelerator structure is shown in Fig. 1.2.

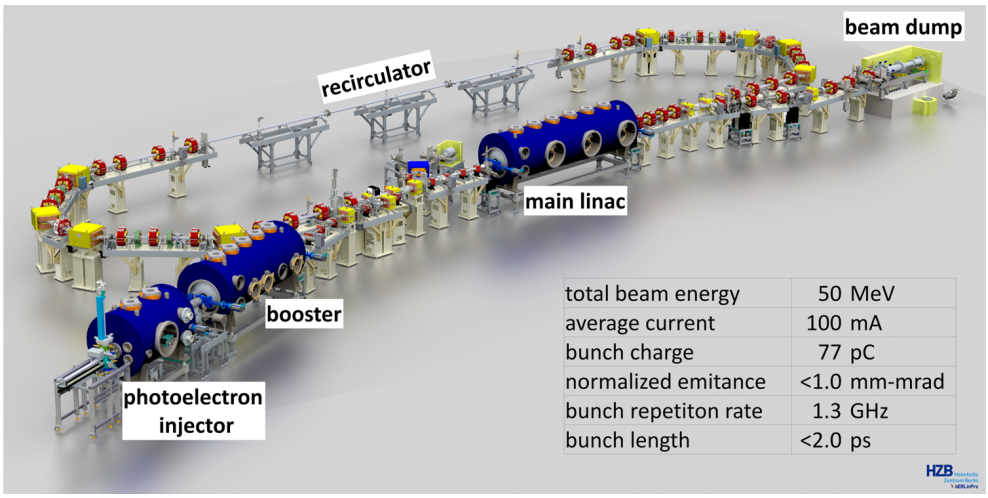

Figure 1.2: Graphic of the bERLinPro accelerator.

The electron bunches are extracted from a photo cathode inside an 1.4 cell SRF cavity (SRF gun) and accelerated to energies up to 2.5 MeV. The three two-cell *booster* cavities compress the bunches longitudinally and accelerate them up to 6 MeV. The main linac structure consists of three seven-cell cavities, accelerating the electron beam to the final kinetic energy of up to 50 MeV. The beam passes the main linac twice: the first time to accelerate the electron bunches and the second time to decelerate them after one turn through the recirculator. With the maximum 1.3 GHz repetition rate of the electron bunches, generated at the source, every RF bucket of the acceleration mode is filled. The crucial element for a high electron quality is the SRF photoelectron injector which provides small electron beam emittance and high average currents up to 100 mA.

Electron extraction in the SRF gun

SRF photoelectron injectors are the most promising technology to produce high brilliant electron beams to fulfill the requirements of future electron accelerators. They combine small transverse emittances and short bunch lengths with high repetitions rates in CW mode. The electron bunches are extracted from a normal conducting photoelectron cathode inside an SRF cavity by a pulsed drive laser synchronized to 1.3 GHz and are accelerated by a high gradient RF field. A solenoid magnet downstream the cavity focuses the beam to a further acceleration stage or an experimental setup. These four components of the SRF photoelectron injector, as well as the space charge of the potential high charged electron beams, determine the parameters of the emitted electron bunches. Therefore a dedicated test facility is necessary to investigate the individual and correlated effects of these components on the electron beam.

1.2 GunLab

GunLab was established at the HZB as compact test facility to measure and characterize the full six dimensional phase space of the extracted photoelectron bunches and to optimize all operation aspects of an SRF photoinjector. GunLab provides the whole infrastructure, such as drive laser, RF power supplies and cryogenic supplies to operate the phototinjector independent of the setup and operation of bERLinPro. With the compact diagnostic beamline, the electron beam can be analyzed with several measurement systems to determine the transversal and longitudinal electron beam phase space.
Within the framework of this thesis the beamline was designed and set up in GunLab. A graphic of the diagnostic beamline, connected to the gun module, is depicted in Fig. 1.3. Several measuring systems and measurement routines were developed and tested. Intense simulations of the SRF photoinjector operation, as well as of the diagnostic devices, were performed, to allow an efficient use of the installations, right from the beginning of beam operation.

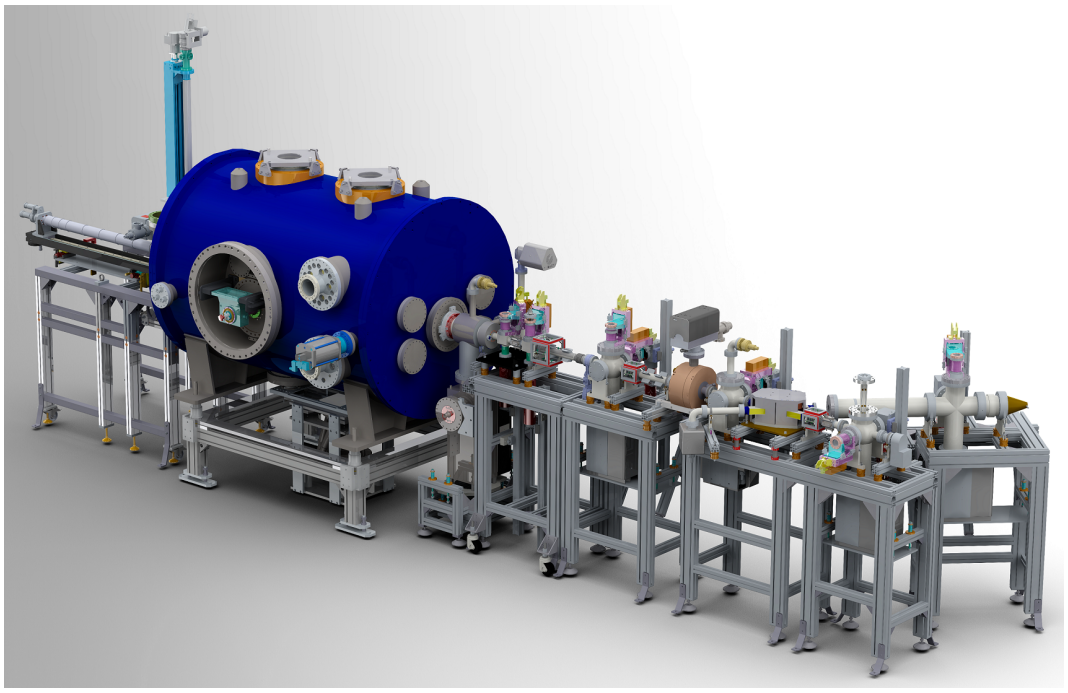

Figure 1.3: Drawing of diagnostic beamline of GunLab with the Gun module.

For the transverse phase space, a phase space scanner system was implemented in the beamline to visualize the horizontal phase space. It required a compact, high quality dipole magnets, based on cosθ coils. These magnets were designed, fabricated, tested and installed. Additionally, two cos(2θ) quadrupole magnets were constructed. In combination with a new developed operation routine, they are used for the measurements of the projected and the sliced phase space. A transverse deflecting cavity (TCav) is used as part of the longitudinal phase space visualization. This thesis has contributed to design the dedicated spectrometer dipole for GunLab. The spectrometer, combined with the TCav, images the longitudinal phase space on a viewscreen, directly.
Several subsystems, like viewscreen monitors and a fast bunch charge measurement system, were developed. With the diagnostic beamline of GunLab, several beam instrumentations can be tested under real-life conditions, such as different viewscreen materials. A multiscreen station was designed, consisting of five different viewscreens and a wire scanner system, to evaluate the impact of screen material and parameters on the accuracy

of the beam size measurement. Furthermore, the performance and the resolution of all GunLab measurement systems and measurement routines were extensively studied in the scope of this thesis, to ensure a high precision of the phase space visualization.

In Chapter 2, the theoretical background about the linear transformation of the electrons phase space inside a photoelectron injector is described and the impact of the different injector components on the transverse phase space, especially the transverse emittance, is discussed. Following, the technical aspects of the first photoelectron injector for GunLab are presented in Chapter 3.
In Chapter 4, the complete GunLab system, consisting of drive laser and diagnostic beamline, is described, starting from the idea of the design to its final realization. Furthermore, several measurement routines are discussed and their performance is analyzed. In Chapter 5 and Chapter 6, the phase space scanner system and the beam halo measurement system are presented in detail.
Prominent, in the context of this thesis is the development and the characterization of superconducting solenoid magnets. In this work, several properties of such a solenoid are studied, such as lens aberrations, astigmatism and higher order magnetic multipole field terms. Chapter 7 shows a measurement method, as well as the results, for the reconstruction of the field axis and higher order multipole amplitudes of the current solenoid in the first gun module. Finally, the whole diagnostic system is summarized in Chapter 8 and an outlook is given for the next steps of GunLab.

Chapter 2

Theory

The beam properties of an SRF photoelectron injector are the result of the injector parameter setting of photocathode, gun cavity, drive laser and solenoid magnet, as well as corrector magnets. They affect the distribution in the transversal and the longitudinal phase space of the emitted electron bunches. In this chapter the important beam parameters and their transformation in an SRF photoelectron injector are defined. As part of this thesis, the influences of a photoelectron injector on the emitted electron bunches were studied with detailed numerical simulations. The results are discussed in the following and are compared with theoretical models.

2.1 Linear phase space and matrix formalism

Each particle in a particle accelerator can be allocated to an individual coordinate in the six dimensional phase space, defined by $V = [x, x', y, y', \zeta, \delta]$. x, y and ζ are the horizontal, vertical and longitudinal positions in the reference frame relative to a reference particle which is guided through the accelerator along the path z with the momentum $p_{z,0}$. The terms $x' = \frac{p_x}{p_{z,0}}$ and $y' = \frac{p_y}{p_{z,0}}$ describe the horizontal and vertical slope in this reference frame between the particle path and the reference path. The parameter $\delta = \frac{\Delta p_z}{p_{z,0}}$ is the longitudinal momentum deviation between a particle and the reference particle. The trajectories of the particles through a component of the accelerator are the result of the Lorentz force [8]

$$\vec{F} = e\left(\vec{v} \times \vec{B} + \vec{E}\right) \tag{2.1}$$

with the magnetic $\vec{B}$ and the electrical field $\vec{E}$. These fields accelerate, bend or focus the particles with the charge value e. Thereby each particle also moves through the six dimensional phase space relative to the reference particle. In general, the transverse movement of a particle along z is given by a differential equation of motion for the radial offset $r = \sqrt{x^2 + y^2}$ with respect to the reference path: [9]

$$r'' + \left(\frac{\gamma' r' + \gamma'' r/2}{\gamma \beta^2}\right) + K_r r - \frac{\Omega}{r^3} = 0 \tag{2.2}$$

The prime represents the derivation of a function with respect to the beam path z. γ and β are the relativistic kinematics of the particles:

$$\gamma = \frac{1}{\sqrt{1-\beta^2}} \ , \ \beta = v/c, \tag{2.3}$$

The second term in Eq. 2.2 combines the influences of the particle acceleration in an axial electric field ($\gamma' \neq 0$) on the transverse movement. K_r represents the external magnetic force, which focuses or defocuses the particle path with respect to the reference axis. The last term implicates the centrifugal potential for non-zero angular momentum beams inside a longitudinal magnetic field, such as in a solenoid magnet. Otherwise, Ω is equal to zero and Eq. 2.2 did not include any transverse coupling terms. Thus r can be replaced by x or y, as well.
Eq. 2.2 can be solved analytically in sections where it is assumed that the coefficients of all terms are constant (hard edge model), e.g. a drift space where γ is constant and K_r is equal to zero. The solution of this linearized model determines a matrix R that transforms the particle coordinates of an passing electron. R is an unitary matrix with 6×6 elements. Each matrix element R_{ij} describes the linear correlation of the coordinate $V_i^{(\text{final})}$ in the final state on the coordinate $V_j^{(\text{initial})}$ in the initial state:

$$R_{ij} = \frac{\partial V_i^{(\text{final})}}{\partial V_j^{(\text{initial})}} \tag{2.4}$$

Such a transfer matrix can be determined for each linear element in an accelerator like a drift space (R_{drift}) or bend magnet (R_{bend}):

$$R_{\text{drift}} = \begin{pmatrix} 1 & L & 0 & 0 & 0 & 0 \\ 0 & 1 & 0 & 0 & 0 & 0 \\ 0 & 0 & 1 & L & 0 & 0 \\ 0 & 0 & 0 & 1 & 0 & 0 \\ 0 & 0 & 0 & 0 & 1 & \frac{L}{\gamma^2} \\ 0 & 0 & 0 & 0 & 0 & 1 \end{pmatrix} \tag{2.5}$$

$$R_{\text{bend}} = \begin{pmatrix} \cos\theta & R\sin\theta & 0 & 0 & 0 & R(1-\cos\theta) \\ -\frac{\sin\theta}{R} & \cos\theta & 0 & 0 & 0 & \sin\theta \\ 0 & 0 & 1 & R\theta & 0 & 0 \\ 0 & 0 & 0 & 1 & 0 & 0 \\ -\sin\theta & -R(1-\cos\theta) & 0 & 0 & 1 & R(\frac{\theta}{\gamma^2} - \theta + \sin\theta) \\ 0 & 0 & 0 & 0 & 0 & 1 \end{pmatrix} \tag{2.6}$$

with L as the drift length, R and θ as the bending radius and bending angle.

2.2 Electron generation and acceleration in a photoinjector

In a photoelectron injector three processes determine the transformation, as well as the initial electron configuration in the six dimensional phase space. These are the photocathode, the SRF cavity and the solenoid.
These three processes are presented in the following.

2.2.1 Photoelectron emission

Electrons are emitted from the photocathode by the photoelectric effect. The emission process defines the transversal and longitudinal momentum of the extracted electrons and depends on the cathode material and the wavelength of the drive-laser. An often used

model for the electron emission from metallic cathodes is described explicitly in Ref. [13]. It divides the process into three steps: the photon entering into the cathode material, the electron excitation in the material and the electron emission through the surface of the cathode. These processes are illustrated in Fig. 2.1(b). For all three steps the individual kinematics and probabilities can be calculated which result in an estimation of the quantum efficiency (QE) and the momentum of the emitted electrons. Thereby the cathode surface is modeled by a step potential that has to be passed by the excited electrons. The electric field of the SRF gun cavity on the cathode surface changes the shape of this potential into a potential barrier (Schottky-effect). The resulting shape is plotted in Fig. 2.1(b), as well. It is obvious that this Schottky barrier results in higher QE values and in a non-zero probability for the tunneling of non-excited electrons (dark current - Chapter 2.6).

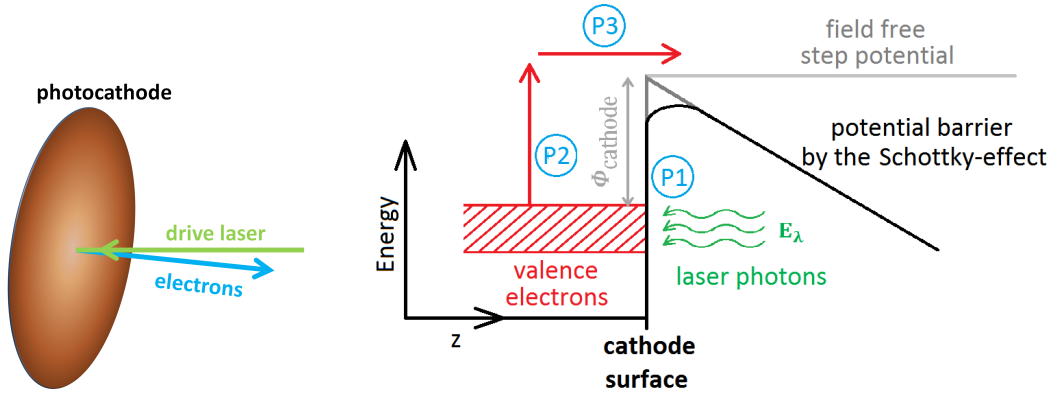

(a) (b)

Figure 2.1: Photoelectron emission inside the SRF gun cavity triggered by the drive laser(a) and the principle of the emission in the three-step-model (b) including the three processes: photon absorption (P1), electron excitation (P2) and electron propagation and emission from the cathode surface (P3). In combination with an external electric field the classical step potential is transformed by the Schottky-effect creating a potential barrier.

2.2.2 SRF cavity

The SRF cavity is an rotational symmetric elliptical 1.4 cell cavity operated in an accelerating π-mode at 1.3 GHz. Fig. 2.2 shows the radial cross section of such a cavity geometry and the resulting field distribution. It was calculated by the field solver program Poisson/Superfish [25]. The electromagnetic field inside the cavity is also rotational symmetric and can be described next to the cavity axis by the longitudinal field profile of the electric field $E_{z,0}$ on axis which is also plotted in Fig. 2.2 as a function of z. The electromagnetic field components next to the central axis are determined as higher order deviations of the field profile. [12] For a standing wave in the first transverse magnetic mode (TM010) these components are given in linear order by:

$$E_z(r) = E_{z,0} \tag{2.7}$$

$$E_r(r) = -\frac{r}{2}E'_{z,0} \tag{2.8}$$

$$B_\phi(r) = \frac{\omega}{c^2}\frac{r}{2}E_{z,0} \tag{2.9}$$

The radial field components E_r and B_ϕ determine the transverse beam optic for the

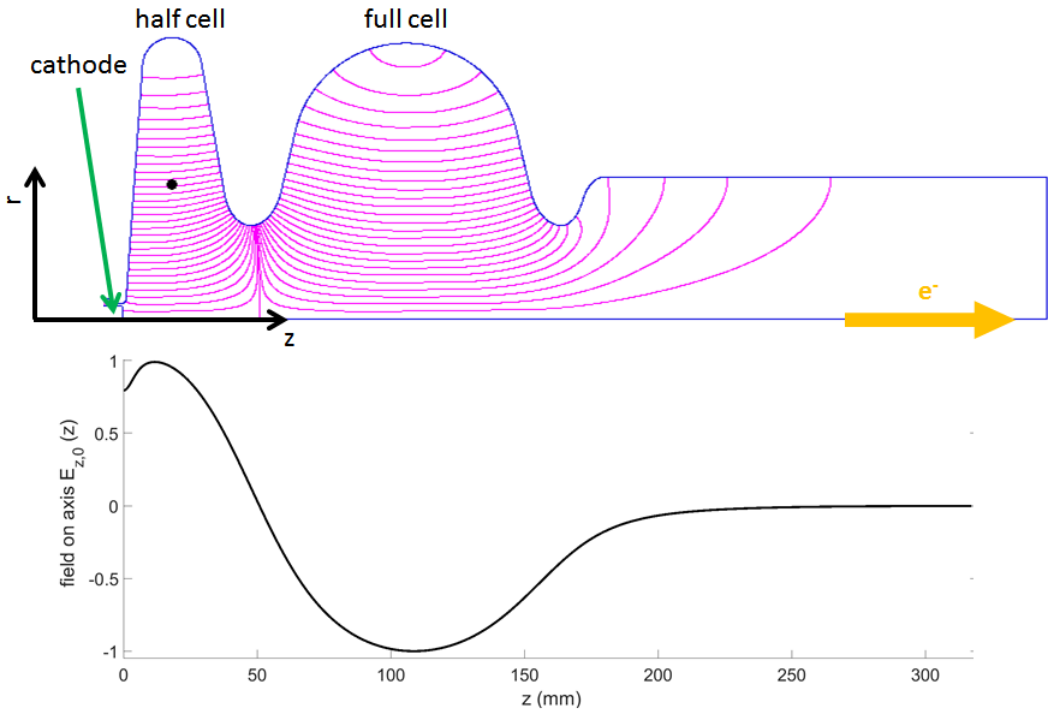

Figure 2.2: Example of a gun cavity geometry as radial cross section with calculated electric field distribution and the field profile on axis of the TM010 mode.

passed electron bunch which starts next to the back wall of the cavity and onwards through accelerating by the longitudinal field in the first half cell. When the electron bunch enters the full cell of the cavity the polarity of the field is changed for further acceleration. The resulting momentum of the emitted electrons as well as the transfer matrix of the cavity depends on the integrated field components (Eq. 2.7 to Eq. 2.9) along the particle trajectories. All components of these equations are also a function of the emission phase from the photocathode. Here, 'Phase' means the time difference in units of radian with respect to the RF period. As an example, the absolute emission phase is the time between the zero crossing of the acceleration field amplitude on cathode and the electron emission.
The emission phase is often given in relation to the on-crest phase. It is defined as the emission time with the maximum achievable kinetic energy of the electrons for a given cavity gradient. This correlation is depicted in Fig. 2.3. The momentum of the reference particle and the slop of an off-axis particle at the exit of the cavity are plotted as function of the absolute emission phase and the peak field in the cavity. The momentum and the optics of the cavity depends strongly and non-linearly on both cavity parameters. This also affects the focal strength of the solenoid magnet positioned downstream from the gun cavity, to focus the emitted electron beam.

2.2.3 Solenoid magnet

A solenoid is a focusing magnet that induces a rotational symmetric magnetic field with a longitudinal field orientation respectively to the beam axis. Often, a return yoke (henceforth referred to as yoke) is used to concentrate the magnetic flux of the excitation coil and to increase the longitudinal flux density on the magnet axis. Fig. 2.4 shows the cross section of the rotational symmetric GunLab solenoid. Furthermore the field distribution

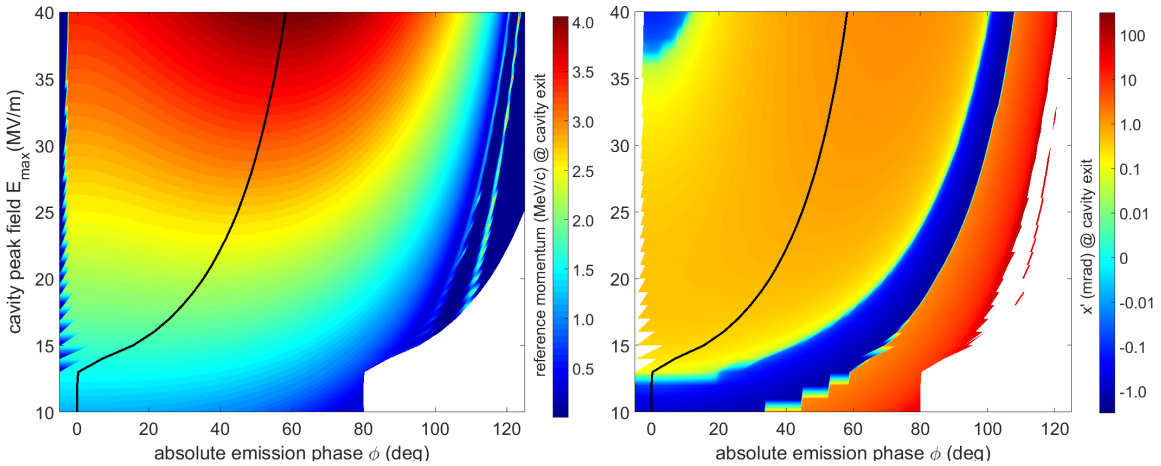

Figure 2.3: Surface plots of the momentum (a) and the optics (b) as function of emission phase and peak field in the cavity for Gun1 with a 1.5 mm retracted cathode relative to the back wall of the cavity. The optic is represented by the slope of a tracked particle at the exit of the cavity. This particle starts with an offset $x = 1$ mm, $x' = y = y' = \delta = \zeta = 0$ from the cathode surface. The black curve in both plots illustrates the on-crest phase for the defined cavity peak fields.

of the magnet geometry is plotted. It was calculated by the field solver Poisson/Superfish. The magnetic field distribution in cylindrical coordinates close to the magnet axis can be described by a series of the deviation terms of the longitudinal field profile.

$$B_z = \sum_{n=0}^{\infty} \frac{(-1)^n}{(n!)^2} \frac{\partial^{2n} B_{z,0}(z)}{\partial z^{2n}} \left(\frac{r}{2}\right)^{2n} \tag{2.10}$$

$$B_r = \sum_{n=1}^{\infty} \frac{(-1)^n}{n!(n-1)!} \frac{\partial^{2n-1} B_{z,0}(z)}{\partial z^{2n-1}} \left(\frac{r}{2}\right)^{2n-1} \tag{2.11}$$

with r as the radial distance to the magnet axis and $B_{z,0}$ as the field profile along the solenoid axis ($B_0 = B_{z=0,r=0}$). Both field components are correlated, but have different effects on the beam. The radial field produces a azimuthal force on a particle with mainly longitudinal momentum. The sign of this force depends on the orientation of the solenoid field. The resulting azimuthal momentum interacts with the longitudinal field component of the magnet and induces an additional radial force term. The sign of this force is independent from the magnetic orientation, charged particles are deflected towards the axis. The combination of both forces produces a rotational symmetric beam focusing and a beam rotation around the magnet axis. The focal strength is the same in both transversal planes, respectively to a quadrupole magnet with only one focal plane. To describe these effects quantitatively, the equation of motion (Eq. 2.2) has to be solved with the hard edge model which simplifies the solenoid field. This calculation is depicted in [9] and results in the characteristic values for a solenoid magnet:

$$\text{peakfield}: \quad B_0, \tag{2.12}$$

$$\text{focal length}: \quad \frac{1}{f} = k^2 L_{\text{eff}}^{(\text{foc})} \text{ and} \tag{2.13}$$

$$\text{the Larmor rotation}: \quad \theta_{\text{Larmor}} = k L_{\text{eff}}^{(\text{rot})}. \tag{2.14}$$

Here $k = \frac{B_0(\text{T})c}{2pc(\text{eV})}$ is the focal strength which depends on the momentum (pc) of the particle beam and the peak field on axis with c as the speed of light. Both effective lengths

($L_{\text{eff}}^{(\text{rotation})}$ and $L_{\text{eff}}^{(\text{focus})}$) can be identified as the normalized linear and squared field profile integrals along the magnet axis.

$$L_{\text{eff}}^{(\text{rotation})} = \int_{-\infty}^{\infty} \frac{B_z(z)\mathrm{d}z}{\max(B_z)} \quad , \quad L_{\text{eff}}^{(\text{focus})} = \int_{-\infty}^{\infty} \frac{B_z^2(z)\mathrm{d}z}{\max(B_z^2)}. \tag{2.15}$$

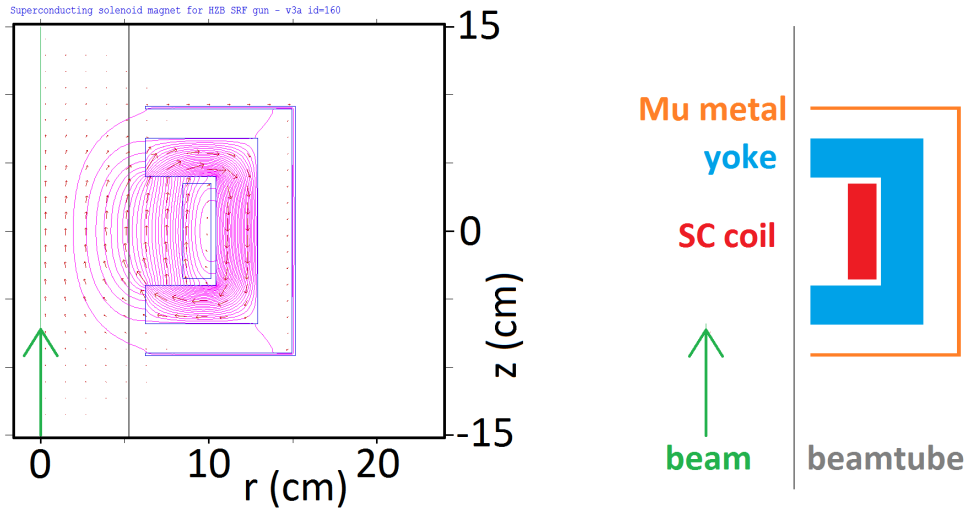

(a) (b)

Figure 2.4: Geometry (SC coil (red), yoke (blue), Mu-Metall (orange)) and field solution of the GunLab solenoid using Poison/Superfish.

The radial forces of the solenoid allows to focus the usally divergent photoelectron beam behind the gun cavity with a single magnet. Addition higher order field deviation terms of the solenoid, as well as the gun cavity, produce non-linear transformations of the phase space. A way to describe the resulting particle distribution in the phase space is the phase space area and the statistical parameter of several particles combined to a bunch.

2.3 Particle ensemble and emittance

Since it is not possible to reconstruct the phase space position of each particle individually, it is more practical to describe the distribution of the complete particle ensemble by statistical values of the particle projection on a phase space axis. These values are the moments of the projected distribution: e.g. the first moment or average position $\langle x \rangle$ as well as the second moment or the *rms* width $\langle x^2 \rangle$ on the horizontal axis. With these *rms* parameters the phase space area (emittance) of a complete particle ensemble can be determined. Two concepts of emittance calculation are described in the following.

2.3.1 Projected emittance

For the projected emittance the complete particle ensemble is projected on one of the three main phase space planes (horizontal, vertical and longitudinal). Fig. 2.5 shows an example of a particle distribution in the horizontal phase space (left) and the describing *rms* parameters (right). The distribution in the left plot is a two dimensional Gaussian distribution which has a correlation between the x and x' axis. The red curve corresponds

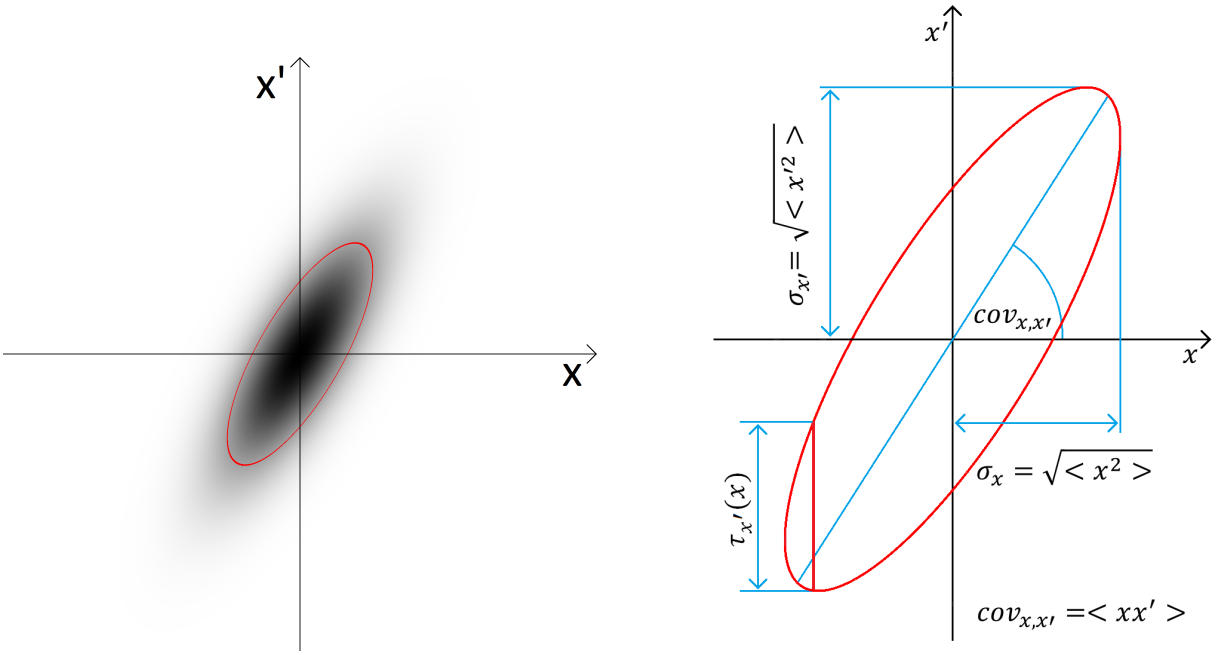

(a) 2d Gaussian distribution

(b) 1σ ellipse

Figure 2.5: Gaussian distribution in the horizontal phase space (a) with the both variances and the covariance (Σ-matrix) of this distribution (b). Additionally, the local divergence $\tau_{x'}(x)$ is depicted. It describes the divergence of the local slice (beamlet) at the position x.

to the 1σ-ellipse which is the envelope of 68% of the distribution. Furthermore it represents the distance to the centroid where the amplitude is decreased to $1/e$ relative to the central amplitude. The ellipse can be described completly by the two variances ($\langle x^2 \rangle$ and $\langle x'^2 \rangle$) and the covariance ($\langle xx' \rangle$). All three terms are the elements of the covariance matrix Σ of the original distribution.

$$\Sigma = \begin{pmatrix} \langle x^2 \rangle & \langle xx' \rangle \\ \langle xx' \rangle & \langle x'^2 \rangle \end{pmatrix} = \begin{pmatrix} \sigma_{x^2} & \sigma_{xx'} \\ \sigma_{xx'} & \sigma_{x'^2} \end{pmatrix} \tag{2.16}$$

The ellipse area in the phase space is named emittance ε and is given by the square root of the determinant of the covariance matrix.

$$\varepsilon_{\text{geo}} = \sqrt{\begin{vmatrix} \langle x^2 \rangle & \langle xx' \rangle \\ \langle xx' \rangle & \langle x'^2 \rangle \end{vmatrix}} = \sqrt{\langle x^2 \rangle \langle x'^2 \rangle - \langle xx' \rangle^2} \tag{2.17}$$

In this particular case Eq. 2.17 describes the geometrical emittance ε_{geo} which depends on the beam energy. To conserve the energy invariance, the normalized emittance $\varepsilon_{\text{norm}} = \varepsilon_{\text{geo}} \gamma\beta$ is needed. It is defined in a phase space with the absolute transverse momenta p_x and p_y instead of the slope x' and y'. Liouvilles law predicts the conservation of this phase space area for specific conditions (Chapter 2.5). The bunch ellipse is transformed through the phase space similar to the movement of a single particle (Eq. 2.2). However, the finite emittance of the bunch ellipse and the space charge forces have to be considered in this equation. For a bunch of equal charged particles the inner space charge forces defocus the beam. Thus, the resulting equation is given by: [9]

$$\sigma'' + \left(\frac{\gamma'\sigma' + \gamma''\sigma/2}{\gamma\beta^2} \right) + K_r\sigma - \frac{\kappa_{SC}}{\sigma} - \frac{\varepsilon_n^2}{\sigma^3(\gamma\beta)^2} = 0 \tag{2.18}$$

Thereby κ_{SC} is the perveance, describing the space charge defocusing term [10],

$$\kappa_{SC} = \frac{I}{2I_A(\gamma\beta)^3} \tag{2.19}$$

with I being the peak current and $I_A \approx 17\,\mathrm{kA}$ as the Alfvén current. Also, Eq. 2.18 cannot be solved analytically in every case. A further approximation to the hard edge model is needed to neglect either one of the last terms. Thereby it is distinguished between space charge dominated ($\frac{\varepsilon_n^2}{\sigma^3(\gamma\beta)^2} << \frac{\kappa_{SC}}{\sigma}$) and emittance dominated beams.
All terms in Eq. 2.18 are functions of the longitudinal position z and ζ, especially in cases where the charge and the momentum are not constant for the complete bunch. This can result in different solutions for the differential equation inside a single bunch as function of ζ. A longitudinal slicing of the bunch can visualize these varying solutions. Thus, the sliced phase space is an important observable to handle the inner bunch phase space variations and ellipse orientations.

2.3.2 Sliced phase space

To obtain the sliced emittance, Eq. 2.18 is solved as a function of ζ. The bunch is divided into transverse slices with the thickness $\delta\zeta$ and the slice charge relative to the bunch charge ($g(\zeta) = q(\zeta)/Q_{\mathrm{bunch}}$). Thereby the transverse emittance $\varepsilon(\zeta)$ can be calculated for each slice. The sliced emittance is than defined as the weighted sum of all emittance values with respect to the slice charge

$$\varepsilon_{\mathrm{slice}} = \sum_{\zeta} g(\zeta) \cdot \varepsilon(\zeta). \tag{2.20}$$

This value can be compared with the projected emittance which is the transverse phase space area of the complete bunch distribution. In case of mismatched slices the projected and sliced emittance differ. An example is shown in Fig. 2.6 where three slices are plotted with different phase space ellipses, but similar emittance and charge values. The black ellipse represents the projected phase space of the three slices with a different emittance and orientation. In this example the projected emittance is $\approx 50\%$ larger than the sliced emittance. These mismatched slices can arise from different effects like the RF focusing, an energy chirp of the beam or space charge, affecting the bunch distribution as function of ζ. For relativistic beams, the isotropic space charge forces in the rest frame of the bunch are compressed to the transverse plane in the laboratory system. Hence, in first approximation space charge affects only the transverse phase space and depends on the charge density in each slice, defined by $q(\zeta)$ and $\sigma(\zeta)$.
Another source for misaligned slices are RF fields in cavities. The slices of a bunch sample slightly different RF field strength, when the bunch passes the cavity. In this case $\varepsilon_{\mathrm{slice}}$ depends on the slice thickness $\delta\zeta$ and consequently on the number of slices in a bunch. In several numerical simulations of the photoelectron injector the convergence of the sliced emittance as function of $\delta\zeta$ was studied, resulting in a maximal slice thickness of ≈ 0.5 ps.
The resulting difference between slice emittance and projected emittance can be reduced by a dedicated focusing of the beam to a realignment of the slices. This process is named emittance compensation.

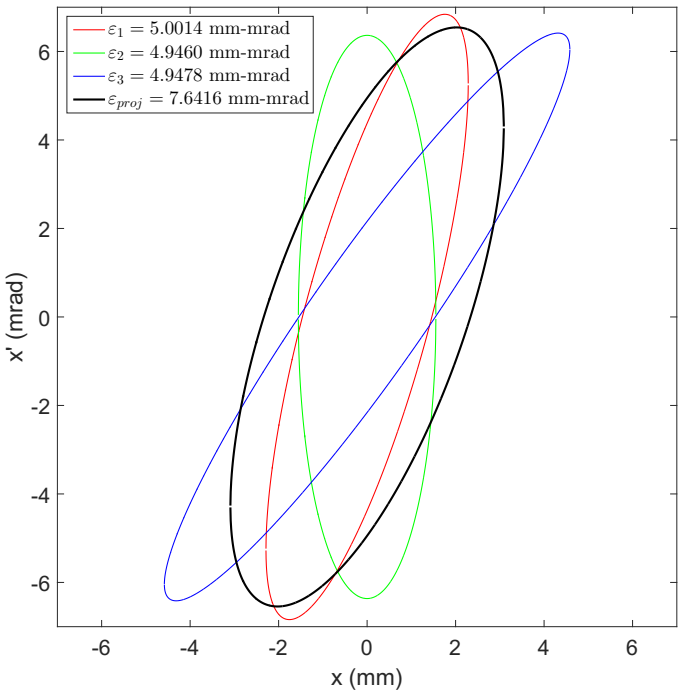

Figure 2.6: Plot of three 1σ ellipses (red, green blue) of phase space distribution with nearly the same horizontal emittance. All three distributions represent slices in one bunch and consist of the same charge value. The resulting projected phase space is characterized by the black ellipse that has an increased emittance value.

2.4 Emittance compensation

A bunch with mismatched slices, passing a section of the accelerator has an increased projected emittance relative to the sliced emittance. This can be compensated for by a dedicated radial focusing of the bunch in a focusing channel. Thereby the ellipses of the slices can oscillate about a reference ellipse which depends on the parameter of the focusing channel. A correct parameter setting attempts to align the ellipses at the end of the channel.

A detailed model of the emittance compensation can be found in the paper of L. Serafini and J. Rosenzweig [11]. They present a model to suppress the misalignment of the slices of a space charge dominated electron bunch. It is assumed that the particles were extracted in a normal conducting electron photoinjector combined with a focusing solenoid around the injector cavity. Their idea was to compensate the space charge force term $\frac{\kappa_{SC}}{\sigma}$ in Eq. 2.18 of a low emittance beam ($\frac{\varepsilon_n^2}{(\gamma\beta)^2\sigma^3} \to 0$) by an external radial focusing force $K_{r,eq}$ inside the focusing channel.

$$K_{r,eq} = \frac{\kappa_{\mathrm{SC}}}{\sigma_{eq}^2} \tag{2.21}$$

Eq. 2.18 is than given for the specific beam size σ_{eq} as $\sigma''_{eq} = 0$. In general σ_{eq} is not constant for all slices, because it depends on the charge density in the slices and therefore on the function $g(\zeta)$. A slice with a slightly different initial size $\sigma(\zeta, 0)$ to $\sigma_{eq}(g(\zeta))$ can be handled as a distortion of the perfect space charge compensated system which results

in an oscillation of $\sigma(\zeta)$ about σ_{eq}.

$$\sigma(\zeta,0) = \sigma_{eq}(g(\zeta)) + \delta\sigma(\zeta,0) \tag{2.22}$$

$$\Rightarrow 0 = \sigma''(\zeta,z) + K_{r,eq}\sigma(\zeta,z) - \frac{\kappa_{\mathrm{SC}}}{\sigma(\zeta,z)} \tag{2.23}$$

With Eq. 2.21 and the assumption that $\sigma(\zeta,z) \approx \sigma_{eq}$ the last terms can be combined.

$$\Rightarrow 0 = \sigma''(\zeta,z) + 2K_{r,eq}\sigma(\zeta,z) \tag{2.24}$$

$$\Rightarrow \sigma(\zeta,z) = \sigma_{eq}(g(\zeta)) + \delta\sigma(\zeta,0)\cos\left(\sqrt{2K_{r,eq}}z + \phi(\zeta)\right) \tag{2.25}$$

Eq. 2.25 shows that all slices have the same constant oscillation wave number $\sqrt{2K_{r,eq}}$, Furthermore, the oscillation is independent from the amplitude $\delta\sigma(\zeta,0)$ which should be small with respect to $\sigma_{eq}(g(\zeta))$. The additional phase shift term $\phi(\zeta)$ in Eq. 2.25 describes the initial misalignment for each slice at $z = 0$. This term was not relevant for Serafini and Rosenzweig, because they defined their start point of the focus channel directly at the photocathode where all slices are extracted with $\sigma' = 0$ and $\sigma(\zeta)$ =const.
The oscillation of the slices also affects the projected emittance of the bunch. This contribution can be obtained by the projected Σ matrix for the complete bunch. Thus $\sigma(\zeta,s)$ and the deviation $\sigma'(\zeta,s)$ have to be averaged over ζ and inserted into Eq. 2.17. The projected emittance contribution of the complete bunch is then given as function of the bunch position s,

$$\varepsilon \sim \sigma(\zeta,0)\sigma_{eq}(I_{\mathrm{peak}})\frac{\sqrt{K_{r,eq}}}{2}|\sin(\sqrt{2K_{r,eq}}s)|F\left(K_{r,eq},s,\phi(\zeta)\right) \tag{2.26}$$

where I_{peak} is the peak current of the bunch. The additional function $F\left(K_{r,eq},s,\phi(\zeta)\right)$ represents the influences of the initial misalignments of the slices. Eq. 2.26 shows that the projected emittance oscillates in the focus channel and can be minimized for a defined position using a specific external focusing force $K_{r,eq}$.
In case of an SRF photoinjector this model cannot be adopted directly. The diamagnetic properties of the superconducting material of the cavity insulate the inner region from any magnetic field of the outside region. Therefore, the solenoid has to be positioned downstream the cavity and can only focus the extracted beam with the misaligned slices. The radial cavity field next to the cathode can be used as compensation field, as well. However, this is not sufficient enough to compensate the complete mismatch. For the emittance compensation in this case, the slices have to be realigned by the focus channel that only consists of the solenoid and the drift space downstream. Even if K_r is not a constant in this channel this process still works, because the solenoid is used to focus the beam which acts as a space charge overcompensation where all slices are bigger than the ideal compensation size ($\sigma_{eq}(\zeta) << \sigma(\zeta,0), \forall\zeta$).
Therefore the third and the fourth term in Eq. 2.18 can be neglected and the beam is focused until the size of the slices is comparable with σ_{eq}. At this position the space charge term is relevant again with the result that the slices starts to oscillate. In this channel, the K_r term is defined as the effective focal force and σ_{eq} can be determined as the beam waist downstream from the solenoid. This means that the emittance compensation point is next to the focal point of the beam. This is plotted in Fig. 2.7. It shows the result of a particle tracking with the tracking program ASTRA [12]. In this simulation electrons are extracted from the cathode and accelerated in the SRF gun. A solenoid ($z_{\mathrm{sol}} = 0.5$ m) focuses the beam at 2.03 m from the cathode. Only linear field deviations of the

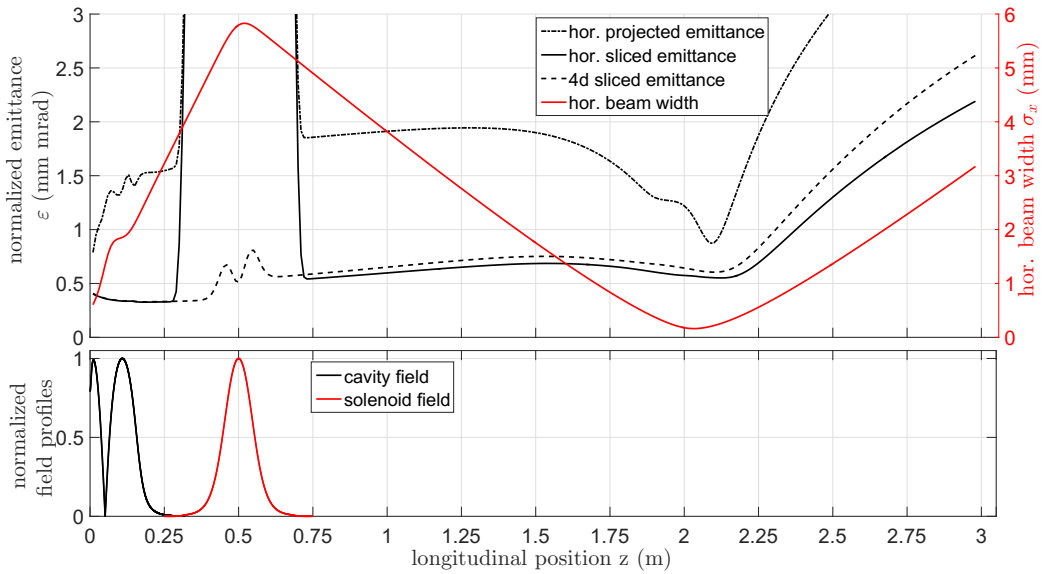

Figure 2.7: Tracking of an extracted photo electron bunch through the SRF cavity and the solenoid up to 3 m downstream from the photo cathode. The projected and sliced emittances are plotted as black curves. Simulation details: The bunch consists of one million particles (77 pQ) with a radial uniform distribution of 0.5 mm (*rms*) and a pulse length of 2.8 ps (*rms*) at the cathode surface, positioned -1.5 mm relative to the cavity back wall. The bunch is extracted at -12 degree relative to the on-crest phase in the cavity field with 30 MV/m field strength. In this simulation the SC solenoid at $z = 0.5$ m focuses the beam with a peak field of 81.6 mT. Only linear field deviations of the solenoid field were used to highlight the emittance compensation and suppress non linear solenoid effects. (see Chapter 2.2.3)

solenoid were used to suppress non linear emittance effects. The resulting beam size is plotted as red curve in Fig. 2.7. The other three curves represent the sliced (solid line) and projected emittance (dotted line) as function of z. The maximum of the beam size is inside the solenoid. The increased emittance values inside the solenoid are a result of the Larmor rotation that connects the horizontal and vertical phase spaces by an azimuthal momentum. This correlation effect is taken into account with the complete transversal emittance ε_{4d}. It is the area of the four dimensional phase space distribution in the transversal plane (dashed line in Fig. 2.7). Thereby, the azimuthal momenta of the particle inside the solenoid (beam rotation) are also applied. Outside the solenoid magnet the 2d and 4d sliced emittance values are similar. The projected emittance behind the solenoid is minimized next to the beam waist (beam size minimum) as it was expected for such a focusing channel. Downstream the solenoid the behavior of the sliced and the projected emittance are similar. Both values have a small emittance growth behind the solenoid, as well as a overlayed structure at the emittance compensation point. These are the result of non-linear space charge effects of the individual slices.

Despite this the simulations show that the concept of the emittance compensation works for an SRF photoelectron injector, as well. A mismatch of sliced emittance and projected emittance can be decreased by the solenoid, but cannot be compensated completely. Furthermore there are other emittance effects, increasing the projected phase space volume in addition to the mismatch of the bunch slices. Some sources for a possible emittance growth are discussed in the following section.

2.5 Sources of transverse emittance in an SRF photoelectron injector

The path of particles defined in a phase space system with independent coordinates will be a closed orbit, if the interacting forces are conservative. The area of this enclosed path is a constant according to Liouvilles law. Coordinates of a projected phase space, like the horizontal phase space, are independent in cases where the distribution is uncorrelated from the vertical or longitudinal coordinates. Otherwise the phase space interaction affects the distribution. This distribution is determined by an electromagnetic field in a region, passed by the charged particles. The resulting force will be conservative, if the net work for a closed path integral is zero. Therefore all static external electromagnetic fields in an accelerator produce conservative forces. However, dynamic fields can manipulate the phase space area. Examples for those are RF cavity fields and space charge forces, which depend on the particle distribution itself.
This definition of the phase space area in Liouvilles law is different to the *rms* emittance definition which describes the area of the 1σ ellipse by statistical parameters of the original distribution. E.g.; a non-linear external field transforms an initial two dimensional Gaussian phase space distribution. The linear emittance value is distorted, however, the phase space area by Liouvilles definition is still constant. (Fig. 2.8).

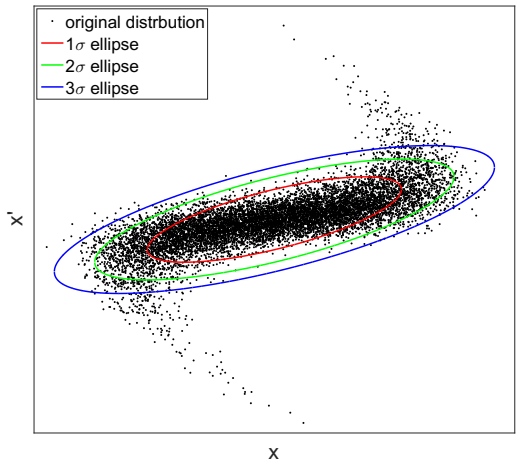

Figure 2.8: Gaussian particle distribution (dots) in the horizontal phase space which was transformed by a focusing element with a third order term. The resulting distribution was sampled behind a short drift space. The three ellipses depict the 1σ-, 2σ- and 3σ-ellipses of the distribution.

There are different sources of these non-conservative or non-linear phase space influences which manipulate the transverse emittance of a bunch. Additional to the mentioned space charge effects or the RF cavity fields other sources exist. Those are the electron emission at the cathode or nonlinearities in the solenoid and other magnets. In most cases it is possible to approximate the impact on the emittance of an individual contributor. They are presented in the following sections.

2.5.1 Photocathode

Electrons are emitted from the photocathode by the photoelectric effect. A model for the photoemission process was depicted in Chapter 2.2.1. It results in a momentum

distribution, depending on the cathode material and the laser wavelength. The *rms* width of this momentum distribution (σ_{p_x}) is used to calculate the normalized transverse emittance of the cathode (intrinsic or thermal emittance) as a function of the *rms* spot size σ_x on the cathode surface:

$$\sigma_{p_x}^2 = mc^2 \frac{E_\lambda - \Phi_{\text{eff}}}{3} \tag{2.27}$$

$$\varepsilon_{n,\text{thermal}} = \frac{\sigma_x \sigma_{p_x}}{mc^2} = \sigma_x \sqrt{\frac{E_\lambda - \Phi_{\text{eff}}}{3mc^2}} \tag{2.28}$$

with E_λ as the photon energy of the drive laser. Φ_{eff} as the effective work function of the cathode material that depend on the cathode material and the electric field strength on the surface (Schottky effect). For a CsK_2Sb photocathode and a drive laser wavelength of 515 nm the intrinsic emittance was experimentally determined by Bazarov et al. [14]:

$$\varepsilon_{n,\text{thermal}} = (0.575\ \sigma_x[\text{mm}])\ \text{mm-mrad} \tag{2.29}$$

Here it was assumed that the electron emission is homogeneous and the cathode surface is flat. If this is not given, additional effects must be considered, that were studied numerically in Ref. [15, 16]. There, two models are presented to analyze the phase space effects of a photocathode. For the first model small spikes were distributed on the surface of the cathode. They produce an electric field enhancement and also transverse electric field components. This can heat up the emitted electron cloud which increases the transverse emittance of the bunch up to a factor of 2. The second problem is a inhomogeneous QE value on the cathode, producing an non-uniform transverse charge distribution, as well. In extreme cases this can distort the reconstruction of the *rms* parameters of the bunch.

2.5.2 RF field in the cavity

Radio frequency (RF) electromagnetic fields inside a cavity influence the slices of an emitted bunch due to different transversal focusing forces and accelerating field amplitudes. This produces a misalignment of the transversal slices, depending on the bunch length and the beam size. A detailed model for the transverse effects of the RF field inside a photoelectron cavity is described by Kim [18]. With this model the projected emittance can be determined for a longitudinal Gaussian pulse which has to be short with respect to the RF period.

$$\varepsilon_{n,RF} = \frac{eE_0}{2mc^2} \sigma_{x,e}^2 \left(|\cos\phi_e| \sigma_{\phi,e} + |\sin\phi_e| \frac{\sigma_{\phi,e}^2}{\sqrt{2}} \right) \tag{2.30}$$

Where E_0 is the accelerating field in the cavity, e and mc^2 are the charge and the mass of the electrons. ϕ_e represents the exit phase of the bunch and $\sigma_{\phi,e}$ the length of the emitted bunch at the exit of the cavity in radian units of the RF period. The description of the bunch parameters in Eq. 2.30 at the exit of the cavity is not practical for the work with the injector. These parameters are not independently adjustable and measurable. The feasible parameters for the beam setup are the spot size radius on the cathode surface, the pulse length of the drive laser and the emission phase of the bunch. The influences of these three start parameters were studied numerically using ASTRA. An SRF gun cavity field profile was simulated with a peak field of 30 MV/m. The radius and the emission phase of the bunches were scanned in a range of 0.5 mm to 4 mm and ±30 degree relative

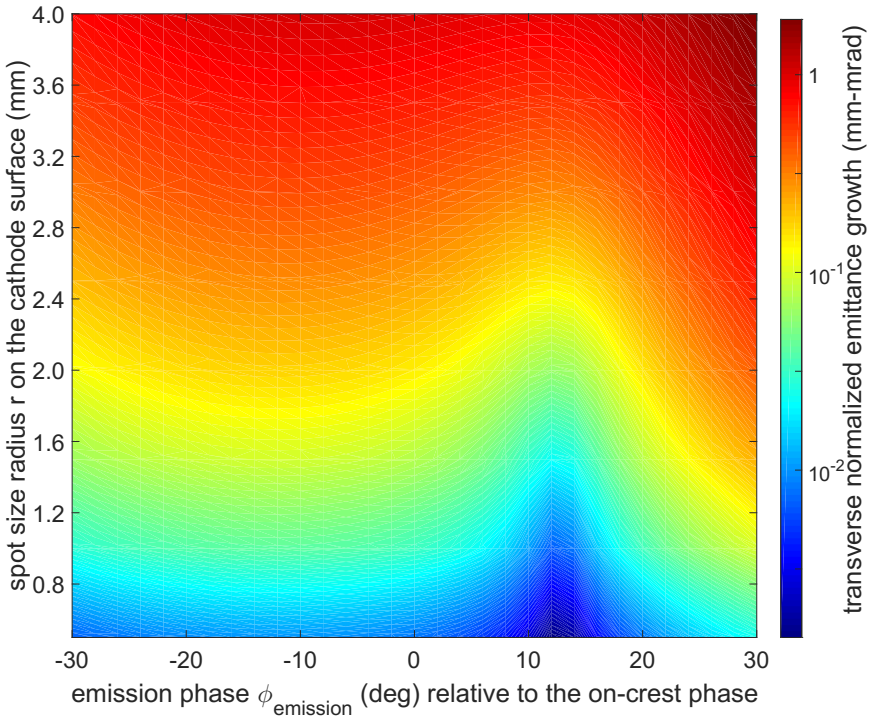

Figure 2.9: Example of calculated emittance growth due to RF effects of the SRF photoinjector. Tracking based on a gun cavity field profile with a photocathode position of -1.5 mm relative to the back wall and a 30 MV/m peak field in the cavity. The initial particle distributions on the cathode surface consist of 10,000 particles with zero space charge, energy spread or transversal emittance. The emitted bunches have a FlatTop profile with a spot size radius r on the cathode surface and temporal Gaussian emission profile with a constant emission length of 4.7 ps (*rms*).

to the on-crest phase, respectively. Thereby, the transverse electron emission was defined as a FlatTop distribution on the cathode, where r is given by $r = 2\sigma_x$. Fig. 2.9 shows the emittance results for a 4.7 ps (*rms*) long pulse on the cathode. The projected horizontal emittance at the exit of the gun cavity is plotted as function of the emission phase and the spot size radius. As it can be seen, the emittance growth of the RF can be reduced by small spot size radii and a positive emission phase relative to the on-crest phase. The simulation results can be compared with Eq. 2.30. Here the relevant bunch values at the cavity exit were sampled in the simulations and used to calculate the emittance growth. It was found that the simulated emittance growth confirms the calculated values with only small differences. These small deviations can be explained by a non well defined exit position of the cavity, which affects the values of beam size and length. Fig. 2.9 shows further that for spot size radii less than 2 mm the projected emittance growth is influenced by $\varepsilon_{n,\mathrm{RF}} \leq 0.1$ mm-mrad. The impact on the sliced emittance is almost independent from these three initial parameters and was approximated to ≈ 0.01 mm-mrad. Therefore the resulting emittance growth could be reduced by an optimal emittance compensation of the solenoid.

2.5.3 Solenoid magnet

A solenoid magnet focuses and rotates an incident beam in the transversal plane (Larmor rotation). The transformation of the phase space by the solenoid can be described similar

to a thick lens in optics. Thereby different non-linear effects (lens aberrations) occur in the solenoid magnet. They depend on the field distribution of the solenoid magnet and scale with the beam size. In the following three important emittance contributions are presented which were determined in [15]. The first one is the chromatic aberration which describes the impact on the focal length of the energy spread. The second is spherical aberration, the next-to-leading-order term in the focal length function of a lens. Finally is the astigmatism of a lens, resulting from a misalignment of the solenoid.

Chromatic aberration

The well known radial focusing of a lens in optics can be used for a solenoid magnet. The final radial slope r'_f downstream from the solenoid is determined in linear approximation using

$$r'_f = r'_i - \frac{r_i}{f} \tag{2.31}$$

where r_i and r'_i as the initial radial position and slope in front of the solenoid. The focal length f of the lens depends on the magnetic field strength B and the momentum of the charged particles p. The passing particles are deflected as function of their individual momentum. For the calculation of the Σ-elements of the final beam distribution the momentum spread σ_δ has to considered. The resulting normalized emittance downstream the solenoid is then given by:

$$\varepsilon_{n,\text{chromatic}} = 2\gamma\beta\frac{\sigma_\delta\sigma_x^2}{f} \tag{2.32}$$

with σ_x as the *rms* beam size inside the solenoid. For a first estimation of the emittance contribution a beam is assumed with a momentum and momentum spread of $pc = 3$ MeV/c and $\sigma_\delta = 0.1\%$, respectively. The focal strength of the solenoid was estimated to 0.5 m, resulting in a beam waist at ≈ 2 m downstream from the cathode, for usually divergent electron beams from the photoinjector. The resulting emittance contribution is then determined to $\varepsilon_{n,\text{chromatic}} \approx 0.023\ (\sigma_x[mm])^2$ mm-mrad.

Spherical aberration

There are several non-linear solenoid effects on the phase space. The contribution with the most impact is the spherical aberration which is defined by the next-to-leading-order term in the focal length function:

$$r'_f = r'_i - \frac{r_i + \tilde{C}_S r_i^3}{f} \tag{2.33}$$

The parameter $\tilde{C}_S$ is the spherical aberration coefficient, depending on the field profile distribution of the solenoid magnet. This coefficient can be quantified by tracking through the solenoid field (Appendix A.2). With this method the coefficient for the Gun1 solenoid was calculated to be $\left|\tilde{C}_S\right| \approx 112\text{m}^{-2}$. Thus, the normalized emittance is given by: [15]:

$$\varepsilon_{n,\text{spheric}} \approx \sqrt{6}\gamma\beta\frac{\left|\tilde{C}_S\right|\sigma_x^4}{f} \tag{2.34}$$

$$\approx 0.0032(\sigma_x[\text{mm}])^4 \text{ mm-mrad} \tag{2.35}$$

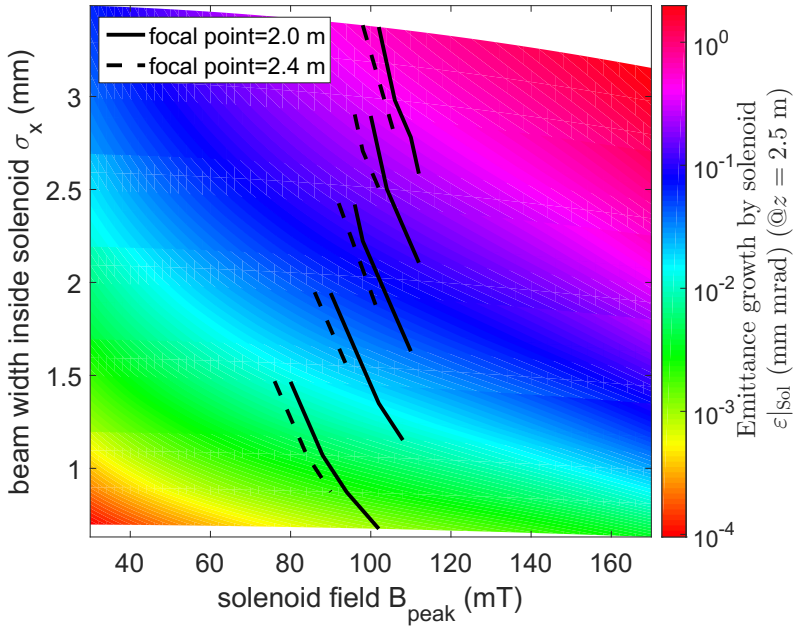

Figure 2.10: Simulation results of the simulated emittance growth for a stand alone solenoid field using in the gun module. The emittance growth is plotted logarithmically as function of the beam size inside the solenoid and its field strength. Tracking was done with ideal Gaussian bunches (each of 10,000 particles) with different beam sizes inside the solenoid. Zero initial momentum spread and transverse emittance was assumed.

Here the same optical and kinetic parameter settings as above are assumed.
Further ASTRA simulations of the other non-linear solenoid contributions were examined. The resulting emittance growth of this tracking includes all eight aberration effects of a magnetic lens, like the isotropic or anisotropic distortion and Coma [17]. The result is depicted in Fig. 2.10. For a better orientation, the field strength values are also marked, that are necessary to focus the given beam to $z = 2$ m (solid line) and $z = 2.4$ m (dashed line). This plot shows that for *rms* beam sizes in the range of 2 mm to 4 mm the emittance contribution can be approximated to 0.1 ... 1.0 mm-mrad. The above used optical parameter setting amounts to an emittance growth by the solenoid of $\varepsilon_{n,\text{solenoid}} \approx$ 0.6 mm-mrad. In case of a misalligned solenoid magnet a further effect has to be kept in mind, the astigmatism.

Astigmatism

The solenoid magnet is positioned in the gun module next to the SRF injector cavity (Chapter 3) where it is aligned to the complete module. Thermal expansion of the holder system and the solenoid can change this alignment during the cool down procedure of the module. Furthermore, the alignment of the magnetic axis relative to magnet geometry is not well-known. As a result the magnetic axis of the solenoid can differ to the beam axis. This difference can be described by a transversal offset (x_{off} and y_{off}) and an angle (pitch and yaw relative to the beam axis). The astigmatism of the lens produces effects, like beam steering and different focal lengths in the horizontal and vertical plane. The impact on the projected transverse emittances was numerically determined in [15] to approximately 20%. There, huge offset parameters in the millimeter range were assumed and tilt angles in the range of several degrees. In the gun module for GunLab the solenoid is movable by a

motorized mount from the outside of the cryo module. Thereby, it is possible to investigate these effects in detail and correct the magnet axis by a beam based alignement.

2.5.4 Space charge

The critical section for space charge influences is in the vicinity of the cathode where the electrons are non relativistic. An analytic model for the space charge effects is presented by Kim [18]. Additional to the RF effects he approximated the influences of the space charge fields near the cathode on the projected transversal and longitudinal emittances. With this model it is possible to calculate the normalized emittance growth $\varepsilon_{n,\mathrm{SC}}$ due to space charge as a function of the peak current I_0:

$$\varepsilon_{n,\mathrm{SC}} = \frac{\pi}{4}\frac{2mc^2}{eE_0\sin(\phi_0)}\frac{I_0}{I_A}\mu(A) \tag{2.36}$$

with ϕ_0 as the absolute emission phase, E_0 as the peak field amplitude on cathode and I_A as the Alfvén current. The peak current I_0 is a function of the emitted bunch charge Q_{bunch} and the temporal pulse length σ_t:

$$I_0 = Q_{\mathrm{bunch}}/\sigma_t \tag{2.37}$$

The function $\mu(A)$ in Eq. 2.36 describes the emittance form factor and can be simplified for Gaussian bunch distributions to

$$\mu_{\mathrm{Gauss}}(A) \approx \frac{1}{3A+5}. \tag{2.38}$$

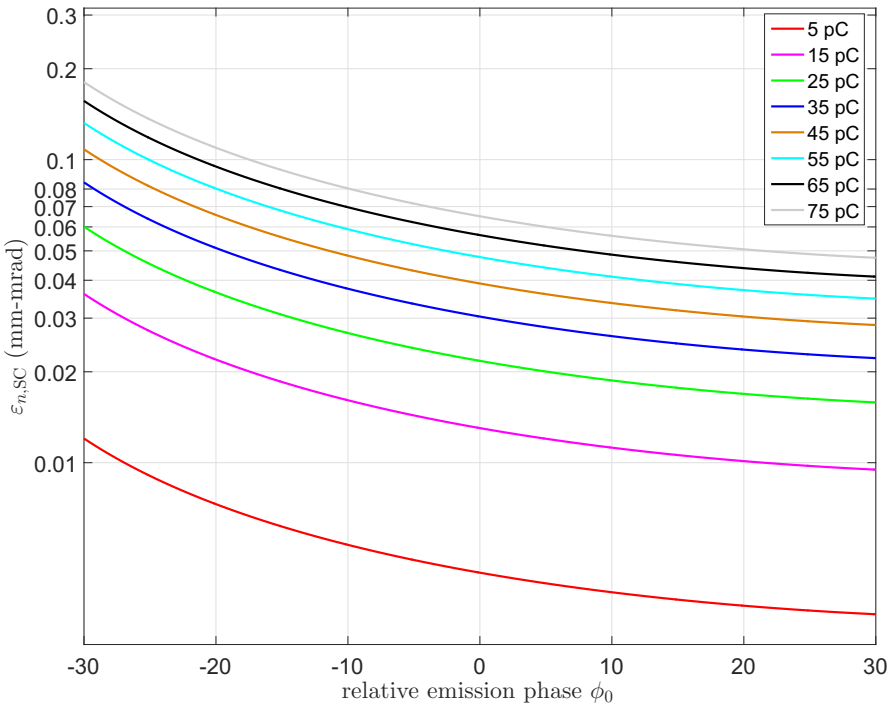

Figure 2.11: Emittance growth by space charge effects calculated by Eq. 2.36 for different bunch charges between 5 and 75 pC (see text).

Where the parameter $A = \sigma_x/\sigma_z$ describes the ratio of the spot size to the emitted bunch length. This has to be determined from the assumption $\sigma_z \approx \beta_0 c\sigma_t$, with $\beta_0 c$ as the

electron velocity next to the cathode. Fig. 2.11 shows the calculated emittance growth for the different emitted bunch charges. For the calculation the same injector settings were used as in 2.5.2: $E_0 = 30$ MV/m, $\phi_0 = \pm 30$ deg relative to the on-crest phase (44.7 deg), $\sigma_t = 4.7$ ps and $\sigma_x = 0.5$ mm.
In this scenario, Eq. 2.36 results in a projected emittance growth of $\varepsilon_{n,\mathrm{SC}} \approx 0.2$ mm-mrad for bunch charges up to 77 pC. It can be assumed that this mismatch of the slices by the space charge forces can be partially compensated by the emittance compensation of the solenoid.

2.5.5 Combined emittance growth

To approximate the expectable emittance value of an emitted electron bunch, the individual emittance contributions for a photoelectron injector, determined in the last sections, can be combined to the total transverse emittance, .

$$\varepsilon_{\mathrm{tot}} = \sqrt{\varepsilon_{\mathrm{therm}}^2 + \varepsilon_{\mathrm{RF}}^2 + \varepsilon_{\mathrm{Sol}}^2 + \varepsilon_{\mathrm{SC}}^2} \tag{2.39}$$

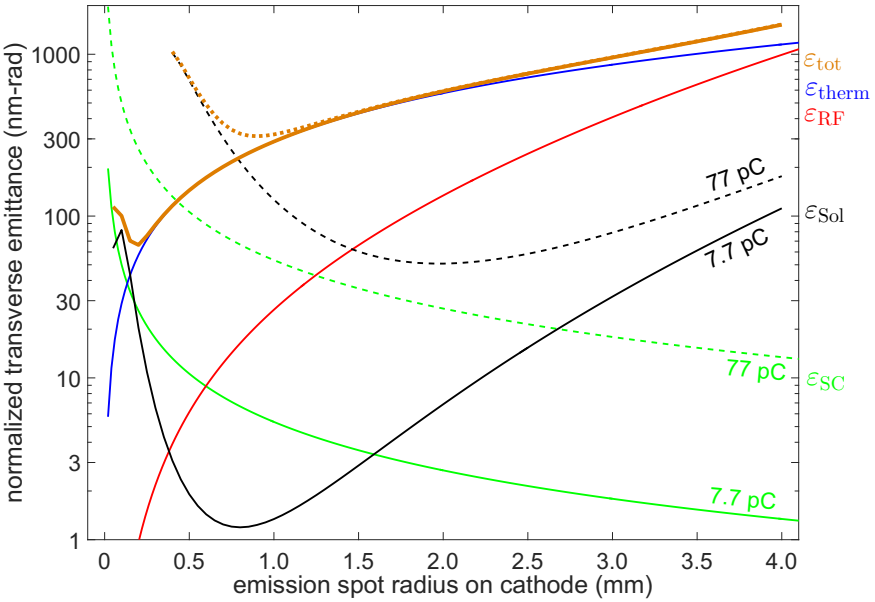

Figure 2.12: Example of the individual emittance contributions of thermal emittance (blue), RF (red), aberration effects of the solenoid (black) and the space charge (green) as an example for an SRF gun cavity gradient of 30 MV/m where the 3.76 ps long laser pulse extracts a 77 pC electron bunch (bERLinPro-scenario) at the on-crest phase (44.7 deg). The photocathode is -1.5 mm retracted relative to the cavity back wall. The total emittance of these contributors (Eq. 2.39) is depicted in orange. The dashed lines represents the emittance contributions in case of 77 pC bunches, the solid line for 7.7 pC. All contributors are plotted as function of the spot radius of a transverse flat-top bunch profile ($r = 2\sigma_x$)

Fig. 2.12 shows an example for the individual emittance contributions and $\varepsilon_{\mathrm{tot}}$ as function of the emission spot size radius on the photocathode. For the calculations and the numerical simulations a cavity peak field of 30 MV/m with an on-crest phase extraction of 44.7 deg and a constant laser pulse length of 3.76 ps were assumed. Furthermore two bunch charges (7.7 pC and 77 pC) are compared. The solenoid contribution is not directly a function of the spot size on the cathode. The necessary beam size inside the solenoid

was determined by a numerical simulation of the Gun cavity with the estimated injector parameters. The plotted functions show that for small bunch charges the transverse emittances are dominated by the thermal emittance of the photoelectron emission. Only for extreme small spot sizes the space charge blows up the beam size and the emittance. On the other hand, for large spot size radii (>3 mm) with less space charge effects the RF effects are increased to the same order as the thermal emittance.
The emittance contributions are assumptions for the emittance growth by the individual influences. Thus, Eq. 2.39 is the uncorrelated sum of these contributors. Such a correlation is a phase space transformation of one contribution that amplifies another emittance contributor. E.g., an increase of the bunch charge, where all other settings are constant, produces additional to the emittance growth by Eq. 2.36 an increase of the transversal and longitudinal bunch size next to the cathode. This then can trigger the RF and the solenoid effects, too.
Eq. 2.39 and Fig. 2.12 can be used to estimate the scaling of transverse emittance, but to achieve the best performance of the injector it is necessary to handle all injector components as an unit, including a global parameter optimization for an intended beam characteristic. [19] This is the only way to consider all emittance and beam size contributions, as well as the collective effects. Numerical simulations of the complete photoelectron injector were also used, to examine potential parameter ranges for the beam operation in GunLab and to test the performance of several measurement systems. A detailed description of the photoelectron injector, as well as the GunLab system is given in the following chapters of this thesis.
Another critical issue is the production of beam halo. Similar the transverse emittance, it is also influenced by the properties of the photoelectron injector, like cathode properties and space charge. Examples and potential problems due to beam halo are discussed, as a short excursus, in the following.

2.6 Beam halo

The analysis of the emittance contributions in a photoelectron injector has shown that the different elements of the injector only interact linear with the electron beam in a small phase space region. This region is called the core region. A distribution beyond the core, the halo, is sensitive to non-linear coupled effects from the injector and further accelerator elements. As a worst case scenario this leads to a kind of run away effect and blows up the bunch. Additionally, a crucial source of halo production is the photocathode. The emission of the photoelectron beam is based on the excitation of electrons by photons from the drive laser. However, electrons are also be extracted by the electrical field on the cathode surface. The change of the original step shape of the potential barrier into a potential wall leads to a possible tunnelling effect for the electrons through the cathode surface. The probability depends on the energy level of the electrons and the electric field strength. A model for this emission process was described by Fowler and Nordheim [20] and can be used to describe this dark current. An example of dark current is depicted in Fig. 2.13. It shows two images of a viewscreen monitor in the original test beamline for Gun0 [16].Without the drive laser, several low intense electron beams where emitted from the injector by the RF field and passed the beamline up to the viewscreen monitor. The observed distributions are determined by the high energy spread that leads to chromatic effects in the cavity and the solenoid. The intensity of the dark current scales with the amplitude of the electric field on the cathode surface. This field strength is a function of the peak field and emission phase, as well as the cathode roughness. A non-flat cathode

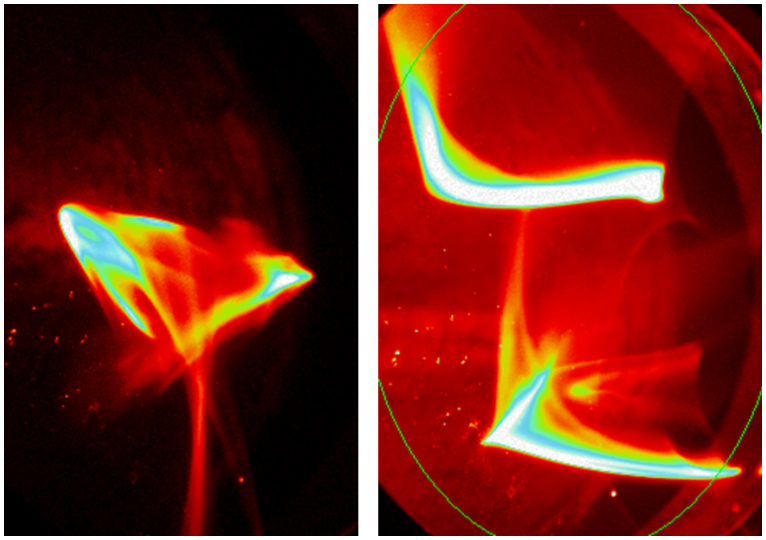

Figure 2.13: Two images of dark current from a Lead photo cathode in Gun0. Images were sampled in an original beamline at the HoBiCaT cryostat which were used during the first tests of an SRF photoelectron injector with fixed metallic photo cathode.

surface can locally enhance the electric field, producing electron emitters. [15].
This beam halo can produce an additional emittance growth, due to the halo-core interaction. Beam halo is also an issue for the machine protection.The properties of beam halo can extremely differ with respect to the core of the photoelectron beam. This includes spatial, temporal and energetic values. The limited accelerator acceptance of these parameters produces, in case of beam halo, electron losses along the complete machine. This increases the radiation, due to electron interaction with the beam line. However, the most critical parts for beam losses are the cryogenic elements like the SRF cavities. Electrons, which come into contact with the cavity wall, deposit energy in the superconducting material. This additional thermal contribution can produce local heating and increase the surface resistance in this region of the superconductor. As a worst case scenario, this leads to a thermal runaway up to a quench of the cavity.
Furthermore, the transport of beam halo causes a decrease in the accelerating efficiency, defined by the ratio between beam power of the photoelectron beam and the necessary accelerating power. All of these problems with beam halo are critical issues for photoelectron injectors. Especially for the application in an ERL like bERLinPro with high average beam power the sources of beam halo have to be suppressed to protect the SRF cavity modules and to increase the efficiency of the ERL process. Therefore the investigation of beam halo is an important aspect for the experiments with GunLab. To visualize a potential beam halo simultaneously to the core beam, a beam halo measurement system with a high dynamic range is implemented in the GunLab beamline (Chapter 6).

Chapter 3

SRF Gun1

The Gun module consists of the cryostat (Cryo module) and the cathode transfer system (Fig. 3.1). Inside the Cryo module the necessary components of the photoelectron injector are installed: the SRF gun cavity, the RF coupler, the superconducting (SC) solenoid magnet and some correcter magnets. The cathode transfer system is positioned at the backside of the Cryo module to exchange photocathodes, delivered in a vacuum suitcase from the cathode preparation system.

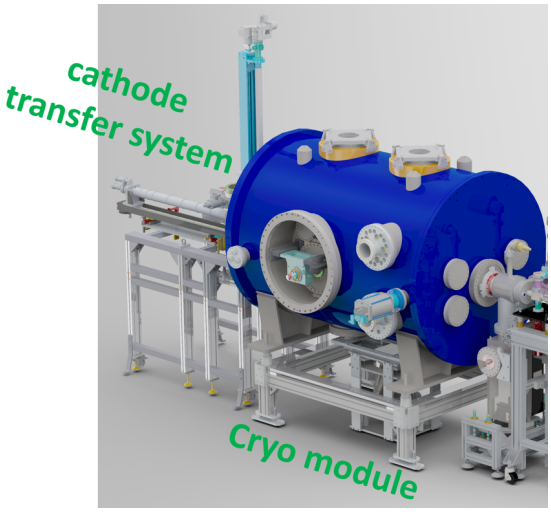

(a) Complete Gun module

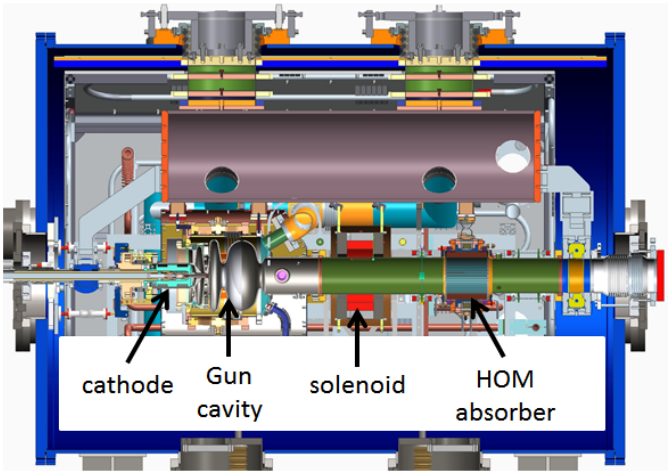

(b) Section of the Cryo module

Figure 3.1: Drawings of the Gun module

3.1 SRF cavity

The SRF gun cavity is an elliptical 1.4 cell cavity for a 1.3 GHz accelerating mode (Fig. 3.2). An additional non-resonant choke cell allows the insertion of the photocathode plug into the cavity [21]. This prevents an escape of RF energy from the gun through the coaxial line which is formed by the cathode holder and the cathode channel (Fig. 3.2) [22].

The Niobium cavity is welded into a vessel which is filled during operation with superfluid Helium to cool down the cavity. The cavity is tunable over a range of $\approx$ 1 MHz by a blade tuner [23].

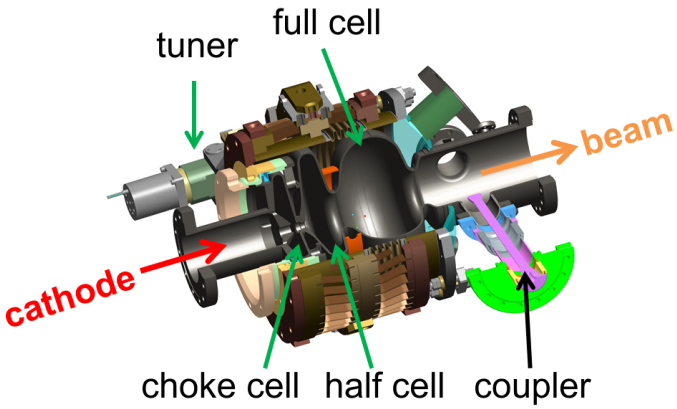

Figure 3.2: Graphic of the SRF gun cavity (Gun1). [21]

Peak fields of more than 30 MV/m can be provided by the cavity. Two CW modified TTF-III couplers transmit the necessary RF power into the cavity. Each of them with a transmission power of up to 10 kW[24]. To suppress higher order modes (HOM) in the cavity an additional ferromagnetic HOM absorber is installed downstream the cavity.

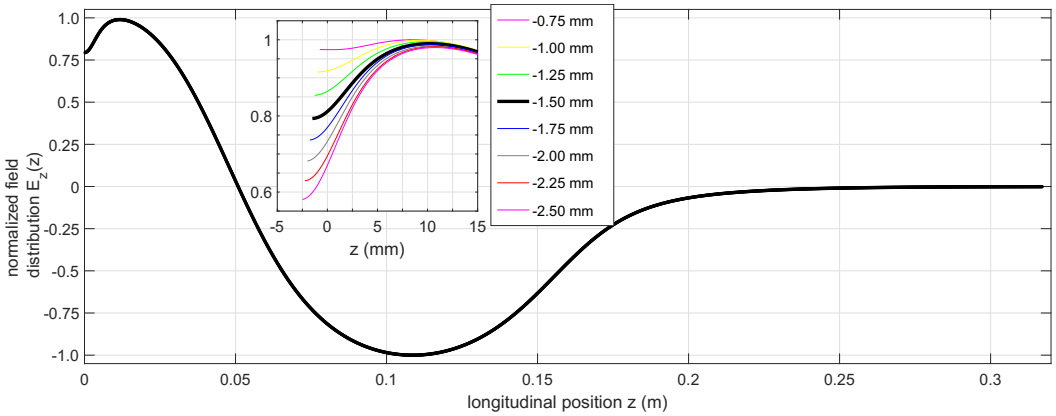

Figure 3.3: Calculated field profile of the cavity for different cathode positions relative to the half cell back wall ($z = 0$ mm).

The longitudinal field profile $E_{z,0}$ on axis, resulting from the cavity design, is plotted in Fig. 3.3. It was calculated by the field solver program Poison/Superfish [25]. A further feature of the cavity is the variable cathode position relative to the back wall of the Gun cavity in a range between -0.75 mm and -2.5 mm. In Fig. 3.3 the resulting field distributions are plotted for different cathode positions. It shows that these small position differences have an immense impact on the field distribution on the photocathode surface. A retraction of the cathode decreases the maximal field on the cathode surface, but produces a more positive slope in front of the cathode. Thus, Eq. 2.8 results in a radial focusing field next to the cathode. This can be used to compensate space charge defocussing. Such a cathode retraction also affects the longitudinal phase space of the extracted electron bunches. With numerical simulations these effects were studied and an optimal cathode position was found to be approximately -1.5 mm.

3.2 Solenoid magnet

A radial focusing solenoid magnet allows to focus the usually divergent photoelectron beam behind the gun cavity with a single magnet (Chapter 2.2.3). Also, it enables emittance compensation, described in Chapter 2.4. However, the aberrations and field asymmetries of the solenoid can produce further emittance growth (Chapter 2.5.3).
In [17], it is shown that each aberration term can be calculated as an integral of several deviation terms of the solenoid profile on axis. As part of this thesis, a solenoid study was undertaken to determine the aberration influences of a given solenoid field profile and to optimize the geometry of such an SC solenoid for a minimum emittance growth. The method and the results are outlined in Appendix A.2. The final solenoid was designed in a collaboration with Niowave [26]. The magnet design is presented in the following section. Furthermore the electrical and mechanical connections with the Gun module, which were developed within the framework of this thesis, are discussed.

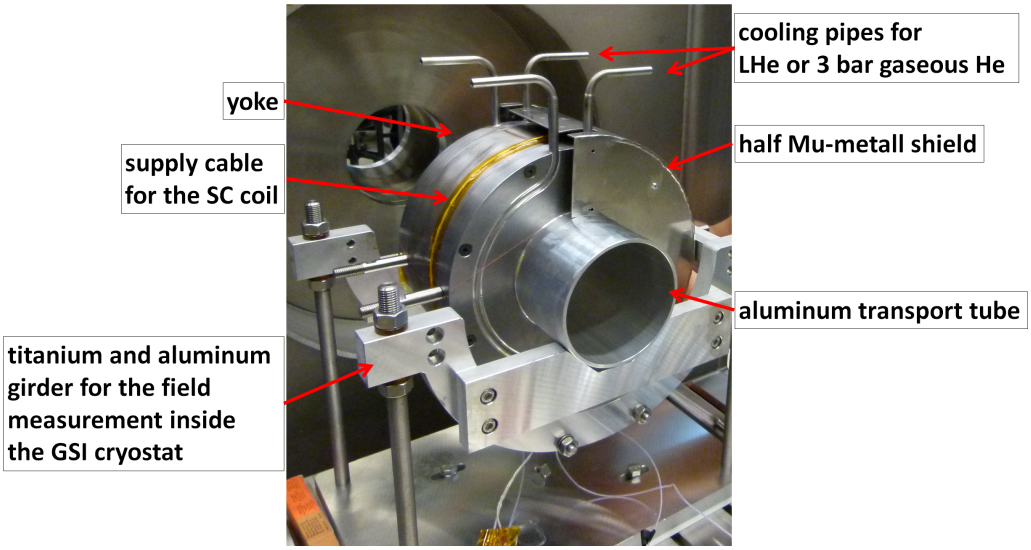

Figure 3.4: Photo of the GunLab solenoid in a holder for the field measurement at the GSI

Solenoid magnet for Gun1

The requirements on the magnet design are on the one hand the geometrical specification of the Gun module and on the other hand the magnetic field parameter, like the shape and the peak field. For the field profile a provisional result of the solenoid study was used.[a] Niowave designed a solenoid geometry with one central superconducting coil and a rotational symmetric yoke (Fig. 3.4). A Mu-metal shield suppresses the residual fields of the yoke outside the solenoid which could be trapped in the SRF cavity during the cool down process. The coil consists of 8350 windings of a thin copper wire with NbTi cores. Above the critical temperature, the SC wire has an ohmic resistance of $\approx 1500\Omega$, but in the SC state it is not quantifiable any more. Tab. 3.1 shows the field specific values for the complete solenoid magnet, imaged in Fig. 3.4.

[a]The solenoid study and the inquiry at manufacturers were simultaneous. After the completion of the study, the magnet design was fixed by the manufacturer. It also based on a completely different technique as assumed for the field calculations.

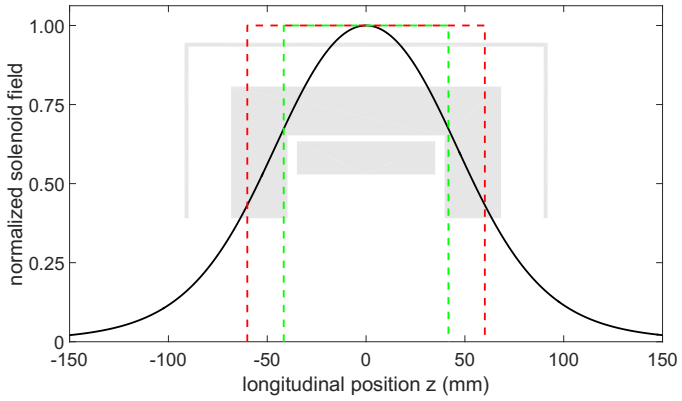

Figure 3.5: Plot of the longitudinal field profile of the solenoid magnet (black). The green and the red dashed lines represent the effective lengths $L_{\text{eff}}^{(\text{foc})}$ and $L_{\text{eff}}^{(\text{rot})}$. The plots are shaded in gray by the solenoid cross section as a geometrical reference.

minimal aperture (mm)	130
geometrical length (mm)	250
coil windings	8350
inductivity (H)	≈ 25
$L_{\text{eff}}^{(\text{rot})}$ (mm)	120.2
$L_{\text{eff}}^{(\text{foc})}$ (mm)	83.3
specified current (A)	7
B_{peak} (mT) (@7A)	600
working temperature (K)	4

Table 3.1: Parameters of the GunLab solenoid.

Some changes in the solenoid construction were necessary to implement the Niowave design in the Gun module between the photoinjector cavity and the HOM coupler of the cavity. Hereby, the problem was that the aperture of the solenoid is smaller than the outer diameter of the beamline flanges. This inhibited an installation of the magnet with this design. The solution was to split the magnet into 5 pieces: the Coil with the central yoke, which pass the outer diameter of the beamline flanges, and 4 identical half torus plates as the two pole shoes of the yoke. Thereby, the coil and the central yoke could be positioned over the beam pipe and connected with the four pole shoe pieces. These pole shoes also contain stainless steel tubes, welded inside the plates to cool down the magnet with 3 bar helium to a temperature of 4 Kelvin.
This solution worked quite well for the geometrical problem of the position, but resulted in some disadvantages for the magnetic field. A split yoke produces additional boundaries inside the material which can result in a locally decreased magnetic permeability. Furthermore, the split pole shoes can affect the rotational symmetry of the flux density inside the yoke. Another symmetry problem arises from the cooling tubes which act as holes in the yoke for the magnetic flux. All these potential flux asymmetries inside the yoke can produce distortions of the field symmetry next to the magnetic axis. A field measurement was undertaken to study these potential field asymmetries. For this measurement, the solenoid was positioned in a test cryostat at the GSI. The measurements and the results are shown in Chapter 7.

Quench protection

A Quench protection system (Fig. 3.6) was designed for the solenoid installed in the Gun module, as well as for the field measurements at the GSI. The solenoid has in the SC state no ohmic resistance but a high inductivity of $L_{\text{solenoid}} \approx 25$ H. In case of a warm up of the complete or parts of the coil above the critical temperature, this resistance rises dramatically and the thermal induced power, as well. For a fast protection of the solenoid in such a destructive scenario, an addition load is installed parallel to the solenoid. It will dump the constant electric current of the power supply and the stored magnetic field energy of the solenoid if the voltage increases above a threshold. This threshold is

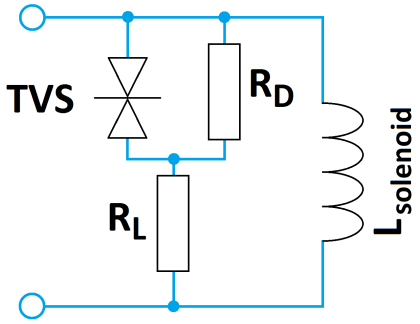

Figure 3.6: Draft of the Quench protection system for the GunLab SC Solenoid.

determined by a transient-voltage-suppression diode (TSV) to 6.8 V [27]. In this overvoltage scenario, the electric current flows through a high power load, that has a resistance of $R_L = 47\Omega$. With this load the self-induced current of the solenoid can be dumped in all cases in a few seconds. A second resistor $R_D = 1$ kΩ suppresses the oscillating circuit[b] for voltages close to the threshold of the TSV.

Solenoid mover

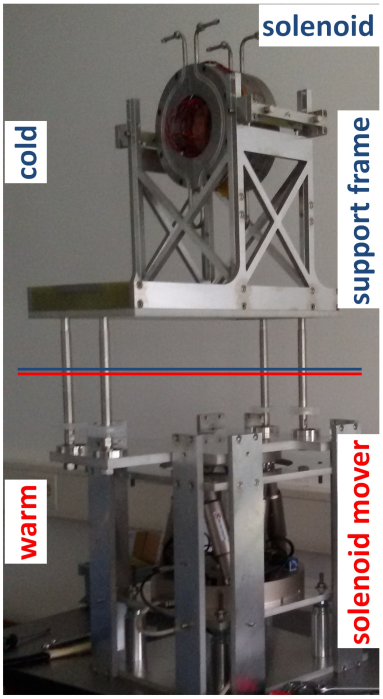

Figure 3.7: Image of the complete Solenoid mover system with the Hexapod (bottom), the solenoid magnet (top) and the holder, including four pillars as feedthrough inside the Gun module.

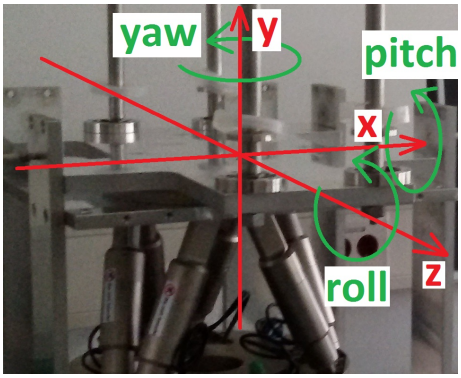

Figure 3.8: Definition of the six moving directions (x, y, z, pitch, yaw and roll) for the Hexapod platform.

Δx	$\pm$50 mm ($\pm 1\mu$m)
Δy	$\pm$50 mm ($\pm 1\mu$m)
Δz	$\pm$25 mm ($\pm 0.3\mu$m)
Δpitch	$\pm$260 mrad ($\pm 5\mu$rad)
Δroll	$\pm$260 mrad ($\pm 5\mu$rad)
Δyaw	$\pm$520 mrad ($\pm 9\mu$rad)
maximal load	250 kg

Table 3.2: Parameter of the Hexapod. The coordinate system and the three tilt angles are illustrated in Fig. 3.8.

[b] The TSV has a small capacitance which produces an RLC circuit in combination with the load and the inductivity of the solenoid.

Another critical parameter of the solenoid setup is the alignment of the magnet in respect to the beam axis. Differences between beam axis and magnetic axis can produce beam steering and rotation, but also a growth of the projected emittance. [15] To handle the solenoid alignment inside the cryostat and in combination with the electron beam (beam based alignment) a motorized mount for the solenoid is installed which can vary the position of the magnet along all dimensions. The mount consists of 3 parts. A Hexapod outside the cryostat, a holder system, connecting the Hexapod with the solenoid inside the Gun module and an electronic controller, including an anti-collision system. The Hexapod and the controller unit were delivered from Physical Instruments (PI) [30]. Thereby 6 stepper motors in the Hexapod allow a platform movement in all three spacial directions, as well as a rotation around all three solid angles. The controller translates the intended position change relative to a user defined pivot point into the six necessary motor signals. An image of the first hardware test of the system is shown in Fig. 3.7. The achievable parameter ranges for the Hexapod are listed in Tab. 3.2. With this system the position of the solenoid can be varied very precisely, despite of the huge mass of solenoid and holder. However, the maximal parameter values exceed the limits of the solenoid movement by nearly one order of magnitude. Therefore an anti-collision software and hardware system was installed. The software verifies the intended path of the mover and the solenoid before any movement starts. Furthermore, the hardware system stops the mover in case of a upcoming collision that was not detected by the software.

3.3 Cathode transfer system

The photocathode inside the SRF injector has to be replaceable to allow studies with different cathode materials with GunLab. Furthermore multi-alkaline photo cathodes have a finite QE lifetime inside the SRF photoinjector, limiting the operational time for a cathode. The cathode exchange requires several technical steps, depicted in Fig. 3.9 and Fig. 3.10. The complete cathode system mainly consists of two subsystems; the cathode holder inside the SRF injector (Fig. 3.9) and the cathode transfer system (Fig. 3.10) outside the Gun module. It is based on the cathode system of the Dresden Rossendorf SRF photoinjector [33]. The photocathode itself is a small plug with a diameter of 10 mm and a length of 6 mm. It consists of molybdenum (Mo) for semi-conductor photocathodes or copper. In the first GunLab setup a polished copper plug with low QE will be used for the first cavity tests and for a first electron beam with the UV drive laser. For further operation, high QE photo cathode films will be tested in GunLab. They are deposited with normal conducting multi-alkali layer like CsK_2Sb [34] onto the Mo plugs. In all cases the design of the different inner plugs is the same to handle them with one external plug holder. This holder is made of copper and fix the plug with CuBe plate springs from the inside of the plug. These springs can be unlocked by a mechanism inside the plug holder (Fig. 3.9). Furthermore, the holder has the function of a thermal and electrical coupling between the plug and the coaxial filter which is passively cooled to a temperature of 80 K.

A manipulator arm of the transfer system can unlock the plug holder from the filter and retrieve the cathode out of the gun cavity (Fig. 3.10). Inside the transfer system chamber the used plug is unlocked from the plug holder and replaced by a new cathode plug. The lock for all cathodes (old and new cathode) is a vacuum suitcase at the bottom of the transfer system. Within this suitcase the cathodes are transported between the cathode preparation laboratory and the Gun module.

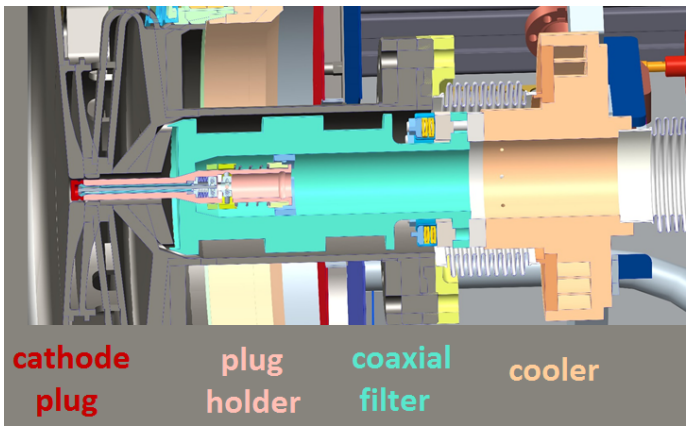

Figure 3.9: Drawing of the cathode system in the gun module. The plug is locked by a spring on top of the holder. It can be opened by a mechanism inside the holder. The holder itself is also locked in the coaxial filter.

(a) Drawing of the cathode transfer system at the cryo module.

(b) Construction of transfer system in the clear room.

Figure 3.10: A schematic of the photocathode transfer system for the Gun module (left) and a photo of the transfer system in the final construction process inside the clean room.

Chapter 4

GunLab

In the previous chapter it was shown that different sources of emittance contributors occurs inside a photoelectron injector that can be correlated to each other. These several effects depend on the parameter setting of each single element in the injector:

- photocathode parameters: quantum efficiency (QE), thermal emittance, surface roughness,
- drive laser parameters: pulse length, spot size, intensity, wavelength,
- cavity parameters: emission phase, peak field, cathode position,
- solenoid parameters: peak field, alignment.

The injector parameters affect the distribution of the bunch in the six dimensional phase space, such as bunch length, energy spread or transverse emittance. It is important to examine the full phase space distribution as function of the injector parameters. It enables a characterization of the photoelectron injector and a separation of the emittance contributions of each individual component. Thus a dedicated beamline was developed - GunLab. It consists of the diagnostic beamline and a drive laser. In this chapter the design of the diagnostic beamline and the specification, as well as the performance of the measurement systems are presented.

4.1 Strategy for the GunLab design

The design of diagnostic beamline has to be able to visualize the full six dimensional phase space of an electron bunch. This electron bunch is extracted from a photocathode inside the gun cavity, illuminated by a pulsed drive laser. The laser beam is guided by a transport beamline from the laser room to GunLab. The emitted electrons are accelerated by the RF field in the SRF gun cavity. A solenoid magnet is positioned downstream of the cavity. It focuses the beam within the diagnostic beamline. The overall length of this beamline is determined by the spatial limitation inside the HoBiCaT bunker to ≈ 4 m. A common reference point for most measurement systems was defined. It is virtually located inside the first booster cavity of the bERLinPro injector at ≈ 2.5 m downstream the photocathode. Thus it is a crucial position for the measurement of several beam parameters.
With numerical simulations of the photoelectron injector the beam parameters along the virtual 4 m beamline were studied. Thereby, the initial drive laser and cavity parameters were varied over a wide range. The field strength of the solenoid was determined to compensate the projected emittance close to the defined reference point. An example

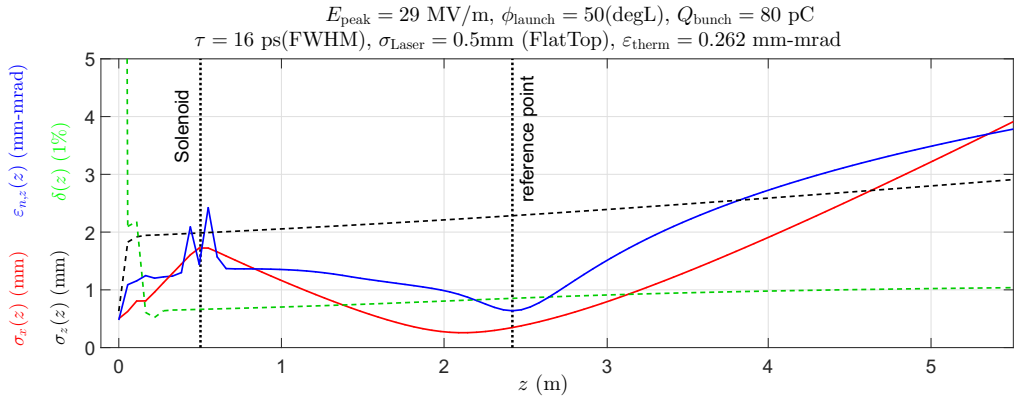

Figure 4.1: Plot of the beam size σ_x, the bunch length σ_z, the transverse emittance $\varepsilon_{n,x}$ and the momentum spread δ along the longitudinal direction z.

is depicted in Fig. 4.1, where the transverse beam size and emittance, as well as bunch length and momentum spread are plotted as function of the longitudinal position z.

bunch extraction energy (MeV)	$1 \cdots 3$
rel. energy spread (%)	$0.2 \cdots 5$
bunch charge (pC)	$0 \cdots 100$
rms bunch length (ps)	$0.1 \cdots 10$
max. average current (μA)	5[1]
normalized emittance (mm-mrad)	$0.1 \cdots 10$

[1] administrative limit

Table 4.1: Beam parameter ranges of the extracted photoelectron beam, determined by ASTRA simulations for several injector parameter settings.

The resulting beam parameters at the reference point were sampled in the simulations and the resulting ranges are depicted in Tab. 4.1.
In the real diagnostic beamline of GunLab, the measurement systems have to be aligned to this reference point. At this point a slit mask is installed to define the transverse object size, which can be used for several measurement systems, such as phase space scanner, double quadrupole and spectrometer system.
For the phase space measurement system the beam has to be moved over the slit mask by two compact dipole magnets. Only a small fraction of the beam can pass the slit mask. The transverse size of this electron beam, downstream from the reference point, can be used to reconstruct the initial phase space distribution.
To measure the momentum spread of the bunch at the reference point a spectrometer dipole is used. It bends the electrons in the bunch horizontally into the dispersive section as function of their momentum. The resulting horizontal beam size is determined by the momentum spread of the bunch and the beam size at the reference point.
Furthermore, a transverse deflecting cavity (TCav) is necessary, to measure the bunch length. It shears the long bunch in vertical direction. Thus, the initial longitudinal bunch size is determined by the vertical beam size downstream of the TCav. In combination with the spectrometer dipole the longitudinal phase space is directly visualized on the viewscreen in the dispersive section.

A quadrupole doublet can be used to examine the projected phase space parameters of the beam, ideally at the reference point. In combination with a downstream positioned TCav the sliced phase space can be reconstructed, as well. This strategy of the measurement

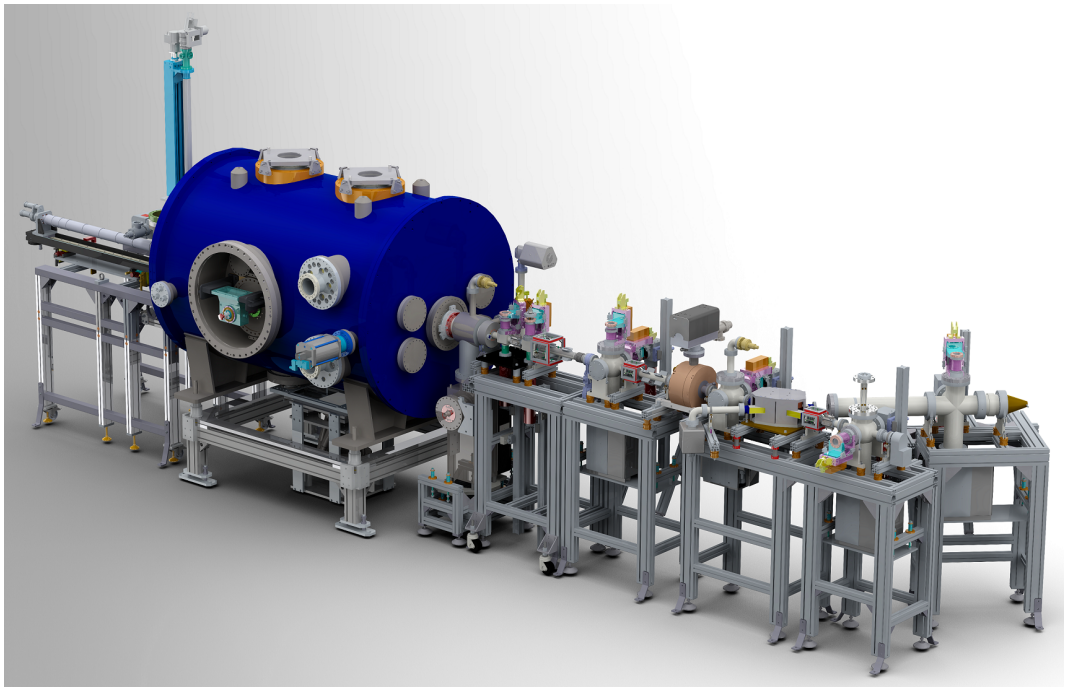

Figure 4.2: Drawing of diagnostic beamline of GunLab with the Gun module.

systems defines the general structure of the diagnostic beamline. The resulting design of the beamline is depicted in Fig. 4.2. In the following sections the important elements of the diagnostic system are presented.

4.2 Diagnostic beamline

The GunLab diagnostic beamline is a four meter compact beamline, designed to analyze the photoelectron beam from the Gun module. Fig. 4.3 shows a draft of the beamline with the six diagnostic crosses (DCs) and the main measurement systems.
The first section of the GunLab beamline consists of the drive laser input port line, as well as two DCs. These DCs are the first beam observation points downstream from the Gun module. Then the beam passes the phase space scanner system which is used to reconstruct the horizontal phase space distribution of the electron beam at DC3, the reference point of the beamline. The method and the design of this system are described in Chapter 5. Following, the beam passes two quadrupole magnets and the TCav, that is not installed for the first run. With a spectrometer dipole behind DC4 the momentum spread can be determined. Each DC has a pneumatic or motorized mover to place a diagnostic insertion directly in the electron beamline. An overview of the various devices in the DCs and detailed information about the measurement systems in GunLab are given in the following sections.

4.2.1 Diagnostic crosses (DCs) in GunLab

All DCs, except of DC2, consist of a viewscreen monitor (VSM) that combines a luminescence screen with an optical readout using a CCD camera. With a VSM the transverse

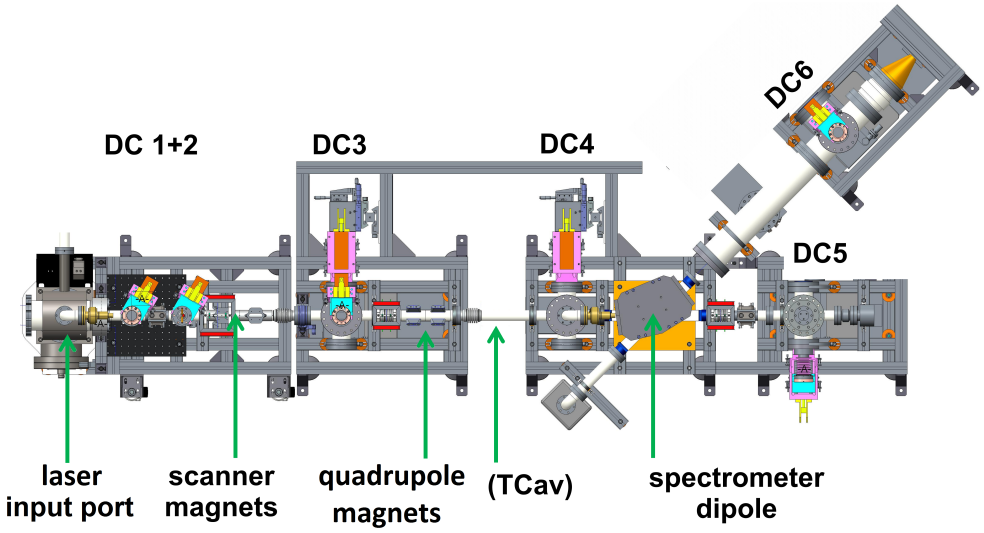

Figure 4.3: Drawing of the GunLab beamline (topview) with six marked diagnostic crosses (DCs), the phase space scanner system at DC3 and the spectrometer dipole. The transverse deflecting cavity (TCAV) will be installed in autumn 2017 in the beamline.

position of the beam centroid and the beam size can be measured directly. The complete system of all VSMs is described in detail in Chapter 4.4.1.

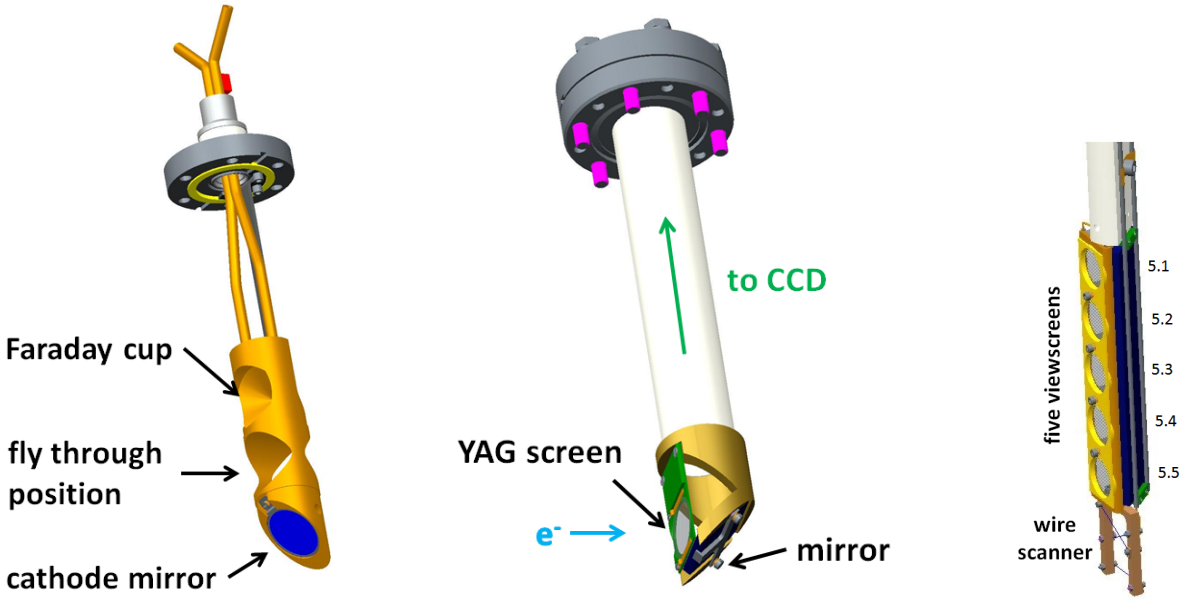

Figure 4.4: Draft of three DC insertions in GunLab. From left to right: DC2, VSM at DC3, multiscreen station at DC5

DC1 and DC2 are components of the first beamline section. It is also a part of the bERLinPro injector line. Thus the diagnostic insertions in both DCs are test constructions for the bERlinPro insertions, as well. One feature is the shape of the insertion combined with a fly through position of the devices (Fig. 4.4(a)). This design minimizes the impedance of the DC in case that no diagnostic is required. Additionally to the fly through position, DC1 has a VSM for the first beam observation. DC2 consists of a Faraday Cup and a single 45 degree aluminum mirror (Fig. 4.4). The Faraday cup is a tapered bore in a copper block and is used for a direct beam current measurement. Therefore the insertion

is electrically isolated. The incident electrons of the beam are stopped completely inside the copper block and the sampled charge can flow to ground through an ampere-meter. With the aluminum mirror in the beamline it is possible to image the photo cathode with a CCD camera. This is necessary to observe the laser spot on the cathode surface or to observe any luminescence effects of the photo cathode. Between DC1 and DC2 a beam position monitor (BPM) is integrated into the beamline. It is used for a fast readout of the transversal beam position. Furthermore the sum of all BPM signals can be used to determine the relative charge of the extracted electron bunches. This is a non destructive measurement and can run permanently.
DC3 consists of a VSM and two slit masks, a horizontal slit and a vertical slit. Both slit masks are combined on a motorized diagnostic insertion and can be moved vertically through the beam. They are necessary for the phase space measurement system and the beam energy measurement with an increased resolution. (Chapter 4.4).
At DC4 and DC6 only VSMs are implemented. Thereby the VSM at DC6 is the only one with a 60 mm viewscreen diameter. This is necessary because of the potentially increased beam size by the beam dispersion of the spectrometer dipole or the beam deflection of the TCav.
The last diagnostic cross, DC5, is positioned downstream of the spectrometer dipole in the straight section. It combines five different screens and a 3-axis wire scanner on one holder. With this multiscreen station it is possible to test different screen materials and thicknesses with the same beam parameter at the same beamline position. The stepper motor switches between the several screens and can move the wire scanners through the beam pipe. An observation of the electrical signals of the 40 μm thick wire scanners allows to reconstruct the beam size. The electrical and the several optical measurements can be directly compared with each other.

4.2.2 Steerer magnets

Steerer magnets are necessary to guide the beam through the GunLab beamline. External magnetic fields, such as the earth magnetic field or misaligned magnets, can deflect the beam with respect to the beamline axis. Two steerer stations inside the cryostat and four along the GunLab beamline can correct the beam axis by small deflections onto the reference axis. Each steerer station consists of four air-core coils which produce two individual perpendicular orientated magnetic fields. Therefore the two coils, that face each other, are serially connected to produce a dipole field in the center of the beamtube. In case of the first steerer magnet in the cold section (Type C in Tab. 4.2) the coil connections are variable to switch between a setup for two steerer magnets and one with a skew quadrupole magnet. The skew quadrupole setup can be used to minimize the quadrupole errors of the solenoid (Chapter 3.2).

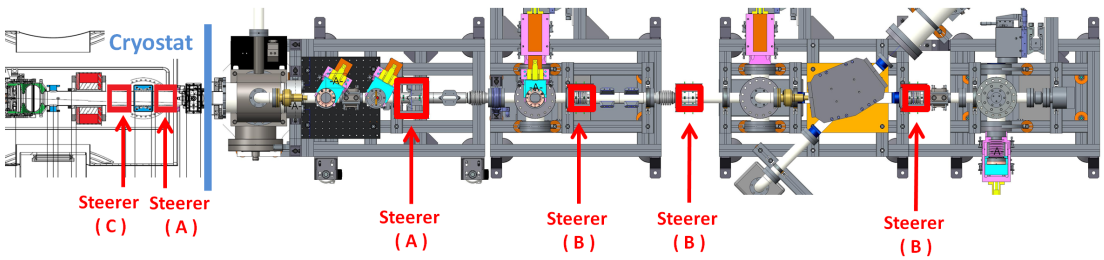

Figure 4.5: Drawing of the cold and the warm section of GunLab with all steerer magnet positions and type.

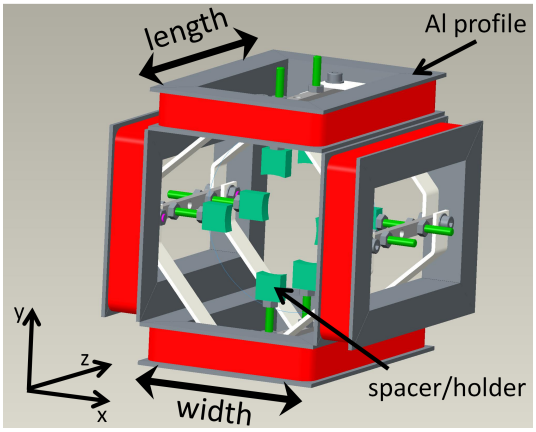

Figure 4.6: Drawing of the GunLab H/V steerer magnets.

Steerer type	A	B	C
Length (mm)	130	110	60
Width (mm)	110	72	110
Cable	rectangular cross section (6×0.3 mm)		
Windings per coil	51		
Kick strength ω ($\frac{\text{mrad-MeV}}{\text{A}}$)	11.1	12.3	4.5

Table 4.2: Three types of steerer magnets in GunLab

For the steerer magnets, there are three different types installed in the GunLab system. Their positions along the beamline is shown in Fig 4.5. All consist of a rectangular wire which is wounded on an u-shaped aluminum profile (51 windings) to achieve a maximal cable packaging. The coils were fabricated similar to the scanner magnets (Chapter 5). These coils can be operated with a continuous current of more than 3 Amps.
Tab. 4.2 lists the three magnet types with their dimensions and kick strengths ω. Thereby, the resulting deflecting angle θ is given by $\theta = \omega \cdot I/pc$, where I and pc are the defined electric coil current and the beam momentum. The width of the magnets in the cold section, Type A and C is due to the larger beamline diameter inside the Gun module of 106 mm. In the warm section the steerer magnets (Type B) are positioned usually to a flange of a DC or next to a vacuum bellow to save space in the beamline. This flange diameter defines the width of the warm steerer magnets. With these steerer magnets the beam axis can be adjusted through the complete beamline.

4.2.3 Laser input port

The first section of the GunLab beamline consists of the laser input port line and the diagnostic crosses DC1 and DC2. The design is the same as for the bERLinPro injector line, maybe redesigned later to merge the two DCs into one. The laser input port line is shown in Fig. 4.7. A taper reduces the 100 mm aperture of the gun module to an aperture of 35 mm for the GunLab beamline. Two tubes are welded at this taper (Fig. 4.7 (right)). Through the right hand side tube the drive laser is guided into the beamline and onto the photocathode. The left one can be used for an analysis of a potential reflection of the drive laser on the cathode surface.

4.2.4 TCav

The transversal deflecting cavity (TCav) is a normal conducting resonator with a design frequency of 1.3 GHz to provide a TM110 dipole mode. This mode produces transversal electrical and magnetic field components on axis. They deflect the incident electron beam vertically. The deflecting angle is a function of the field amplitude and the RF phase ϕ_{RF} of the cavity. For bunch length and sliced emittance measurements the zero crossing phase ($\phi_{\text{RF},0}$) is used where the centroid of the bunch passes the TCav without deflection ([35]). However, the head and the tail of the bunch receive a sinusoidal field amplitude relative to the zero crossing phase so that they are deflected in opposite directions. This

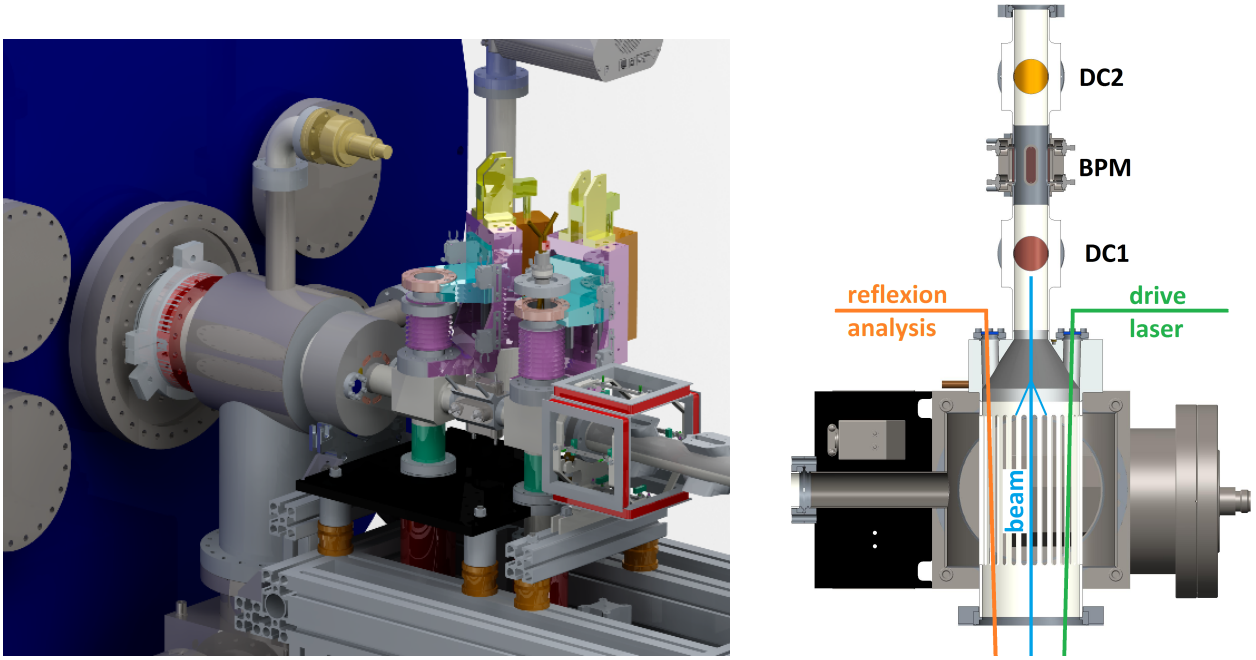

(a) Drawing of the first beamline section.

(b) Sketch of the laser input port line.

Figure 4.7: First beamline section in GunLab

principal is depicted in Fig. 4.8. The design of the cavity is based on the one cell deflecting cavity of Cornell [36] and is finally designed and constructed by RI [37].

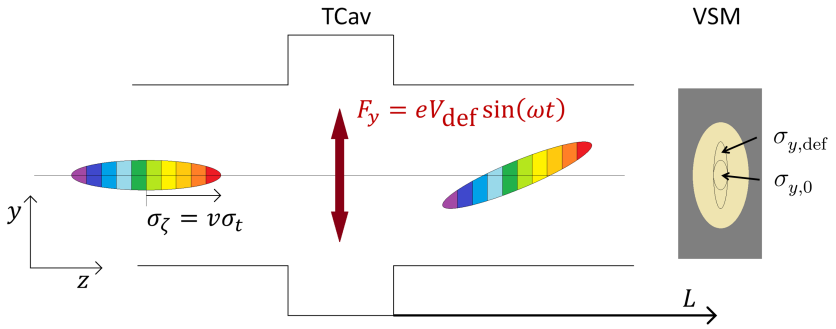

Figure 4.8: TCav operation principle: Shearing of a bunch with spatial and temporal *rms* length of σ_ζ and σ_t. Here $v = \beta c$ represents the bunch velocity. Inside the TCav the vertical deflecting voltage V_{def} oscillates with the RF frequency $\omega = 2\pi f_{\mathrm{RF}}$. For the bunch length measurement the longitudinal centroid of the bunch passes the TCav without deflecting and the longitudinal position is sheared into the vertical position. The resulting vertical *rms* bunch size $\sigma_{y,\mathrm{def}}$ can be measured and compared with the non-deflected bunch size $\sigma_{y,0}$.

The transverse beam size downstream from the cavity $\sigma_{y,\mathrm{def}}$ is than given as a convolution of the non-deflecting size $\sigma_{y,0}$ and the sheared bunch length $\left(\sqrt{\langle\zeta^2\rangle}\right)$.

$$\sigma_{y,\mathrm{def}}^2 = \sigma_{y,0}^2 + \left(\frac{S \cdot L}{pc[\mathrm{eV}]}\right)^2 \langle\zeta^2\rangle \tag{4.1}$$

For all bunch parameters a Gaussian distribution is assumed. Furthermore the three parameters in the bracket are the shearing parameter S, the drift length L to the screen

TM110 frequency	1300 MHz
Tuning range	3.5 MHz
transverse shunt impedance	5.3 MΩ
peak power per pulse	10 kW
repetition rate	10 Hz
shearing parameter S for 10 kW	$8.87\frac{\text{MeV}}{\text{m}}$

Table 4.3: Parameters of the GunLab TCav.

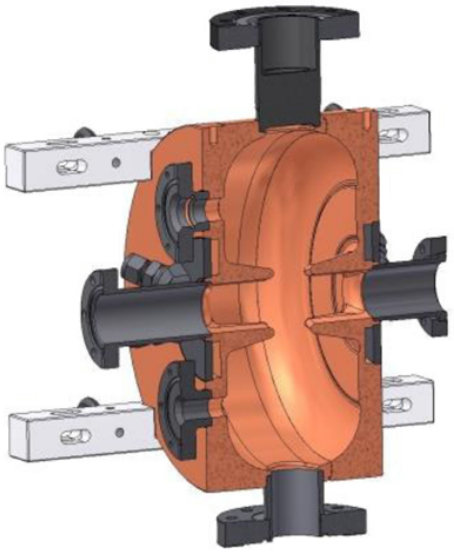

Figure 4.9: Drawing of the inner contour of the final TCav.

and the momentum of the electron beam pc in units of [eV]. Thereby S is given by the geometrical and electrical TCav parameters:

$$S = \frac{2\pi f_{\text{RF}}}{c}\sqrt{2PR_T} \tag{4.2}$$

with the resonator frequency f_{RF}, the transversal shunt impedance R_T, the transmitted peak power P and c as the speed of light. These parameters are listed in Tab. 4.3 which were determined by the final design of the cavity, depicted in Fig. 4.9.

4.2.5 Spectrometer dipole

A spectrometer dipole is used to measure the momentum distribution of the photoelectron beam. Thereby the particles are bend horizontally in the dispersive section according to their momentum. Together with the TCav, that streaks the beam in the vertical direction, the complete longitudinal phase space can be visualized on the VSM at DC6. In this section the design and the parameter of the GunLab spectrometer are presented.

Model of the GunLab spectrometer

In a collaboration with the Moscow state university [38, 39] a spectrometer dipole magnet was designed for very precisely spectrometry measurements of electron beams with kinetic energies up to 10 MeV. Therefore the design was optimized to achieve a maximal sensitivity on the particle momentum with a minimal impact of the initial transverse emittance. This optimization starts with a first order approximation through the calculation of the transfer matrix of the complete system. It consists of the two drift spaces L_1 and L_2 and the horizontal bend magnet itself, including edge focusing at both sides of the magnet (Fig. 4.10).

$$R_{\text{S}} = R_{\text{drift}}(L_2) \cdot R_{\text{edge}} \cdot R_{\text{bend}} \cdot R_{\text{edge}} \cdot R_{\text{drift}}(L_1) \tag{4.3}$$

In first order the horizontal beam size $\langle x_f^2 \rangle$ on the VSM at DC6 is given by

$$\langle x_f^2 \rangle = R_{\text{S},11}^2 \langle x_i^2 \rangle + 2R_{\text{S},11}R_{\text{S},12}\langle x_i x_i' \rangle + R_{\text{S},12}^2 \langle x_i'^2 \rangle + R_{\text{S},16}^2 \langle \delta^2 \rangle \tag{4.4}$$

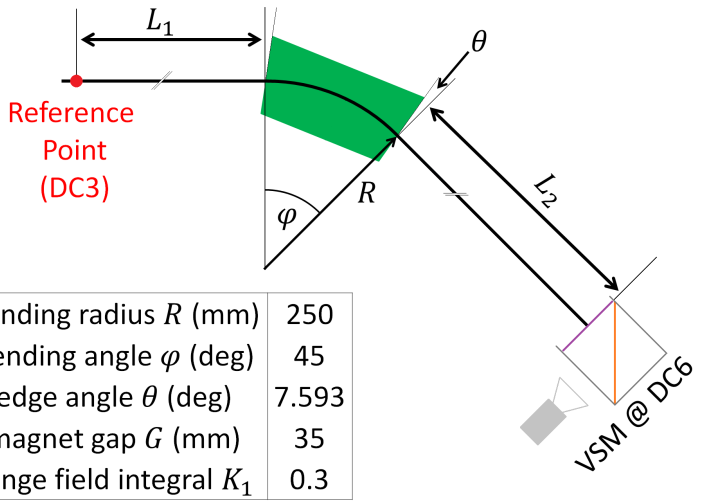

bending radius R (mm)	250
bending angle φ (deg)	45
edge angle θ (deg)	7.593
magnet gap G (mm)	35
fringe field integral K_1	0.3

Figure 4.10: Drawing of the spectrometer system with the reference point imaged on the VSM at DC6. The design parameter of the spectrometer are listed in the table below. The given fringe field integral is thereby defined by: $K_1 = \int \frac{B_y(s)\cdot(B_{y,0}-B_y(s))}{GB_{y,0}^2}\mathrm{d}s$, with $B_y(s)$ as the vertical magnetic field component along the path s, and G as the magnet gap

with $\delta = \frac{\Delta p_z}{p_z}$ and $\langle x_i^2 \rangle$ as the initial beam width at the reference point. Here, it is assumed that the initial bunch distribution has no correlation between the transverse coordinates and δ, and that the matrix elements $R_{\mathrm{S},13} = R_{\mathrm{S},14} = R_{\mathrm{S},15} = 0$. To minimize the influence of the initial horizontal phase space on the measurement a horizontal imaging ($R_{\mathrm{S},12} \stackrel{!}{=} 0$) in combination with a minimal absolute magnification ($R_{\mathrm{S},11} \to 0$) of the system is aspired. This results in the final beam width on screen:

$$\langle x_f^2 \rangle = R_{\mathrm{S},11}^2 \langle x_i^2 \rangle + R_{\mathrm{S},16}^2 \langle \delta^2 \rangle \tag{4.5}$$

The optimization goal for the spectrometer design was to achieve a minimum of the ratio $R_{\mathrm{S},11}/R_{\mathrm{S},16}$, using a symmetric spectrometer dipole with a 45 deg bending angle. The resulting magnet parameters are listed in the table in Fig. 4.10. The drift lengths are correlated with each other by the requirement of the horizontal imaging of the system. Thus, the necessary space between the reference point (DC3) and the spectrometer dipole defines the drift length L_2 between the spectrometer dipole and the VSM at DC6 (Chapter A.3).

In a further step, colleagues from the moscow state university (MSU) designed a coil and yoke geometry with the software CST [40], calculating the resulting magnetic field. Thereby, the geometry parameters were varied to achieve a magnetic field which transfers the phase space similar to the calculated transfer matrix.

Fig. 4.11 shows the CST model and the final design of the spectrometer dipole.

The magnet is operated by a bipolar high DC power supply (WME PA4008\11 [41]) with a relative current stabilization of 10^{-4}. Furthermore a control box calibrates the resulting field inside the spectrometer magnet. It measures the magnetic field using a Hall probe and calculates the momentum of a virtual electron which passes the magnet on an ideal path and hits the viewscreen center at DC6. Furthermore it determines the compensation current of the actual magnetic field in case the electron beam has to pass straight through the magnet.

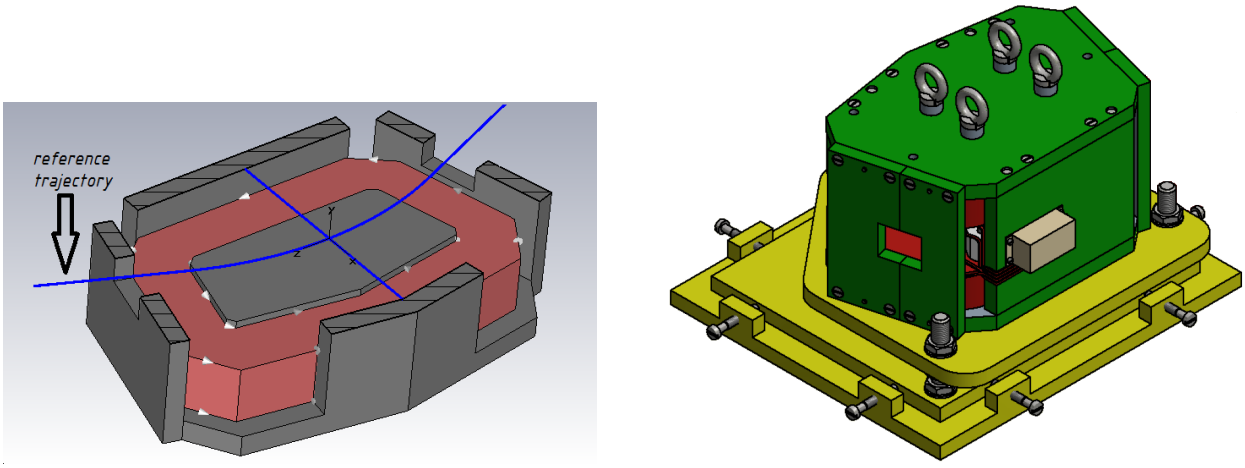

(a) transversal cross section of the CST model for the field calculation.

(b) Drawing of the final magnet design including an adjustable holder.

Figure 4.11: Drawings of the spectrometer dipole for GunLab

4.3 Drive laser

The drive laser for GunLab is a pulsed Yb:YAG laser, developed by the Max Born Institute (MBI). It is placed in a separate laser room next to the GunLab beamline bunker. The generation of the laser pulses takes place in four stages (Fig. 4.12). Firstly, a laser oscillator produces pulses with a repetition rate of 54 MHz synchronized to the 1.3 GHz RF source of the gun cavity. In the second stage, a pulse stretcher modulates the length of the final laser pulse. The final pulse length is measured with an auto-correlator at the end of the laser generation and can be adjusted manually in the stretcher module between 2 and 7 ps (rms). The stretched pulse is guided into a regenerative amplifier which can operate at repetition rates between 120 Hz and 30 kHz. It consists of an externally exited Yb:YAG crystal between two Pockels cells. These Pockels cells reflect the laser pulse so that it passes the amplification crystal several times. This intensifies the pulse power stepwise, until the final pulse energy is reached and the "switch-out" Pockels cell lets the laser pulse pass. The last stage converts the initial laser wavelength of 1030 nm to the second (515 nm) and fourth harmonic (258 nm). The auto-correlator uses a fraction of the green converted laser light for the pulse length measurement. The green laser is mainly used for the semiconductor photocathodes and the UV laser is used for the metal cathodes. Those have a higher work functions for the electron emission as the semiconductor cathodes. The important drive laser parameters are listed in Tab. 4.4.

Crystal material	Yb:YAG
pulse length (ps)	$2 \cdots 7$ (rms)
(@515 nm)	$4 \cdots 16$ (fwhm)
repetition rate (Hz)	$10 \cdots 10.000$
wavelength (nm)	515 (2ω) | 258 (4ω)

Table 4.4: Drive laser parameters for GunLab.

The final laser pulses are guided by a laser beamline to the GunLab facility. This beamline is shielded with a tube which is partially evacuated. A motorized beam shaping aperture in the laser beamline is imaged by a lens optic onto the photocathode of the injector.

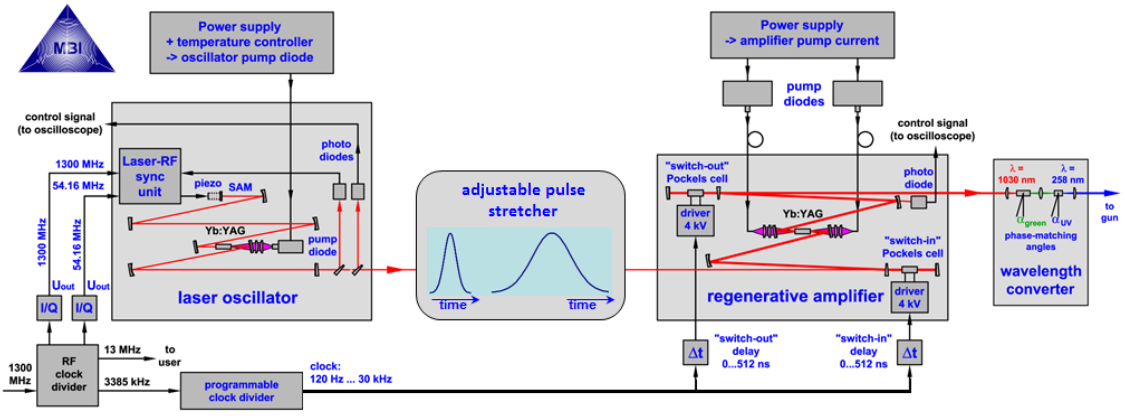

Figure 4.12: Scheme of the four stages of the drive laser for the GunLab test facility: Oscillator, pulse stretcher, amplifier and converter. (Courtesy by I. Will and G. Klemz)

This produces a good pointing stability of the laser on the photocathode and defines the spot size radius of the emitted bunch. For the later measurements with GunLab it is important to examine the laser parameters, like spot size on cathode, pulse energy or spot movement. This is done with a laser measurement system (virtual cathode) [28, 29]. The laser parameters are controlled during operation. An optical splitter deflects $\approx 2\%$ of the incident laser beam into the virtual cathode system, which has the same distance to the splitter as the photocathode in the gun cavity. It samples the laser intensity and transverse distribution on the photocathode. This system allows a correlated measurement of electron beam and drive laser parameter in GunLab.

4.4 Measurement tools

In the last section the technical design of GunLab was presented. In this section the measurement setup and the measurement procedure are depicted. Those are the beam size measurements with viewscreen monitors (VSMs) and the phase space reconstruction with a double quadrupole scan. Furthermore the measurements of the longitudinal phase space are discussed, such as bunch length and momentum measurements. In the context of this thesis, further measurement systems for the phase space reconstruction and beam halo observation were developed. These are described in Chapter 5 and Chapter 6, explicitly.

4.4.1 Viewscreen monitors

A viewscreen monitor (VSM) consists of three elements; the luminescence screen, the imaging optic and the camera (Fig. 4.13). The resulting image depends on the transverse charge distribution of the beam, that hits the luminescence screen and produces photons. This process of luminescence is almost identical for all scintillator materials whether organic or anorganic sheets. Electrons, passing the screen, deposit a fraction of their kinetic energy by Coulomb scattering processes in the material. Thereby luminescence light is produced. However, this multiple scattering of the incident electrons increases the beam size, too. The emitted light is imaged by an optic to a CCD camera. The individual characteristics of the VSM components affect the performance of a VSM, such as the measured resolution or the linear scaling between bunch charge and image intensity. Both are discussed in the following sections.

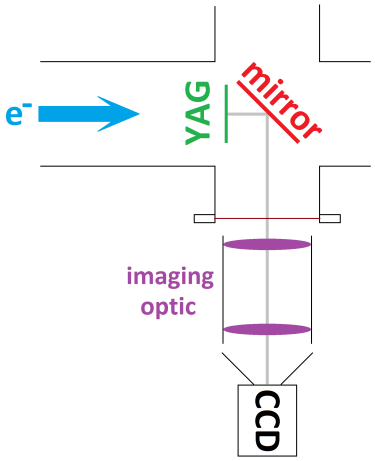

Figure 4.13: Drawing of a viewscreen monitor with a viewscreen inside the electron beamline, a vacuum mirror which deflects the emitted luminescence light to the imaging optics and the CCD outside the beamline.

Luminescence of a viewscreen

The energy loss $\frac{\mathrm{d}E}{\mathrm{d}x}$ of the incident electrons can be calculated by the Bethe formula [42]:

$$-\frac{dE}{dx} = \frac{4\pi\rho_e}{m_e c^2}\left(\frac{e^2}{4\pi\epsilon_0\beta}\right)^2\left[\ln\left(\frac{2m_e c^2\beta^2}{I(1-\beta^2)}\right)-\beta^2\right] \tag{4.6}$$

It is a result of the scattering processes of the electron beam with the electrons in the valence band of the crystal. These valence electrons can be excited to the conduction band producing an electron-hole pair (e-h). There are different decay channels for the e-h pair, depending on the scintillator material. For luminescence screens like YAG:Ce (Yttrium Aluminum Garnet doped with Cerium) or LuAG:Ce (Lutetium Aluminum Garnet doped with Cerium) the dominant decay channel is the transition of the excited electrons at the doped Cerium ions. It has a decay time of typically less than 100 ns and produce photons in the visible range. [49] The quantity of emitted photons is given by the photon yield value of the material (Tab. 4.5) which determines the number of emitted photons respectively to the deposited energy in the material. As an example, a single electron with a kinetic energy of 3 MeV deposits $\approx$ 0.15 MeV in a 200 μm thick YAG screen. This energy corresponds to more than 5000 photons. However, the photon yield combines different processes like the transport and quantum efficiency of the screen, as well as the densities of doped ions and e-h pairs.

In [50] it is shown that the complete process can be described by an exponential function of the transversal charge density ρ_{beam}. This density results from the incident beam, passing the screen in the same time range as the decay time:

$$R = 1 - exp\left(-\frac{\beta_{\mathrm{opt}}\rho_{\mathrm{beam}}\kappa\left(\frac{\mathrm{d}E}{\mathrm{d}x}\right)}{\rho_{\mathrm{Ce}}e}\right). \tag{4.7}$$

Thereby R describes the relative light emission, β_{opt} the transport efficiency of the material, κ and ρ_{Ce} the e-h pair production coefficient and the Cerium density, respectively. [52]

material (name)	YAG:Ce	LuAG:Ce[a]	Cry19[a b]
thickness	20μm[a c]| 100μm[a]| 200μm	200μm	200μm
density (g/cm^3)	4.55	6.76	7.1
refraction index	1.82	1.84	1.82
photon wavelength (nm)	550	535	420
photon yield (Ph/MeV)	35000	25000	24000
decay constant (ns)	70	70	41

[a] Installed in DC5
[b] Cry19 is the product name of a luminescence screen developed by Crytur.
[c] The thin YAG layer was glued on a 500μm quartz substrate

Table 4.5: List of the used screens at GunLab and their material properties. [49]

The typical length of an extracted electron bunch at GunLab is ≤ 6 ps *rms*. That is less than the decay time of the luminescence screens. Thus, the light emission is independent of the longitudinal charge distribution. It is obvious that for small charge densities R is linearly correlated to ρ_{beam}, but for higher charge values the emission increases non-linear and can also saturate. To examine these linearity of R for the GunLab VSMs an extreme electron beam scenario can be assumed with a bunch charge of 100 pC and a transverse beam size of 100 μm *rms*. The peak charge of a Gaussian beam profile with these values results in 1.6 fC/μm^2. Here, an ideal transport efficiency is assumed with $\beta_{\text{opt}} = 1$. In this case the exponents for the different viewscreen materials are determined to ≈ -0.02. Therefore a linear dependency between the emission intensity and the charge density can be expected. Even for this extreme scenario, the difference to the linear model is in the range of $\approx 1\%$.

Multi electron scattering inside a viewscreen

The multi electron scattering processes in the screens increase the transverse beam size. Thus the measured beam size is overestimated with respect to the original beam size in front of the luminescence screen.

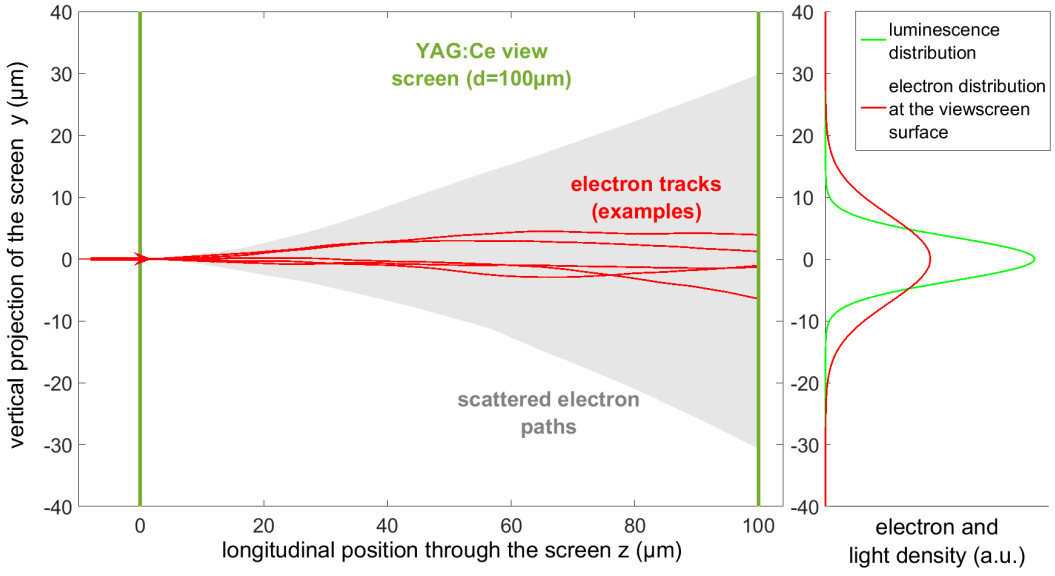

Figure 4.14: Scattering of electrons ($pc = 3$ MeV/c) inside the viewscreen.

Pos	screen	thickness	σ_λ (2 MeV/c)	σ_λ (3 MeV/c)
5.1	YAG:Ce	20 μm	0.6 μm	0.9 μm
5.5	YAG:Ce	100 μm	7.1 μm	4.7 μm
5.3	YAG:Ce	200 μm	20.9 μm	13.7 μm
5.2	LuAG:Ce	200 μm	28.2 μm	18.5 μm
5.4	Cry19	200 μm	29 μm	19 μm

Table 4.6: Growth of the measured *rms* beam size for the viewscreens at GunLab. (The parameters for Cry19 were extrapolated using the density of the material.)

Fig. 4.14 shows the scattering process inside an 100 μm thick YAG screen for several 3 MeV/c electron trackings that start at the same transverse position and perpendicular to the screen surface. Thereby the gray area is the projection of all electron trackings. Five electron paths are marked red as a tracking example. The rms width of the electron distribution on the exit surface can be described in first order as a Gaussian distribution with the Molière angle $\theta_{\text{Molière}}$ [42] (red curve in the right plot of Fig. 4.14):

$$\sigma_y = \theta_{\text{Molière}} \cdot d \tag{4.8}$$

Here σ_y is the *rms* width of the electron distribution on the exit surface and d the thickness of the screen. The projected Molière angle depends on the material properties, combined in the radiation length X_0, and the momentum of the incident charged particle:

$$\theta_{\text{Moliere}} = \frac{13.6 \text{ MeV}}{\beta cp} z \sqrt{\frac{d}{X_0}} \left(1 + 0.038 \ln\left(\frac{d}{X_0}\right)\right) \tag{4.9}$$

Here it is assumed that the target material is thin and the electron energy losses can be neglected. The electrons produce luminescence light along their scattered path through the screen. The projected emission size of this luminescence is the average of the electron distribution sizes inside the screen and can be determined by

$$\sigma_\lambda = \theta_{\text{Molière}} \cdot \frac{d}{2} \tag{4.10}$$

The resulting *rms* influences on the beam size measurements for the GunLab viewscreens are tabulated in Tab. 4.6 for an electron momentum of $pc = 2$ Mev/c and $pc = 3$ MeV/c. It shows that for the standard VSMs at GunLab the screen resolution error can be estimated to σ_λ<20 μm.

Optical read out using a CCD camera

For GunLab, Prosillica AVT cameras are used with 2.8 Megapixel CCD chips. Tab. 4.7 shows the important parameters of these cameras which have a dynamic range of 14 bit for the monochrome CCD and 12 bit for the color CCD.
The dynamic range for CCD cameras is typically defined as the ratio of the full well electron capacity value $C_{\text{full well}}$ per pixel to the average noise of the camera. Thereby $C_{\text{full well}}$ is the electrical charge which can be sampled on a pixel. The value is in general small and often given as number of electrons. If more electrons are generated on a pixel as can be sampled by $C_{\text{full well}}$, the pixel will be saturated. The overload cannot be distinguished by the electronics and can flow into neighbored pixels (blooming) [54]. The average noise of the CCD chip is the sum of pixel noise from the CCD combined with

CCD camera	AVT GT1920	AVT GT1920C
Sensor size type	2/3″	
Resolution (HxV)	1936x1456	
Pixel size	4.54μm x 4.54μm	
max. frame rate	40.7 fps	
Image read out	monochrome	color
image bit depth	14	12
exposure time control	10μs ... 26.8 s (1μs increment)	
Gain control	0 ... 33 dB	
full well electron capacity	> 17000	

Table 4.7: Properties of the CCD cameras for GunLab. [53]

the read out and filter effects of the electronic read out system. This dynamic range of the monochrome CCD limits the observable light intensity of an object to $I_{max}/2^{14} \approx I_{max}/16000$. A region on the viewscreen with a relative charge density (with respect to the peak charge density on screen) below this threshold cannot be sampled by the CCD camera without a saturation of the peak charge density region.

Resolution of the optical read out

The complete optical read out of the VSMs consists of an optical imaging system with a fixed focal length objective and the already introduced AVT-CCD cameras. To image the 25 mm screen diameter completely on the CCD chip a magnification of $|M| \approx 0.26$ is needed. This results in a object pixel size of 17.2 μm which is also the ideal resolution σ_{CCD} of the CCD camera. Furthermore, the resolution is limited by the Rayleigh criterion of the imaging system, determined by

$$\sigma_{\mathrm{optic}} = 1.22\frac{\lambda}{D}L \tag{4.11}$$

with λ as the wavelength of luminescence light (s. Tab. 4.5), D as the optics diameter and L as the distance between optics and object plane. For the chosen optics with an aperture of 40 mm the resolution can be approximated for the different viewscreens to σ_{optic}<8 μm. The final resolution for the measurements with the viewscreen monitor is the squared sum of all optical resolutions

$$\sigma^2_{\mathrm{VSM}} = \sigma^2_{\lambda} + \sigma^2_{\mathrm{CCD}} + \sigma^2_{\mathrm{optic}} \tag{4.12}$$

VSM	σ_{VSM}(pc=2 MeV/c)	σ_{VSM}(pc=3 MeV/c)
standard[1]	28 μm	24 μm
DC5.1	19 μm	19 μm
DC5.5	20.4 μm	19.7 μm
DC5.2	34 μm	27 μm
DC5.4	35 μm	27 μm
DC6	47 μm	45 μm

[1] standard VSM is installed at DC1, DC3, DC4 and DC 5.3

Table 4.8: Combined resolution of the viewscreen monitors at GunLab for two beam momenta. The screen order of DC5 is the same as in Tab. 4.6.

The resulting resolution of all VSMs at GunLab are tabulated in Tab. 4.8. For the standard viewscreen monitors in GunLab, with the 200 μm thick YAG:Ce screens, σ_{VSM} is less than 30 μm. For the thin screens in the multiscreen station in DC5 the resolution is dominated by the optical read out, but can be improved with a higher absolute magnification. However, this leads to a smaller region of interest which are necessary for the measurement of very small transverse emittances (phase space scanner) or extremely short electron bunches (bunch length measurement with the TCav).

4.4.2 Bunch length measurement

For experiments with high temporal resolution the bunch length of the photoelectron beam is an important parameter. It has to be measured as part of the longitudinal phase space analysis in GunLab. Therefore a transverse deflecting cavity (TCav) is installed in the beamline (Chapter 4.2.4). It shears the beam in vertical direction over the VSM at DC5, where the resulting beam size ($\sigma_{y,\mathrm{def}}$) is sampled and compared with the non-deflected beam size ($\sigma_{y,0}$), resulting in the *rms* bunch length:

$$\langle\zeta^2\rangle = \left(\frac{pc}{SL}\right)^2 (\sigma^2_{y,\mathrm{def}} - \sigma^2_{y,0}) \tag{4.13}$$

Here, S and L are the shearing parameters and the drift length between TCav and DC5. In combination with the bunch velocity v, the spacial bunch length can be transformed into a temporal bunch length σ_t:

$$\sigma_t = \frac{\sqrt{\langle\zeta^2\rangle}}{v} \tag{4.14}$$

$$= \frac{E_{\mathrm{tot}}}{SLc}\sqrt{\sigma^2_{y,\mathrm{def}} - \sigma^2_{y,0}} \tag{4.15}$$

with $E_{\mathrm{tot}} = \sqrt{pc^2 + (mc^2)^2}$ as the total energy of the electron bunch and c as the speed of light. The term in the bracket is named in the following transformation factor $A = \frac{E_{\mathrm{tot}}}{SLc}$, which can be determined easily in the experiment by a phase scan of the TCav. Thereby, the position of the vertical centroid $\langle y_{\mathrm{def}}\rangle$ is measured as function of the cavity phase ϕ_{TCav}.

$$A = \left(\frac{\partial\langle y_{\mathrm{def}}\rangle}{\partial\phi_{\mathrm{TCav}}}\right)^{-1} \frac{2\pi}{f_{\mathrm{RF}}} \tag{4.16}$$

This method minimizes the error of the transformation factor. The measurement error F_t of σ_t is dominated by the systematic errors of the beam size measurement σ_{VSM}. A calculation of the error propagation of Eq. 4.15 results in:

$$F_t = A\sqrt{\frac{\sigma^2_{y,\mathrm{def}} + \sigma^2_{y,0}}{\sigma^2_{y,\mathrm{def}} - \sigma^2_{y,0}}}\sigma_{\mathrm{VSM}} \tag{4.17}$$

This error also determines the minimum bunch length which can be reconstructed significantly. Therefore the measured *rms* beam size difference has to exceed the screen resolution σ_{VSM}.

$$\sigma_{y,\mathrm{def}} - \sigma_{y,0} > \sigma_{\mathrm{VSM}} \tag{4.18}$$

$$\Rightarrow \sigma_{t,\mathrm{min}} \approx \sqrt{2\sigma_{\mathrm{VSM}}\sigma_{y,0}}A \tag{4.19}$$

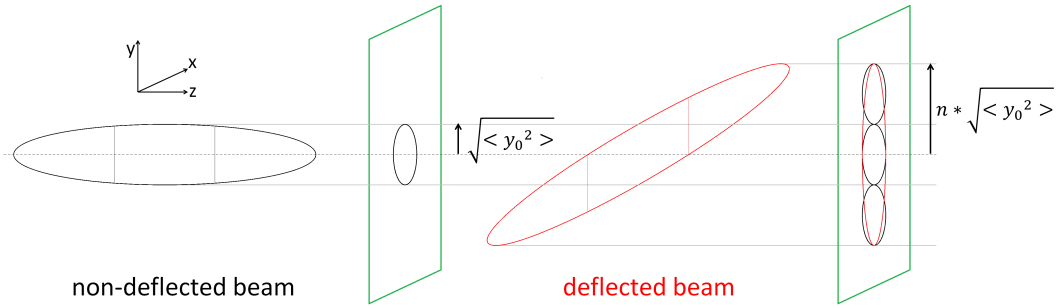

Figure 4.15: Example of non-deflected and a deflected beam, with $n = 3$ slices, at the same VSM for a sliced emittance measurement. The deflected beam size has to be at least n times bigger than the non-deflected beam, so that the n slices do not overlap with each other.

For the calculated resolution of the VSM at DC5, $\sigma_{t,\mathrm{min}}$ results in less than 200 fs for an initial beam sizes of $\sigma_{y,0}$ $\leq$1 mm, beam momenta of 3 MeV/c, $L \approx 1$ m and $S = 8.87$ MV/m. This resolution can be reduced to $<$ 100 fs for $\sigma_{y,0} \leq 200\mu$m.
Another definition of the minimal bunch length exists for the slice emittance measurement. Thereby the slices of a bunch have to be displaced completely so that each slice can be observed independently [43]. Fig. 4.15 demonstrates this requirement which results in a minimal bunch length definition, depending on the number of the defined slices:

$$\sigma_{y,\mathrm{def}} \geq \sigma_{y,0} \cdot n \tag{4.20}$$

$$\Rightarrow \langle \zeta^2 \rangle \geq \frac{(n^2-1)pc}{SL}\,\sigma_{y,0}^2 \tag{4.21}$$

The smallest bunch length value for a slice emittance measurement with n slices is than given by:

$$\sigma_{t,\mathrm{min,slice}} = \sqrt{n^2-1}\sigma_{y,0}A \tag{4.22}$$

In contrast to Eq. 4.19, Eq. 4.22 is directly correlated to the beam size of the non-deflected beam. For the same beam energy and TCav setup, a minimal bunch length is determined to $\sigma_{t,\mathrm{min,slice}} \approx 400$ fs, if the initial beam is focused to an *rms* beam size of 200 μm and only 2 slices are observed. In conclusion, the TCav for GunLab is used to reconstruct bunch lengths down to 200 fs even for a high beam momenta of 3 MeV/c. Thus, the necessary slice thickness of $<$500 fs (Chapter 4.4.1), for the slice emittance analysis, can be achieved by this TCav and beam parameters.
For short electron bunches ($<$ 1 ps) or a high number of slices this initial beam size has to be as small as possible. Furthermore this value has to be constant for a measurement, because otherwise the resulting overlap variation distorts the sliced emittance measurement. In the following section a technique is presented to achieve a constant horizontal beam size during a sliced emittance scan.

4.4.3 Double Quadrupole Scan

Two quadrupole magnets are installed in the GunLab beamline between DC3 and the TCav. They allow a reconstruction of the projected and the sliced phase space (Chapter 2.3.2) of the electron bunches. For the sliced emittance measurement the TCav is used which streaks the beam in the vertical direction. The reconstruction process is in both

cases the same. The focal strengths k_1 and k_2 of both quadrupole magnets are varied and the resulting horizontal and vertical beam sizes at DC5 are sampled. These beam sizes can be also calculated in first order by the given transfer matrix R_{sys} of the double quadrupole system and the initial beam parameters which are the elements of the initial Σ-matrix (Eq. 2.16).

$$R_{\mathrm{sys}} = R_{\mathrm{drift}}(L_3)R_{\mathrm{QP}}(k_2)R_{\mathrm{drift}}(L_2)R_{\mathrm{QP}}(k_1)R_{\mathrm{drift}}(L_1) \tag{4.23}$$

R_{sys} consists of the two quadrupole magnets, described by R_{QP}, and the three drift spaces $R_{\mathrm{drift}}(L_i)$. Thereby, the transfer matrix R_{QP} is a function of the focal strength k. For a given initial Σ matrix at the reference point of the system the transformation results in a beam size F:

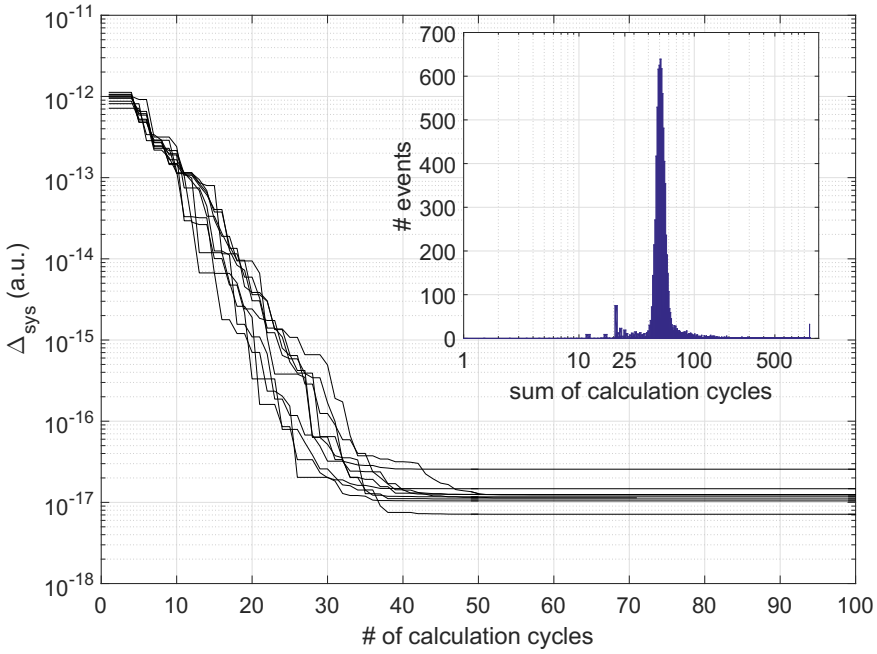

Figure 4.16: Statistics of the reconstruction algorithm. The black curves represent 10 examples for the integration difference Δ_{sys}. The algorithm ends if the relative change of Δ_{sys} fall below 10^{-4} in several cycles. The sum of cycles is shown in the histogram for the reconstruction of more than 8000 simulated double quadrupole scans.

$$F^2(\Sigma) = R^2_{\mathrm{sys},11}\Sigma_{11} + 2R_{\mathrm{sys},11}R_{\mathrm{sys},12}\Sigma_{12} + R^2_{\mathrm{sys},12}\Sigma_{22} \tag{4.24}$$

F is also a function of k_1 and k_2. These calculated beam sizes can be compared with the measured beam sizes σ_m at DC5. The integrated differences Δ_{sys} between both beam sizes will be minimal, if the defined Σ matrix is similar to the original beam parameters at the reference point.

$$\Delta_{\mathrm{sys}} = \sum_{k_1\,,\,k_2} \Big(\sigma_m(k_1,k_2)^2 - F^2(\Sigma,k_1,k_2)\Big)^2 \,\mathrm{d}k_1\mathrm{d}k_2 \tag{4.25}$$

This optimization is done with a geometrically optimization algorithm that reconstructs the original Σ matrix by minimizing the difference value Δ_{sys}.

This algorithm was numerically tested with ASTRA simulation of the double quadrupole system in GunLab. It was assumed that the reconstruction algorithm works with any kind of correlation between k_1 and k_2 , as well as any initial beam parameter setting. Thus, the focal strengths of both quadrupole magnets were randomly varied in a defined range. Furthermore, several ideal Gaussian bunches (without space charge and momentum spread) with different initial parameter settings were tracked from the reference point up to DC5. There, the final beam sizes were sampled on a virtual screen. The reconstruction algorithm needed on average 50 steps to find the optimal Σ matrix. The accuracy of the reconstructed Σ-matrix depends on the number of measurement points (k_1-k_2-combinations) and on the initial beam optic. For beam scenarios with a focal point next to the reference point, an uncertainty of the reconstructed emittance was achieved in the same order as the statistical error of the simulations. Here, at least 20 measurement points were defined and ideal Gaussian bunches without space charge assumed. The limited screen resolution of a VSM (≈ 30 μm) produces an additional systematic error of $< 2\%$[a].

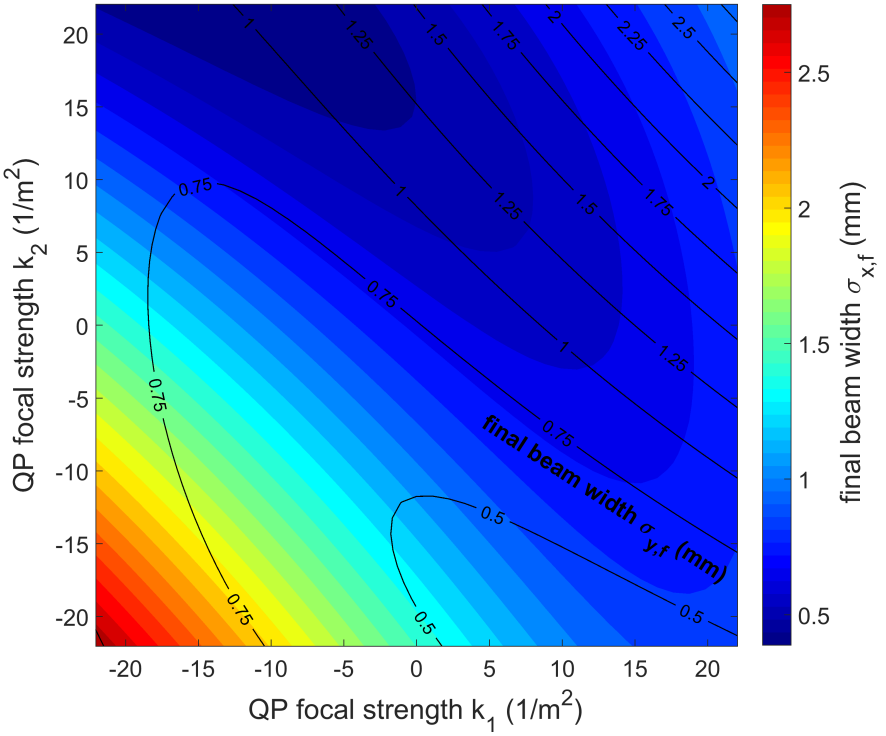

Figure 4.17: Simulated beamwidth at screen (@z = 1.5 m) in horizontal direction as function of the quadrupole strengths k_1 of the first quadrupole (@z = 0.5 m) and k_2 of the second quadrupole (@z = 0.7 m). The black contour lines describe the vertical beamwidth between 0.5 mm and 2.75 mm.

This result confirms the above assumption, which is important for the analysis of the sliced emittance. For this measurement the TCav streaks the bunch in vertical direction. Thus, the vertical bunch distribution on a VSM is a convolution of the non-streaked longitudinal and vertical beam distributions. Thereby the vertical beam size of the non-streaked beam on screen should be as small as possible to achieve highest longitudinal resolution. Furthermore, this beam size has to be constant for the complete sliced emittance

[a]For the calculation of the meassurement error the sampled beam sizes in the simulations were added to σ_{VSM}.

measurement with the TCav. Otherwise the overlap of the defined slices change which disturb the analysis. For an initial Σ matrix, only one curve in the k_1-k_2-plane exists to fix the defined vertical beam size on screen. Fig. 4.17 shows an example of these curves for different fixed vertical beam sizes $\sigma_{\mathrm{y,f}}$. Thereby, the horizontal beam size is plotted as contour of the both focal strengths k_1 and k_2. A sliced emittance scan works with one of these curves for the both quadrupole magnets during the TCAV streaks the beam in the vertical direction. The horizontal beam size on the screen is measured with respect to the vertical position and is used to reconstruct the initial horizontal distribution of each slice.

4.4.4 Energy measurement

A spectrometer dipole magnet is installed in the GunLab beamline to determine the kinetic energy and the energy distribution of the photoelectron beam (Chapter 4.2.5). The magnet deflects the incident beam in the dispersive section of GunLab. Thereby the deflecting angle ϕ depends on the peak field value of the spectrometer and the momentum of the beam. Thus the average momentum is determined by the necessary peak field value in the magnet to center the beam on the viewscreen at DC6 ($\phi = 45$ degrees). Also, the momentum spread δ can be reconstructed by the horizontal beam size on the screen and the known transfer matrix R of the spectrometer system (Eq. 4.5):

$$\delta_{rec} = \frac{\sqrt{\sigma^2_{x,\mathrm{screen}} - \sigma^2_{r,\mathrm{ref}} R^2_{11}}}{R_{16}} \tag{4.26}$$

with $\sigma_{x,\mathrm{screen}}$ and $\sigma_{r,\mathrm{ref}}$ as the beam size on the screen at DC6 and the reference point of GunLab. The necessary calibration for the reconstruction was achieved by numerical simulations of the magnet with ASTRA. With these simulations also systematic measurement errors can be estimated.

Field calibration of the spectrometer magnet

The calculated field profile was implemented as a 3d field file in the tracking code with similar orientation as the real magnet in the GunLab beamline. Afterwards the field calibration factor was determined by tracking particles through the magnet. In Fig. 4.18 some particle tracks are plotted exemplarily, on top of the field profile and the yoke geometry of the magnet. Here, the feasible parameter range for the following analysis is presented as thick black particle tracks. The green line shows the tracking in the case of a switched off magnet.
The field calibration factor $B_{\mathrm{cal,peak}}$ describes the necessary peak field of the magnet to bend a particle with a given momentum pc onto the viewscreen center of DC6.

$$B_{\mathrm{cal,peak}}(pc) = 13.31 \frac{\mathrm{mT}}{\mathrm{MeV}} \cdot pc \tag{4.27}$$

In a second step the physical drift lengths for the imaging and the transfer matrices for these systems were examined. This was done with a tracking algorithm which determines the particle phase space transformation for a given magnetic or electric field map. Therefore it calculates the linear and non-linear elements of the resulting transfer matrix. The algorithm and the results of the transfer matrix calculation are shown in Appendix A.3. For this reconstruction method, only the matrix elements $R_{11} = (-0.793 \pm 0.004)$ and $R_{16} = (0.7213 \pm 0.0009)$ m are necessary.

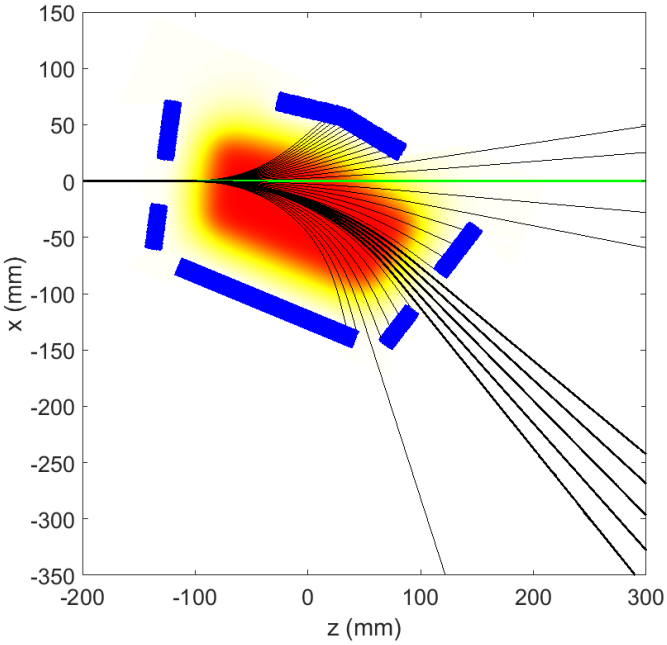

Figure 4.18: Tracking of mono-energetic electrons with $pc = 7.7$ MeV (black lines) through the spectrometer dipole magnet where the peak field amplitude is varied in a range of ± 208 mT. The magnetic field distribution inside the magnet yoke is depicted as a red and yellow contour plot. The green line shows the tracking for the switched-off magnet.

Systematic errors of the spectrometer measurements

With the determined matrix elements and the known initial and final beam widths it is possible to calculate the momentum spread of the bunch at the reference point. This measurement has systematic errors of several potential sources such as

- a non-linear phase space transformation which is not accounted for the transfer matrix,
- an unknown initial phase space distribution,
- a limited screen resolution and
- the field accuracy.

The first and the second items were determined by tracking simulations through the spectrometer system with several initial particle distributions. Thereby the initial bunches consist of one million particles to suppress numerical uncertainties. An average momentum of 3 MeV/c was defined. At the reference point they are cut by a slit mask with a slit width of 50 μm. The tracking starts at the reference point with different momentum spreads for the beamlets from $\delta_0 = 10^{-4}$ to $\delta_0 = 10^{-1}$. Eq. 4.26 was used for the reconstruction of the momentum spreads δ_{rec}. These values were compared with the δ_0 at the reference point. Fig. 4.19 shows the systematical and statistical errors of this simulated measurement. The systematical error describes the difference between δ_{rec} and δ_0. On the other hand, the statistical error is defined as the standard deviation of δ_{rec} for beamlets with the same initial momentum spread. This plot shows that for momentum spreads between $\delta_0 = 1‰$ and $\delta_0 = 3\%$ the measurement error is $\approx 2\%$. For a momentum spread less than 0.5‰ and more than 5% the error measurement error increases up to 10%. This can be explained

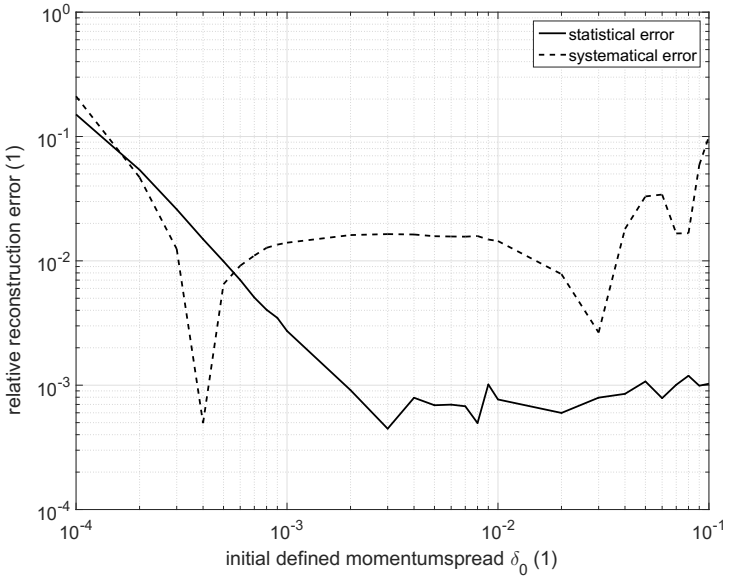

Figure 4.19: Simulated momentum spread measurement for different initial defined momentum spreads and averaged over 20 bunches with different initial optical functions. The measurement was done at the image plane 757 mm downstream the spectrometer dipole (flange of the spectrometer vacuum chamber).

for high δ_0 values by the non linear terms of the R_{16} element. However, for extreme small δ_0 values the error is dominated by the non-linear phase space transformation and further systematic errors in the imaging system of the transfer matrix elements ($R_{11}...R_{14}$).
The alignment of the vertical slit can be neglected because all viewscreen monitors and slit masks in the GunLab beamline were calibrated by an optical leveling instrument with a standard tolerance of 100 μm. These offsets results in a relative uncertainty of $\approx 10^{-4}$ for the average momentum measurement. The same applies to the effect of the screen resolution, estimated to $\sigma_{\mathrm{VSM}}(DC6) < 50\mu$m (Chapter 4.4.1). Thus the impact on the momentum spread reconstruction results to an error of $< 7 \cdot 10^{-5}$. The last item for possible systematic errors of the spectrometer system is the field accuracy. Therefore the field of the magnet was already measured by the MSU and a controller box for the spectrometer dipole was developed to sample the field amplitude during operation and to calculate beam momentum on the VSM. Furthermore a power supply is used (WME PA4008\11 [41]) which provides a constant current value with an accuracy of 10^{-4} as sum of ripple currents and reproducibility. This reduces also fast field fluctuations in the spectrometer dipole. In conclusion, the spectrometer dipole for the GunLab system allows to observe electron beams with energies up to 10 MeV and momentum spreads until 10^{-4} with a systematic error of less than 10%, dominated by the linear momentum reconstruction model.

Chapter 5

Phase space measurement system

It is important to visualize the transverse phase space distribution of the extracted electron bunches, to characterize the impact of the individual SRF photoelectron components on the electron beam. This allows a direct observation of the transverse emittance, as well as non-linear distributions, as function of the photoinjector settings. Therefore the phase space scanner system is installed at GunLab. It consists of a slit mask, a viewscreen monitor (VSM) and a pair of compact dipole magnets. Both magnets move the beam parallel to beam-axis over the slit mask. In this chapter the concept and the setup of this system are presented. It is shown that this setup requires high quality dipole magnets, realized using cosθ-magnets. The model and the realization of these magnets for GunLab are also discussed here. With the resulting magnet designed, the limitations and measurement errors of the complete phase space scanner system are determined by numerical calculations and particle trackings.

5.1 Transverse phase space reconstruction

For the reconstruction of the transverse phase space a pair of compact dipole magnets (scanner magnets) moves the beam parallel to the beam axis over a narrow slit mask. This slit mask is a 1.5 mm thick tungsten plate with a 50 μm slit. Only a small fraction of the initial electron bunch (beamlet) can pass this slit (Fig. 5.1). The remaining electrons will be stopped completely by the tungsten plate, if their kinetic energies are less than 3.7 MeV. The beamlet drifts a length L downstream the beamline to a viewscreen monitor (VSM - Chapter 4.4.1). A measurement of the width $\langle x_2^2 \rangle$ and the average position $\langle x_2 \rangle$ of the beamlet determines the phase space distribution of the beamlet at the position of the slit mask, which can be used to reconstruct the local divergence of the initial beam. Thus, a transverse scan of the beam over the slit mask results in the complete phase space distribution of the initial bunch.
Both *rms* beamlet values $\langle x_2^2 \rangle$ and $\langle x_2 \rangle$ at the VSM depend on the initial parameters ($\langle x_1^2 \rangle$, $\langle x_1 x_1' \rangle$ and $\langle x_1'^2 \rangle$) of the beamlet at the slit mask position and can be calculated in first order by:

$$\langle x_2 \rangle = \langle x_1 \rangle + L\langle x_1' \rangle \tag{5.1}$$

$$\langle x_2^2 \rangle = \langle x_1^2 \rangle + 2L\langle x_1 x_1' \rangle + L^2\langle x_1'^2 \rangle \tag{5.2}$$

Thereby two assumptions were made: $\langle x_1 \rangle$ depends on the fixed transverse slit mask position which is constant and can be set to zero as a transverse reference. Furthermore the correlation term $\langle x_1 x_1' \rangle$ is neglected in first order, because it is assumed that the local

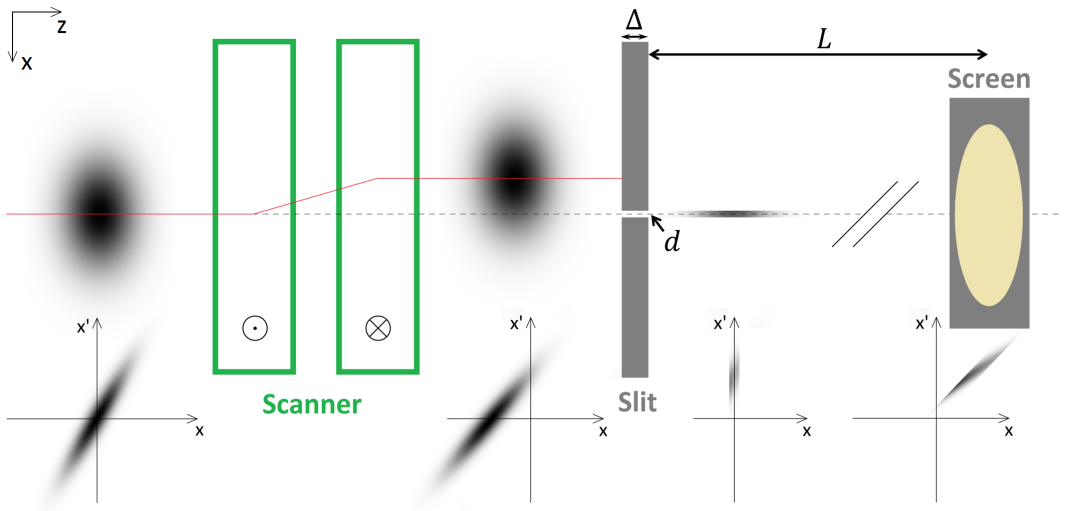

Figure 5.1: Drawing of the phase space scanner system with the scanner magnet doublet, the slit mask and the viewscreen monitor. The scanner magnet doublet consist of two compact dipole magnets moving the beam parallel to the beam axis. The tungsten slit mask has a thickness Δ of 1.5 mm and a slit width d of 50 μm. Below the draft of the horizontal phase space distributions of the beam and the beamlet is plotted with respect to the longitudinal position.

divergence is much bigger than the correlated divergence of the beam. Thus, the second term in Eq. 5.2 is suppressed relative to the third term. Furthermore, the slit width d determines the initial beamlet size to $\langle x_1^2 \rangle = \frac{d^2}{12}$. Thereby Eq. 5.1 and Eq. 5.2 can be written as:

$$\langle x_1' \rangle = \frac{\langle x_2 \rangle}{L} \tag{5.3}$$

$$\langle x_1'^2 \rangle = \frac{\langle x_2^2 \rangle - \frac{d^2}{12}}{L^2} \tag{5.4}$$

For a phase space scan $\langle x_2 \rangle$ and $\langle x_2^2 \rangle$ are measured for each beamlet i as function of the initial beam offaxis position x_i. This beam position is varied in the scan range x_{scan} (Fig. 5.2 (a)). The intensity or particle number n_i of the beamlets depends on x_i, too. With these four functions the phase space distribution of the initial beam can be reconstructed by:

$$\langle X \rangle = \frac{1}{N} \sum_i (n_i x_i) \tag{5.5}$$

$$\langle X^2 \rangle = \frac{1}{N} \sum_i \left(n_i (x_i - \langle X \rangle)^2 \right) \tag{5.6}$$

$$\langle X' \rangle = \frac{1}{NL} \sum_i (n_i \langle x_{2,i} \rangle) \tag{5.7}$$

$$\langle X'^2 \rangle = \frac{1}{N} \sum_i \left(n_i (\langle x_{2,i} \rangle / L - \langle X' \rangle)^2 \right) + \frac{1}{NL^2} \sum_i \left(n_i \langle x_{2,i}^2 \rangle \right) \tag{5.8}$$

$$\langle XX' \rangle = \frac{1}{N} \sum_i (n_i (x_i - \langle X \rangle)(\langle x_{2,i} \rangle / L - \langle X' \rangle)) \tag{5.9}$$

with N as the intensity sum of the beamlets $N = \sum_i n_i$. Thus the reconstructed geomet-

rical emittance are determined by:

$$\varepsilon_{geo} = \sqrt{\langle X^2 \rangle \langle X'^2 \rangle - \langle X X' \rangle^2} \tag{5.10}$$

Such a non-continuous integration over a limited transverse range with respect to the beam size can produce a systematic error of the reconstructed beam parameters. For the calculation of the systematic error the model was numerically tested with several ideal $2d$-Gaussian functions in the x-x'-phase space, used as initial bunch distributions. Thereby the number of steps and the range for the scans were varied. The reconstructed parameters were compared with the initial Gaussian distributions. It was detected that an increase of the x_{scan} with respect to the initial beam size will improve the reconstruction of the beam parameters, if at least 10 scan steps are used. Fig. 5.2 (b) shows as an example the reconstruction error of the beam emittance as function of x_{scan} and the number of scan steps. It can be seen that the scan range has to be at least 7σ (3.5σ in each direction

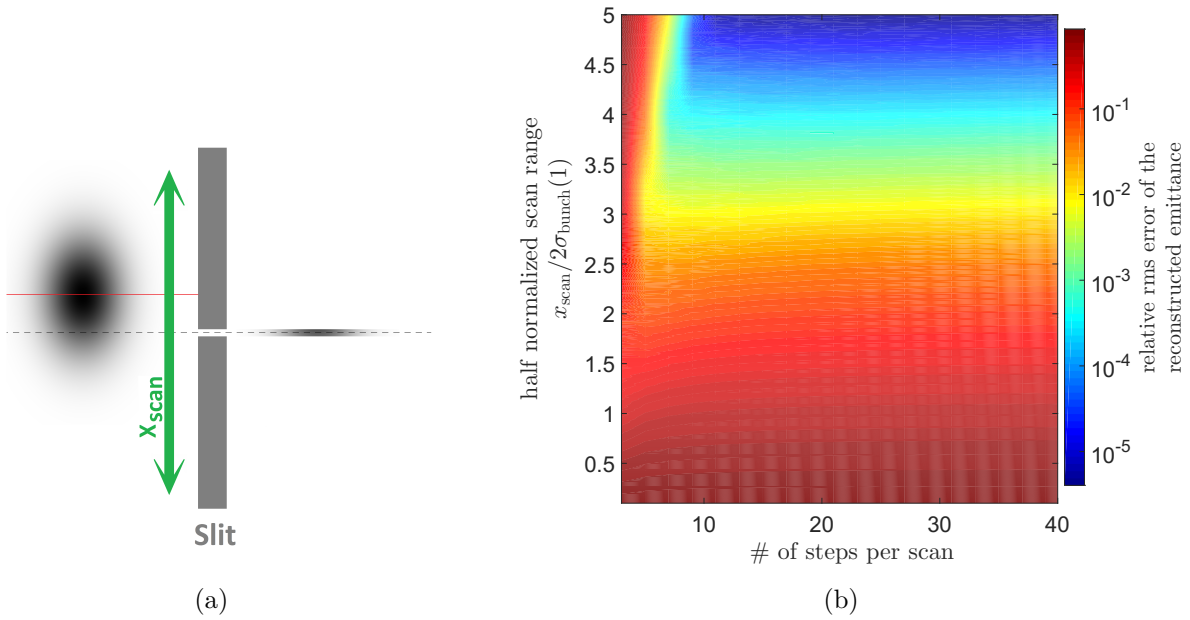

(a) (b)

Figure 5.2: Left: Scheme of the beam movement over the slit mask. Right: Reconstruction error of the emittance value as function of the scan range normalized to the rms beam width and the number of scan positions.

relative to the centroid) of the initial bunch size and 10 steps to achieve a reconstruction error less than 1‰. A further increase of the step number to more than 20 steps per scan does not improve the measurement uncertainties. This wide scan range has to be considered for the specification of the scanner magnets which are discussed in the following section. They need to have the ability to move electron beams with different momenta over a range of several millimeters.

5.2 Phase space scanner magnets

The scanner magnet doublet consists of two identical dipole magnets with a different sign of their field polarity. This configuration moves the electron beam parallel over the slit mask. Due to spatial limitations in the GunLab beamline the magnet system can have a maximal length of only 240 mm. This concerns the length of the magnets itself, as well

as the space between them. With this geometrical limitations the needed field strength can be calculated to fulfill the requirements of the wide scan range. It can be written in linear approximation by:

$$\int B_y(z)\mathrm{d}z = \frac{x_0}{L}\frac{pc(\mathrm{eV})}{c} \tag{5.11}$$

where x_0 represents the horizontal offset behind the magnet system and L the distance between both magnet positions. As an assumption: a beam with a momentum of 3 MeV/c which has to be moved 5 mm offaxis by a magnet double with $L = 100$ mm, Eq. 5.11 results in $\approx 5 \cdot 10^{-4}$ Tm. This integrated field value can be achieved by air-core coil magnets without the risk of residual magnetic fields, resulting of a ferromagnetic return yoke. Thereby the shape of the magnetic field is mainly determined by the electric current distribution through the magnet coils. However, the resulting magnetic field should suppress higher order multipole field components which can distort the transverse phase space distribution of the scanned beam and thereby the phase space measurements, as well. A cosθ magnet is a promising design to create a pure dipole field with a high magnetic flux density on axis. For such a magnet the coils are placed directly on the beam tube. Thus a minimal distance between electrical current and beam produces a maximal field strength for the beam deflecting without any residual magnetic fields. In the following the design of an ideal cosθ magnet is presented, including a realization for GunLab.

5.2.1 Ideal designs for air-core coil magnets

Air-core coil magnets are electromagnets without a ferromagnetic return yoke (in the following: yoke). In this case, the magnetic field is determined by the distribution of the electric current density and can be calculated using Biot-Savarts law [48]. Here, the magnetic field $\vec{B}$ at the position $\vec{P}$ is described by:

$$\vec{B}(\vec{P}) = \frac{\mu_0 I}{4\pi}\int \frac{\mathrm{d}\vec{r}\times(\vec{r}-\vec{P})}{\left|\vec{r}-\vec{P}\right|^3}, \tag{5.12}$$

with I as the current along the path $\vec{r}$. For the estimated kinetic energies of the SRF cavity the magnetic field strength for beam steering and focusing can be generated with normal conducting air-core coils. The field strength of an air-core coil depends on the ratio of the magnetic flux and the cross section of the magnet. Both values are limited for the GunLab magnets, because of the maximal magnet length and electrical current density in the magnet coils. Consequently the magnet coils have to be positioned as close as possible to the electron beam to achieve the necessary magnetic flux density. Furthermore the amplitudes of unwanted multipoles and thereby the non-linear effects have to be minimized. Both requirements can be achieved with cos(θ)-magnets.

Design of cos($n\theta$)-magnets

A cos($n\theta$)-magnet consists of air-core coils, bent on the surface of a cylinder. An idealized model can be used to demonstrate the principle field generation of this class of magnets. Therefore a current density $\vec{j} \parallel \vec{z}$ around the surface of an infinite long cylindrical beam tube with radius R_0 in $\vec{z}$ direction is proportional to a cos($n\theta$) function (Fig. 5.3). The value n defines the resulting multipole field, generated by this magnet design. This model

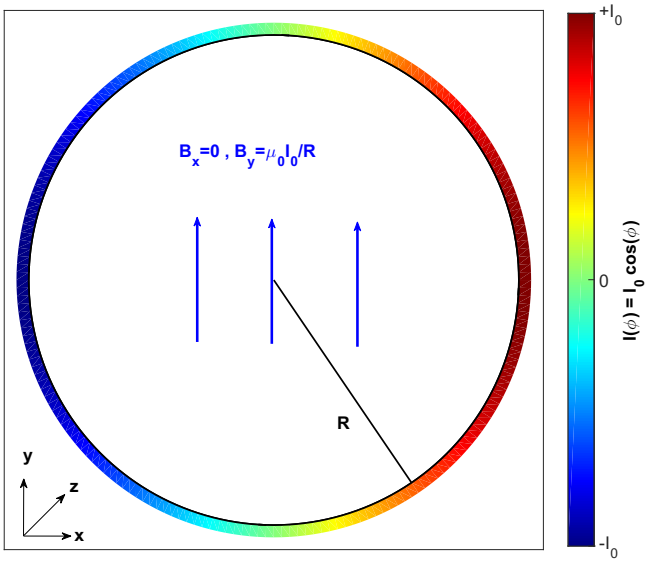

Figure 5.3: An ideal cosθ magnet with a longitudinal current density proportional to cosθ. It produces a pure dipole field in the transversal plane.

can only give an idea of the real magnet design that has a finite cross section of the wire. Thereby the current density can only approach a cos($n\theta$) distribution. All deviations of the ideal current distribution produce additional multipole field components. Therefore, a realistic design can only minimize some of the unwanted multipole field terms, but not all. In case of a dipole magnet, those are dipole-like multipole terms, such as sextupole or decapole. Two examples of such a transversal magnet geometry are shown on Fig. 5.4. The constant current density in the red and blue marked areas have an opening angle of 120 degrees, producing a dipole field (Fig. 5.4(a)) and suppresses the next-to-leading-order multipole term (sextupole). Thus, the additional multipole terms starts with a decapole. The shown quadrupole geometry (Fig. 5.4(b)) suppresses dipole-like terms in general. It is impressive that for an opening angle of 60 degrees the geometrical differences in the current distribution have no impact and the resulting field consists of a pure magnetic quadrupole field. Such cos(2θ)-magnets were also developed for the GunLab beamline for beam focusing next to the transverse deflecting cavity (Chapter 4.2) but will not be discussed here.
Another important difference to the ideal magnet model are the end caps. These are the regions of the finite long magnets where the longitudinal wires are closed to a loop. The resulting magnetic fields differ to the ideal magnetic field and have longitudinal field components, as well. These differences depend on the length of the end caps with respect to the overall length of the magnet. It is shown in the following that the magnet design for GunLab consists of more than half of end caps. Thus, the two regions of the magnet cannot be optimized individually. It is necessary to calculate the field of the whole magnet.

5.2.2 Field calculation for a real coil geometry

The calculation of the magnetic field of a real cos($n\theta$)-magnet is done by integration of the current along the coil geometry with the Biot-Savart law. This equation can be solved easily for straight lines, but not for arbitrary current curves. The design of the scanner magnets, especially the end caps, consists of bent current lines on the surface of a cylinder. For these functions the Biot-Savart law results in elliptical integrals which

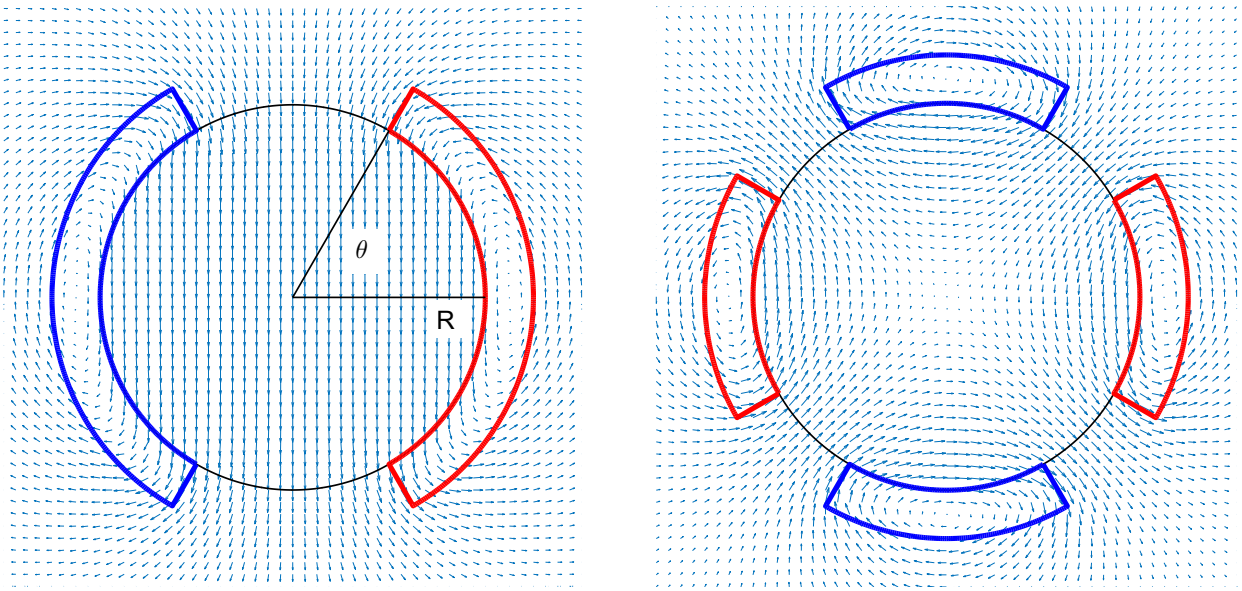

(a) Dipole (b) Quadruple

Figure 5.4: Cross section of simple air-core coil magnets for dipole magnet (120 deg coil angle) with suppressed sextupole terms (left) and a pure quadrupole magnet (60 deg coil angle) (right). Coils with positive current density are plotted in red, negative in blue. (The coordinate system is the same as in Fig. 5.3)

cannot be solved analytically. Therefore it is necessary to separate these current paths into short sections that are approximately linear and integrable. This results in a formula [45] for the magnetic field $\vec{B}$ at the point $\vec{P}$ that has only geometrical inputs of the defined current line:

$$\vec{B}(\vec{P}) = \frac{\mu_0 I}{4\pi} \left(\frac{|\vec{r}_1| + |\vec{r}_2|}{|\vec{r}_1|\,|\vec{r}_2|} \right) \left(\frac{\vec{r}_1 \times \vec{r}_2}{|\vec{r}_1|\,|\vec{r}_2| + |\vec{r}_1 \cdot \vec{r}_2|} \right) \tag{5.13}$$

with $\vec{r}_1$ and $\vec{r}_2$ as the start and end points of the linear current line with respect to $\vec{P}$, I as the electric current value and μ_0 as the vacuum permeability. With this formula a magnetic field map can be calculated for any given 3d coil geometry of the phase space scanner magnets. An analytic model for these coil geometries and the criteria for the final magnets are presented in the following sections.

Analytical model for the geometry of the scanner magnets

The geometry of the end caps is described by an analytical model which consists of a high number of degrees of freedom. It defines the current path of the coil by a two dimensional function, wound on a beamtube with the radius R_0. This function is the hyper-elliptical function

$$\vec{F}(a, b, n, \phi) = [a \cdot \cos(\phi)^{\frac{2}{n}}, b \cdot \sin(\phi)^{\frac{2}{n}}] \tag{5.14}$$

with a and b as the radii of the main axis and n as the power of the hyper-ellipse. The shape of the function can be modified from a circle with radius a ($a = b$ and $n = 1$) to a rectangular with a and b as the length of both sides ($n \to \infty$). This two dimensional function is transformed on the surface of a tube. In Cartesian coordinates this results in:

$$\vec{P}_{\text{end cap}}(a, b, n, \phi) = [R_0 \sin(a/R_0 \cdot \cos(\phi)^{\frac{2}{n}}), R_0 \cos(a/R_0 \cdot \cos(\phi)^{\frac{2}{n}}), b \cdot \sin(\phi)^{\frac{2}{n}}]. \tag{5.15}$$

This function describes a current line directly on the cylindrical surface. To generate a complete 3d coil it is important to know what kind of wire shape and cross section is intended for the magnet. The standard power supplies for GunLab achieve DC currents up to 5 Amps. This requires a cables cross section of more than 1.5 mm^2 for current densities that do not significantly exceed the maximal acceptable value of $\approx 3A/mm^2$ without cooling[a]. A round cable with such a large cross section relative to the dimension of the coil does not achieve a good packing density. Therefore a rectangular wire shape was chosen with a cross section of 0.3x6 mm^2 and a 25 μm Kapton layer as insulator. [46] With this cable a higher packing density and currents up to 5 Amps can be achieved. However, for the rectangular cross section the geometrical effects of the torsion of the wire can not be neglected in the end cap regions. This effect is discussed in the following section.

Real model for Scanner magnet design with a rectangular wire

A wire with a finite thickness, laid on the hyper elliptical path, rotates around his central axis. This torsion is only relevant for cables that do not have a round cross section. An example is depicted in Fig. 5.5.

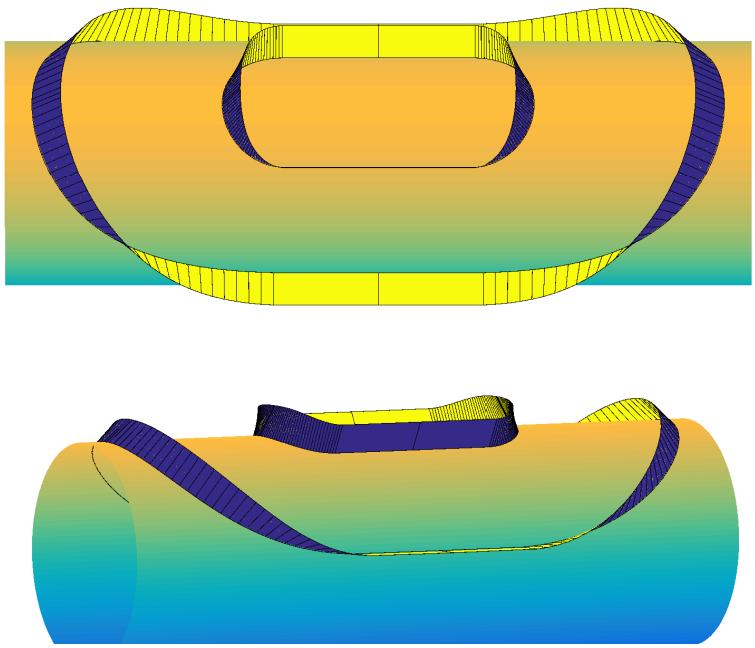

Figure 5.5: Example of two rectangular wire loops on the surface of the beam tube.

It shows two windings of a rectangular wire on the surface of a cylinder. The wires have a radial orientation in both straight sections. However, they have to rotate around their central axis to follow the defined path at the end caps. This produces on top of the beam pipe a tilt angle η between the cylinder axis and the normal vector of the current path. This angle depends on the beam tube radius R_0 and on the parameters of the hyper-elliptic function (Eq. 5.15). The torsion function can be calculated by the rotation of the associated coordinate system, based on the tangential, normal and binormal vector

[a] Privat communication with Thomas Gehrig, Karl Schupp AG (2014).

(Fig. 5.6). All three function results from the Frenet-Serret fomulae. As a result one gets the general torsion along the path s ([45]):

$$\tau = \frac{\left(\vec{P}'(s) \times \vec{P}''(s)\right) \cdot \vec{P}'''(s)}{\left|\vec{P}'(s) \times \vec{P}''(s)\right|^2}, \tag{5.16}$$

$$s = \int_0^{\phi} \left| \frac{\partial \vec{P}_{\text{end cap}}(a, b, n, \tilde{\phi})}{\partial \tilde{\phi}} \right| \mathrm{d}\tilde{\phi}, \tag{5.17}$$

$$\vec{P}'(s) = \frac{\partial \vec{P}(s)}{\partial s}, \tag{5.18}$$

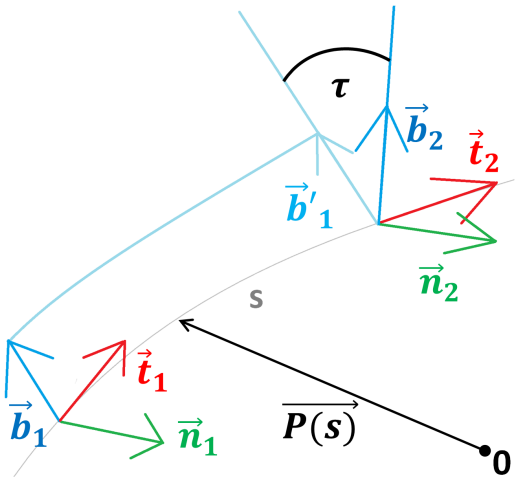

Figure 5.6: The tangential, normal and binormal vector ($\vec{t}$, $\vec{n}$, $\vec{b}$) at different positions along a curve. The rotation of this system is the torsion τ.

with the function $\vec{P}(s)$ as a current line along the defined hyper elliptical path. Thereby the wire rotation angle η can be calculated at the turning point of the current path on top of the beam pipe by Eq. 5.16:

$$\tan(\eta) = \frac{R_0 b}{a^2} \tag{5.19}$$

with R_0, a and b as the parameter of the elliptic function. The influence of the torsion on the end cap geometry is presented in Fig. 5.7. It shows a cross section of different coils in the y-z plane as cut through the turning point of the coil on top of the beam tube with 40 mm diameter. The end caps in each coil start at $z = 20$ mm and have different end cap radii b. For small values of b the wire lies nearly flat on top of the beampipe and produces an overwinding, resulting in edges between the straight section and the turning point (Fig. 5.7, top). On the other hand, if b increases, the needed rotation through the end caps could be realized over a longer distance. Thus η also increases, producing a more upright position of the cable at the turning point (Fig. 5.7, bottom). In both cases η is not a constant for a coil. Each new layer with the cable thickness d_{cable} produces an increase in the main axis values $a_i = a_{i-1} + d_{\text{cable}}$ and $b_i = b_{i-1} + d_{\text{cable}}$ for the hyper elliptic function. This constant growth of both parameters decreases the tilt angle of each layer, which can be seen in all three plots of Fig. 5.7. It shows that the torsion of the wire affects the complete design of the end caps.

This is relevant for the overall coil length and the definition of the end cap parameters. Especially the end cap radius has to be limited for small values, because of unwanted edges in the coil geometry by the overwinding effects.

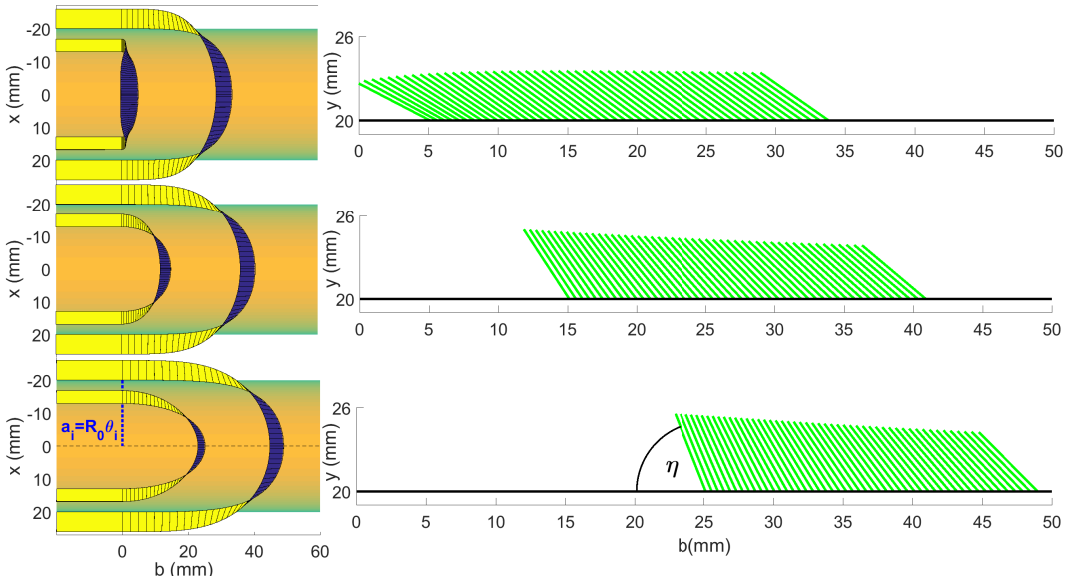

Figure 5.7: Three examples of end cap designs with different elliptic radii b (5 mm (top), 15 mm (center), 25 mm (bottom)). On the left side the inner and outer layer on the beamtube are plotted as 3D plot with topview. The right side shows the cross section through the coil in the central vertical plane (y-z) with the tilt angle η of the inner contour at the turning point.

Geometry optimization

The geometry of the scanner magnets has three free parameters: the straight length L, the long side opening angle θ, the elliptical half axis b of the elliptical function (end cap radius). R_0 is fixed by the beamtube radius and the coil thickness d by the selected wire. Nevertheless the influence of d was studied, but no significant impact was noticed. The optimization of the magnet design was achieved in three steps:

1. Field calculation for a given set of parameters (L,θ,b,d)
2. Reconstruction of the magnetic multipole terms of the resulting fields
3. Analysis of the wanted and unwanted magnetic multipoles to define the best magnet geometry

The field calculations were done with the above described method and for the multipole reconstruction two different techniques were tested. The first technique is based on the cylindrical surface measurement (see Chapter 7 for more details). Thereby the magnetic field is calculated on circles with a constant radius along the longitudinal axis. The resulting radial and azimuthal field components can be transformed with a Fourier analysis to the amplitudes of the different multipoles. For the second method the calculated 3d field map was examined by a direct phase space tracking. A defined particle distribution was tracked through a given field map and the results are used to observe the phase space distortions and multipole influences.
The cylindrical surface measurement reconstructed the multipole terms inside the magnet. The amplitudes of these terms depend on the longitudinal position inside the magnet. To quantify the quality of a design of a magnet or a magnet doublet, is is necessary to calculate the impact of the field on the transverse phase space of the electrons. However, this was not possible for reconstructed multipole terms, because a linear integration through both

fields of the scanner coils results in zero, due to the different sign of the field polarity. Therefore, it is necessary to solve the path integral through the magnet doublet, which is already incorporated in the second method. Thus, the cylindrical surface measurement gives only a first hint on an optimal magnet design.

Particle tracking through the scanner system

For the tracking through the calculated scanner fields a linear phase space distribution is used, consisting of particles on a transverse grid without transverse momentum, energy spread and particle charge. It starts with an initial offset value between 0 and 10 mm and is moved by the scanner magnets into the center of the beamline. The final distribution is observed directly behind the second scanner magnet field. It represents the transformation

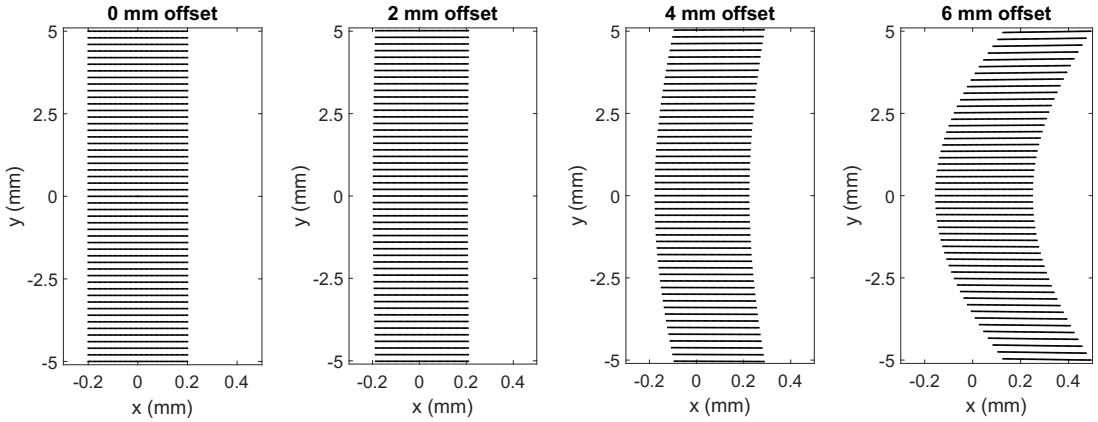

Figure 5.8: Example of 4 tracking results for a phase scanner magnet doublet with an initial slit-like phase space distribution (400 μm $\times$ 10 mm). The initial horizontal offset values are 0 mm, 2 mm, 4 mm 6 mm (left to right).

of a supposed beamlet inside the bunch through the scanner magnets up to the slit. Fig. 5.8 shows four tracking examples of a distribution with initial dimensions of 400 μm in the horizontal and 10 mm in the vertical axis. They have different initial offset values x_{off}. The higher order multipole fields generate a banana-shape distribution in the final phase space downstream of the magnets. An optimization of the magnet design has to minimize these effects.
To quantify the deformation of the tracked phase space distributions, a function χ_m was calculated. It is the *rms* distance between the initial (m_0) and the final (m_1) particle positions on one of the four phase space axes (x, x', y, y'), expressed by m.

$$\chi_m(x_i) = \frac{\sum_{i=1}^{N_p} \left(m_1(i) - m_0(i)\right)^2}{N_p} \tag{5.20}$$

with N_p as the number of tracked particles. Thus, the total phase space deformation χ_{tot} is the sum of the four χ_m functions:

$$\chi_{tot} = \chi_x + \chi_{p_x} + \chi_y + \chi_{p_y} \tag{5.21}$$

The goal of the optimization of the coil geometry was the minimization of the χ_{tot}-value. The final geometry of the scanner coils were found by a combination of field optimization and technical feasibility, limiting the geometry parameters of the coils, like the maximal length of one coil ($\leq$ 120 mm).

Parameter variation for the design optimization

In a first step it was tested which geometry parameter has the most impact on the field quality. As expected for a cos(θ)-magnet, this parameter is the coil opening angle θ.

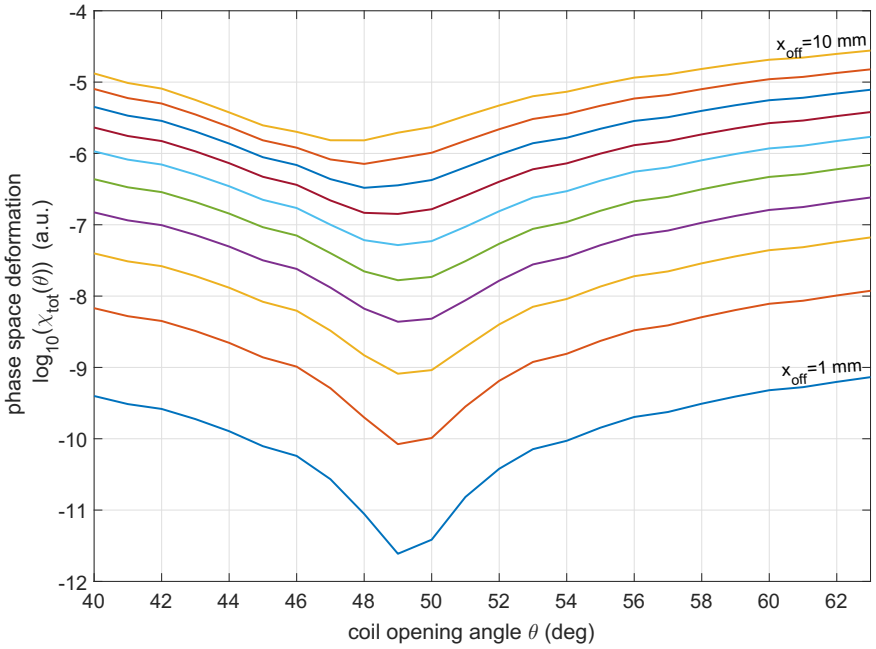

Figure 5.9: Curve of family for χ_{tot} as function of the coil opening angle θ. Ten initial horizontal offsets x_{off} between 1 mm and 10 mm are plotted.

The results of the θ-variation are depicted in Fig. 5.9. The plot shows exemplarily the family of curves of the total phase space deformation χ_{tot} as function of θ and the initial horizontal offset x_{off}. Here a magnet design was used with a beamtube radius of $R_0 = 20$ mm, a straight section of $L = 40$ mm and an end cap radius of $b = 20$ mm. The shown banana-shape deformation of the beamlet phase space (Fig. 5.8) produces the correlation between χ_{tot} and x_{off}. Nevertheless, for all curves a global minimum for the tested angle range was found in the region of 49 degrees.
In the following the range of the three parameters (L,θ,b) were determined, resulting in acceptable coil geometries. These geometries do not exceed the maximum length of 120 mm and have an opening angle of almost 49 degrees. An expectation was that a decrease of the end cap length would increase the overall field quality, because of the smaller ratio of end cap length to coil length. However, in section 5.2.2 it was shown that for too small values of b the torsion of the wires produce unwanted edges in the coil geometry. Thus, the end cap radius has to be at least 15 mm for coils with $R_0 = 20$ mm and $\theta \approx 49$ degrees to minimize the overwinding of the rectangular wire. Therefore the parameter L also depends on b when the complete length of the coil should be ≈ 120 mm. A good solution was found with a parameter setting of $\theta = 48$ degrees, $b = 20$ mm and $L = 40$ mm. It fulfills the maximal length and produces minimal phase space distortions.

Construction of the final scanner magnet

In the engineering process an aluminum yoke was created which was used as a winding former for the coil (Fig. 5.10). The idea was to use a CNC milling machine for the

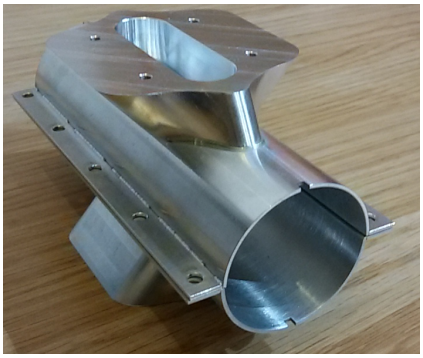

Figure 5.10: Image of the yoke for the final scanner magnet design.

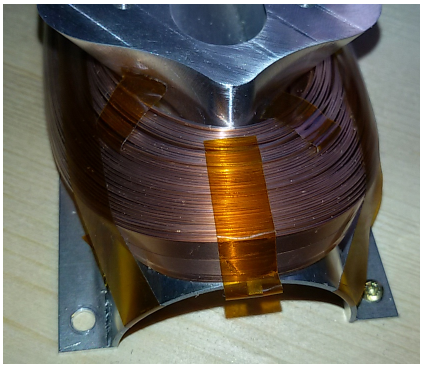

Figure 5.11: first layer

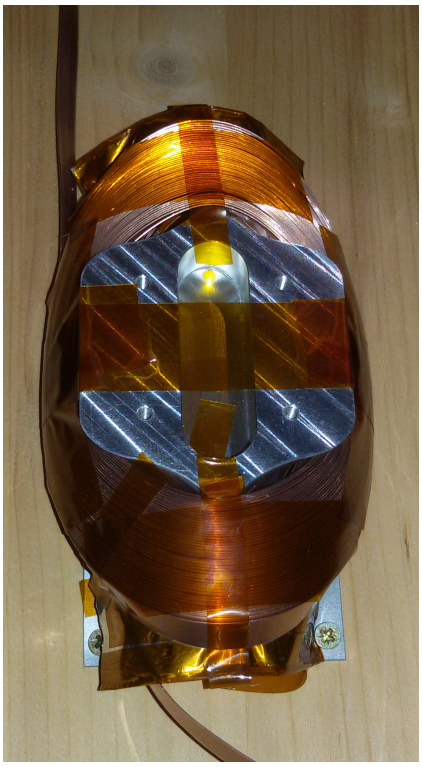

Figure 5.12: second layer

fabrication of a former, based on the inner contour of the calculated coil design. However, it was not possible to transfer the coordinates of the complete inner contour to this CNC system. Therefore only the significant were considered. These necessary simplifications created a yoke which consists only of the turning point of the wire and the coil opening angle over the coil length. Unfortunately the rounded edges of this reduction changed the length of the straight section and the end cap radius, as well. The consequences of this design change are discussed in the following section. The resulting aluminum yoke is depicted in Fig. 5.10. The complete yoke consists of a tube as holder of the wires and the milled winding former, welded on the tube surface. The rectangular wire was wounded on the former in two layers by a motorized winding machine[b]. The two images show the construction of the first layer as an intermediate step of the winding process (Fig. 5.11) and the final scanner magnet with both layers (Fig. 5.12). After completion of the four coils, the field of a complete magnet was measured. The measurements and results are presented in the following section.

5.2.3 Field measurements of the scanner coils

To verify the calculations in the last section, the magnetic field of the fabricated scanner coil was measured. Therefore, a compact 3 axis mapper was constructed which moves a

[b]This machine is a wooden turn table which was planed and constructed for the fabrication of all air-coil magnets for GunLab (steerer, quadrupole and scanner magnets). It consists of an 12 V DC motor which runs a gearwheel with a final rotation frequency of ≈ 0.3 Hz. The rotation number of the table is counted by a TTL circuit including an optical barrier and visualized by a LED strip. Two further rotatable stages can be used as cable suspensions for the winding of two layer coils.

3 axis Hall probe through the scanner magnet. The setup of the test stand, as well as the measurements are presented in this section.

Technical setup of the field measurements

The magnet for this field measurement consists of two cos(θ) coils positioned upright (horizontal scanner configuration) on a beamtube dummy in the test construction, depicted in Fig. 5.13. The coils are serially connected with a Kepco BOP 20-20M power supply with DC currents between ±20 Amp and ripple less 1‰.

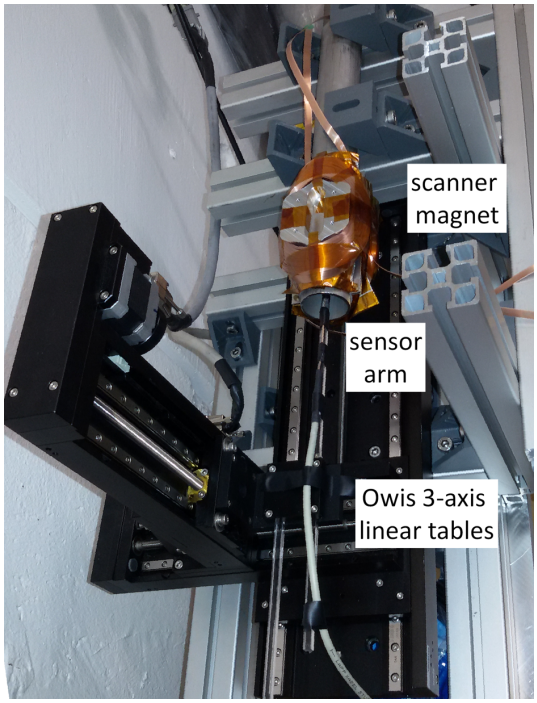

Figure 5.13: Image of the field mapper and one scanner magnet on a beamtube. The Hall probe is in this picture positioned inside the magnet.

The mapper itself consists of three motorized linear tables from the manufacture Owis [66]. A three axis Hall probe sensor, glued on an acrylic glass arm, is moved by the mapper through the beam tube. The Hall probes are calibrated sensors between ±2 T from the manufacture Senis [65]. They also produce the readout systems for the sensors. This readout transforms the three measured field values into three bipolar voltages with a coefficient of 5 V/T. To digitalize the estimated small bipolar voltages, a two stage instrumentation amplifier and signal shifter were used for signal processing between readout and the analog-to-digital converter (ADC) for each channel. Both elements were adjusted to a measurable field strength for the ADC of ±10 mT. The ADC has four unipolar channels with a dynamic range of 12bit. The uncertainty and noise level was tested for each step of the signal processing by a reference voltage source with a relative voltage uncertainty of 10^{-4}. An overall uncertainty of the measurements was detected in the range of ≈ 1‰ and a measurement noise level of 5 μT. This is negligible to the 120 μT noise of the Hall sensor and the readout system. This large noise value cannot be explained completely. The expected noise level, given by the data sheet of the transceiver, is in the range of ≈ 60 μT. It was not possible to clarify the additional noise source for the measurements. This uncertainty of the measurements dominated the complete measurement error.

In the following the measurements and the analysis of the mapped magnetic field are presented.

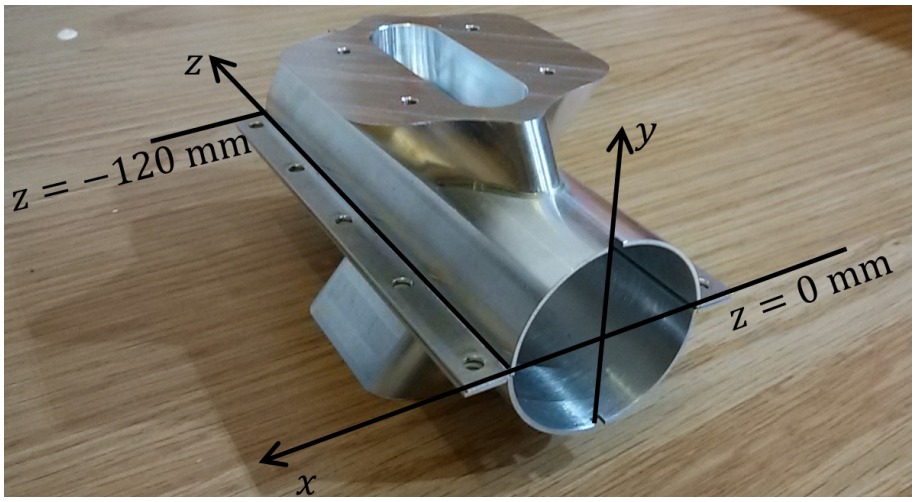

Figure 5.14: Image of the 120 mm long aluminum yoke as reference of the coordinate system for the field mapping.

Measurement of the magnetic field of the scanner magnet

The experiences of the field mapping of the solenoid magnet (Chapter 7) show that it is complicated to analyze the fields, as well as the higher order multipole terms of the field, even for a high accurate calibrated mapper and magnet system. Furthermore, the sensor movement in this setup is limited by the small beampipe aperture and the thick measurement arm of the mapper. Therefore only a qualitative field characterization was possible with two kinds of measurement. First, two field maps were sampled in the horizontal and in the vertical central plane of the magnet. Second, a hysteresis measurement was undertaken to test the estimated linear correlation to the coil current.

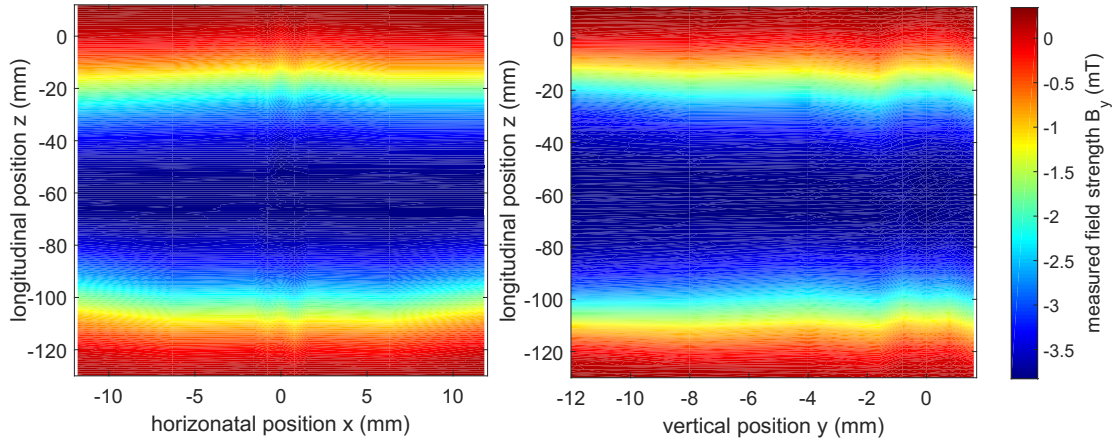

Figure 5.15: Contour plot of the vertical magnetic field component B_y in the central horizontal (x-z) plane (left) and in the central vertical (y-z) plane (right).

At the beginning the mapper was calibrated to the coordinate system of the magnet. Therefore the sensor head was moved to significant points of the magnet and the inner wall of the beamtube to determine the geometrical axis of the magnet. For the field

mapping a constant DC current of 2 Amps flowed through the serial connected coils. Fig. 5.15 shows the distribution of the vertical field component B_y in the horizontal and vertical plane.

The coordinates are given as absolute values in the coordinate system of the magnet, which is depicted in Fig. 5.14. Both field maps are nearly constant in the transverse direction, even for extreme positions like 12 mm offaxis (Fig. 5.15). The absolute field maximum near the center of the magnet is 3.81 ± 0.12 mT.

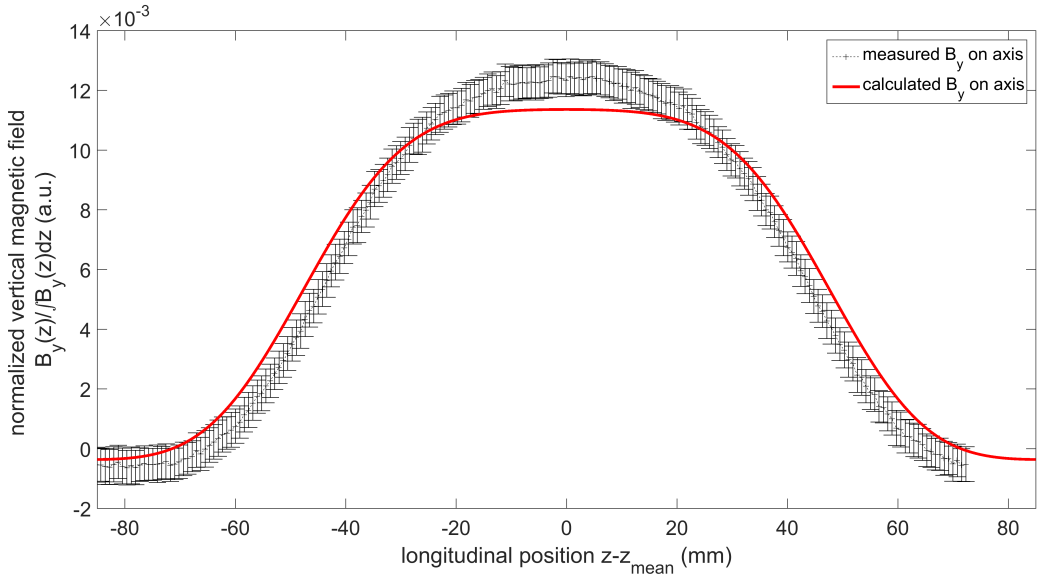

Figure 5.16: Plot of the vertical magnetic field component B_y measured along the geometrical axis (black) and calculated in the design magnet along the magnet axis (red). The field values are normalized to their longitudinal integrals and plotted as function of z with respect to the determined longitudinal center of the magnet z_{mean}.

This value can be compared with the calculated field strength, scaled to the same number of Ampere-turns per magnet[c]. The resulting field strength on axis is 3.93 mT for the calculated magnet. For a comparison of the calculated and measured longitudinal distributions of B_y, both fields were plotted in Fig. 5.16.

Both distributions are plotted with respect to z_{mean}. It is the field weighted average position of z and determines the centroid of the distribution. The calculated field profile is ≈ 7 mm longer than the average measured field. Furthermore it has a longer plateau than the real magnet, which is discussed below.

For the hysteresis measurement, the sensor was positioned at the geometrical center of the scanner magnet and the DC current was increased from 0 to +5 Amps in a first run and decreased from −5 to +5 Amps in a second run. The current remained constant between both runs. The results of this measurement are plotted in Fig. 5.17. It shows the measured field strength of the vertical field component B_y as function of the defined DC current. Both runs looks quite linear but with small offset differences. The results of all measurements are discussed in the following section.

[c]For the field calculation a high granularity of the current lines was used with a current value of 1 Amp. This results in a current density of 25 Amps/mm^2 or 6048 Ampere-turns.

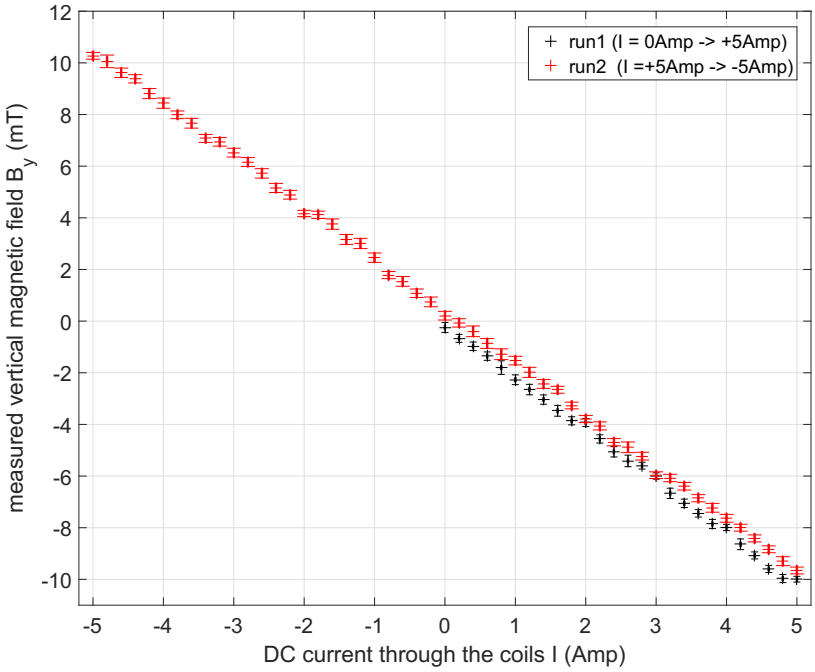

Figure 5.17: Measured hysteresis of the scanner magnet at the geometric center of the magnet.

Analysis of the field measurements

The vertical magnetic field measurements of B_y confirm the calculated field with a relative variance of 8%, where the relative uncertainty of the measurements is $\approx$ 5%. Thus, the detected difference in the longitudinal profiles is significant. There are two possible explanations for this difference. The first one concerns the mentioned design change of the magnets. It can be assumed that the rounded corners at the end of the straight sections, as well as the loss of the guidelines up to the turning points, affect the resulting shape of the end caps and the length of the straight sections. A shorter straight section and a tighter end cap shape decrease the enclosed area of the coil. However, the magnetic flux is constant. Therefore, the field strength (flux density) increases, but is longitudinally compressed.

The second possible source for the field change is the smaller number of windings in the real magnet then in the calculated design. It was not possible to wound the same number of wire loops on the former than calculated ($N = \frac{R_0 \cdot \theta}{d_{\text{wire}}}$), because of problems with the packing of the wires. Thereby, the end caps are shorter which decrease the field length, as well. This packing problem can be also affected by the geometry error. If the geometry of the end caps is changed, the tilt angle η at the turning point will differ from the calculated angle. Thus, two different definitions for the torsion exist in the coil geometry. In the fabrication of the coils, it was observed that the wire is more fixed to the turning point, defined by the yoke geometry, because of the smaller bending radius at this position. Due to the change of a and b, but a constant η, Eq. 5.19 results in a larger R_0 than defined. This affects the construction of the coils, as well. It was complicated to pass the wire along the surface of the tube. The distance between tube surface and wires increased with each additional layer. To avoid this problem, a softer winding of the coil was necessary to compensate the wrong η value. However, this was only possible with a less coil packing.

Nevertheless, the measured field distribution fulfills the expectation from the calculated

coil design quite good, in respect to this complex magnet design. Furthermore it was observed that the field amplitude is directly proportional to the coil current as expected for an air-core coil. The small differences can be explained by a saturation of the ADC next to the limit of the measurement, because the signal processing was designed for a field measurement in the range of ±10 mT. The additional noise of the sensor transceiver, however, exceeds this voltage limit. The used ADC has simple safety features for overvoltage inputs. These electronics can produce signal offsets and measurement off-times.
Despite the lower number of windings than designed, a scan range of the magnet doublet is achievable of more than 6 mm ($x_{\text{scan}} = 6.0143 \frac{\text{mmMeV/c}}{\text{A}}$), in case of an average momentum of 3 MeV/c and a coil current of 3 Amps. Also, higher DC currents as 3 Amps are possible for several minutes without thermal problems.
The possible impacts on phase space reconstruction of the calculated scanner coils, as well as the measured field differences, are discussed in the last part of this chapter. Thereby also the overall performance and achievable resolution of the complete phase space scanner system are presented.

5.3 Numerical studies of the scanner system

In the last sections the model for the transverse phase space reconstruction was presented. Furthermore, it was described how a magnet design, based on cosθ magnets, was optimized for the scanner magnet doublet, moving the beam parallel over the slit mask. The optimal design was constructed and the field was measured. The results confirms the calculations. It was found that the constructed scanner magnet doublet fulfills the requirements of the reconstruction model, even for electron beams with momenta of 3 MeV/c and huge *rms* beam sizes (>1 mm). For an estimation of the performance of the complete phase space scanner system, detailed numerical studies were performed to analyze the different influences on the final measurements. The impact of the stepwise measurement on the reconstruction algorithm was already discussed and it was found that this error can be suppressed to 1‰ by a scan range of 7σ with 20 measurement steps. These parameters were used for all simulations, presented in the following. In addition to this methodical error there are further sources of systematic errors on the phase space reconstruction. Those are:

- Limited resolution of the VSM
- Phase space cuts of the slit mask,
- Phase space distortion of the scanner magnet doublet,
- Energy spread of the scanned beam,
- Space charge effects on the beam and on the beamlet

The first item implies the error of the beam size measurement of the beamlets due to the VSM (see Chapter 4.4.1). To calculate this impact, the minimal resolvable beam size is assumed as the final beamlet size for the reconstruction algorithm (Eq. 5.5- 5.10). This results in an emittance offset which is given by:

$$\varepsilon_0 = \frac{\sigma_{x,\text{beam}} \sigma_{\text{VSM}}}{L} \tag{5.22}$$

with $\sigma_{x,\text{beam}}$ as the initial *rms* beam size at the reference point (slit mask position), σ_{VSM} as the resolution of the used VSM (see Tab. 4.8) and L as the drift length between reference

point and VSM. This emittance offset can be approximated to $\varepsilon_0 < 15$ nm-rad for the given values of the VSMs, an initial *rms* beam sizes of less than 0.5 mm and a drift length of $L \approx 1$ m.

Simulation settings

The other four items were determined with several numerical simulations to analyze the individual influences on the phase space reconstruction. For all simulations electron bunches were defined with one million particles to minimize numerical errors, especially for the generated beamlets. To examine the resilience of the reconstruction, the used bunches have different initial distribution parameters (Σ-matrix values), but a constant normalized emittance of 100 nm-rad[d] and an average momentum of 3 MeV/c. For the first simulations the initial distributions consist of mono-energetic electrons without internal interactions to suppress the effects of energy spread and space charge on the calculations. The initial bunches were moved by the scanner magnet doublet, implemented as a 3d field in ASTRA, over the slit mask, positioned 120 mm downstream of the second magnet. This slit mask was defined the same geometrically parameters as the one at GunLab.
The beamlets drifted 1 m downstream to a virtual screen where the position and the *rms* beam size were measured. The sampled values were put in Eq. 5.5- 5.10 and the initial beam parameters were reconstructed. These results were compared with the initial distributions at the reference point. The differences are defined as reconstruction errors.

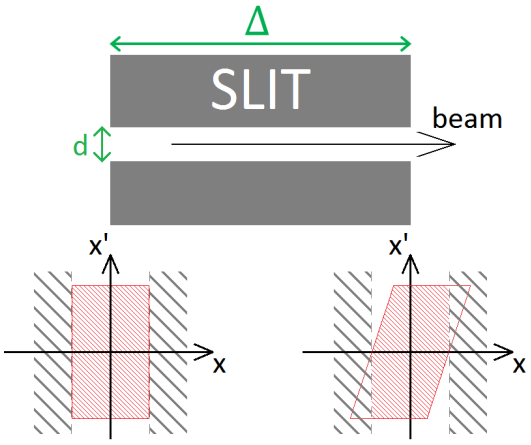

Figure 5.18: Influence of the slit mask width Δ on the production of beamlets. Both phase space plots show the beamlet distribution at the entrance and at the exit of the slit mask.

Simulation results

In all simulations it was detected that the slitmask itself has the most impact on the reconstruction process. This results from the two geometrical parameters of the slitmask; the slit width d and the slit mask thickness Δ. The slit width d defines the size of the

[d]This tiny value is necessary for high sensitivity of the systematic errors and for a further reduction of numerical errors. It can be assumed that for higher emittance values the systematic errors decrease because of the increase of the local beam divergence which improves the phase space reconstruction. Also, the emittance value is correlated to the beam size at the slit mask. An increase of the beam size reduces the number of particles which pass the slit mask. Thus a small emittance value is also preferred for smaller numerical uncertainties in the simulations.

beamlets, as well as the residual information of the initial correlation of the beam. The influence of Δ is depicted in Fig. 5.18. The necessary thickness of the slit mask produces a further cut in the phase space distribution of the beamlet. This cut is directly correlated with the ratio of d/Δ.
The results of the simulated reconstruction are plotted in Fig. 5.19. For three different d-values (10, 50, 100 μm), it shows the reconstructed emittance and the correlated beam divergence $\langle xx' \rangle$ of the initial beam, exemplarily for all reconstructed parameters. Both parameters are plotted as function of the initial $\langle xx' \rangle_{\text{slit}}$ at the slit mask, which is neglected in this reconstruction model (Eq. 5.2). Thereby the decrease of d improves the reconstruction of the emittance values, but not of the individual beam parameters. The plots show furthermore, that the systematic error mainly depends on the initial parameter $\langle xx' \rangle_{\text{slit}}$. An increase of the absolute value $\langle$xx'$\rangle_{\text{slit}}$ produces for constant emittance a decrease of the local divergence. Thus, the absolute $\langle$xx'$\rangle$ value of the beamlet increases. In this case, the neglecting of the second term in Eq. 5.2 produces the distortion of the parameter reconstruction. Furthermore d affects the number of passing electrons and therefore obviously the numerical uncertainty of the simulation, too.

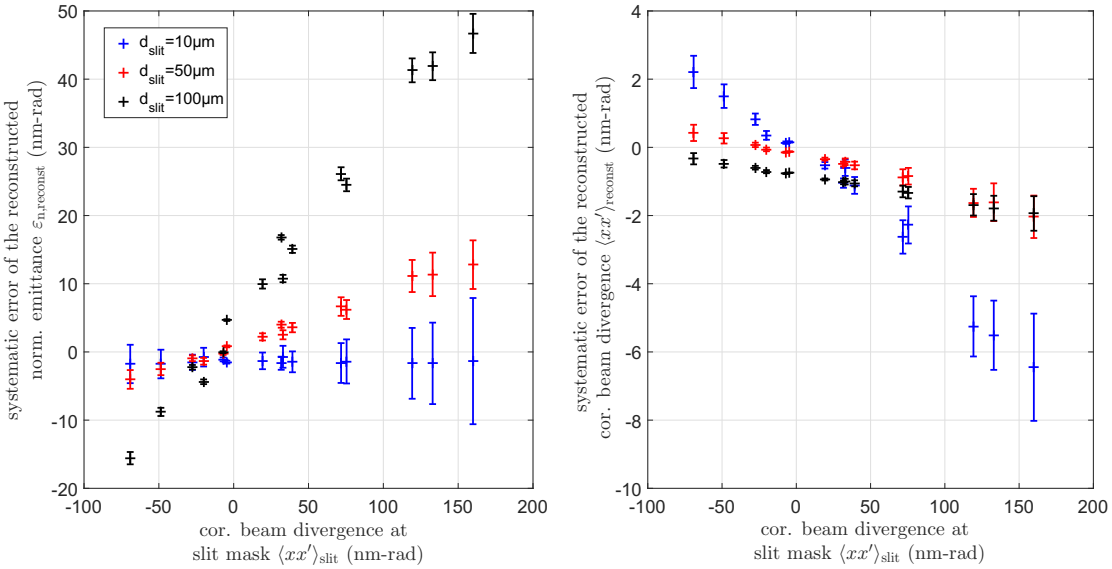

Figure 5.19: Results of the simulated phase space scanner system for initial beams with a normalized emittance of 100 nm-rad, but no energy spread and space charge. The reconstructed emittance (left) and the correlated beam divergence (right) are plotted as function of the initial beam correlation at the slit mask $\langle xx' \rangle_{\text{slit}}$. Furthermore three different slit mask widths d (10, 50 and 100 μm) were used for the simulation. The errorbars of the data points combine the numerical uncertainties of the simulation and the systematic errors of the scan method (1‰).

In these simulations the chosen correlated beam divergences at the slit mask are exaggerated to visualize the systematic impact. For realistic parameters in this scenario of the correlated beam divergence ($\pm$50 nm-rad) with respect to the defined transverse emittance, the systematic error is determined to $\sigma_{\text{slit}} \approx 3\%$. In relation to this systematic error and the statistical uncertainties of the simulations it was not possible to detect a significant impact of the scanner magnet doublet. However, in case of an initial momentum spread of the scanned electron bunches ($\delta = \sigma_p/\langle p \rangle$), the magnets can affect the measurement by the additional dispersion (Fig 5.20(b)) of the bunches at the slit mask. For two examples with small $\langle xx' \rangle_{\text{slit}}$-values, Fig 5.20(a) shows that for $\delta > 5\%$ the dis-

persion produces a further contribution for the phase space reconstruction in the same range as the systematic error of the slit mask.

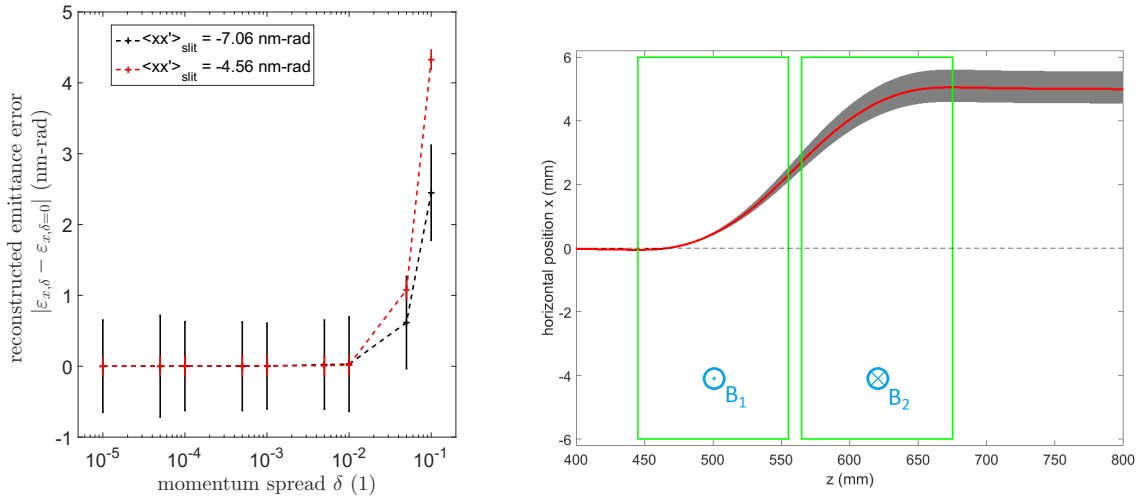

(a) Reconstructed emittance

(b) Example of dispersion in the phase space scanner system

Figure 5.20: Left: Plot of the reconstructed horizontal normalized emittance as differences between samples with and without momentum spread. The data are plotted as function of the defined momentum spread $\delta = \sigma_p/\langle p \rangle$. The scans are for two initial beam parameters with small correlated beam divergence values at the slit mask. Right: Example of a particle tracking with momentum spread. On axis particles with ±10% (gray) and ±1% (red) for a 3 MeV/c beam with a 5 mm shift. Both scanner magnets, with the opposite magnetic field orientations, are described by the green boxes.

Space charge effects

The last potential contributor for the reconstruction is the bunch charge or, more precisely, the peak current of the bunch as a quotient of the bunch charge Q_{bunch} and the temporal *rms* bunch length σ_t. The effect of the space charge on the measurements results mainly from the additional defocussing of the beamlets along the drift to the viewscreen. The defocusing forces of the space charge are reduced inside the beam by the outer beam regions which are cut-off by the slit mask. Thus, the beamlet, especially beamlets next to the beam core region, are defocused by these uncompensated space charge forces. The change of the horizontal beamlet size $\tilde{\sigma}_x$ at the VSM downstream of the slit mask is calculated by the differential equation Eq. 2.18 for an emittance dominated beam inside a drift space. Thereby the space charge, described by the perveance κ_{SC}, is handled as perturbation of the exact solution σ_x without space charge.

$$\tilde{\sigma}_x'' - \frac{\kappa_{SC}}{\tilde{\sigma}_x} - \frac{\varepsilon_n^2}{\tilde{\sigma}_x^3(\gamma\beta)^2} = 0 \tag{5.23}$$

$$\tilde{\sigma}_x = \sigma_x + \kappa_{SC}\hat{\sigma}_x \tag{5.24}$$

Here $\hat{\sigma}_x$ represents the solution of the differential equation of the space charge perturbation. The relative change of the beamlet size by the space charge defocusing is thereby given as

$$R_x = \frac{\tilde{\sigma}_x - \sigma_x}{\sigma_x} = \kappa_{SC}\frac{\hat{\sigma}_x}{\sigma_x} \tag{5.25}$$

A relation for the leading order term of R_x can be found:

$$R_x \propto \frac{\kappa_{SC}\sqrt{\sigma_{x,0}}}{\varepsilon_{n,0}^2} \tag{5.26}$$

$\sigma_{x,0}$ and $\varepsilon_{n,0}$ are the horizontal beam size and the horizontal normalized emittance of the beam at the position of the slit mask. Furthermore the perveance is approximated for a beamlet by $\kappa_{SC} \propto Q_{\text{bunch}} d/(\sigma_t \sigma_{x,0})$ which results in

$$R_x \propto \frac{Q_{\text{bunch}} d}{\sqrt{\sigma_{x,0}}\sigma_t \varepsilon_{n,0}^2} \tag{5.27}$$

Thereby, $d/\sigma_{x,0}$ describes the charge ratio of the beamlet with respect to the intial beam.

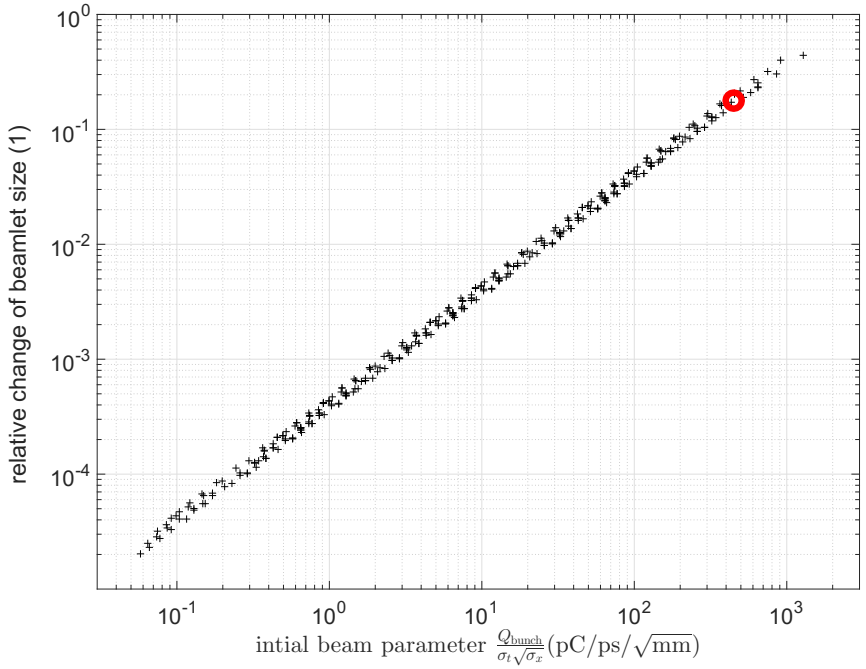

Figure 5.21: Tracking results of ideal beamlets including space charge calculation. The beamlets were generated by a slitmask with a 50 μm slit width. The initial bunch distributions consist of one million particles with different Gaussian bunch lengths and beam sizes, as well as bunch charges. Each sampled beamlet size was compared with a tracking of the same beamlet without space calculation for the tracking.

This behavior of the beamlet size was detected with a tracking of ideal charged beamlets, as well. Therefore several rotational symmetric Gaussian bunches with a constant normalized emittance of $\varepsilon_{n,0}$ =1 mm-mrad were defined at the slit mask. The three initial bunch parameters (σ_x, σ_t and Q_{bunch}) were varied and the beamlets were tracked including space charge effects up to a VSM 1 m downstream the slit mask. There, the beamlet sizes were sampled and compared with the same beamlet tracked without space charge calculation. The results are plotted in Fig. 5.21. It shows the relative change of the beamlet size as function of the calculated scaling term (Eq. 5.27) $Q_{\text{bunch}}/(\sqrt{\sigma_{x,0}}\sigma_t)$. This quotient describes the simulated data in the leading order over the complete simulated space charge range. The red circle in the plot represents a beam scenario with $Q_{\text{bunch}} = 100$ pC, $\sigma_t = 0.5$ ps, $\sigma_{x,0} = 0.5$ mm, $pc = 3$ MeV and $\varepsilon_{n,0} = 1$ mm-mrad. With this overestimated parameter setting the maximum systematic error of the space charge

can be determined. The resulting beamlet has an $\approx 18\%$ increased beamlet size with respect to the tracking without space charge effects. The calculation of the systematic error of the beam parameter reconstruction is similiar to the error of the VSMs. However, this effect is directly correleated to the charge of the generated beamlets, which is used as weighting factor in the reconstruction, as well. This convolution produces a systematic error of the reconstructed beam parameters which is given by

$$\sigma_{\mathrm{SC}} = \frac{R_x}{\sqrt{2}} \tag{5.28}$$

In the case of the above defined parameter setting, this error results in $\sigma_{\mathrm{SC}} \approx 13\%$.
In conclusion, the analysis of the systematic errors for the phase space reconstruction shows that for a GunLab operation with bunch charges < 20 pC, $\delta < 5\%$ and $\varepsilon < 1\mu$m-rad, the leading errors are the limited resolution of the VSMs and the geometrical parameter of the slit mask. They result in sum to a systematic error of $\approx 5\%$. For bunch charges up to 100 pC a space charge driven systematic error of up to 14% can be assumed. In this regard, the above defined scan range ($x_{\mathrm{scan}} = 7\sigma$) can be reduced to 5σ without any impact on the accuracy of the phase space reconstruction.
Here it is important that the impact of the magnetic field of the scanner magnet doublets is not significant in these simulations. Also, the accuracy and the stability of the field amplitude for the standard GunLab power supplies ($\approx 1‰$) is negligible. Further simulations were performed with other field profiles to isolate the influence of the field profile on the measurements. These results show only a tendency towards the optimized scanner coil design. However, in all simulations the influence is not significant. Thus, it can be assumed that the detected small differences between the calculated and the measured field are negligible, as well.

Chapter 6

Image separation system for beam halo measurements

Beam halo is a crucial part of an electron beam for high efficient accelerators, like ERLs, and SC accelerator components, like the SRF cavities (Chapter 2.6). Thus, it is important to study these low intense particle distributions outside the beam core region. The intensity of the halo distribution, corresponding to the charge density, is several orders of magnitude smaller than the beam core intensity. The transverse electron distribution is studied in GunLab with viewscreen monitors (VSM - Chapter 4.4.1) which consists of a thin scintillator screens inside the electron beamline and an optical readout channel using a CCD camera. (Fig. 6.1)

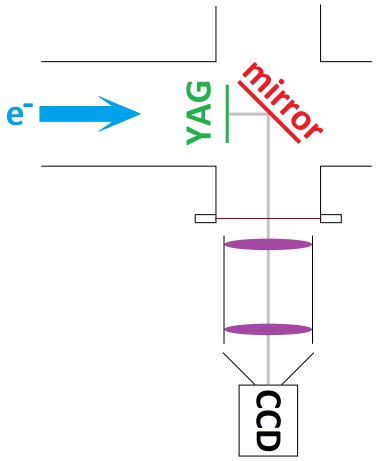

Figure 6.1: Scheme of a viewscreen monitor for GunLab. It consists of a luminescence screen (commonly YAG:Ce) with normal incidence to the beam and a mirror to deflect the light to the readout channel. Both elements are inside the vacuum of the beamline. The readout is an optic, imaging the screen plane on a CCD camera.

The luminescence light of the screen is imaged on the CCD chip of the camera. Thereby, the visible range of the charge density in the electron beam, as well as the halo detection is limited by the dynamic range of the VSM. Chapter 4.4.1 showed that this dynamic range is dominated by the used AVT CCD cameras (14 bit). With those cameras only the core of the main beam can by analyzed, but the outer regions, with intensities less than the threshold of the CCDs, are not visible. In this chapter a method is presented to increase the dynamic range of a VSM by a digital micromirror device (DMD) as an image separator system. Thereby, two images of the same screen are sampled with different

camera thresholds, but equal dynamic ranges. The combined image has an extended dynamic range to analyze potential halo distributions, as well. First, a short example is shown of the limited dynamic range effects of the standard VSM and what are the problems.

Example of halo analysis with a standard VSM at GunLab

The used luminescence screen at GunLab works quite linear in respect of the incident charge density for standard beam operation (Chapter 4.4.1). Therefore, only the effect of the dynamic range of the CCDs has to be considered in this numerical example. The starting point of this example is a defined light intensity distribution at the object plane, imaged $1:1$ on a virtual CCD.

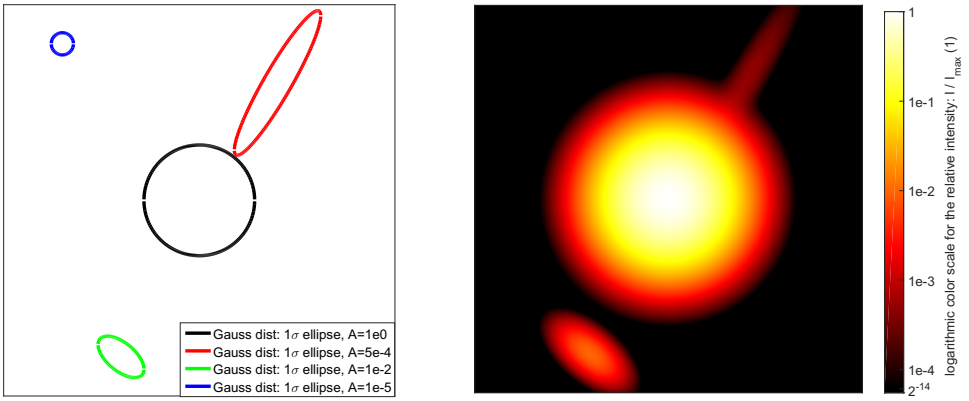

Figure 6.2: Example of a luminescent object with 4 Gauss distributed sources. Each distribution has different amplitudes and Gauss parameters. The complete object is a superposition of all four distributions. The left plot shows the 1-σ ellipsoids of the distributions. On the right side the image in a logarithmic scaled colormap is plotted, sampled using a simulated 14 bit camera.

Fig. 6.2 shows this distribution and the simulated image by the virtual CCD camera. Four different Gaussian distributions are added on a grid with different amplitudes $(1, 10^{-2}, 5 \cdot 10^{-4}$ and $10^{-5})$. The virtual camera in this consideration has a 14bit dynamic range. The pixel values of the camera are plotted logarithmically to visualize the dynamic range. The image is normalized to the maximum pixel value $I_{\max} = 2^{14}$. Here, the first three distributions can be seen on this image, but the upper right ellipsoid in blue is below the threshold. Also, for a characterization of the third distribution in red with an amplitude of $5 \cdot 10^{-4}$ this image is not sufficient. It is necessary to increase the dynamic range of the optical read out. A way to visualize regions with smaller intensities than the threshold is to increase the exposure time. A higher exposure time of the camera amplifies the background of the distribution, but produces an over saturation of the other full scaled pixels. An over saturation means that more electrons are created by the incoming photons than can be sampled on the pixel capacitor (full well capacity). The additional electrons overflow partially into adjacent pixels during the time of light sampling and the read out. This produces so called blooming and streaking artifacts in the sampled image. They disturb the observation of regions next to this saturated regions. [54] To image the background of the distribution without saturation effects the high gained image regions have to be blocked in front of the CCD. Some of these blocking techniques are shown in the following section.

6.1 Techniques to improve the dynamic range

Common techniques use some kind of blocking mask to observe intensity distributions with a high dynamic range without camera saturations. This mask blocks the high intensity light from the source . Thus, the camera can observe the low intensity parts. Three methods of such a blocking mask technique are presented in this section.

6.1.1 Coronagraphy

Corornagrahy is a non dynamic technique to block a region of incident light and observe the background of the source. This method was described and realized by Lyot [55]. A technical realization can be found in the LASCO experiment at the SOHO satellite [56]. This system on SOHO observes the Corona of the sun with a light intensity, up to 8 orders of magnitude less then the intensity of the central region of the sun. Three optical systems (C1, C2, and C3) are installed with different inner and outer blocking masks (Lyot-mask) to observe only a defined region respectively to the sun radius. Thus, each optical system needs a dynamic range of approximately 10^3 to achieve in sum eight orders of magnitude. A special system is installed at C1, observing the inner corona region ($1.1R_{\text{sun}}$ ... $3.0R_{\text{sun}}$). It uses a elliptical focusing mirror inside the optical system with a hole in the center. The direct sunlight passes the hole and is bent out of the system. Thereby the optical readout samples only the background light.
Such a method can also be used for luminescence screens [59]. Therefore a screen with a central hole is placed in the particle beamline, so that the main beam pass the screen without interaction and only the outer parts are visible. At one position of the beamline, the group at CERN installed three screens with different hole diameters. They observed the core and the halo distribution with a combined dynamic range of 10^5.

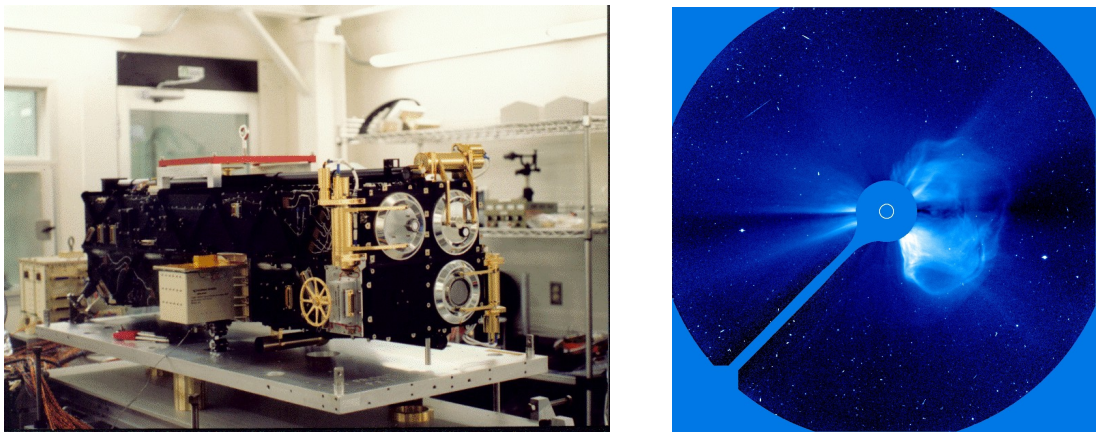

(a) LASCO-system (b) Image of C3

Figure 6.3: The LASCO system at the SOHO satellite. (a) Image of the LASCO system, consisting of the three subsystems C1, C2 and C3 (courtesy of [57]), (b) Image by the LASCO C3 subsystem of a large coronal mass ejection of 29 March 1998.(courtesy of [58])

However, this coronagraphy techniques are not dynamical to work with different beam core parameters or positions. In case of non-rotational symmetric tiny core beams (focal point next to the screen), this steady blocking masks have the wrong shape or dimensions to handle all possible beam parameters. This problem can be solved with a dynamic blocking mask, such as a digital optical mask.

6.1.2 Digital optical mask

An optical mask can be positioned between the luminescence screen and the camera, so that the luminescence screen is imaged on the mask. It can be defined by the digital optical mask individually, which part of the image has to be blocked. This was done at the University of Maryland Electron Ring (UMER) [60]. They used a digital micromirror device (DMD) to deflect defined image regions to a camera, while the rest of the image was sent to a dumping plate. With this technique the transverse profile of a stable laser beam, as well as the electron beam profile on two different screens inside the UMER ring were detected. Here they increased the exposure time of the camera stepwise and blocked the saturated regions on the screen by the DMD. A dynamic range of 5 orders of magnitude was achieved with this setup. For the GunLab halo measurement system an expanded version of this system was developed. Thereby a second CCD is installed in the beamline instead of the dumping plate for the high intense image parts so that two CCDs image the DMD surface simultaneously. Such an image separator would allow to image the viewsreen with an automated optical read out with a high dynamic range.

6.1.3 Image separator with a digital micromirror device (DMD)

The idea is to separate an initial image into high intensity and low intensity parts. Both regions can be observed with two standard CCD cameras A and B. This means that CCD B samples regions with lower or equal light intensity than the threshold of CCD A. Therefore the image amplification at B has to be increased, so that a pixel with a value of the threshold of CCD A has a gained value at CCD B. Both measured intensity distributions are retransformed to the DMD surface and can be combined to one image at the DMD plane. Such a separation of the above defined Gaussian distributions (Fig. 6.2)

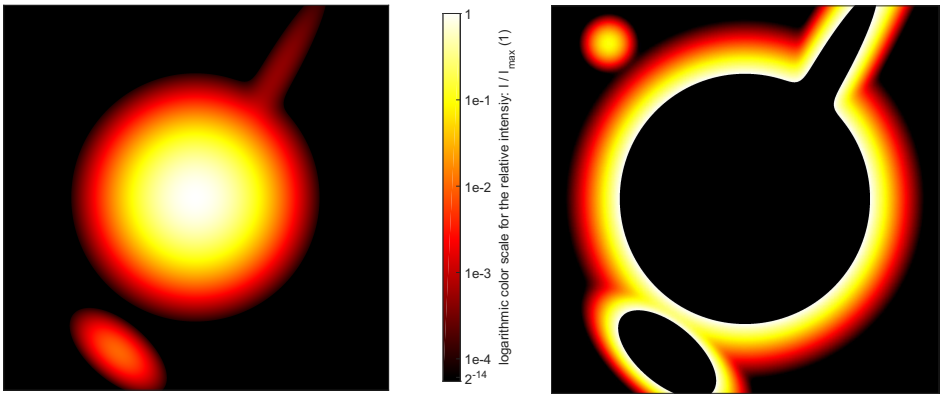

Figure 6.4: The same distribution on the object plane as in Fig. 6.2. Here, the image was separated in high intensity (left) and low intensity regions (right). High intensity is defined by signals between $I_{\max}$ and $I_{\max}/10000$, low intensity with a full 14 bit dynamic range for all signals less than $I_{\max}/10000$.

is shown in Fig. 6.4. With a defined threshold value of $I_{\max}/10000$ two images of the object are sampled. The image on the left consists of the original scaled image with all pixels that have higher values as the threshold. This image looks nearly identically to the standard camera image (Fig. 6.2(right)), because this threshold value is next to the dynamic range of the simulated CCD. The image on the right shows the remaining parts with values lower than the threshold. Without saturation the sampling can be amplified

so that the threshold value is equal with the full well capacity of the camera. The most noticeable is the cut of region in the center of CCD B by the separation (black masked center). This low intensity image has a complete 14 bit dynamic range which allows to observe the fourth distribution in the top left corner, as well. This idealized example has an overall dynamic range of more than 26bit$\approx 1:67e6$. It can be assumed that in reality the dynamic range of this system is smaller than this ideal value, because of several optical effects, such as the background light in the system, thermal noise of the CCDs itself or scattered light of the DMD mirrors. In the following this technique, and how it could be realized for GunLab, is discussed in more details.

6.2 Digital Micromirror Device (DMD) for image separation

Figure 6.5 shows the principle design of a DMD mirror array. A complete device consists of more than 100,000 small squared mirrors. Each of them can be flipped over its hinge axis to two angle positions, respectively to the DMD plane. The mirrors have a stable position only for one of these two angle positions. The manufacture Texas Instruments

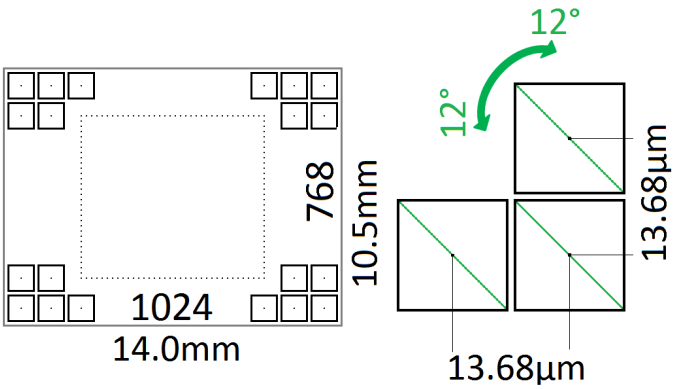

Figure 6.5: Design and dimensions of a VGA Digital micro Mirror Array (DMD) (left). On the right side the pixel size of the arrays and the hinge axis (green) are shown. Each mirror can be switched ±12 deg about its axis.

produce mirror arrays up to ≈ 5 million mirrors on one array.
The DMD has to be positioned in the optic beam line instead of the initial single CCD camera. To image the DMD plane on both CCD cameras, two additional optic beamlines are installed. They have an angle to the incoming optic beamline, twice as large as the tilt angle of the mirrors. All three beamlines have a common point of intersection on the surface of the DMD.
For the Halo measurement system at GunLab a VGA DMD chip was purchased with 768×1024 mirrors [61] [62]. Each of them has a squar shape with ≈ 13.4 μm side length[a] and an electro-mechanic hinge axis which can tilt the mirror to angle positions of ±12 deg. The hinge axis is along the diagonal of a mirror. The electro-mechanics of the mirrors are controlled by a supply board, consisting of a FPGA. It translates a black/white (B/W) image from the PC to the electronics of each mirror. This image has to be the same pixel

[a] The size of each pixel on the array is 13.68 μm. Between the mirrors is a small gap to avoid collisions of neighbored mirrors.

Figure 6.6: Image of the DMD surface with a mirror test setup which was uploaded as B/W image from the PC and send to the DMD control board.

number as the DMD size. The FPGA uses the binary info of the B/W image to define the angle position of each mirror.(Fig. 6.6).
In the context of this thesis, an aluminum breadboard was designed for the setup of the three beamlines with the correct angle values and positions of the optical parts. This board can be installed in the GunLab beamline, as well. Here, the DMD is placed on a 2d linear table with an additional rotation function in the object plane. Thereby, the transverse position and rotation angle of the chip can be varied for small corrections. The

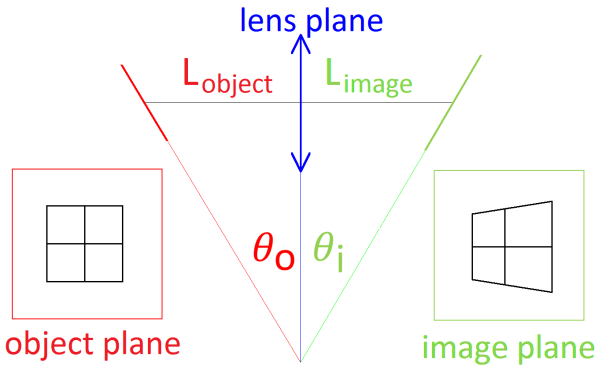

Figure 6.7: Imaging of a tilt object plane, compensated by the Scheimpflug angle θ_i of the image plane. This angle depends on the magnification $M = \frac{L_{\text{image}}}{L_{\text{object}}}$ of the system. However, this compensation also produce a distortion of the image.

additional two optic beamlines consist of optical rails to test different optical systems and adjust them for a correct imaging. For the optic design of both beamlines, the Scheimpflug angle has to be keep in mind (Fig. 6.7). The DMD plane, perpendicular to the incoming beamline, is tilted by $\theta_o = 24$ deg in the horizontal plane from the viewpoint of the CCD beamlines. This angle has to be compensated in the imaging process by the Scheimpflug angle of the CCD. This angle depends on the magnification M of the optical system.

$$\tan(\theta_i) = M \tan(\theta_o) \tag{6.1}$$

For this angle compensation, the CCD cameras are positioned on sliders with rotational tables to adjust the correct compensation angle for the different imaging systems. A

further effect of the Scheimpflug compensation is the distortion in the image plane (see fig. 6.7). In the Scheimpflug system the magnification is a function of the horizontal position on the object plane. A method to compensate the distortion is shown in the following section.

6.3 Initialization of the DMD system

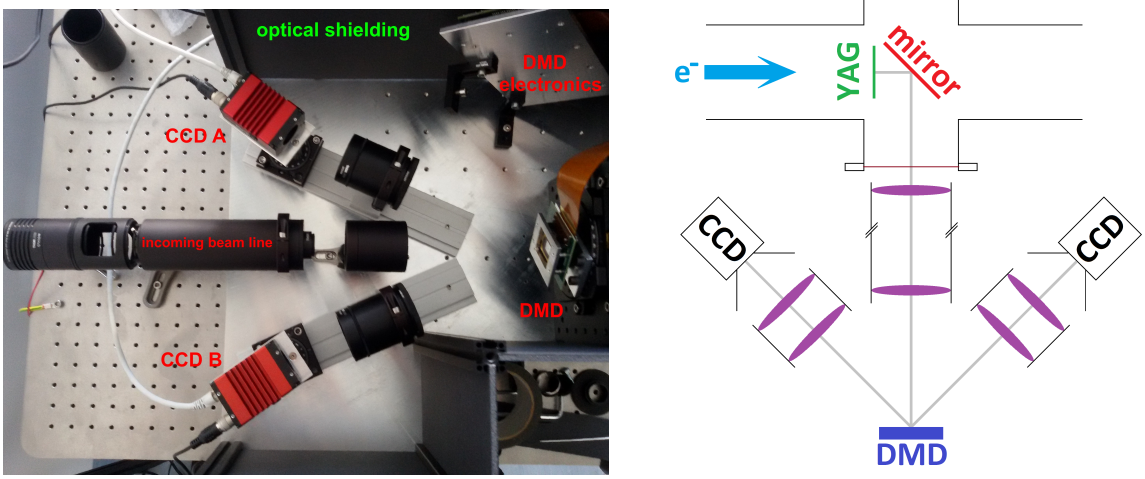

(a) Optic plate

(b) Scheme of the DMD viewscreen

Figure 6.8: Image of the optical plate for the DMD system with both imaging beamlines and their optic rails with a 24deg angle to the incoming beamline (a). All three beamline intercept at the surface of the DMD. The optic plate was designed with a L-shape to install and adjust it in the girder system of GunLab. A scheme of these GunLab installation can be seen on the right side (b).

After the installation of all components both imaging beamlines A and B were tested individually. This was achieved step by step with imaging and transformation tests and at the end with a coordinate transformation measurement in both beamlines. These tests are shown in the following.

6.3.1 Imaging test in both beamlines

In a first step the optics were tested with a chess board image on the DMD. Here squared mirror arrays with 32×32 pixels deflect the light to CCD A or CCD B. With this checkered mask the correct imaging and the magnification can be observed, but not the orientation of the DMD coordinate system respectively to the CCD system. Therefore, an image was used which consists of three letters F, G and L (Fig. 6.9). All three letters have no kind of symmetry which is important to observe rotation or mirror effects of the system.
Figure 6.10 (a) and (b) show the resulting images of both CCD cameras. It can be seen that the DMD coordinate system is rotated by 135 deg clockwise to the CCD systems. Furthermore, it can be recognized that both images are not sharp at the outer regions. This results from the very low depth of sharpness in both beamlines. The first idea was to capture as much light intensity as possible by the CCDs. Therefore, it was not planed to install apertures in the beamlines. To achieve better resolutions for the final tests, apertures were installed after this first test.

Figure 6.9: Image of the DMD surface with a mirror setup to test the imaging beamlines A and B.

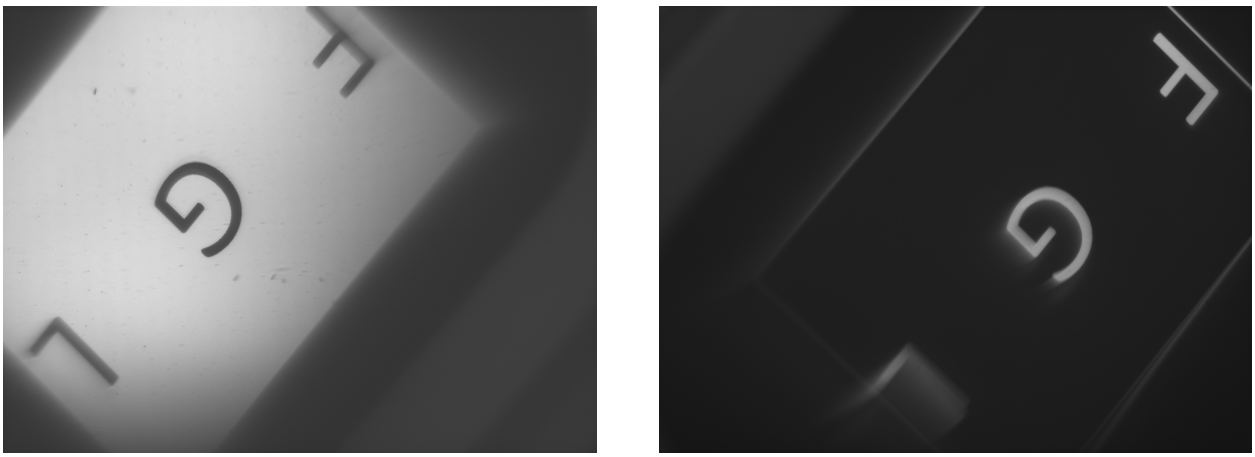

(a) CCD A

(b) CCD B

Figure 6.10: Images of the DMD by CCD A and CCD B. The mirror setup of the DMD consist of an image with the three letters F, G and L. This image has no kind of symmetry. Therefore, the orientation of the coordinate systems can be tested.

Effect of correlated light distributions on the DMD surface

However, this aperture increases the impacts of the correlated light distribution in the image plane at the DMD which is an effect of the imaging process itself. This can be seen in the linear transfer matrix R_{optics} of any imaging system:

$$R_{\text{optics}} = \begin{pmatrix} M & 0 \\ \frac{1}{f_{\text{sys}}} & \frac{1}{M} \end{pmatrix} \tag{6.2}$$

with M as the magnification and f_{sys} as the average focal length of the optical system. Thereby the covariance of the final distribution depends on the initial variance $\langle x_i^2 \rangle$ and the initial covariance $\langle x_i x_i' \rangle$:

$$\langle x_f x_f' \rangle = -\langle x_i^2 \rangle \frac{M}{f_{\text{sys}}} + \langle x_i x_i' \rangle \tag{6.3}$$

The new light source for the CCDs has a correlated distribution on the DMD surface, in case of an initial uncorrelated light distribution ($\langle x_i x_i' \rangle = 0$) with fixed values for

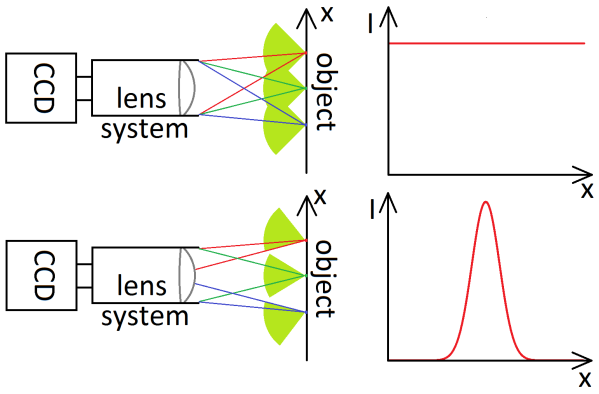

Figure 6.11: Two one dimensional examples of light emission with a constant intensity distribution on the object plane, but with different emission characteristics: The first one is a 4π emitter (uncorrelated phase space distribution) (top left) and the second one a correlated emission source with an narrow emission angle (bottom left). On the right side the transverse intensity distributions in the image plane are plotted. (These examples are only true for positions of x next to the optical axis.)

M and $\langle x_i^2 \rangle$, as well as $\frac{1}{f_{\text{sys}}} \neq 0$. As a result the light intensity is a function of the transversal positions on the DMD, demonstrated in Fig. 6.11 for an one dimensional imaging system. An uncorrelated light emission in the object plane produces a constant intensity distribution in the image plane. Here, the emitted phase space at any position fits in the first order the acceptance of the aperture. However, for a correlated light this overlap between emission and acceptance depends on the transverse position and therefore on the intensity, too. This effect is amplified by a reduced aperture of the optics. To minimize this effect in the first tests, an illuminated white paper was used as an uncorrelated initial light source. A lens doublet imaged the surface of the paper onto the DMD plane. The correlation on the DMD surface is also important for the design of the optical transfer line between screen and DMD (see Appendix A.4).

6.3.2 Coordinate transformation between CCD and DMD

The last step for the initialization of the DMD system is the retransformation of the sampled CCD images onto the DMD surface. For the following measurements it is important to know how the DMD mirrors are linked to the CCD pixels. Otherwise it is not possible to separate the image correctly. For this retransformation not only the rotation between the systems needs to be compensated, the magnification and the distortion by the Scheimpflug compensation have to be included, as well. It was found that the best method is a coordinate measurement with both CCD cameras.
Therefore some of the DMD pixels with known coordinates were flipped. These pixel positions were observed with both cameras and used for a linear plane fit:

$$F_i(x, y) = a_i * x + b_i * y + c_i \tag{6.4}$$

with F_i as the horizontal or vertical position on the DMD, x and y are the measured coordinates of CCD A or B. The fit coefficients are represented by a_i, b_i and c_i. For each camera a set of 6 coefficients are necessary to retransform a pixel from the camera into the DMD plane. With this method all three impacts on the imaging process (rotation, magnification and Scheimpflug correction) can be handled for both beamlines individually. Furthermore small misalignments of the optics in the beamlines can be compensated, too.

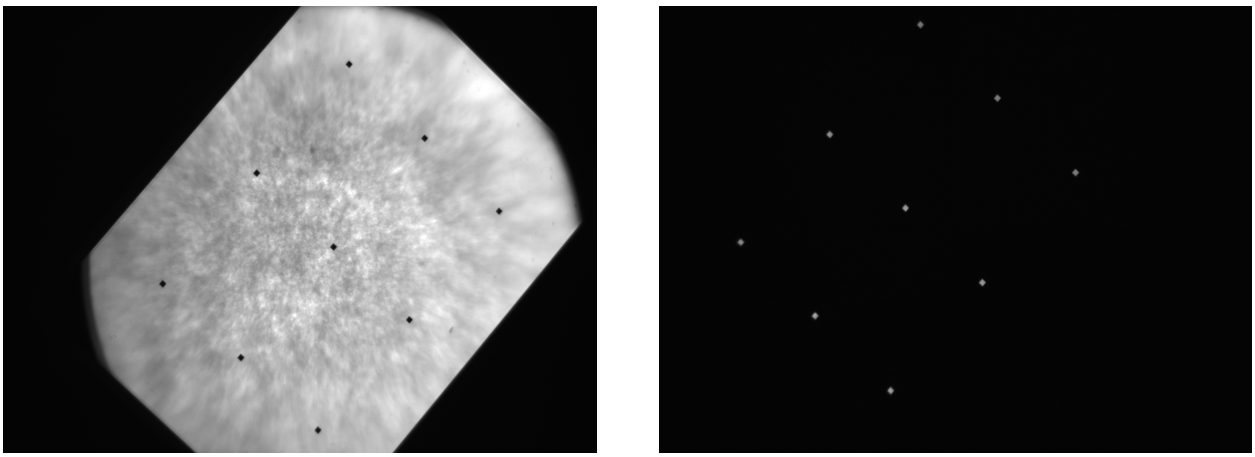

(a) CCD A (b) CCD B

Figure 6.12: Images of the DMD by CCD A and CCD B. A 9-dot image was sent to the DMD. Each dot consists of 11×11 white pixels which means that these mirrors are flipped to CCD B

Fig. 6.12 shows the images of both CCDs of the defined 9 dot mask of the DMD. Each dot of the mask consists of 11 mirrors which are switched to CCD B. The measurement of the coordinates at the CCDs was done manually. For a future software solution of the system it is planed to implement and automate this measurement as a start program. This is important in case that the optics of the transfer line need to be changed. Otherwise small misalignments or non-linear effects produce small changes in the coordinate transformation. This disturbs the complete image separation process.

6.3.3 Software test for the image separation

For a first test of the software an additional aperture was installed next to the white paper light source, imaged on the DMD. The resulting image on the DMD plane should be separated by the DMD, sampled by the CCDs and afterwards combined to a single image. Thereby it was not expected that the dynamic range of the combined image has the intended values of $> 10^5$, due to the used light source. The original image on the DMD plane is shown in Fig. 6.13 and was sampled by CCDA.
The image separation test was performed by the following steps:

- The DMD deflected the complete image to CCDA and the maximum exposure time of the camera was determined. The resulting image was sampled and used as reference image. The parameters of CCDB were set to the same values as CCDA.
- The complete image was then deflected temporarily to CCDB to sample the background image of CCDA with the defined exposure time.
- A threshold of (1:1000) was defined, determining the pixels of the reference image that have to be cut out by the DMD. The pixel coordinates were transformed to the DMD plane. This resulted in an image (DMD setting mask) that deflected the chosen regions to CCDB.
- The exposure time of CCDB was gained by a factor of 1000 and a background image was sampled.

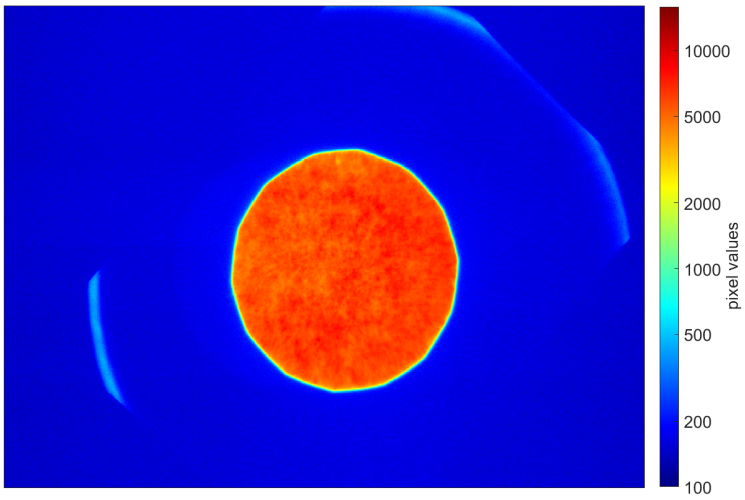

Figure 6.13: Image of the DMD plane where all mirrors were flipped to CCDA. The image is logarithmic scaled. (Exposure time: 10μs, Gain: 0dB, $\gamma = 1$)

- The calculated mask was executed by the DMD and the resulting images of both cameras were sampled.

Fig. 6.14 shows both background reduced images of the CCDs. They are plotted with the same logarithmic scale and their individual coordinates were converted into the DMD plane by the defined coordinate transformation. The used cutoff mask of the DMD is recognizable on CCDB as the spot with the same background noise as the outer regions. Additional to the central aperture spot, a ring structure is noticeable. It results of the outer diameter of the used aperture, which is smaller than the inner diameter of the central beamline.

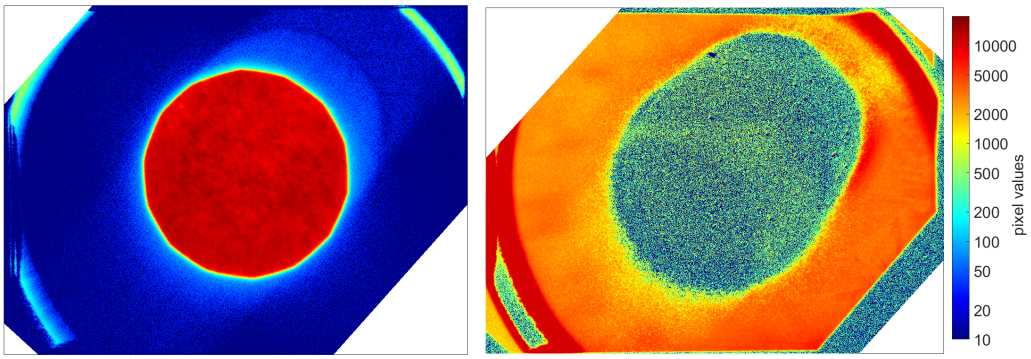

Figure 6.14: Logarithmic scaled images of the DMD plane sampled by CCDA (right) and CCDB (left). Both images are background corrected and converted into the DMD coordinate system.

The crucial element is the combination of both images. The sampled and converted images of both CCDs are quite congruent, but the individual pixel coordinates differ. To add the signals of both images, the overlap of the projected CCD pixels with the DMD pixels have to be calculated in the DMD plane. Afterwards, both resized CCD images are convolved with the original DMD mask and add to one complete DMD image. This is numerically expansive. The resulting image of this test is visualized in Fig. 6.15. It shows the combined information of both CCDs on the pixel grid of the DMD. The overlap calculation lasted several minutes, because of the huge image sizes of the CCDs

(2.8 MP) combined with the DMD size (≈ 0.7 MP). The colorbar on the right side shows the dynamic range of the resulted image. The maximum value results from the CCD pixel integration over one DMD pixel to ≈ 69400. On the other hand, the lower limit is given by the inverse threshold level integrated over the DMD pixel ≈ 0.01. The used light source (light emitting white paper) produces much background light next to the imaged aperture. Therefore, it was not possible to measure the full dynamic range of the DMD system.

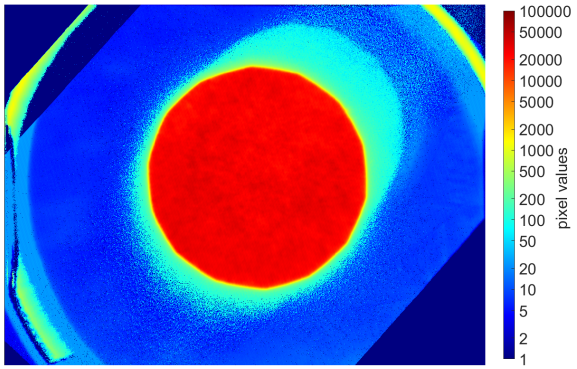

Figure 6.15: Combined Image of both CCDs as logarithmic scaled image of the DMD plane. Both images are background corrected, converted into the DMD coordinate system and combined to one image with the same size as the DMD. Due to the 45 degree rotation of the DMD, the resulting image is rotated, too.

In conclusion, the DMD system can handle two CCD cameras that sample the separated image of a light source with a digital micromirror device. The imaging process in all beamlines was tested. Thereby, the linear distortions in the CCD images, produced by the individual Scheimpflug imaging, could be compensated by a coordinate transformation between CCDs and DMD plane. With a defined threshold level, a mask for the DMD was determined from a given reference image. This reference could be separated into an intensity region above the threshold and a regions with lower intensities. The sampling and the following recombination of both images onto the DMD plane was successfully tested.
Some further testings of the system are planed to determine the full dynamic range of this system, too. Thereby, the used light source will be replaced by a scattered laser beam, which produces in first approximation a transverse Gaussian intensity distribution. For a real measurement of the full dynamic range, a transverse distributed neutral density filter combination can be used. These filter define the intensity distribution of the light source, sampled by the DMD system. However, some modification are also necessary to achieve the estimated dynamic range of 10^6 for the complete DMD system. Here, scattered light inside the DMD system, as well as in the optic beamlines, has to be suppressed. This light pollution limits the measurement of the low intense regions of the image. During the optimization of the central transferline (Appendix. A.4), it was detected that a large part of the light from the object, accepted by the first aperture of the lens system, cannot pass the complete beamline. This also produced scattered light at the edges of the lenses or at the walls of the beamline. Further apertures need to be installed in front of the beamline to cut out only the phase space region of the object light which fulfills the acceptance of the complete beamline.

Chapter 7

Field characterization of an SC solenoid

In Chapter 3.2 the solenoid for Gun1 was presented. The final design and the resulting construction were shown. It is based on a segmented yoke to install the solenoid between the SRF cavity and the higher order mode (HOM) coupler. Thereby, the magnetic flux in the yoke has to penetrate at least two boarders of different yoke segments. The sur-

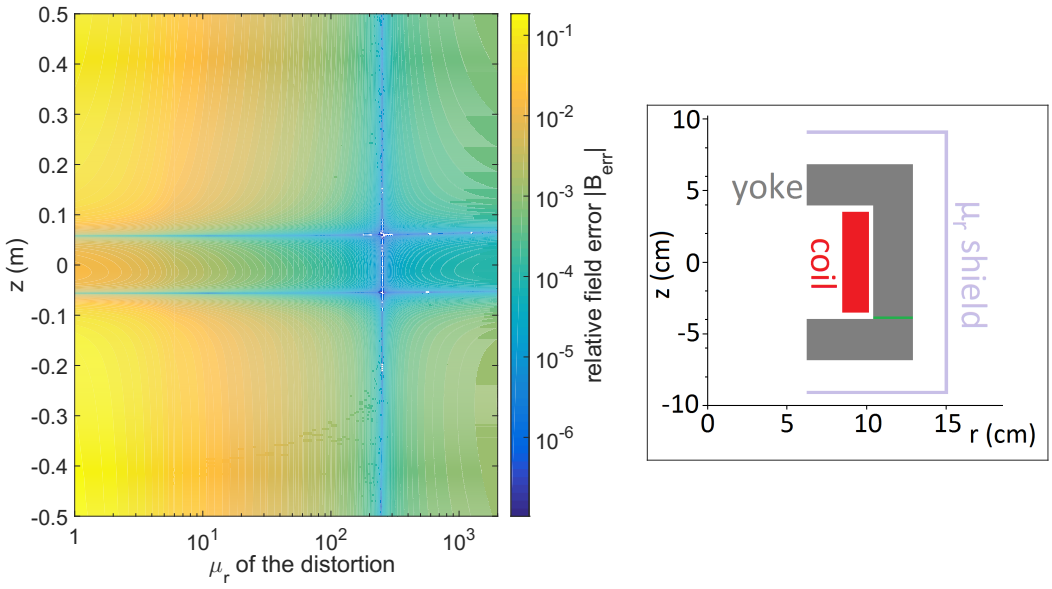

Figure 7.1: Plot of the relative error of the field profile on axis (left) as function of the yoke permeability μ_r in the disturbed region (green slice in the yoke) of the solenoid (right). This scheme shows the cross section of the GunLab solenoid in the radial (r) and longitudinal (z) plane, consisting of the coil (red), yoke (gray) and Mu-metal shield (violet). The green slice is a 2 mm thick region of the yoke with variable μ_r between 1 (vacuum) and 2000.

faces at the boarders have finite surface roughness. Thus, an additional resistance for the magnetic flux at the transition can be assumed. The magnetic conductance of a material is comparable to the permeability. Therefore the effective permeability μ_r in this region can differ to an ideal yoke without any borders. A numerical calculation with Poisson/Superfish was performed where the μ_r in a small slice of the yoke was varied (green region in the yoke in the right figure). Fig. 7.1 shows the relative field profile error on the magnet axis as a function of the local μ_r in the 2 mm yoke slice. The vertical line in the

left plot results from a similar μ_r-values as in the yoke. However, a different μ_r affects the complete field profile of the magnet. In this example, a μ_r variation of 20% produce average profile differences of 1‰. This effect appears to be small, but Poisson/Superfish assumes a rotational symmetric geometry, which should not be the case for the effective μ_r distribution in the solenoid. For off-axis positions this effect is further amplified by the change of the field expansion terms in Eq. 2.10 and Eq. 2.11. Finally, the complete solenoid yoke consists of six similar surfcace transitions.
Another source of field distortions are geometry errors, such as elliptical or toroidal deformations, or longitudinal distortions of the magnet. Thus, all these errors can disturb the rotational symmetric magnetic field of the ideal solenoid. The resulting field can be described by an ideal solenoid field with additional magnetic multipole field terms. Such an asymmetric field is also a source for emittance growth and unwanted beam effects like steering and asymmetric beam focusing. In the following the cylindrical surface measurement is presented to characterize and observe these multipole fields in the solenoid magnet. It is based on a Fourier analysis of sampled field data on a virtual cylinder surface. With these reconstructed field amplitudes the impact on the electron beam was simulated. These simulations were also used to test a compensation method, that use skew quadrupole magnets.

7.1 Multipole field terms in a solenoid

In general, an arbitrary magnetic field can be described as the sum of magnetic multipole fields, such as dipole or quadrupole:

$$B^{(\mathrm{MP})} = \sum_{n=1}^{\infty} \left(A_n \cdot (x + j \cdot y)^{n-1} \right) \tag{7.1}$$

$$B_x^{(\mathrm{MP})} = \Re(\tilde{B}) \ , \ B_y^{(\mathrm{MP})} = \Im(\tilde{B}) \tag{7.2}$$

with x and y as the Cartesian coordinates in the transverse plane and A_n as the complex amplitude of the n-th multipole ($n = 1 \rightarrow$dipole, $n = 2 \rightarrow$quadrupole, etc.). j represents the imaginary unit. The real element of A_n can be interpreted as the normal multipole field terms and the complex elements as the skew multipole field term. Finally, the real ($\Re$) and the complex ($\Im$) parts of the combined multipole field are defined as the vertical and horizontal magnetic field components, respectively. In case of asymmetries in the geometry of a solenoid the resulting field can be described as a combination of a symmetric solenoid field and further multipole fields like Eq. 7.1.
The dipole and quadrupole fields in the solenoid produce unwanted steering and asymmetric focusing effects, but do not influence directly the overall transverse emittance. However, non-linear multipole fields, like sextupole components, transform the phase space in a non-linear way. They have an impact on the linear emittance. Nevertheless, the linear multipole fields are also undesirable, because of the transverse coupling effect by the solenoid due to the Larmor rotation of the solenoid. This is not detectable for a rotational symmetric bunch. In case of a broken field symmetry, the resulting bunches are sensitive for coupling effects. A dipole field steers the beam inside the solenoid, leading to a rotation of the beam centroid as function of the solenoid strength. Another example is a further quadrupole field which disturbs the rotational symmetric focal strength of the solenoid. This results in a transverse elliptical bunch with strong transverse coupling. Such a coupled beam is also a source for projected emittance growth in the horizontal and vertical phase spaces, because of the non zero elements in the x-y covariance matrix. In

both cases, steerer and quadrupole magnets are necessary to correct these beam errors. Therefore, it is important to observe the magnetic solenoid field and to reconstruct the unwanted multipole field terms. In case of a superconducting magnet such a measurement is not simple and requires special technical conditions. A necessary test cryostat, combined with an anti-cryostat, is operated at the Gesellschaft für Schwerionen (GSI - Darmstadt).

7.2 Field measurements setup at the GSI

The magnetic field of the solenoid has to be measured with realistic conditions like in the photoinjector beamline. This means that the solenoid has to be positioned inside a cryostat and cooled down to the working temperature of 4 K. On the other hand, it is also necessary to map the magnetic field of the solenoid with a sensor inside the cryostat. For such a setup an anti-cryostat is used. It consists of a cryostat with a thermal insulated and non magnetic insertion tube. Inside this tube normal room temperature and atmospheric pressure conditions can be achieved. Thereby the magnetic field can be observed with standard hall probes, usually calibrated for room temperatures. A mapper moves the sensor through the anti-cryostat. Such a measurement system is used at the GSI in Darmstadt. In a collaboration, a test stand was developed to place the solenoid inside the GSI cryostat together with the anti-cryostat tube (Fig. 7.2). This tube consists of glass fiber reinforced plastic (GRP) with a heater inside its wall which is a pair of twisted heat cables to suppress electrical current induced magnetic fields. The field mapper is a

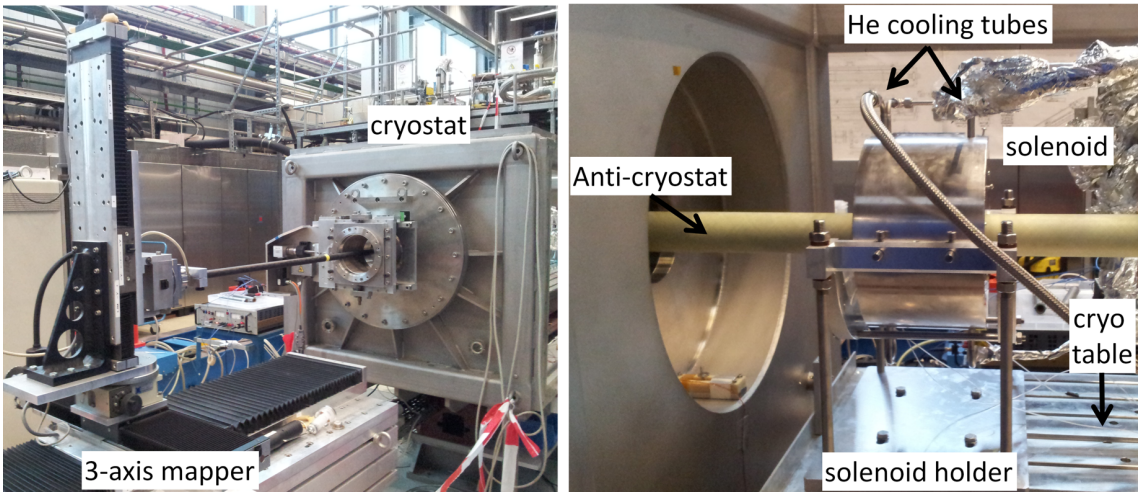

Figure 7.2: Image of the mapper with the sensor arm in front of the cryostat (left). Image of the Gun1 solenoid positioned on magnet holder inside the cryostat at the GSI (right). The green tube through the magnet is the thermal insulated anti-cryostat for the field measurement of the cold magnet.

combined system of three linear tables and a measurement sensor. The linear tables can work in a range of ±0.5 m with a reproducible precision of ±0.01 mm.[a] This precision is achieved by an optical leveling instrument, focusing on the sensor head of the mapper. The sensor itself consists of three orthogonal hall probes for an independent measurement of the three field components in respect to the coordinate system of the laboratory system.

[a]The mapper and the sensor head were designed and constructed at GSI. The system is used for precision field measurements of compact normal conducting magnets. It is calibrated by an optical leveling system.

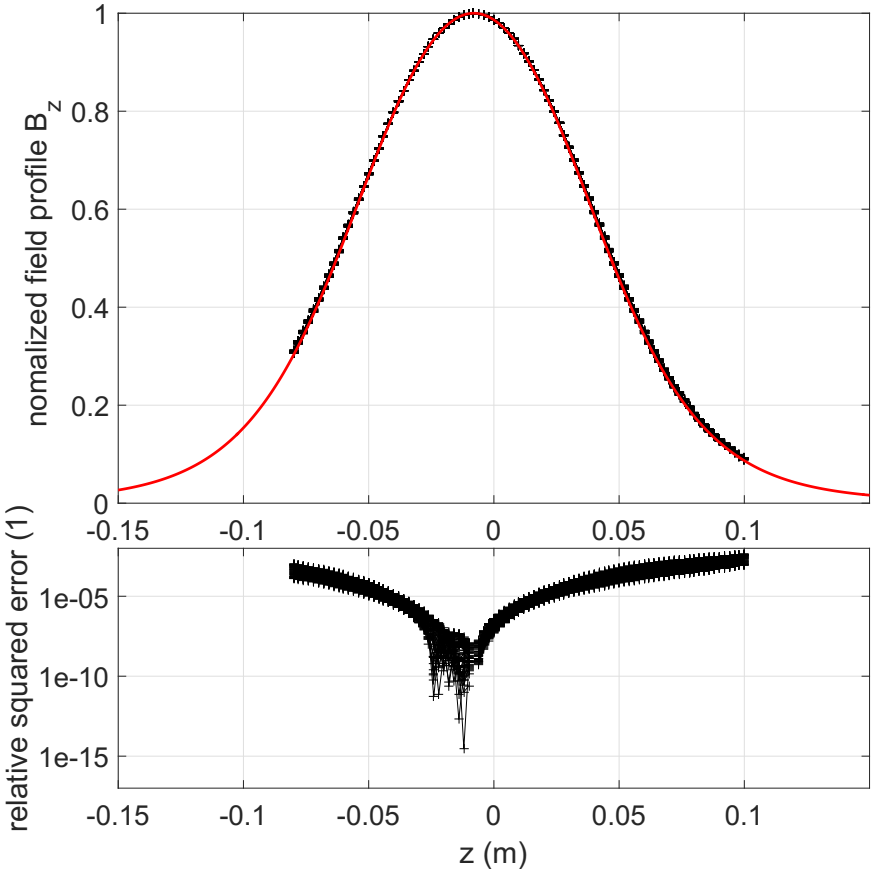

Figure 7.3: Top: Measured field profile of the longitudinal field B_z (black) normalized to the calculated field profile of the ideal solenoid geometry by Poisson/Superfish (red). Bottom: Relative squared differences to the calculated profile.

Position uncertainties of the hall probe were determined to ± 100 μm for the position alignment. For the important measurement of the solenoid field, the mapper moved the sensor along coordinates on the surface of a virtual cylinder with a radius of 6 mm. As an example, the longitudinal field component B_z for all cylinder coordinates is plotted in Fig. 7.3 as function of the longitudinal position z. The maxima of the measured data are normalized, as well as the profile of the calculated solenoid field by Poisson/Superfish (red curve). The differences between measured and calculated profiles are less than 1%, which is a good confirmation of the solenoid model. Furthermore, the variation of the B_z as function of transverse position is not significant with respect to the measurement uncertainties.

The measured magnetic fields were used to reconstruct the magnetic field axis with respect to the laboratory system, as well as the higher order magnetic field components. Both methods are presented in the following sections and are based on the cylindrical surface measurement.

7.3 Cylindrical surface measurement

The method of the cylindrical surface measurement was used for a quadrupole measurement system at ALBA [63, 64]. Therefore a three axis hall probe was moved over the surface of a virtual cylinder around the magnet axis. This virtual cylinder has a radius

R that defines the measurement positions by

$$\begin{pmatrix} x & y & z \end{pmatrix} = \begin{pmatrix} R\cos(\phi) & R\sin(\phi) & z \end{pmatrix} \tag{7.3}$$

where ϕ is the azimuthal coordinate. For each position, the three Cartesian field components B_x, B_y and B_z are measured simultaneously. Fig. 7.4 shows this measurement

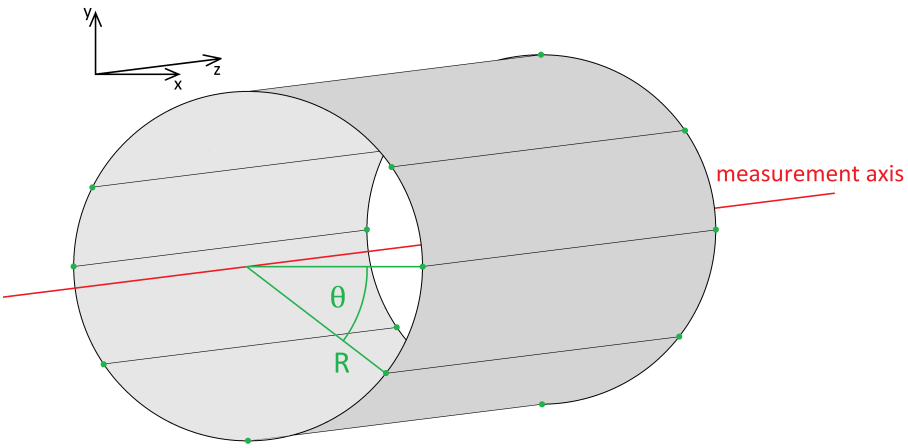

Figure 7.4: Draft of the cylindrical surface measurement. Along the virtual cylinder (grey) with cylindrical axis (red), the magnetic field is measured on defined position (green dots) with constant step size in azimuthal and longitudinal direction.

method. With the known measurement positions on the virtual cylinder surface, the measured field components can be represented in cylindrical coordinates, as well.

$$B_r = \frac{B_x x + B_y y}{r} \tag{7.4}$$

$$B_\theta = \frac{-B_x y + B_y x}{r} \tag{7.5}$$

$$B_z = B_z \tag{7.6}$$

$$r = \sqrt{x^2 + y^2} \tag{7.7}$$

For an ideal solenoid with perfectly aligned magnetic axis to the virtual cylinder, the resulting field components are identical to the field expansion of the solenoid profile on axis (Eq. 2.10, Eq. 2.11). In this case, the azimuthal field component is zero. Thus, potential multipole terms (Eq. 7.1) in the solenoid produce additional field components in cylindrical coordinates (Eq. 7.4 and Eq. 7.5):

$$B_r^{(\mathrm{MP})} = r^{n-1}\Im\left[\sum_{n=1}^{\infty}\left(A_n \exp(i\theta n)\right)\right] \tag{7.8}$$

$$B_\theta^{(\mathrm{MP})} = r^{n-1}\Re\left[\sum_{n=1}^{\infty}\left(A_n \exp(i\theta n)\right)\right] \tag{7.9}$$

with the radius r and the azimuthal angle θ in the system. Both equations show that a given multipole term produces an oscillation of the field components along θ. The periodicity depends on the multipole order n. The amplitudes of the additional multipole amplitudes can be determined by a discrete Fourier analysis for both field components as

function of the longitudinal position z

$$C_\theta^{(n)}(z) = \frac{2}{N_\theta r^{n-1}} \sum_\theta \left(B_\theta(\theta, z) \cdot \exp(i\theta \cdot n)\right) \tag{7.10}$$

$$C_r^{(n)}(z) = i\frac{2}{N_\theta r^{n-1}} \cdot \sum_\theta \left(B_r(\theta, z) \cdot \exp(i\theta \cdot n)\right). \tag{7.11}$$

Thereby, N_θ is the number of defined azimuthal position on the cylinder surface. An important requirement for the discrete Fourier analysis is the constant step size of θ.
In general, the axis of the virtual cylinder differs to the magnetic axis. In case of an ideal solenoid magnet, this results in a magnetic field along θ, which is similar to an additional magnetic multipole distribution. For example, an offaxis position x_0 in the horizontal direction relative to the cylinder axis produces a radial field distribution on the cylinder surface, given by:

$$B_r|_{\text{Cylinder}} = B_r|_{\text{ideal}} - \frac{B_z'}{2} x_0 \cos\theta + O(x_0^2) \tag{7.12}$$

$$= B_r|_{\text{ideal}} + B_r|_{\text{ideal}} \frac{x_0}{R} \cos\theta + O(x_0^2). \tag{7.13}$$

Thereby $B_r|_{\text{ideal}}$ is the ideal radial solenoid field component for the given cylinder radius R. The second term with $B_z' = \frac{\partial B_z}{\partial z}$ describes an additional dipole term in the observed field on the cylinder surface. The radial field expansion in a solenoid produces further terms, combined in the function O. These terms produce pseudo multipole components[b]. To reduce this effect in the multipole analysis, the Fuorier transformations has to be convolved with the geometry of the virtual cylinder, described in the solenoid system. Therefore, the orientation of the magnet axis has to be determined with respect to the axis of the virtual cylinder.

7.4 Cylindrical surface measurement for a solenoid

There are several sources of uncertainties for an SC solenoid that can produce a different axes orientations between magnet and virtual cylinder:

1. unknown magnetic field axis relative to the geometry axis of the magnet
2. misalignment of the solenoid magnet respectively to the defined laboratory system of the mapper
3. thermal expansion of the magnet holder during the cool down process

For the cylindrical surface measurement of a solenoid, it is important to determine the orientation of the magnetic axis of the solenoid with respect to the axis of the virtual cylinder, defined in the laboratory system. Afterwards, the coordinates of the virtual cylinder and field components need to be transformed into the solenoid system. Also, Fourier analysis have to be corrected by the transformed coordinates.

7.4.1 Reconstruction of the magnetic field axis

There are four parameters that describe the difference between both axes. The transversal offsets x_0 and y_0 in Cartesian coordinates and two angle offsets in polar coordinates

[b]These components cannot be depicted as field oscillations along θ with a constant amplitude. The resulting terms have a similar behavior as the classical mutlipole field terms, but with further convolution terms.

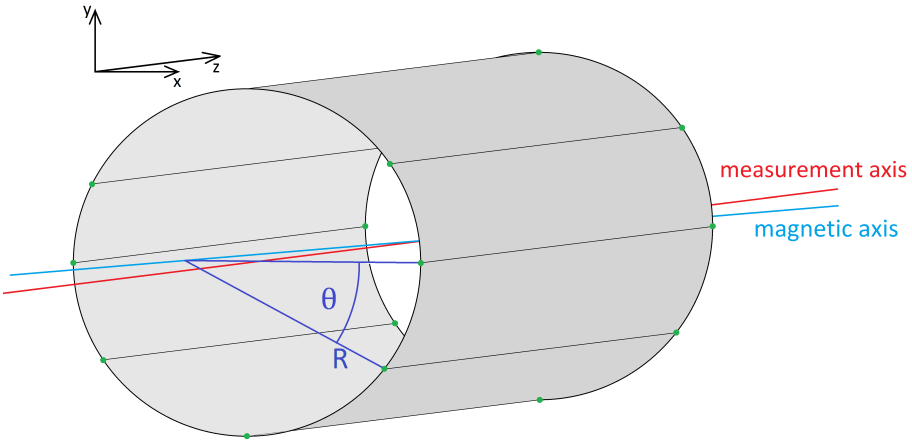

Figure 7.5: Draft of the cylindrical surface measurement. Along the virtual cylinder (grey) with cylindrical axis (red). Here, the solenoid axis (magnetic axis in blue) differs to the cylinder axis. The magnetic field is measured on defined position (green dots) with constant step size in azimuthal and longitudinal direction.

(η =polar angel , κ =azimuthal angle). The final coordinate transformation from the laboratory system into the solenoid system consists of four steps:

1. a first rotation in azimuthal direction by $-\kappa$,
2. rotation in the xz-plane by $+\eta$,
3. a second rotation in azimuthal direction by $+\kappa$ and
4. a transverse shift by the offsets x_0 and y_0.

The first rotation by $-\kappa$ conserves the orientation of the laboratory system in the Solenoid system. The three rotations can be described by the product of the rotation matrices $R_{\text{azimuth}}(\kappa)$ and $R_{\text{polar}}(\eta)$:

$$R_{\text{rot}} = R_{\text{azimuth}}(\kappa) \cdot R_{\text{polar}}(\eta) \cdot R_{\text{azimuth}}(-\kappa) \tag{7.14}$$

$$= \begin{pmatrix} \cos^2\kappa\cos\eta + \sin^2\kappa & (\cos\eta - 1)\cos\kappa\sin\kappa & -\cos\kappa\sin\eta \\ (\cos\eta - 1)\cos\kappa\sin\kappa & \cos\eta\sin^2\kappa + \cos^2\kappa & -\sin\kappa\sin\eta \\ \cos\kappa\sin\eta & \sin\eta\sin\kappa & \cos\eta \end{pmatrix} \tag{7.15}$$

The resulting matrix can be simplified by the assumption of only small polar angles $\eta << 1$. resulting in $\cos\eta \approx 1$ and $\sin\eta \approx \eta$. This approximation cannot be done for κ, because of the non predictable orientation of the magnetic axis in the laboratory system

$$R_{\text{rot}} = \begin{pmatrix} 1 & 0 & -\eta\cos\kappa \\ 0 & 1 & -\eta\sin\kappa \\ \eta\cos\kappa & \eta\sin\kappa & 1 \end{pmatrix} \tag{7.16}$$

In general, the four offset parameters are unknown and have to be determined by a recursive reconstruction algorithm. Thereby the measured magnetic field components and the defined coordinates of the cylinder are transformed by R_{rot} from the laboratory

system into a possible solenoid system.

$$\begin{pmatrix}\tilde{x}\\ \tilde{y}\\ \tilde{z}\end{pmatrix} = R_{\text{rot}} \cdot \begin{pmatrix}x\\ y\\ z\end{pmatrix} \tag{7.17}$$

$$\begin{pmatrix}\tilde{B}_x\\ \tilde{B}_y\\ \tilde{B}_z\end{pmatrix} = R_{\text{rot}} \cdot \begin{pmatrix}B_x\\ B_y\\ B_z\end{pmatrix} \tag{7.18}$$

Afterwards, the measured and transformed Cartesian coordinates and field components can be translated into cylindrical coordinates.

$$\tilde{B}_r = \frac{\tilde{B}_x\tilde{x} + \tilde{B}_y\tilde{y}}{\tilde{r}} \tag{7.19}$$

$$\tilde{B}_\eta = \frac{-\tilde{B}_x\tilde{y} + \tilde{B}_y\tilde{x}}{\tilde{r}} \tag{7.20}$$

$$r_t = \sqrt{\tilde{x}^2 + \tilde{y}^2} \tag{7.21}$$

$$\theta_t = \arctan\left(\frac{\tilde{y}}{\tilde{x}}\right) \tag{7.22}$$

These radial and azimuthal field components are comparable with the calculated field components of solenoid in its own coordinate system, which are given in first order approximation by:

$$B_r|_{\text{ideal}} = -\frac{r}{2}\frac{\partial B_z(z)}{\partial z} + O(r^3) \tag{7.23}$$

Here, the measured longitudinal field profile $B_z(z)$ is used. The profile measurements of the magnet show no correlation between B_z and θ with respect to the measurement uncertainties (see Fig. 7.3). Thus, the field profile is not affected by the misalignement of the axis.
The difference between Eq. 7.19 and Eq. 7.23 is defined as error of the offset parameter setting:

$$\chi^2 = \sum_N (\tilde{B}_r - B_r|_{\text{ideal}})^2/(N-1) \tag{7.24}$$

with N as the number of all measurement positions. This equation is multiplied by r. The resulting formula is numerically easier to handle, because of the loss of the quotation and the square root.

$$\chi^2 = \sum_N \left[\left(\tilde{B}_x\tilde{x} + \tilde{B}_y\tilde{y}\right) - \left(\frac{x^2+y^2}{2}\frac{\partial B_z}{\partial z}\right)\right]^2 /(N-1) \tag{7.25}$$

χ^2 is calculated for a given offset parameter setting and has a global minimum in case of the most promising setting. In general, this minimum of χ^2 is non zero, because of further field components that are not involved in this model, such as higher order terms in Eq. 7.23, multipole fields of the solenoid and uncertainties in the measurements.
For the measured field data, a geometrical optimization was used to minimize χ^2. Therefore, a range for the four offset parameters needs to be defined. The algorithm decreases this parameter range stepwise next to the settings, producing minimum χ^2-values. It stops

when no further decrease of the χ^2-value after several steps is detected. This algorithm was checked numerically by different solenoid fields in combination with several superimposed multipole fields like dipoles and quadrupoles. Thereby, the axis orientations were correctly reconstructed in most cases with differences in the order of the numerical uncertainties. Only for solenoid fields with directly proportional dipole field configurations, a correlation between the dipole amplitude and the off-axis positions were detected. This results from the radial field expansion in an off-axis solenoid (Eq. 7.13).
For the final analysis of the measurements, a start range was defined for the unknown offset parameter, with ±8 mm transversal offsets, ±8 mrad azimuthal offset and 0...2π polar angle offset. The results of the axis reconstruction can be seen in Fig. 7.6. It shows the contour of the minimum χ^2-values of the parameter projections onto the transverse offset plane (x_0,y_0 - left plot) and the angle offset plane (η_0,κ_0 - right plot). Both plots

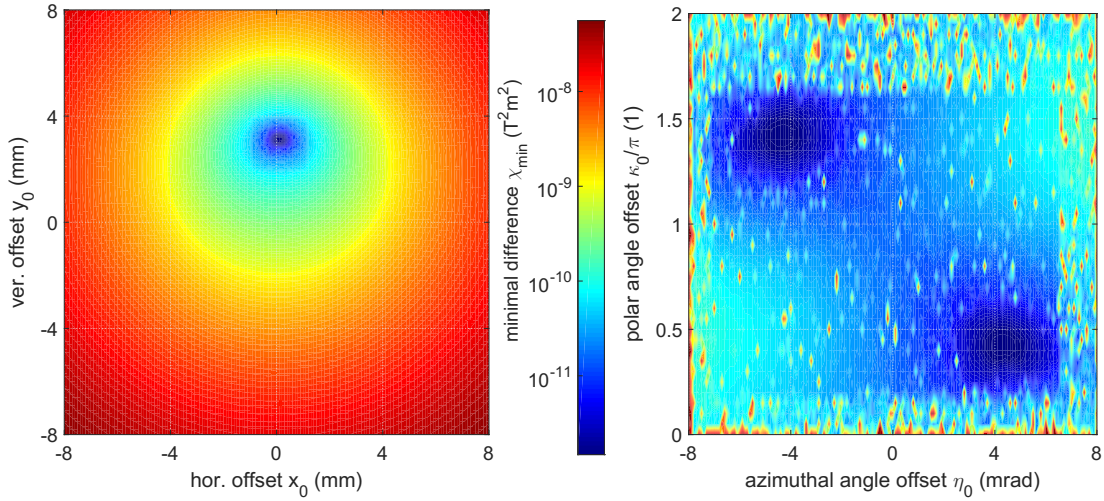

Figure 7.6: Results of the magnetic axis reconstruction of the solenoid. Left: projection of the χ^2-minimas onto the transversal offset parameters (x_0,y_0). Right: projection of the χ^2-minimas onto the angle offset parameters (η_0,κ_0).

show that the method produces unique offset settings for x_0 and y_0 with a minimum average axis error. For the angle offsets there are two spots with small χ^2. However, both positions determine the same axis angle. This can be seen in the parameter differences of both spots. They have the same absolute azimuthal values, but with different sign. Furthermore, the difference in the polar angles is π.
Therefore, this plot in the angle offset plane is a good verification of the transformation method. The final values of the axis reconstruction can be seen in Tab. 7.1. The uncertainties for the final results were determined by a variation calculation of the measured field components and the sensor positions in the range of their individual uncertainties.

x_0 (mm)	y_0 (mm)	η (mrad)	κ (rad)
0.11 ± 0.03	3.15 ± 0.05	4.4 ± 0.1	1.32 ± 0.04

Table 7.1: Offset parameter of the magnetic axis of the solenoid relative the defined axis of the virtual cylinder in the laboratory system.

It is noticeable, that the vertical offset value, as well as the pitch angle of the solenoid axis, are quite high with respect to the estimated thermal expansion of the solenoid holder. The design of the holder consists of Titanium to minimize the thermal expansion over

the complete length to ≈ 1 mm between 4 K and room temperature. This value was considered for the alignment of the solenoid to compensate this offset error. A more likely explanation is the thermal expansion of the complete table inside the cryostat (Fig. 7.2). It is a 3 m long aluminum table that is only fixed on one side, where the supply lines enter the cryostat (less thermal stress). The solenoid was placed on the other side of the cryo table. In two independent measurements during the cool down of the cryostat, it was detected that this magnet place was shifted more than 8 mm away from the mapper. Thereby it is conceivable that there is a comparable movement in the vertical dimension, as well.
These calculated offset parameters of the magnetic axis of the solenoid were used to transform the measured field components and to reconstruct multipole field components of the solenoid.

7.4.2 Reconstruction of the magnetic multipole fields

For the reconstruction of the magnetic multipole fields, the above described Fourier analysis (Eq. 7.10 and 7.11) of the measured and transformed field components is used. Thereby the analysed functions are convolved with the transformed coordinates of the measurements. This results in the multipole amplitudes inside the solenoid system. Therefore, r and θ have to be replaced by the transformed coordinates Eq. 7.21 and Eq. 7.22. For the Fourier analysis of the convolved functions the discrete Fourier has to be modified into a numerical integration over the azimuthal angle θ_t.

$$C_\theta^{(n)}(z) = \frac{1}{\pi}\sum_{\theta_t}\left(\tilde{B}_\theta(\theta_t,z)\frac{\Delta\theta(\theta_t)}{\langle r_t\rangle^{n-1}(\theta_t)}\exp(i\theta_t n)\right) \tag{7.26}$$

$$C_r^{(n)}(z) = \frac{i}{\pi}\cdot\sum_{\theta_t}\left(\tilde{B}_r(\theta_t,z)\frac{\Delta\theta(\theta_t)}{\langle r_t\rangle^{n-1}(\theta_t)}\exp(i\theta_t n)\right). \tag{7.27}$$

Thereby $\Delta\theta(\theta_t)$ is the integration step length and $\langle r_t\rangle(\theta)$ the mean radius to the transfered axis over $\Delta\theta$. Both functions depend on θ_t. For the solenoid measurements at the GSI 40 different azimuthal positions were defined to suppress numerical uncertainties by the varying integration step sizes and the averaging of the functions. This method was tested with idealized solenoid fields superimposed with multipole fields similar to the test of the axis reconstruction. The reconstructed multipole distributions for dipole, quadrupole and sextupole components in the solenoid field are plotted in Fig. 7.7 as function of z. Thereby the real parts of the amplitudes (standard multipole) and the imaginary parts (skew multipole) are depicted in red and blue, respectively. The errorbars of the plots represent the uncertainties of the offaxis settings (Tab. 7.1) combined with the field and position errors. All three multipoles indicate no direct correlation, but have a similar longitudinal asymmetry. Several geometry errors of a solenoid magnet, such as elliptical, toroidal or distorted solenoids were studied, to examine possible correlations between measured and calculated multipole distributions. Hereby, a single geometrical origin is not detectable for the reconstructed multipole distributions.
The dominating multipole contribution in the solenoid field is are the quadrupole fields for radial distances between 1 and 10 mm. This quadrupole component along z is mostly orientated as a standard quadrupole. It was expected that the gaps of the split pole shoes at the top and the bottom of the yoke produce a slightly reduced radial field in these section, resulting in a superimposed skew quadrupole component. However, there is no indication for this.

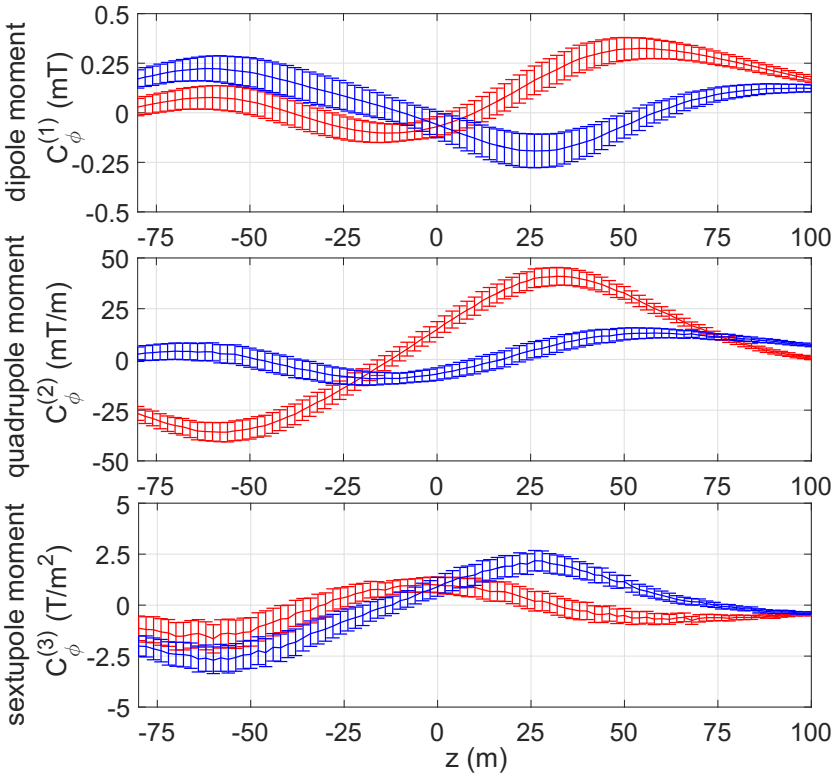

Figure 7.7: Plot of the first three reconstructed multipole fields as function of the longitudinal position z. Each multipole term is separated in a real (red) and an imaginary (blue) part which can be interpreted as normal and skew multipole elements.

On the other hand, the field strength of all multipole fields along z for $r \approx 6$ mm is in the range of $\approx 4\%$ relative to the radial field strength of the solenoid. The impact of this additional magnetic field on a passing electron beam was studied with a particle tracking with ASTRA. The implementation and the results of this tracking are presented in the following section.

7.5 Impact of the reconstructed multipole field on the transverse beam emittance

The reconstructed multipole profiles were implemented in the transversal field calculation (Eq. 7.1). All 3d multipole fields and the ideal solenoid field were superimposed at the geometrical position of the solenoid magnet.[c] The tracking of the electron bunches through the resulting field was performed similar to the study of the emittance contribution of the Gun1 solenoid (Chapter 2.5.3). Thereby, several solenoid field strength are used, where it was assumed that the multipole field amplitudes are linear correlated with the ideal solenoid amplitude over the complete range of the defined solenoid field strength. Furthermore, several ideal Gaussian distributed bunches were tracked through the resulting field and the transverse emittances were measured next to the reference position in GunLab. The superimposed magnet fields produce beam steering and an elliptical beam distributions in the transverse plane. An example for this is shown in Fig. 7.8(left). The

[c] Any 3d AC, electrical or magnetic DC field can be implemented in ASTRA as a 3d cavity field on a defined mesh.

transverse distribution of a bunch 0.9 m downstream of the solenoid is plotted for three different solenoid field strength.

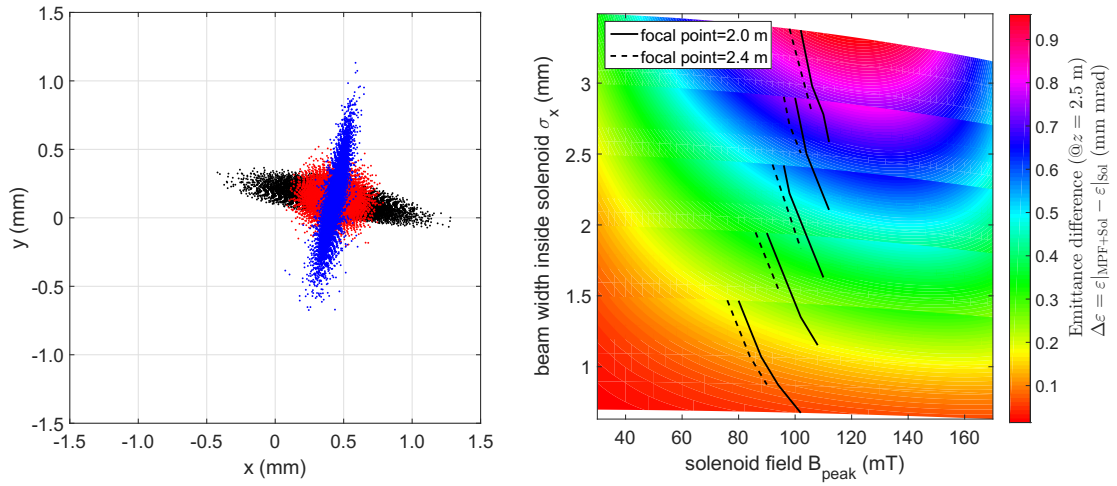

Figure 7.8: Impact of the reconstructed multipole fields on the transverse electron phase space. Left: Plot of three transverse particle distribution of a bunch at 0.9 m downstream of the solenoid. Here, the solenoid has a field strength of 100 mT (black), 102 mT (red) and 104 mT (blue). Right: Contour plot of the solenoid emittance impact as difference of uncompensated real solenoid to the emittance of the ideal solenoid. The values are plotted as function of the peak solenoid value B_{peak} and the beam width in the center of the ideal solenoid. The dashed and the full line describe the necessary peak field to focus the incoming beam to $z = 2.0$ m or $z = 2.4$ m downstream from the cathode. (Solenoid position: $z_{\text{solenoid}} = 0.5$ m downstream from the cathode)

Thereby the centroid of the bunch has still a small offaxis position which is the result from the dipole field components. More conspicuous are the elliptical effects by the quadrupole components. They change the focal lengths in the horizontal and vertical plane, producing the elliptical distributions. The Larmor rotation of the solenoid produces a further rotation in the transverse plane. The resulting coupled phase space is also relevant for the projected emittance calculation of the horizontal or vertical plane, depicted in the right plot of Fig. 7.8. The sampled horizontal normalized emittance is subtracted of the emittance growth of the ideal solenoid (see Chapter 2.5.3) and plotted as a function of the ideal solenoid peak field and the beam width in the center of the solenoid. The multipole components produce obviously an additional emittance growth of several 100 nm-rad, up to more than 1 mm-rad for large bunch sizes inside the solenoid. However, this effect concerns only the 2d projected emittance. The complete 4 dimensional phase space emittance is in first order still independent of the multipole fields. Thus, it is necessary to correct the coupling in the transverse plane to compensate this emittance effect. This can be done with skew quadrupoles. Furthermore the steering of the beam can be compensated by steerer magnets.

7.5.1 Compensation of the solenoid quadrupole errors

A skew quadrupole focuses and defocuses in a transverse system which is $\pi/4$ rotated to the Cartesian coordinate system. An initial elliptical beam in the transverse plane with a rotation angle $\neq \pi/4$ is rotated by the skew quadrupole, as well. Thereby, a single skew quadrupole can be used for a overcompensation of the beam rotation, where the ellipse

is further rotated until the beam has no coupling in the x-y-plane at a defined position downstream of the magnet. The bunch still has a rotation in the transverse plane, so that the emittance compensation works only for this position. The best solution would be a combination of two skew quadrupoles and two standard quadrupoles, which can compensate the rotation, the coupling and the ellipticity of the beam. Unfortunately this is not possible in the spatial limits inside the Gun module or at GunLab. To test the concept of a single skew quadrupole downstream of the solenoid, the first steerer magnet between the solenoid magnet and the HOM coupler is used. Thereby, the coil connections of the steerer magnet are changed into a skew quadrupole configuration. Therefore, the electrical contacts of each coil was directly conducted out of the cryostat, where the coils can be connected with each other to create a single skew quadrupole or two individual steerer magnets. A further numerical calculation was performed to check whether the single skew quadrupole, with the given behavior of the air coils, can compensate the projected transverse emittance. Therefore, the field for the skew quadrupole configuration was calculated. The resulting effective magnetic length and the maximal gradient were used to determine the transfer matrix of the magnet. For this test the magnet was placed 500 mm downstream from the solenoid center which is more than in reality but easier to handle for the tracking. The bunches, tracked through the superimposed solenoid field, were transfered by the skew quadrupole matrix and the drift matrix. The final phase space distribution was sampled at the same position as before. The minimum emittances were determined by scans of the skew quadrupole gradient. The result is plotted in Fig. 7.9.

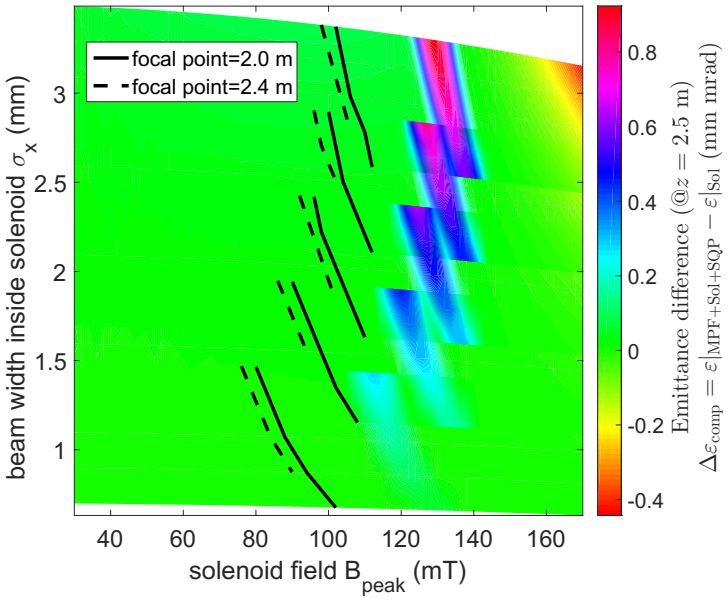

Figure 7.9: Results of the multipole compensation in the solenoid using a skew quadrupole magnet downstream of the solenoid. Plot of the emittance difference between the real solenoid with compensated multipole influences and the emittance growth of the ideal solenoid (compare with Fig. 7.8). The differences are plotted as a function of the solenoid peak field on axis and the beam width in the center of the solenoid.

It shows the emittance difference of the scan minimum to the ideal solenoid. For nearly all peak field values and beam sizes inside the solenoid the skew quadrupole can compensate the additional emittance growth of the multipole field terms ($\Delta\varepsilon \approx 0$). Only the region near 130 mT peak field still has high emittance values. These are setups where the focal point of the beam is inside the skew quadrupole magnet. Therefore, the magnet cannot

focus the beam, resulting in emittance values that are approximately independent from the quadrupole gradient. However, the compensation works for scenarios with a focal point in front of the skew quadrupole ($B_{\mathrm{peak}} > 130$ mT), as well. For focal points next to reference point in GunLab (solid line in Fig. 7.9), the skew quadrupole in the Gun module can compensate the emittance growth completely. The necessary gradients are quite small so that the installed air coil magnets can handle the compensation. Afterwards, the steered beam can be adjusted with the steerer magnets in the cold and warm section.

7.6 Discussion of the solenoid measurements

This chapter has shown that it is quite complicated to reconstruct the multipole field terms in a superconducting solenoid without absolute references of the magnet position or the magnetic axis. Therefore, a measurement system is desirable that detects the final position of the magnet in the cold system with respect to the laboratory system. Unfortunately, this could not be realized for the measurement at the GSI. Therefore, a method was developed and tested to reconstruct the axis of the solenoid magnet with respect to the laboratory system. The measured magnetic field components were transferred into this determined solenoid system and analysed by a multipole reconstruction algorithm based on a Fourier analysis. They resulted in multipole field terms, dominated by the dipole and quadrupole components with non-negligible amplitudes. These additional fields to the ideal solenoid field produce a beam steering and bunch asymmetries, including bunch coupling. Furthermore the projected emittance of a passing electron bunch is increased which can be locally compensated by a skew quadrupole magnet downstream of the solenoid. The installed steerer magnet between the solenoid and the HOM absorber in the Gun module can be reconnected to a skew quadrupole for this procedure and requires the necessary gradients to compensate the beam coupling of the reconstructed quadrupole components. Additional to the unknown field axis of the solenoid magnet, the limitation in the radial position of the sensor is a problem for the reconstruction of higher order multipole terms, because the amplitudes of the n-th multipole depends on r^{n-1}. Thus, an anti-cryostat with an increased aperture radius would also increase the sensitivity of the multipole reconstruction.
However, the main problem is the reproducibility of the measurements. The yoke of the magnet consists of five pieces which have to be connected to each other. Thereby it is not clear that a second measurement with a dismantled and than rebuilt solenoid produces the same results. Thus the reconstructed multipole amplitudes can only be used as an estimation for the field of the solenoid installed in the Gun module. This has to be tested directly with the electron beam in GunLab.

Chapter 8

Status and outlook

GunLab is a compact test facility for the characterization and optimization of photoelectron injectors. In GunLab, all injectors for bERLinPro will be commissioned. In this thesis the concept, the design and the characteristics of the GunLab system were presented in details. Main tasks of GunLab are the visualization of the complete six dimensional phase space of electron beams, extracted from a photoelectron injector, and to test new beam instrumentation concepts. Central elements of the beam diagnostic devices are the phase space scanner system, an optimized spectrometer system and a transverse deflecting cavity (TCav). Furthermore a new beam halo measurement technique will be tested to observe low intense electron distributions next to the beam core with a flexible setup and a high dynamic range. This visualization cannot be achieved by a standard camera. A conclusion and further steps for the presented measurement systems and methods, developed in the context of this thesis, are presented in the following.

Phase space scanner

The phase space scanner system consists of two dipole magnets, that cause a parallel movement of the beam over a slit mask downstream the magnets. These magnets, based on air-core coils with a $\cos\theta$ design, were optimized for a high integrated dipole field with suppressed higher order multipole amplitudes. This was achieved by self-developed and tested computational tools for field calculation, combined with a particle tracking tool for numerical field integration. The magnetic field of the optimized magnet design was tested by numerical simulations of the complete phase space scanner system. These simulations show no significant contribution of the scanner magnets on the reconstruction error. The error of the system is dominated by the slit mask geometry and is in the order of $\approx 5\%$ for beam parameter settings with $\delta < 5\%$, $Q_{\text{bunch}} < 20$ pC and a beam focus near to the slit mask. For the construction of the optimized magnet an aluminum yoke was milled and used as a former for the winding. The thermal effects and the electric isolation inside the scanner magnets were tested for DC currents up to 5 Amps. The resulting magnetic field map was compared with the calculated field. Thereby, the transverse and longitudinal field profiles confirmed the calculated magnetic field with a relative variance of 8% by a relativemeasurement uncertainty of 5%. The small differences in the profiles can be explained by a necessary design change of the aluminum yoke, that results in a smaller enclosed coil area. The measured field amplitude provides a horizontal scan range of up to 6 mm for an electron beam with a momentum of 3 MeV/c and an electric coil current of 3 Amps. Both scanner magnets were installed at the GunLab beamline and serially connected to generate two opposite orientated dipole magnets.
Further tests of the scanner system are scheduled during beam operation such as a cal-

ibration of the transverse beam off set to the beam momentum. It can also be used for fast energy measurements in the beamline without the spectrometer dipole.

Beam core and halo observation

Viewscreen monitors (VSM) are used in the GunLab beamline for the investigation of the transverse beam core and possible beam halo distribution. A design for the VSM was developed, that consists of a luminescence screen with normal incidence to the beam, a highly reflecting aluminum mirror in the vacuum and an AVT CCD camera. It was shown that for standard GunLab operation the charge density of the bunches is well below the saturation threshold of the luminescence screens. Thus, the emitted light intensity is directly correlated to the incident transverse charge density on the viewscreen. Furthermore a multiscreen station was constructed. It allows an investigation of the influence of different viewscreen materials and parameters on the beamsize measurement. These optical measurements can be compared with an implemented wire scanner.
It was also shown that the dynamic range of a standard CCD is not useful for the investigation of possible beam halo, with particle densities several orders of magnitudes smaller than the beam core region. An optical system was developed based on image separation, where the original image of the charge density distribution on the viewscreen is separated into high intensity and low intensity regions. This is achieved with a digital micromirror device (DMD). A DMD consists of several squared mirrors which can be individually flipped between two angle positions (± 12 degree). The idea is to observe both regions individually with two CCD cameras and sample the resulting images with the full dynamic range of the respective cameras. Thereby, a combination of both images at the original image plane on the DMD, results in a combined dynamic range of both cameras for the complete image.
To test this technique for the GunLab system, an optical breadboard was designed and fabricated, where the DMD is positioned at the intersection point of the three optical beamlines; the central transfer line and two camera imaging lines. The small distortions of the images on the CCDs, due to Scheimpflug imaging, were compensated by a linear coordinate transformation from the DMD to the CCDs. Hardware and software of the system were step-by-step tested up to the recombination of a separated image.
Thereby, it was detected, that the image separation works. However, some modifications are necessary to achieve the estimated dynamic range of 10^6. The main problems originate from light pollution inside the system, resulting from light scattering in the beamlines and reflecting parts in the system. This limits the measurement of the low intense regions of the image. Further apertures need to be installed in front of the beamline to reduce these stray light sources. With the modified setup it is planed to determine the dynamic range of the system by specific light sources, as well.
The complete DMD system will be installed at the diagnostic beamline of GunLab.

Solenoid

In Chapter 2 the principle and the influence of a solenoid magnet on the beam emittance were discussed. Here, the solenoid is used to focus the electron beam and to compensate the projected emittance by a realignment of the individual transverse bunch slices. Aberrations and a misalignment of the magnet itself produce emittance growth by non-linear phase space distortions. Thus, a motorized mount (Hexapod) was installed in the Gun module to correct the solenoid axis with respect to the beam axis during beam operation. Furthermore the field of the actual solenoid magnet was measured in a test cryostat at

the GSI. A method, based on a Fourier transformation, was developed to analyze the measured field map. It allows to reconstruct the solenoid field axis and to determine the higher order multipole field terms. The analysis of the multipole field terms resulted in additional field components of $\approx 4\%$ with respect to the radial field of the solenoid. They were dominated by the quadrupole and dipole fields. The reconstructed profiles of these components could not be allocated to a single geometrical error of the solenoid. However, the profiles could be used to calculate the impact on the electron beam. The additional fields produced beam steering and elliptical beam shapes, as well as an additional projected emittance growth. This can be compensated by a skew quadrupole downstream of the solenoid. The first steerer magnet in the Gun module can be used for this, by rewiring the individual accessible coil connections outside the cryostat. The solenoid was installed in the Gun module including the mechanical hardware and the anti-collision system of the Hexapod.

Measurement setups

Several measurement routines were developed for the characterization of bunch length, transversal phase space, sliced phase space and beam momentum. The bunch length can be measured with a TCav, which will be installed at GunLab in autumn 2017. With the defined setup it is possible to measure the length of a bunch down to 100 fs. In combination with two quadrupole magnets, the sliced and projected emittance of a bunch can be measured. Therefore, the beam size downstream of the TCav is sampled as function of the focal strength of both magnets, to reconstruct the initial phase space configuration. This method and the numerical realization were presented in this thesis, as well.
In this context, a spectrometer dipole was designed for GunLab in collaboration with the Moscow state university. Thereby, the transverse imaging of the electron beam was optimized for a high sensitivity on the momentum spread. Field profile calculations and construction work were realized by the MSU. The calculated field was used to determine the achievable resolution of the momentum spread δ of the electron beam. In combination with a slit mask at the reference point, a relative measurement error below 2% was detected for initial δ values between 0.5‰ and 5%. The final spectrometer magnet and the calibration electronics were installed at the GunLab beamline and already tested.

Overall GunLab system

At the time of the end of this PhD thesis the GunLab beamline is in the final realization phase. All components of the GunLab system are installed and the cabling is finished. The diagnostic insertions are tested and the viewscreen monitors (VSM) are adjusted. Furthermore the steerer and scanner magnets, as well as the spectrometer dipole, are connected and their field polarity was checked. The operation license is granted and therefore the beamline is ready for beam operation.
Also, the Gun module is closed and the vacuum and cryogenic systems are tested. First performance tests of the Gun cavity are running. The photocathode transfer system is connected to the Gun module and has been vacuum checked, as well. Thus, GunLab is ready and well characterized to support the start of the operation and commissioning of the first SRF photoinjector for bERLinPro. First electron beam is planed for July 2017.

Appendix A

Appendix

A.1 Fast charge measurement system for sub-pC bunch charges

GunLab is designed for SRF photoelectron injectors, generating electron beams with a wide range of beam parameters like transverse emittances, energy or energy spread. The parameter with the most dynamic range is the average beam current which depends on the charge of the extracted bunches and the repetition rate of the drive laser. The installed viewscreen monitors (VSMs) in GunLab can handle this huge range using linear dependent viewscreens which can detect single electrons and CCDs with long integrations times to sample extremely low light intensities, as well. However, for a direct measurement of the bunch charge this system is not applicable.
Therefore, a Faraday cup is installed in addition with electronic read out to sample the incident electrons. The crucial element hereby is the electronic read out which has to handle a high dynamic range with bunch charges between a few fC and 100 pC and repetition rates of 10 Hz up to 10 kHz. The solution is a triggered charge measurement system which is designed for the sampling of small charge pulses.

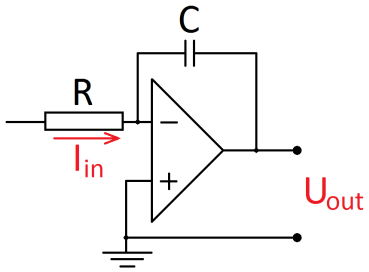

Figure A.1: Integrator circuit, consisting of an operation amplifier (OPAmp).

The central element is the ACF2101, a gated integrator based on an extreme low noise operation amplifier (OPAmp). The principle of an integrator is depicted in Fig. A.1. The electric charge Q at the input is sampled on a laser trimmed capacitor $C = 0.1$ nF, resulting in a voltage U.

$$U = \frac{Q}{C} = \frac{\int I \mathrm{d}t}{C} \tag{A.1}$$

The non-inverted input is connected to ground. The OPAmp compensates the voltage difference between the inverted and the non-inverted input, which results in a negative

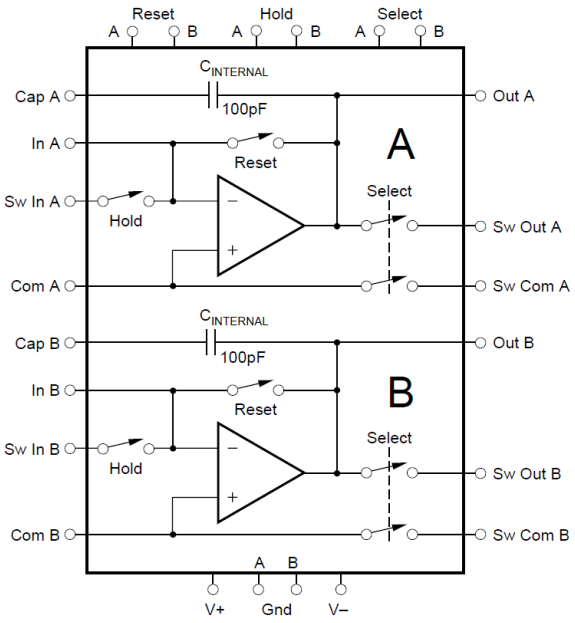

Figure A.2: Two integrators in an ACF2101

value of the capacitor voltage at the output of the OPAmp. Thus, the voltage on the inverted input corresponds to a virtual ground. The ACF2101 consists of two integrators with voltage offset noises of less than one nV. Furthermore three externally controlled switches (S1, S2, S3) are implemented to define different measurement modes. The complete circuit is depicted in Fig. A.2 with the important parameters shown in Tab. A.1. The maximum switching rate of 100 kHz for the measurement modes allows a bunch-by-bunch measurement for the typical GunLab repetition rates. The switches S1 and S3 connect the input and the output of the circuit with the OPAmp. S2 works as a gated resistor which can discharge the capacitor to reset the charge integration. All three switches are based on two decoupled MOSFETs to minimize the impact on the charge measurement to a few atto coulomb. With these switches, three different operation modes of the circuit can be defined:

1. an integration mode, to sample the charge current at the input (S1=ON,S2=S3=OFF),

2. a readout mode, to put the voltage signal on the output line without any further charge sampling (S1=S2=OFF,S3=ON),

3. a reset mode, to discharge the capacitor (S1=S3=OFF, S2=ON),

With two integrators in a push-pull scanning mode a quasi continuous charge measurement can be achieved. Thereby one integrator is in the integration mode and the second integrator is in the readout or reset mode.

A.1.1 Time signal generation

For a triggered bunch-by-bunch measurement the laser clock is used as a reference clock which determines the time of measurement and the combined time for readout and reset of the ACF2101. All three modes have to be triggered by this signal realized with an external Clock Signal Generator.

Parameter	value	units
max input current	100	μA
integration slew rate	3	V/μs
impedance of switches		
OFF	1000	GΩ
ON	1500	Ω
Reset Mode (Settling Time)	5	μs
Internal Capacitor	100	pF
Accuracy (typ)	0.5	%
Output		
Nonlinearity	$\pm$0.005	%FSR
Total Output Noise	2	μV *rms*
Op Amp Bias Current (typ)	100	fA

Table A.1

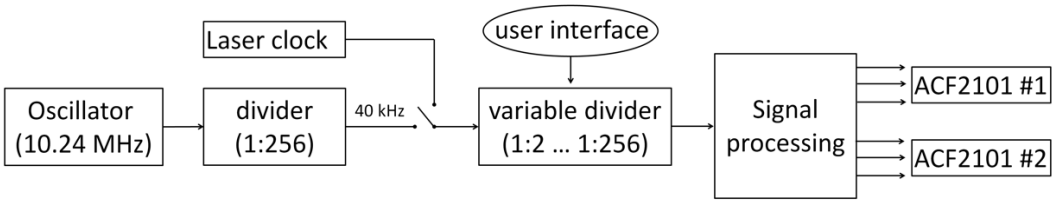

Figure A.3: Draft of the Clock Signal Generator electronics. The resulting frequency for the integration is defined by an user interface. The number of sampled bunches per integration cycle can be determined from 1 to 128.

The scheme of this circuit is depicted in Fig.A.3. It can work with an external trigger signal (laser clock signal) or an internal signal source with a frequency of 300 Hz - 40 kHz which is based on a 10.24 MHz TTL oscillator with a relative accuracy of 10^{-4}. The central part of the electronics is the signal processing that produces the four signals for the measurement modes: INT = integration mode, RD = read mode, RST = reset mode. The timing of the four signals is depicted in Fig. A.4. Thereby the read-out mode time is equal to the integration mode time, so that the RD-signal for ACF2101#2 is the inverse INT-Signal of ACF2101#1. Only the RST signals have to be individually placed for both integrators at the end of the read out phase, respectively.
The absolute time value for the reset of the ACF2101 has to be ≈ 5 μs to ensure that the capacitor is completely discharged. These specifications for the signal process are solved with a tunable TTL circuit, depicted in Fig. A.5. The resulting board for the signal processing is shown in Fig. A.6).
Timing accuracy of the four modes and jitter of the signals were studied by a 2 GHz oscilloscope and were determined to be in the nano second scale (Fig. A.7) which is negligible for the time range of the measurements of at least 25 μs.

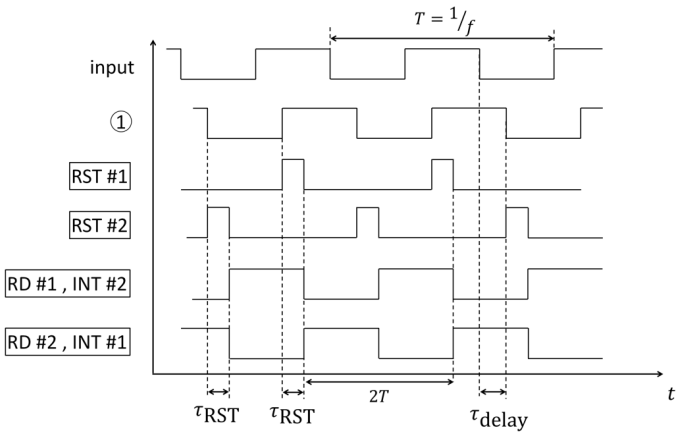

Figure A.4: Timing of the four signals (Fig. A.5) to control ACF2101 charge measurement. Important here are reset time $\tau_{\mathrm{RST}} \approx 5\ \mu$s and the delay time between the master clock and measurement.

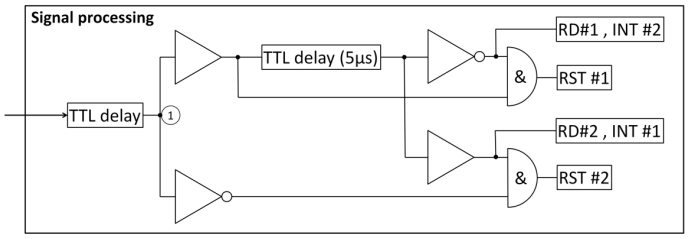

Figure A.5: TTL scheme of the signal processing for the four mode signals to control the charge integration electronics.

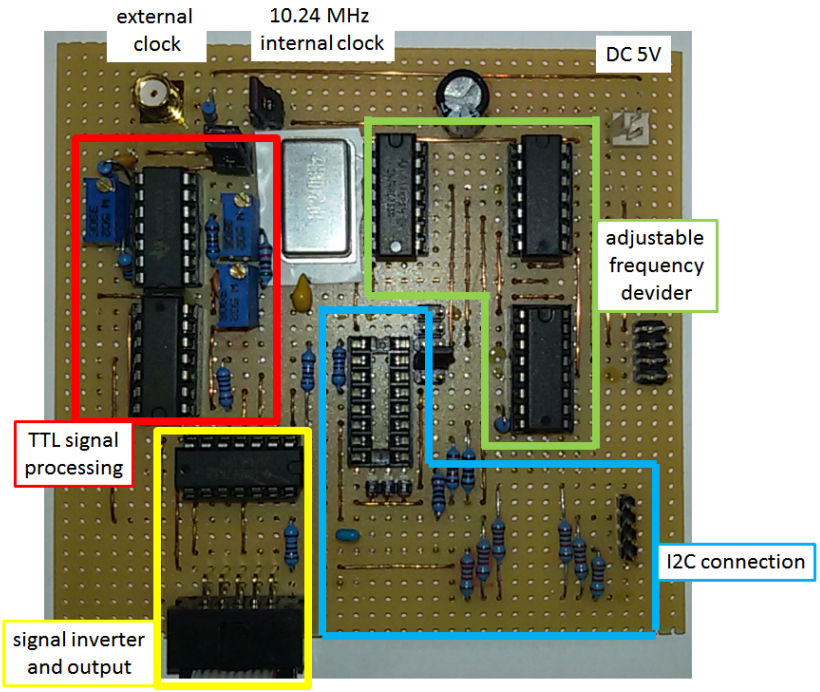

Figure A.6: Electronic board for the signal processing for the CMB timing. It consists of an internal clock and an adjustable frequency divider, controlled by an I2C interface.

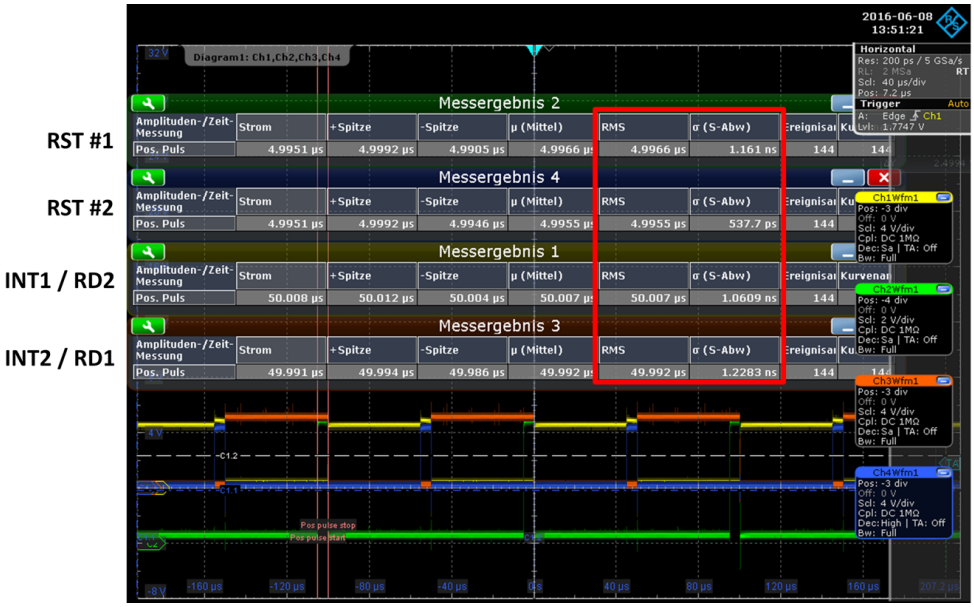

Figure A.7: Snap shot of the signal measurement with an oscilloscope. The red box marks the average and the *rms* time values of the four mode signals

A.1.2 Charge measurement board

An electronic board was developed which consists of the integrator circuits, a constant current source and an overcharge protection system. The layer design of the prototype of the charge measurement board (CMB) is depicted in Fig. A.8.

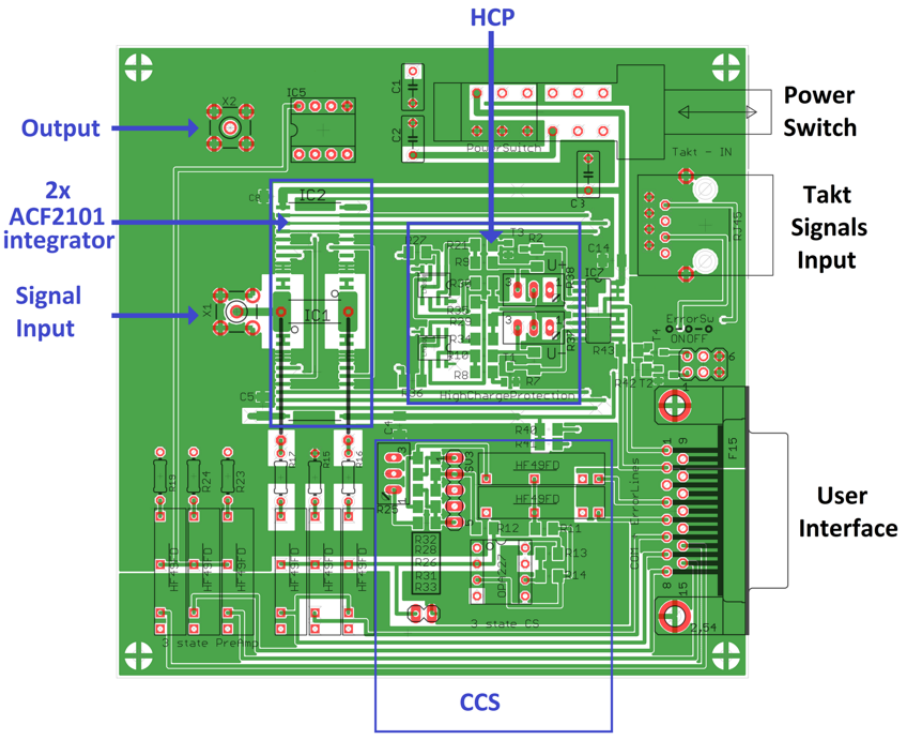

Figure A.8: Design of the CMB top layer, including the integrator system, the Constant Current Source (CCS) and the High Charge Protection (HCP). Input and Output of the signals are realized by SMA connectors.

A special feature of the ACF2101 circuit is the optimized integrator for small positive charges on the internal capacitor up to +1 nC (U = 10 V). However, there is no specification for the negative charges of the sampled electron bunch. This behaviour of the ACF2101 was studied with a first test circuit. It was observed that for negative charges up to 100 pC the output signal has the same linear dependency as for positive charges. Thus, this circuit can be used directly for the single bunch measurements at GunLab in standard mode. Nevertheless, an additional constant current supply (CCS) with an adjustable positive current was installed to compensate the negative bunch charge. With the CCS system a possible long term damage of the circuit can be avoided. Furthermore higher bunch charges as 100 pC can be sampled. Therefore, the CCS is connected to two integrators by two identical high precision resistors (1‰). Each integrator samples the half of the CCS current. The output voltages ($U_{\#1}$ and $U_{\#2}$) of both integrators are subtracted afterwards by an INA114 (extreme low noise instrumentation amplifier). The resulting voltage U_{INA} at the output of the INA114 is then the sampled charge signal of the electron bunch.

$$U_{\#1} = -I_{\mathrm{CCS}} \cdot t_{\mathrm{INT}} \cdot C \tag{A.2}$$

$$U_{\#2} = (-I_{\mathrm{CCS}} \cdot t_{\mathrm{INT}} + Q_{\mathrm{bunch}}) \cdot C \tag{A.3}$$

$$U_{\mathrm{INA}} = U_{\#2} - U_{\#1} = Q_{\mathrm{bunch}} \cdot C \tag{A.4}$$

Thereby, neither the absolute value nor an extreme stability of the current value are

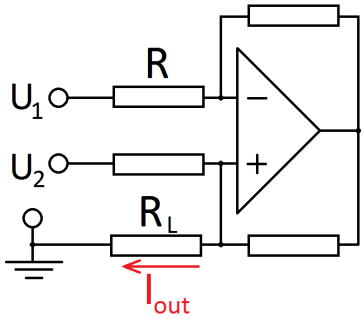

Figure A.9: Constant current source (CCS), basing on an OP-Amp with four identical resistors. The current I_{out} is independent of the resistor R_L.

important, as long as the integrated charge of the CCS is larger than the absolute charge signal, but smaller than the maximal charge for the ACF2101. The CCS used on the board consists of an OPI227 circuit which is an low noise OPAmp and is depicted in Fig. A.9. If all four resistors have the same value R, the current I at the output to ground is given by

$$I_{\text{out}} = \frac{U_1 - U_2}{R} \tag{A.5}$$

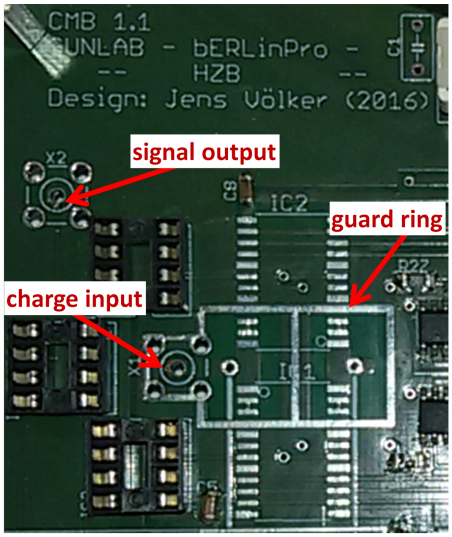

Figure A.10: Image of a part of the CMB test board, before soldering the integrator circuits (ACF2101).

Three user selectable voltage differences are implemented for the CCS on the board. They result in current values of 200 nA, 2 μA and 20 μA. Thereby, each integrator samples half of the charge flow.
For the automation of this board some safety elements are necessary to secure the electronics in case of an overcharge or overvoltages. Therefore, additional differential amplifiers are implemented as discriminators which sample the output signals of the ACF2101 and switch off the INT mode in case of voltage values which exceed or fall below defined thresholds, respectively. These thresholds are -0.9 and $+9.9$ V. The 0.1 V difference to the absolute allowed maximal values is a result of the limited discriminator delay time ($\leq$ 10 ns). Even for high input currents up to 1 mA the integration can be switched off

before the integrator reaches the charge limit. Additionally to the RST of the ACF2101 a flipflop is switched on. It sends an error signal to the read out system. The reset of the flipflop requires user input.
Input charge and output voltage signal of the board are realized by 50 Ω SMA connectors. The user interface and the digital signals are individually grounded, with respect to the input charge signal. The charge input line is completely enclosed with a ground layer up the ACF2101. The ground level of both SMA connectors are connected to this layer. To suppress currents on the surface of the board, a guard ring around the charge input line was implemented (Fig.A.10). First tests with the trigger signals were performed. Further charge measurements could not be realized in the context of this thesis. However, the infrastructure was realized; DC power supply for all necessary voltages, a precision signal generator, synchronized to the laser clock, including an amplifier for the signals for up to ten integrator boards. With this equipment a first test of the Charge Measurement Board (prototype) is scheduled.

A.2 Solenoid optimization

A solenoid magnet is comparable to a thick optical lens. Non linear effects like aberrations or distortions produce errors in the focal length and in the image plane. These errors translate to an emittance growth of the electron bunch as it passes the magnet. For low emittance photoinjectors it is important to decrease this solenoid effect which is one of the biggest contributors to the transverse emittance. Therefore, a study of the solenoid geometry was performed to minimize the non-linearities and thereby also the emittance growth. The second point for this study was to use an air-core coil design for the superconducting (SC) solenoid, without a ferromagnetic return yoke which could produce residual fields.
El-Kareh [17] gives in his book a detailed theoretical description of several kinds of aberrations and how they depend on the shape of the solenoid field. The spherical aberration has the most impact on the non-linearities of the solenoid magnet. This value can be calculated by a path integral through the magnetic lens and depends on a combined function of different deviation and power terms of the magnetic field profile. Thus, the aberration terms can be minimized by an optimization of the solenoid field. However, the field profile and the geometry of the magnet are not bijective which means that there is no unique geometry for a given field profile. Therefore an analytical optimization of the field profile is not useful. The here discussed method is based on a direct geometry optimization. The following steps were performed:

- definition of a promising magnet geometry,
- calculation of the magnetic field,
- determination of the spherical aberration.

For the field calculation the field solver Poison/Superfish was used, which calculates the field profile for given geometry. The solenoid aberration is determined by the path integral through the field, which can be solved by a particle tracking with ASTRA, numerically. All three steps are combined in MATLAB scripts for the final field optimization. They are discussed in the following sections

Geometry of the solenoid model

There are several technical and model specific requirements for the solenoid design in the Gun module. The first point is the spacial limitation inside the cryostat. This means that the complete length of the solenoid is limited to 300 mm. Furthermore the solenoid has to be positioned between the SRF photoinjector and the HOM coupler of the cavity. At this position the beamtube has an huge diameter of 106 mm. The inner aperture of the solenoid has to be large enough to handle this beamtube. To increase the number of degrees of freedom for the variation of the field profile, at least two SC coils are implemented. In case of two independent coils for the magnet, the field profile can be changed during beam operation. Thus it is possible to measure the influences on the beam emittance as function of the profile.
Fig. A.11 shows an example of such a two coil solenoid geometry as a radial cross section. Around the solenoid coils a Mu-metal shield is implemented. It suppresses magnetic fields of external sources in the coils of the magnet and vice versa. The SC coils can be influenced by external magnetic fields at the phase transition at the critical temperature of the superconductor. However, small magnetic fields in the coils (Eddy currents) can also produce magnetic flux next to the SC cavity.

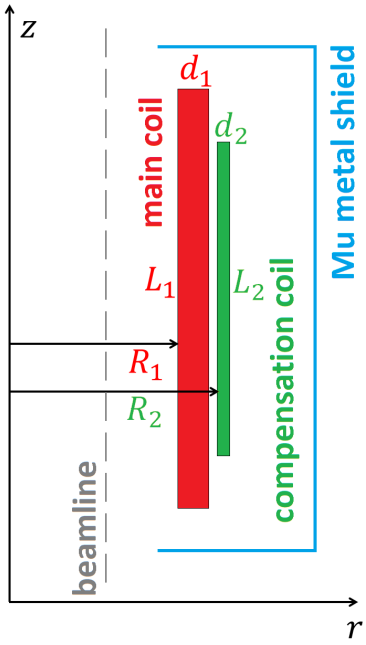

Figure A.11: Geometry of a symmetric two-coil solenoid (radial cross section), including a Mu-metal shield.

For the final optimization, the parameter of both SC coils are varied. This implementation is explained in the following section.

Field calculation and aberration determination

The field calculation was done with the field solver Poisson/Superfish. For a given input file, consisting of the magnet geometry in the r-z plane (rotational symmetric magnets), it calculates the radial and longitudinal field components on a defined mesh. The mesh properties, as well as the material specifications of the magnet, are also defined in this file. The calculation results in the field profile on axis of the given geometry, which is translated into an ASTRA readable solenoid field for the particle tracking.
An initial particle distribution was defined for all trackings. This distribution consist of 50 mono-energetic electrons, uniform distributed on the horizontal axis between 0 and 10 mm, without any divergence or space charge. It is tracked through the calculated field and is sampled downstream the solenoid. For the analysis the same definition for the spherical aberration is used as in Eq. 2.33. Thus, the radial offsets r_f of the particles are measured at the defined focal point of the magnet.

$$r_f = \tilde{C}_S r_i^3 \tag{A.6}$$

A cubic fit of these offsets as function of the initial horizontal position results in the spherical aberration coefficient $\tilde{C}_S$. This was done for each chosen magnet geometry.

Geometry variation

The geometry example in Fig. A.11 shows the important geometry parameters for a longitudinal symmetric two-coil solenoid, consisting of a main and a compensation coil. These parameter were varied during the optimization: the radial position R, the length L and the radial thickness d for both coils. All six parameter were defined by a random

generator in the geometry boundaries given by the Mu-metal shield. The overall length of the coils had to be less then 280 mm and the maximal radial size 165 mm. Furthermore an overlap between both coils was prevented that determines a variation of the coil thickness in the range of 5 to 25 mm. The last parameter for the field calculation is the ratio of the electric currents I_2/I_1 in the main and the compensation coils. This current ratio was varied over a wide range of ± 1.

Results

The spherical coefficient C_S was determined for each solenoid geometry. The obtained values are plotted in Fig. A.12 as a function of the effective length of the solenoid field, which is given by Eq. 2.15.

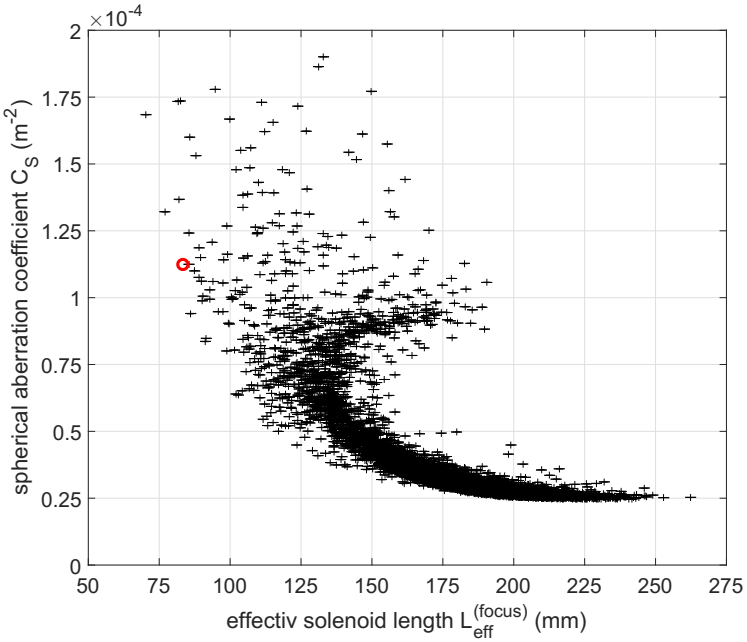

Figure A.12: Spherical aberration coefficients C_S as function of the effective length of the solenoid field $L_{\text{eff}}^{(\text{focus})}$. The black crosses represents the coefficients for the two-coil solenoid geometry. The red circle describes the C_S value for the actual solenoid in the Gun module.

The plot shows the tendency for small spherical coefficients to be caused by large effective lengths of $\approx$ 200 mm. A further increase of $L_{\text{eff}}^{(\text{focus})}$ does not improve C_S. The results of the used geometries can be compared with the spherical aberration of the field from the actual used solenoid for the Gun module (red circle) with $C_S \approx 1.12\ 10^{-4}\ \text{m}^{-2}$. The geometry with the smallest spherical aberration coefficient ($C_S \approx 0.246\ 10^{-4}\ \text{m}^{-2}$) is listed in Tab. A.2.

R_1 (mm)	R_2 (mm)	L_1 (mm)	L_2 (mm)	d_1 (mm)	d_2 (mm)	I_2 / I_1
108	140	277	186	20	6	0.58

Table A.2: Geometry parameter for the two-coil solenoid producing the smallest spherical aberration in this study.

This coil geometry consists of two quite long coils with a positive current ratio. There are other magnet geometries with similar C_S values, that consist of shorter compensation coils

and negative current ratios. Those geometries can have the advantage of less construction effort. Nevertheless, for the following calculations of the emittance contribution of such a solenoid design, the geometry with the smallest C_S was used. The results are presented in the following section.

Emittance impact

The optimal field profile was used to measure the impact on the transverse emittance, performed similar to the tracking in Chapter 2.5.3. Thereby it was considered, that the effective length of this solenoid is ≈ 2.5 times longer than the actual used solenoid in the Gun module. This results in smaller peak field values to focus the beam with the same focal strength. Fig. A.13 shows the resulting emittance growth of this tracking.

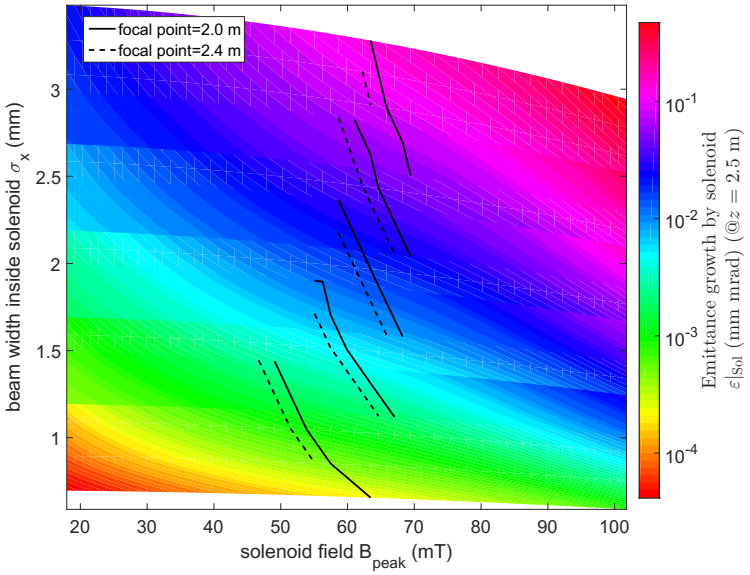

Figure A.13: Plot of the transverse emittance growth of the optimized two-coil solenoid as function of the magnetic peak field value and the beam size in the center of the magnet. The necessary field strength values are marked, focusing the given beam to $z = 2$ m (solid line) and $z = 2.4$ m (dashed line).

For similar focal length and beam size values for the optimized solenoid with respect to the actual solenoid the emittance growth is decreased by a factor of ≈ 4.3, which is consistent with the value of the ratio of the spherical coefficients (≈ 4.56) for both solenoids. This correlation is also given by the Eq. 2.35, which describes the emittance growth as function of C_S and the fourth power of the *rms* beam size in a solenoid.

In conclusion the spherical aberration is the driving contributor for the emittance growth of a solenoid. However, it's impact can be reduced by an optimization of the magnet geometry. One possible solution is a two-coil solenoid without a return-yoke. Such a solenoid geometry can fulfill the requirements of the actual Gun module. The optimization of this design minimized the spherical aberration coefficient resulting in a smaller emittance growth.

A.3 Transfer Matrix Reconstruction Algorithm (TMRA)

Magnetic and electric fields deflect charged particles, depending on the field distribution and the field amplitude. However, the stand alone field distribution cannot be used directly to calculate the phase space transformation of a passing particle beam. The solution of the path integral through the field is necessary. This is done by an algorithm that reconstructs the transformation of the phase space, separated into linear, as well as non-linear correlations, with the initial phase space distribution. For a complete transfer analysis, 36 different correlations have to be reconstructed only for the linear transformation. These are the elements of the 6×6 transfer matrix for the complete 6 dimensional phase space. For the reconstruction, a special particle distribution is defined to minimize statistical effects on the analysis. This distribution consists of 101 particles for each phase space axis. Thus, the final distribution consists of 606 particles. For higher order calculations, correlated axes coordinates have to be considered.
The particle distribution is tracked through the field and is analyzed afterwards with a polynomial fit second order[a] of the final position $V_{1,i}$ as function of the initial position $V_{0,j}$ (see Eq. 2.4).

$$V_{1,i} = a_{i,j} \cdot V_{0,j}^2 + b_{i,j} \cdot V_{0,j} + c_{i,j} \tag{A.7}$$

Thereby a and b are the squared and linear correlation terms and c is the absolute offset. All three terms depends on the used axes-combination (i, j). For the linear reconstruction, the matrix elements are equal to the linear elements b of this fit.

$$R_{i,j}^{(\text{linear})} = b_{i,j} \tag{A.8}$$

The solutions for higher order correlation reconstructions are given as tensors with the same order as the correlation order. They can be used to describe the tracking through non-linear magnets, such as sextupole magnets. In the following the linear reconstruction is used to examine the transfer matrices from the field data of the spectrometer dipole for GunLab and the scanner magnets.

A.3.1 Transfer matrix of the spectrometer dipole

The transfer matrix of the spectrometer dipole is necessary to verify the optimum imaging system. The TMRA was used with the correctly aligned and rotated field of the spectrometer magnet described in Chapter 4.2.5. For the calculation, the start position for the TMRA was varied, which is the first drift space between object plane and the spectrometer position. The tracked particle distribution were sampled 1 m behind the magnet. This distribution was put in the calculation for the matrix elements.
With the resulting matrix elements $R_{1,2}^{(\text{TMRA})}$ and $R_{2,2}^{(\text{TMRA})}$, the distance ΔL to the image plane of the system relative to the end position of the tracking can be determined as a function of the initial drift length:

$$\tilde{R} = R_{\text{drift}}(\Delta L) \cdot R^{(\text{TMRA})} \tag{A.9}$$

$$=> \tilde{R}_{12} = R_{12}^{(\text{TMRA})} + \Delta L \cdot R_{22}^{(\text{TMRA})} \stackrel{!}{=} 0 \tag{A.10}$$

$$=> \Delta L = -R_{12}^{(\text{TMRA})} / R_{22}^{(\text{TMRA})} \tag{A.11}$$

[a] For this kind of problem a polynomial fit of second order improves the results also for the linear coefficients.

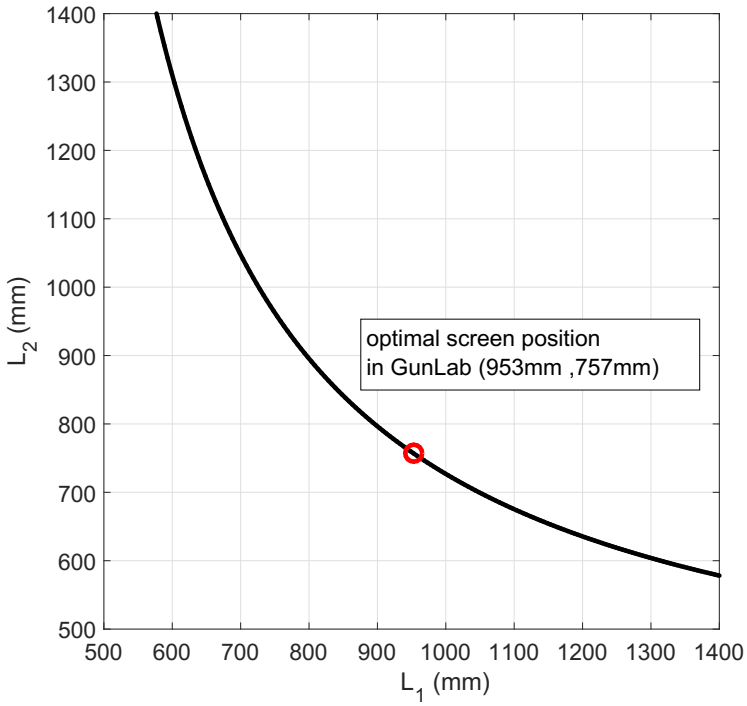

Figure A.14: Correlation plot between the both drift lengths in the spectrometer system. The length values are defined relative to the flange position of the dipole vacuum chamber. The red position marks the optimum position for the actual drift length L_1 in GunLab.

The result is a plot of the distance L_2 as function of L_1 (Fig. A.14). The L_1 and L_2 values are the lengths between the flange positions of the spectrometer vacuum chamber and the object and image plane, respectively. The final transfer matrix for the physical lengths at GunLab is given in Eq. A.12.

$$R^{(\text{dipole})} = \begin{pmatrix} -0.793(4) & \pm 2e-4 & \pm 8e-4 & \pm 2e-4 & 0 & 0.7213(9) \\ -1.884(4) & -1.2060(2) & \pm 9e-4 & \pm 2e-4 & 0 & 0.74723(4) \\ 0 & 0 & 0.1908(2) & 1.17532(3) & 0 & 0 \\ 0 & 0 & -0.8465(2) & 0.02411(8) & 0 & 0 \\ -0.7415(6) & -0.85769(2) & 0 & 0 & 1 & 0.0483(8) \\ 0.0029(3) & 0 & 0 & 0 & 0 & 1.0016(1) \end{pmatrix} \quad \text{(A.12)}$$

All values are defined in SI units. The number in the brackets are the uncertainties of the last decimal digit. Matrix elements with a value equal to zero, like $R_{31}^{(\text{dipole})}$, have only numerical uncertainties of the Matlab calculation in the range of 10^{-16}. The shown matrix describes the phase space transformation of a 3 MeV/c beam. Almost all matrix elements are quite independent from the bunch momentum. The influences can be determined only as higher order effect. However, the $R_{56}^{(\text{dipole})}$ element has a strong correlation with $p_z c$ in the range of 1 to 8 MeV/c which can be seen in Fig. A.15.
This algorithm was also used to reconstruct the transfer matrix of the phase space scanner doublet, implemented in the phase space scanner system.

Transfer matrix of scanner magnet doublet

The scanner magnets are described in Chapter 5. The combination of two identical dipole magnets with opposite orientated fields results in a parallel movement of the beam in the horizontal plane. Also, in this combined magnetic field the transfer matrix was determined

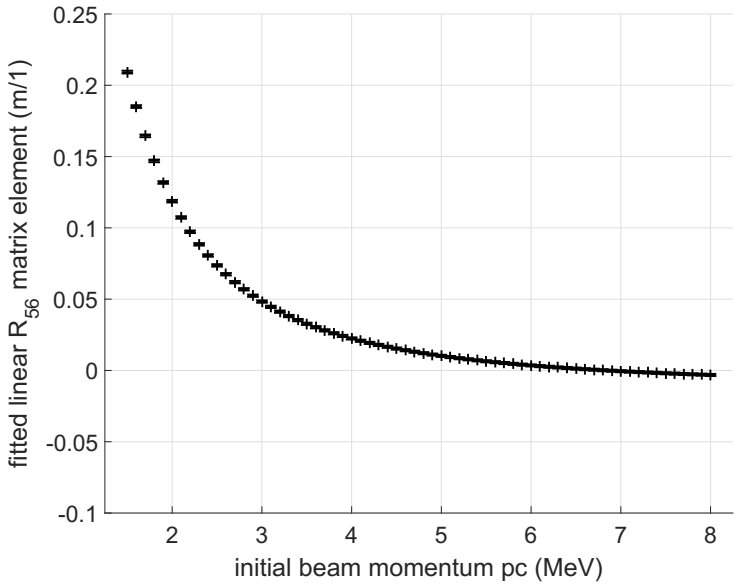

Figure A.15: Correlation of the matrix element $R_{56}^{(\mathrm{dipole})}$ and beam momentum.

as a further test of the field linearity. Additional to the linear transfer matrix of the TMR algorithm, the absolute position as function of the field amplitude is interesting, as well.

The phase space scanner system was implemented in ASTRA with two scanner magnet fields at 0.6 m and 0.72 m. The tracking was performed with the same distribution as used for the spectrometer dipole. It starts at zero and was sampled 1.5 m downstream. Furthermore, eight different off axis positions were defined, resulting in 8 defined field amplitudes for the tracking with respect to the kinetic energy of the beam.

The effect of the beam momentum on the matrix elements is qualitatively the same as for the spectrometer dipole. Only the R_{56} element depends on the initial momentum. All other terms are quite independent. The first important function is the correlation between the absolute offset term of the final distribution and the defined off axis position. The results are plotted in Fig. A.16, together with the absolute slope of the beam downstream of the scanner magnets, which should be zero for a parallel movement. It shows that the beam movement is directly correlated to the defined offset parameter for the measurement with an uncertainty of less than 1%. However, a small non-linear slope dependency was detected in the range of 10^{-2} mrad for beam offsets above 3 mm, which is neglectable for the GunLab system.

In the following the horizontal (Fig. A.17) and vertical (Fig. A.18) transfer matrix elements are plotted as a function of the defined horizontal beam offset of the scanner magnets. Fig. A.19 shows the matrix elements for the correlation of transversal and vertical phase space.

These plots can be used to analyze the properties of the scanner magnet doublet, as well: The horizontal magnification of the system (R_{11}), depicted in Fig. A.17(top-left), is equal to one with respect to the fit uncertainties, for beam offsets less than 5 mm. For larger beam offsets it is reduced in the range of 2%. Also, R_{12} and R_{34} (top-right in Fig. A.17 and Fig. A.18) show a difference of $\leq 4\%$ to the 1.5 m of an equivalent system as drift matrix, switched-off magnets. In general, the differences in the horizontal matrix elements with respect to a switched off magnet is $< 2\%$ for offsets up to 8 mm. However in the vertical matrix elements the differences can achieve differences up to $\approx 8\%$. For beam offset less than 2 mm, which is the important range for the phase space scanner

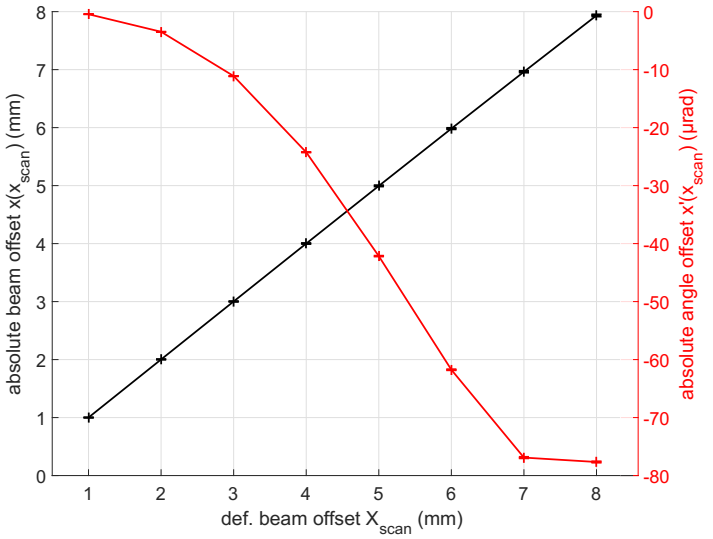

Figure A.16

system, all differences are less then 1‰. This results explains, why it was not possible to reconstruct a significant impact of the scanner magnets on the simulated measurements in Chapter 5.3.
As an exception, the R_{16} element is plotted in Fig. A.19. It describes the correlation between momentum spread and horizontal position. The plot shows that R_{16} depends linearly on x_{scan}, which is the dominating impact on the transformation error of the scanner magnets. As an example: a beam with an *rms* beam size of 0.25 mm and a 5% momentum spread is 2 mm shifted horizontally by the scanner magnet doublet. Downstream the magnets, the beam size results in $\sqrt{(0.25\text{ mm})^2 + (-2\text{ mm} * 0.05)^2} \approx 0.27$ mm or 8% beam size growth. This influence of such high momentum spread values were also observed in the simulated measurments of the phase space measurement system.

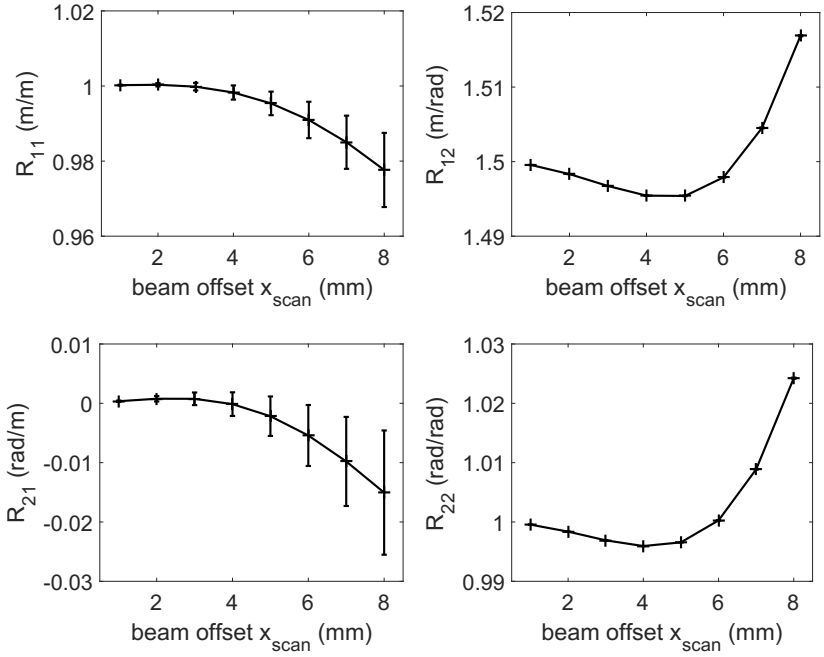

Figure A.17: Matrix elements of the horizontal phase space transformation as a function of the horizontal beam offset downstream the magnets x_{scan}.

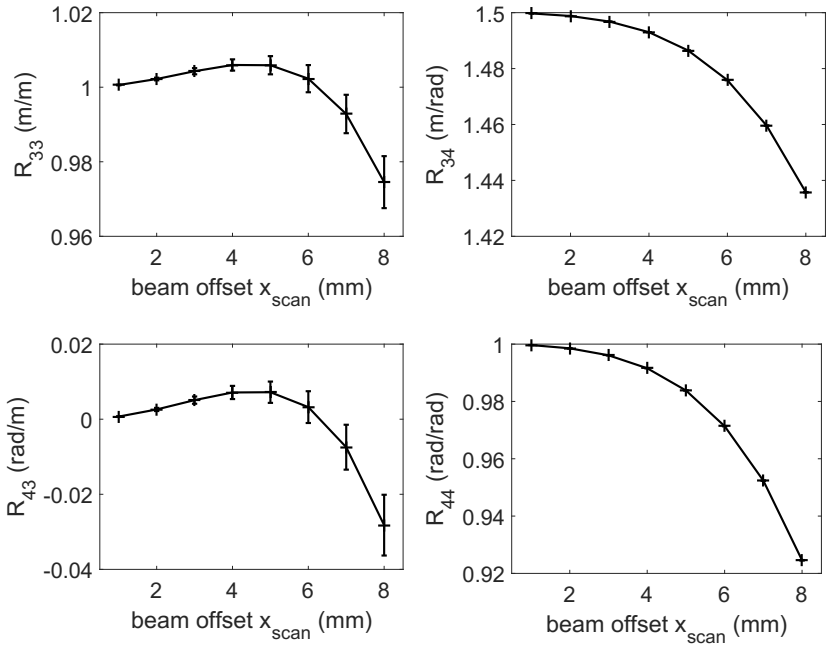

Figure A.18: Matrix elements of the vertical phase space transformation as a function of the horizontal beam offset downstream the magnets x_{scan}.

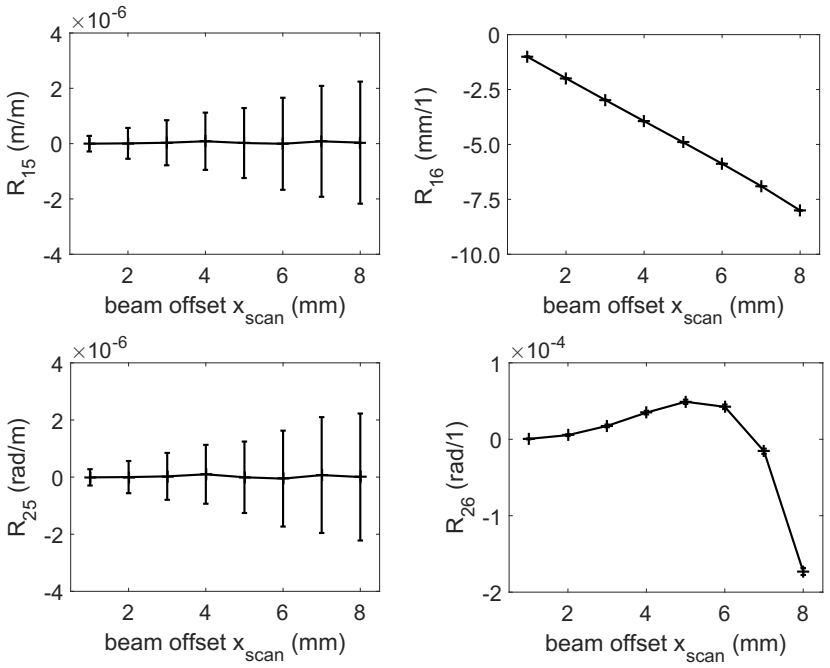

Figure A.19: Matrix elements of the correlated phase space transformation (x-z-plane) as a function of the horizontal beam offset downstream the magnets x_{scan}.

A.4 Image transport line for the DMD system

One important part of the complete DMD system, described in Chapter 6, is the beam transport line between the view screen and the DMD itself. It has to combine the following aspects:

- transport of the emitted light from the viewscreen at the diagnostic cross (DC5) to the DMD,
- correct magnification of the object plane onto the image plane,
- a maximal light transmission coefficient through the beamline,
- generating of an uncorrelated distribution on the DMD.

The beamline has to bridge a long distance between the viewscreen and the DMD, because of a high radiation level next to the electron beamline and limited space in this part of diagnostic beamline of GunLab. The best position of the DMD plate is roughly 800 mm below the electron beamline inside the girder. There, it is enough space to install the complete plate with all setups, including the radiation protection, as well. Hence, the distance between screen and DMD has to be in a range between 1400 mm and 1800 mm. The needed magnification value for the optics results from the ratio of viewscreen diameter and the DMD size ($|M_{\text{screen}->\text{DMD}}| = 0.413$).
The last requirements were met by an optics calculation and a parameter optimization. The optics calculation was based on a linear transfer matrix calculation by the defined drift and focal lengths of the beamline system. To optimize the five requirements (imaging, magnification, overall length, transmission coefficient and the uncorrelated distribution) at least five degrees of freedom for the optical system are necessary. Thus the beamline has to consist of more than two lenses. These lenses are commercially achromatic lenses with standard focal lengths.[b]
All parameters of such a beamline with a defined number of lenses were randomly variated ($> 10^8$ samples) and the transfer matrix of the beamline was calculated. For the further analysis only those parameter settings were sampled which fulfill the above define geometrical and optical requirements. Afterwards, the light transmission coefficient C_T and the resulting image distribution were determined by an optical tracking. The transmission coefficient is the ratio of passing light intensity I_{end} to the incoming light intensity I_1 (Fig. A.20). Another, but usually unknown value, is the incidence coefficient C_I which is the ratio of incoming intensity to the initial intensity I_0 on the object and describes the relative acceptance of the system. The product of both coefficients is the total intensity ratio $C_{\text{tot}} = I_{\text{end}}/I_0$. The coefficients depends on the beamline parameters. A sampled beamline setting with a huge beam size magnification inside the system has also a huge intensity loss at the aperture of the lenses and thereby a small C_T value. An example of the optical tracking through a beamline with a low transmission coefficient is shown in Fig. A.20. It shows a beamline with three lenses (blue lines) with a imaging of the screen (green) onto the DMD (red). The gray areas describe the projected light tracks between the lenses. The numbers above are the intensity at this position relative to the initial intensity at the object. In this example 95% of the intensity behind the first lens is lost on the way to the second lens which results in a $C_{\text{tot}} < 1\%$. In addition to the

[b] Standard values are $[75, 80, 100, 150, 180, 200, 250, 300, 400, 500, 750, 1000]$mm.

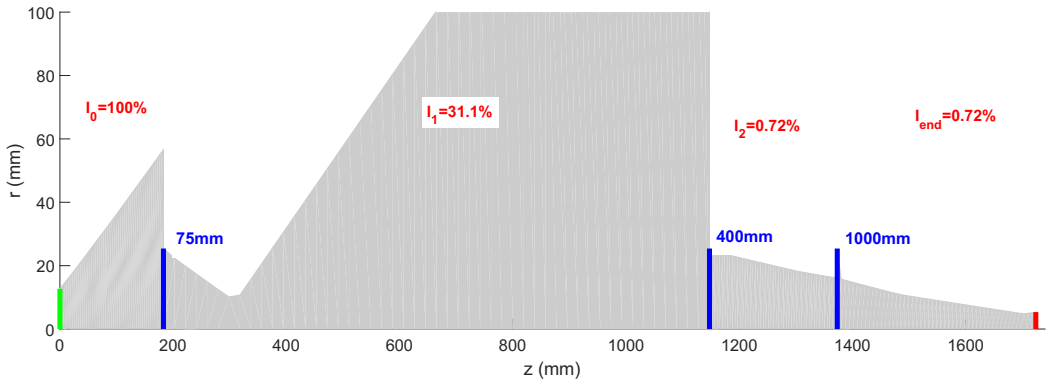

Figure A.20: Example of a beamline that image the screen (green) on the DMD (red). It consist of three lenses (blue) but has an extremely low light transmission coefficient. The gray area is the radial projection of the phase space which passes a lens and drifts further downstream to the next lens or the DMD.

transmission coefficients, the correlation term ρ of the accepted distribution on the image plane was analyzed for all sampled beamline settings.

$$\rho = \frac{< xx' >}{< x^2 > \cdot < x'^2 >} \stackrel{!}{=} 0 \tag{A.13}$$

For the final analysis, only beamline settings were used which also fulfill this uncorrelated beam requirement. The transmission coefficients and the incidence coefficients for these beamline settings are plotted in Fig. A.21. It shows the samples with the highest total intensity ratio for a three lens (red), a four lens (green) and a five lens system (blue). The resulting C_{tot} scale is plotted as dashed lines.

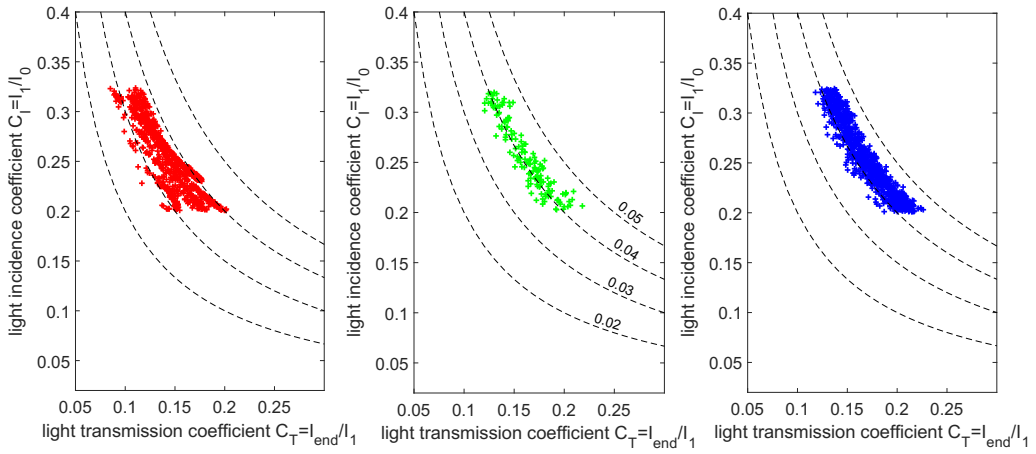

Figure A.21: Results of optical tracking through beamline settings which fulfill all geometrical and optical requirements. For a better presentability the results were separated by the number of lenses per system (red = three lenses, green = four lenses, blue = five lenses). All three coefficients depend on the initial phase space distribution at the object plane and cannot be interpreted as absolute values. Only the relation among the beamline settings are relevant.

In all three plots the C_I-values are similar for all three systems. However, C_T can be improved by using beamline setups with more than 3 lenses. The differences between the best parameter settings for the four lens and the five lens system are so small that a four lens system is preferred, to reduce the complexity of the system.

Bibliography

[1] G. R. Neil, et al., "The JLab high power ERL light source",Nuclear Instruments and Methods **A 557**, 9-15, (2006)

[2] E. A. Antokhin et al., "First lasing at the high-power free electron laser at Siberian center for photochemistry research", Nuclear Instruments and Methods **A 528**, 15-18, (2004)

[3] S. L. Smith, "The status of the Daresbury Energy Recovery Linac Prototyp (ERLP)", Proc. ERL07, (Daresbury, UK, 2007)

[4] M. Sawamura et al., "Performance and Upgrade of the JAERI ERL-FEL", Proc. PAC03, (Portland, Oregon US, 2003)

[5] S. Sakanaka et al., "The First Beam Recirculation and Beam Tuning in the Compact ERL at KEK", Proc. of LINAC14 (Geneva, Switzerland, 2014),

[6] B. Kuske, N. Paulick, A. Jankowiak, J. Knobloch, "Conceptual Design Report bERLinPro", tech. rep., Helmholtz-Zentrum Berlin für Materialien und Energie, Helmholtz-Zentrum Berlin für Materialien und Energie, Institut Beschleunigerphysik und Institut SRF - Wissenschaft und Technologie, Albert-Einstein-Str. 15, D-12489 Berlin, 2012.

[7] I. N. Bronstein, K. A. Semendjajew, G. Musiol, "Taschenbuch der Mathematik" **6** (2005)

[8] K. Wille, "The Physics of Particle Accelerators", Oxford University Press 2000

[9] M. Reiser, "Theory and Design of charged Particle Beams" - Electrical Enginneering Department and Institute for Plasma Research, University of Maryland, College Park Maryland, WILEY-VCH Verlag GmbH & Co.KGaA (2004);

[10] M. Ferrario, "Space charge effects", CAS 2013, (Trondheim, Norway, 2013)

[11] L. Serafini, J. B. Rosenzweig, "Envelope analysis of intense relativistic quasilaminar beams in rf photoinjectors: A theory of emittance compensation", Phys. Rev. E **55**,7565 (1997)

[12] K. Flöttmann, "Astra (a space charge tracking algorithm)", `http://www.desy.de/~mpyflo/`

[13] M. Schmeißer, "In-situ measurements of the intrinsic emittance of photocathodes for high brightness electron beams", master thesis at the Humboldt-Universität zu Berlin and the Helmholtz-Zentrum Berlin, not published, (2014)

[14] I. Bazarov et al.,“Thermal emittance measurement of a cesium potassium antimonide photocathode”, Appl. Phys.Lett.**98**, 224101 (2011);

[15] J. Völker, “Untersuchungen zur transversalen Strahldynamik in einem Supraleitenden Hochfrequenz (SHF) Photoelektroneninjektor”, master thesis at the Humboldt-Universität zu Berlin and the Helmholtz-Zentrum Berlin, not published, (2012)

[16] J. Völker et al. “Operational experience with the Nb/Pb SRF photoelectron Gun”, Proc. IPAC12 (New Orleans, Louisiana, USA, 2012),

[17] A. B. EL-Kareh, J. C. J. EL-Kareh, “Electron Beams, Lenses and Optics”, Volume 1+2 - Academic Press, Inc. (28th January 1970);

[18] K.-J. Kim, “Rf and space-charge effects in laser-driven rf electron guns”, Nuclear Instruments and Methods **A275**,2, P201-218;

[19] E. Panofski, “Multi-Objective Optimization of an SRF Photoinjector for ERL and UED Applications”, Proc. IPAC17 (Copenhagen, Denmark, 2017),

[20] R. H. Fowler, L. Nordheim, “Electron Emission in Intense Electric Fields”, Proc. of The Royal Society **119**, 781 (1928)

[21] A. Burill et al., “Processing and Testing of the SRF Photoinjector Cavity for BERLinPro”, Proc. IPAC2014 (Dresden, Germany, 2014),

[22] A. Arnold et al., “Development of a superconducting radio frequency photoelectron injector”, NIM A (2007), p.440-454,

[23] O. Kugler et al.,“Warm Test of a Modified TTF-III Input Coupler up to 10 kW CW RF-power”, Proc. SRF09 (Berlin,Germany, 2009)

[24] A. Neumann et al.,“SRF Photoinjector Cavity for bERLinPro”, Proc. IPAC2013 (Shanghai, China, 2013),

[25] K. Halbach, R. F. Holsinger, “SUPERFISH - a computerprogram for evaluation of RF cavities with cylindrical symmetry”, Part. Acc., 7:213222, 1976

[26] Niowave Inc., `http://www.niowaveinc.com`

[27] Vishay, "transzorb - transient voltage suppressor",

[28] E. Panofski, “Virtual Cathode Diagnostics for a SRF Photoinjector Gun at bERLinPro”, master thesis at the Humboldt-Universität zu Berlin and the Helmholtz-Zentrum Berlin, not published, (2014)

[29] E. Panofski, A. Jankowiak, T. Kamps, G. Klemz, “Virtual cathode diagnostics with a large dynamic range for a continuous wave SRF photoinjector”, Proc. IPAC14 (Dresden, Germany, 2014)

[30] Physik Instrumente (PI) GmbH & Co. KG, `https://www.physikinstrumente.com/`

[31] LT Ultra-Precision Technology GmbH, `http://www.lt-ultra.de/`

[32] I. V. Bazarov, et al., “Benchmarking of 3D space charge codes using direct phase space measurements from photoemission high voltage dc gun”, Phys. Rev. ST Accel. Beams **11**, 100703 (2008),

[33] J. Teichert,“Initial commissioning experience with the superconducting RF photoinjector at ELBE”, Proc. FEL08 (Gyeongju, Korea, 2008);

[34] M. A. H. Schmeißer, A. Jankowiak, T. Kamps, J. Kühn, “CsK_2Sb Photocathode development for bERLinPro”, Proc. ERL2015 (Stony Brook, NY, USA 2015);

[35] W. K. H. Panofsky, W. A. Wenzel, “Some considerations concerning the transverse deflection of charged particles in radiofrequency fields”, Rev.Sci.Instrum. **27**, 967, (1956)

[36] S. Belomestnykh, V. Shemelin, K. Smolenski, V. Veshcherevich, “Deflecting Cavity for Beam Diagnostics in ERL Iinjector”, Proc. PAC2007 (Albuquerque, NM, USA 2007);

[37] RI Research Instruments GmbH, `http://www.research-instruments.de`

[38] Lomonosov Moscow State University, `http://www.msu.ru`

[39] I. Yu. Vladimirov, “Spectrometer for SRF gun”, Proc. IPAC2014 (Dresden, Germany, 2014);

[40] CST - Computer Simulation Technology, `https://www.cst.com/`

[41] WME Power Systems GmbH, `http://www.wme.de`

[42] C. Leroy, P.-G. Rancoita, “Principles of Radiation Interaction in Matter and Detection”, World Scientific Publishing Co. Pte. Ltd., 2nd Edition, (2009);

[43] J. Rudolph, “Instruments and techniques for analysing the time-resolved transverse phase space distribution of high-brightness electron beams”, (Dissertation, Universität Rostock, 2012) , (urn:nbn:de:gbv:28-diss2013-0019-0),

[44] M. McAteer,“Astra Simulations of Energy and Energy Spread Measurements In GunLab”, internal study, not published, (2017)

[45] S. Russenschuck, "‘Field Computation for Accelerator Magnets"’, WILEY-VCH Verlag GmbH & Co. KGaA (2010).

[46] Karl Schupp AG, `http://www.schupp.ch`

[47] W. Kühnel, “Differential Geometry”, American Mathematical Society (2002),

[48] W. K. H. Panofsky, M. Phillips,“Classical Electricity and Magnetism”, Addison-Wesley publishing company, Inc.(1*st edition*, 1955),

[49] CRYTUR, spol. s r.o., `http://www.crytur.cz`

[50] A. Murokh, J. Rosenzweig,“Limitations on the resolution of YAG:Ce beam profile monitor for high brightness electron beam”, Proc. 2nd ICFA Advanced Accel. Workshop (Los Angeles 1999)

[51] Thorlabs Inc, `http://www.thorlabs.com`

[52] R. H. Bartram, A. Lempicki, “Efficiency of electron-hole pair production in scintillators”, Journal of Luminescence **68** (1996)

[53] Allied Vision, http://www.alliedvision.com

[54] Review Articles of Hamamatsu, (03.07.2017), http://hamamatsu.magnet.fsu.edu/articles

[55] B. Lyot, "La couronne solair etudiée en dehors des éclipses", Bulletin Astronomique **6** (1930)

[56] "LASCO on the SOHO satellite" **1** (1994), https://lasco-www.nrl.navy.mil;

[57] Public picture gallery of the LASCO system, (10.01.2017), https://lasco-www.nrl.navy.mil/public_images

[58] Public picture gallery of the SOHO system, (10.01.2017), https://sohowww.nascom.nasa.gov/gallery/SolarCorona

[59] G. Haouat et al., "Halo of a High-Brightness Electron Beam", Proc. PAC 95 / HEACC 95 (Dallas, USA, 1995)

[60] H. D. Zhang, R. B. Fiorito, A. G. Shkvarunets, R. A. Kishel, C. P. Welsch, "Beam halo imaging with a digital optical mask", Phys. Rev. ST Accel. Beams **15**,072803 (2012);

[61] DLP system of Texas Instruments, http://www.ti.com/lsds/ti/dlp/dlp-overview.page (29.06.2017)

[62] ViALUX Messtechnik + Bildverarbeitung GmbH, http://www.vialux.de

[63] https://www.cells.es/en

[64] J. Campmany, J. Marcos, V. Massana "Determination of magnetic multipoles using a Hall probe", Proc. IPAC14 (Dresden, Germany, 2014)

[65] SENIS AG, http://www.senis.ch

[66] OWIS GmbH, http://www.owis.eu/

Acknowledgement

On this last page of my thesis, I would like to thank many people who have helped me in the last few years.
First of all I would like to thank Andreas Jankowiak and Thorsten Kamps. They have inspired me for the topic of accelerator physics and gave me the opportunity to go deeper into details for different subtopics within the framework of the GunLab project. In addition, they always were an important support in thematic, as well as in personal, concerns. I would like to thank my appraisers Prof. Dr. Kurt Aulenbacher and Prof. Dr. Wolfgang Hillert, as well.
In the context of the realization of the GunLab test facility, I had the pleasure of working with many people, involved in this project. I would like to thank the complete GunLab team and especially: Georgios Kourkafas, Guido Klemz, Julius Kühn, Alexander Büchel, Nina Ohm-Krafft, Axel Neumann, Oliver Kugeler, André Frahm, Emmanuel Cambas, Nicole Leuschner, Sascha Klauke, Michael Schuster, Tobias Schneegans, Ines Seiler, Rayk Horn, Andrew Burrill and Hans Kirschner.
A special thanks goes to Daniel Böhlick and Mario Schenk, for the design of the technical model of the GunLab system and the realization of the beamline hardware and electronics. They also helped me to build up and to test different measurement systems over the last years.
Furthermore, I am grateful to many of the above mentioned people for their help with the solenoid for Gun1. This also includes Kerstin Martin and Tom Beutler, who designed the test set-up, organized and supported the measurements at the GSI.
In this regard, I would like to thank all GSI colleagues, who supported the measurements: Anna Mierau, Franz Klos, Harald Weiss, Franz Walter, Mischa Weipert, Claus Schroeder. I also want to thank for administrative support: Pierre Schnizer, Carsten Mühle, Winfried Barth and Oliver Kester.
In the recent years, I did many calculations and simulations to study different beam effects and to optimize the beam parameters for GunLab, as well as for bERLinPro. Thanks for always open doors and stimulating discussions: Michael Abo-Bakr, Terry Atkinson, Hans Walter Glock, Paul Goslawski, Jeniffa Knedel, Jens Knobloch, Bettina and Peter Kuske, Aleksandr Matveenko, Meghan Jill McAteer, Atoosa Meseck and Markus Ries.
Addionally, a thank you goes to the colleagues from HZDR for their support and discussions about solenoids and gun cavities, especially: Hannes Vennekate, Jochen Teichert, André Arnold, Petr Murcek, Rong Xiang, Pengnan Lu. For their work on the spectrometer dipole, I want to thank the colleagues from the MSU, especialy Vasiliy Shvedunov and Ivan Vladimirov,
In some of the above listed groups, the following names should already been given, but I would like to thank them especially. We solved several theoretical, numerical and experimental problems, but even more we went through the ups and downs outside the lab. Thereby, jackets were lost, stones were buried, heads were banged, hats were made, server were crashed, ...
Many thanks for all the time, the many discussions, the coffee and the beer: Julia Köszegi, Eva Panofski, Stephanie Rädel, Sebastian Keckert, Martin Schmeißer, as well as Claudia.
The last part, I want to dedicate to my family (in German): Ich möchte meiner ganzen Famile für ihre Unterstützung und Motivation in den letzten Jahren danken; für all die aufmunternden Worte und den Rückhalt - gerade in den letzten Wochen. Besonderen Dank gilt meinen Eltern und Schwiegereltern, die vieles in meinem Leben erst möglich gemacht haben. Im Entstehungsprozess dieser Arbeit hat sich aber vor allem auch meine eigene kleine Familie verdoppelt. Ihr drei - Elinn (*15), Marek (*13) und Sandra - seit mein "Referenzpunkt" in diesem großen System und dafür bin ich euch sehr dankbar.

Selbständigkeitserklärung

Ich erkläre, dass ich die Dissertation selbständig und nur unter Verwendung der von mir gemäß §7 Abs. 3 der Prormotionsordnung der Mathematisch-Naturwissenschaftlichen Fakultät, veröffentlicht im Amtlichen Mitteilungsblatt der Humboldt-Universität zu Berlin Nr. 126/2014 am 18.11.2014 angegebenen Hilfsmittel und Literatur angefertigt habe.

Berlin, den 03.07.2017 Jens Völker